Corrosion of Steel in Alkali-Activated Materials

Shishir Mundra

Supervisors:

Prof John L. Provis

Dr Susan A. Bernal

A thesis submitted in partial fulfilment of the requirements for the degree of

Doctor of Philosophy

The University Of Sheffield.

Department of Materials Science & Engineering

The University of Sheffield

2018

Abstract

The alkaline environment in reinforced concrete structures allows the embedded steel reinforcement to be passivated by a thin film, composed of a complex solid assemblage of iron oxides and hydroxides. When in service, the alkalinity of the pore solution in mild steel reinforced concretes needs to be sufficiently high (pH > 9-10) to ensure the stability of the passive film. Corrosion of the embedded steel reinforcement has been identified as one of the primary causes of premature degradation of reinforced concrete structures. Corrosion of steel in concrete environments is primarily driven by either the lowering of the pH of the pore solution (leaching of alkalis, or carbonation) which can lead to uniform corrosion; or due to the ingress of chloride in significant concentrations resulting in localised breakdown of the passive film. In developed parts of the world, where the use of de-icing salts and occurrence of marine sprays (in coastal regions) are frequent, chloride ingress is one of the major causes of premature failure of reinforced concrete structures. Therefore, the durability or the service life of a structure is often described by the rate of chloride ingress, or the time required for chloride ions to achieve a threshold concentration at the steel-concrete interface.

Alkali-activated materials (AAMs) are the products of the reaction between an aluminosilicate source and an aqueous alkaline 'activator' and have galvanised significant interest within industry and academia as a sustainable and technically sound alternative to Portland cement (PC). The pore structure and pore solution chemistry of AAMs have been found to be significantly different from those of PC-based concretes; and within the class of materials that can be described as AAMs, the composition of the pore solution and the pore network vary due to the differences in the precursor chemistry. The ingress of chloride into AAMs has also been found to differ from the behaviour of PC-based concretes. The development of AAMs as an alternative to PC has seen substantial progress in the past decades, however, there still remains significant uncertainty regarding their long-term performance when used in steel-reinforced structures. This study investigates the durability of steel-reinforced AAMs through a simulated pore solution approach, understanding the interaction of the steel reinforcement with the pore solution at the steel-concrete interface, and the initiation of chloride-induced corrosion.

In the case of simulated pore solutions representative of low-Ca AAMs (such as alkali-activated fly ashes and metakaolin), the passive film on the steel rebars was complex in chemical

makeup, composed of Fe–hydroxides, oxy-hydroxides and oxides. However, in the case of high-Ca AAMs, the surface of the steel reinforcements were found to be primarily composed of Fe^{2+} species, with the inner layer being $Fe(OH)_2$ (that could potentially oxidise to a hydrated Fe^{3+} oxide if sufficient oxygen is available at later stages) and the outer layer being a Fe-S complex, possibly resembling disordered mackinawite.

The onset of corrosion or the chloride 'threshold' value in both low-Ca and high-Ca AAMs were found to be very different from PC based binders. In the case of low-Ca AAMs, the chloride 'threshold' value ($[Cl^-]/[OH^-]$ ratio) required to induce depassivation of steel was strongly dependent on the alkalinity of the pore solution, and a novel relationship to predict the onset of pitting, interlinking chloride concentration and the solubility of the passive film, given by $[Cl^-]/[OH^-]^3 = 1.25$, was developed. In the case of high-Ca AAMs, chloride-induced corrosion was usually not evidenced. The high concentration of HS^- in the pore solution of high-Ca AAMs not only creates a highly reducing environment around the SCI and hinders the development of passive iron oxide film (and creates a different 'surface' film consisting of mackinawite), but also restricts the cathodic reduction of oxygen and the formation of a macro-cell. Additionally, the influence of $[HS^-]$ and time of exposure on the chloride 'threshold' value were investigated, and for pore solutions with intermediate concentrations of HS^- (0.01 M) were found to be the most susceptible to chloride-induced corrosion.

Finally, a user-defined framework for predicting the service-life of steel reinforced AAMs (relevant to alkali-activated slags as of now) was developed that investigates diffusion of chloride in slag-based binders activated using various activators (NaOH, Na_2SiO_3, $Na_2Si_2O_5$, Na_2CO_3 and Na_2SO_4). The model predicts the chemistry of the concrete cover, and the influence of the reaction products on the chloride binding capacity of the binder used, for any user defined composition of slag and choice of activator. Based on the calculated chloride binding capacity of the binder, the model uses an explicit numerical method to estimate the ingress of chloride through the concrete cover as a function of space and time.

Table of Contents

Acknowledgments

This thesis would not have been possible without the great support I have received over the last four years, from various people within the University of Sheffield and elsewhere:

I'd like to thank my supervisors Prof. John L. Provis and Dr Susan A. Bernal for giving me the opportunity to do a PhD and working with you at the Cements@Sheffield group, and for continuously supporting and inspiring me since my undergraduate days. I would like to express immense gratitude towards your desire for me to maximise my learning and scientific output in all these years. I have thoroughly enjoyed the freedom that you have given me to carry out research, and your constant encouragement to gain a deeper insight into every aspect of the project. I will always be grateful for your friendship, guidance, and guardianship, without which I don't think I would have been able to complete this work.

Thanks to Dr Oday Hussein for training me within the cements lab and being so helpful and supportive over all these years, and without you, it would have been so difficult to get work done in the lab. Thanks to Dr Maria Criado, for helping me with the set-up of electrochemical experiments, and the countless discussions about whether steel is corroding or not. Thanks, are also due to Dr Deborah Hammond for helping me with the XPS measurements. Thanks to Dr Andrew Osbourne and Dr Joanne Holmes from Metrohm UK for helping me with any issues associated with the electrochemical kit. Thanks to Mr Kieran Nash from the Department of Civil Engineering for providing the steel reinforcement. Thanks to Dr Martin C. Stennett for training me on some of the equipment. I must also thank Mr Dinghao Liang for conducting some experiments. Thanks to Ms Nicola Stehling for helping me with MATLAB.

I must thank my colleagues in the Cements@Sheffield and the Immobilisation Science Laboratory for all the help, fun and patience over all these years. Without you guys, life in Sheffield would be quite comparable to the gloomy weather in Sheffield. Thank you to everyone else that I have worked with, met or learned from over these years, from those that I have seen present at scientific conferences and RILEM/EFC TC's and to those that I have only learned through their publications.

Thanks to European Research Council for funding my PhD under the European Union's Seventh Framework Programme (FP7/2007-2013) / ERC Grant Agreement #335928 (GeopolyConc). Thanks are also due to the MIDAS facility at the University of Sheffield

(established with the support from the UK Department of Energy and Climate Change) for allowing me to use some of the equipment.

Finally, I’d like to thank my family who have been a constant source of inspiration, support, and encouragement. Without your backing I would have never had the courage to pursue my goals.

List of Figures

List of Tables

Chapter 1: Introduction

With an annual production of around 4.6 billion tonnes, cement is by far the largest manufactured product in the world by mass, equivalent to almost 626 kg per capita – higher than average human food consumption [1]. Cement is mixed with water and mineral aggregates to produce concrete, one of the most widely used construction materials. On a volumetric basis, concrete is the second largest commodity in the world after fresh water [2]. The importance of the construction industry in the world economy is not only highlighted by the enormous volumes of cement and concrete consumption, but also by the direct and indirect employment it generates. The construction industry accounts for almost 10 % of world gross domestic product (GDP) (6.4 % of GDP of the United Kingdom in 2014 [3]) and this value is expected to rise with rapid industrialisation and urbanisation in the less developed regions of the world [4,5]. The development of a particular country is directly correlated to its built infrastructural environment, and given that the majority of the worlds' population resides in the emerging or developing economies, the demand for cement and concrete is bound to rise [6]. Figure 1-1 highlights the correlation between world population and the consumption/production of cement in the world. By 2050, only 12-15 % of the population is expected to be residing in the developed parts of the world [7], where the demand for the construction industry has saturated [8,9]. Therefore, cement consumption and the demand for construction in the following decades is going to be dominated by the less developed economies of the world.

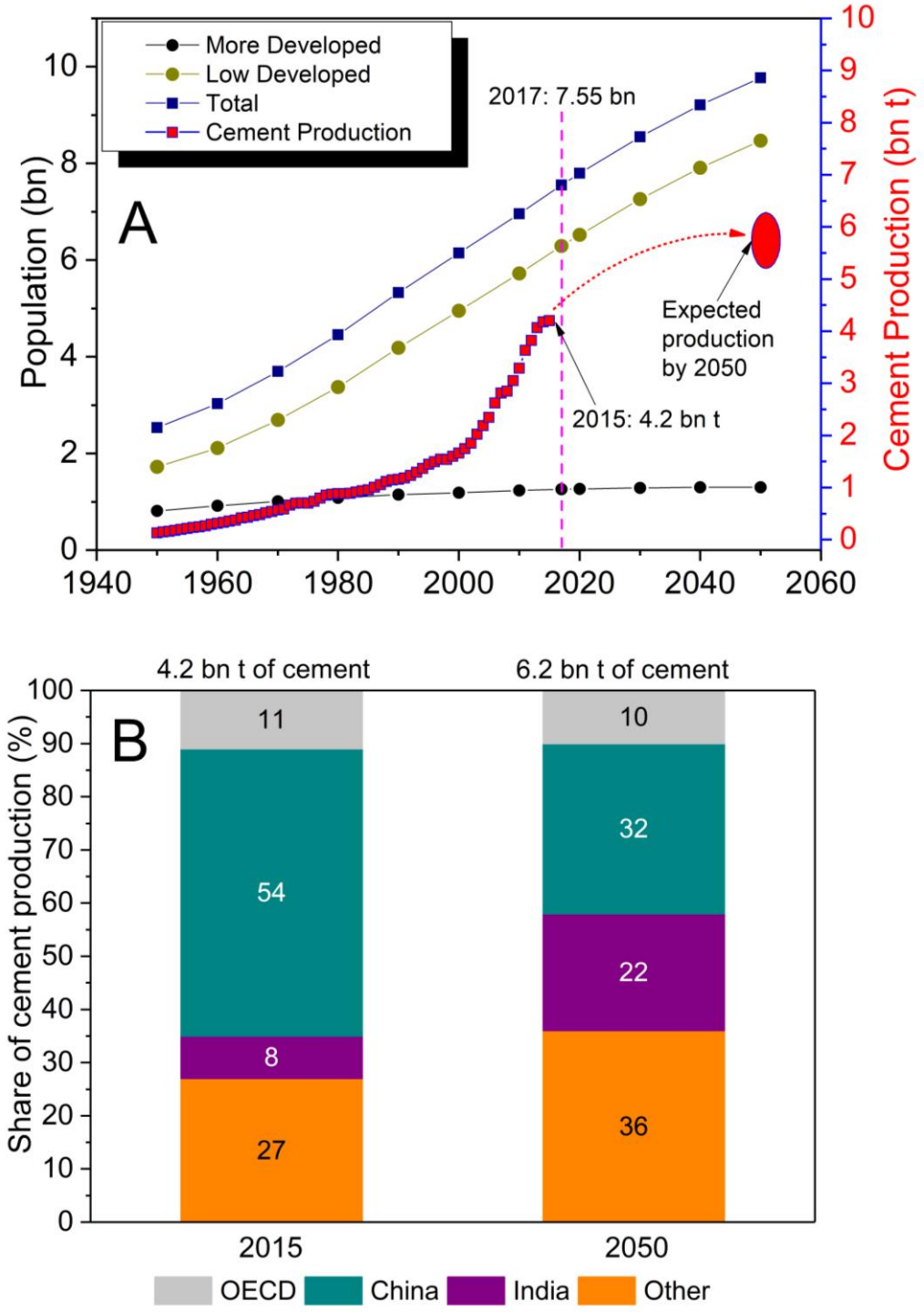

Figure 1-1: (A) Schematic showing the correlation between world population (subdivided into more developed and low developed regions of the world) and total cement production/consumption. Projected population figures (2017- 2050) have been used from the medium fertility figures of the United Nations population database [7]. Values for cement production in 2050 have been used from the studies of IEA and UNEP [1,10]. (B) Evolution of cement production across various regions of the world [1].

Of the total cement produced in the world, around 25-30 % is used to make steel-reinforced concrete [1]. This value is highly dependent on the extent of urbanisation and development of a region, e.g. Brazil and South Africa use approximately 25 % of the cement they manufacture in steel-reinforced concrete, whereas it is estimated that in the EU, this figure is around 58 % [1]. Steel-reinforced concrete can be described as a composite material, where the weak tensile and flexural properties of the concrete are compensated by the inclusion of steel reinforcement, to make the system more resilient to cracking due to the action of tensile stresses. The first use of reinforced concrete as a technique for building structures dates back to the mid-nineteenth century, when French industrialist François Coignet built a house using iron-reinforced concrete [11]. 'Critical' infrastructure in the modern world, such as transportation (bridges, tunnels, roads etc.), marine (dams, offshore platforms etc.), and construction (housing, factories etc.), rely heavily on the use of steel reinforced concrete. Owing to such a wide range of important applications, the requirement for durable and sustainable infrastructure is critical in the functioning of a society and its economy; a true reflection of that can be demonstrated by the amounts of money spent on the repair and the maintenance of reinforced concrete structures. In the UK, such activities cost the exchequer around half a billion pounds annually, whereas this figure surpasses $50bn per annum in the US [12]. In addition, it is important to highlight that the indirect costs (traffic delays, loss of productivity etc.) incurred due to these activities, are much greater than the official figures reported.

Structures built out of steel reinforced concrete are subjected to various environmental conditions such as extreme cold, marine, industrial and other severe conditions, and therefore, it is important to design structures that are durable in such extreme conditions. The performance of concrete structures can deteriorate due to various reasons such as freezing-thawing, sulfate and acid attack, however one of the most frequent problems encountered with steel reinforced concrete structures is premature deterioration due to the corrosion of the steel reinforcement. In general, the alkaline environment within concrete allows the embedded steel reinforcement to be protected by a thin passive film on the surface of the reinforcement [13]. However, this passive film is vulnerable to breakdown when there is a reduction in alkalinity in the concrete cover due to carbonation or leaching; and/or due to the ingress of chloride [14]. In the present work, chloride-induced corrosion is particularly considered. Steel reinforced concrete can be contaminated by chloride stemming from various sources such as raw materials being contaminated with chloride, de-icing salts and marine water. In most northern European countries and North America, where the majority of the roads and structures are exposed to either seawater or the use of de-icing salts is quite prevalent, chloride-induced corrosion of the

embedded steel reinforcement is a major concern. In the UK alone, the amount of de-icing salts used exceeds 2 million tonnes annually [15], and the consumption is much higher in the United States, Canada, Norway and Sweden. The costs on the repair and maintenance of chloride-induced corroded infrastructure is significant and needs careful consideration. Modern day standards such as EN 206 and ACI 318-14, take into account the various issues concerning the durability of steel reinforced structures in chloride-rich environments and have prescribed various methods to enhance the durability of such structures. However, these standards are only valid for Portland cement (PC) based concretes.

Cement manufacturing has a significant impact on the environment and is responsible for around 5-10 % of total anthropogenic CO_2 emissions [16]. The manufacturing of modern-day PC clinker can be described by the process shown in Figure 1-2. Manufacturing PC is intrinsically an energy intensive process and produces approximately 0.8 t CO_2/t of PC clinker [17]. The majority of this CO_2 (around 60 %) is produced from the decomposition of limestone during the calcination process. Therefore, in order to reduce the total CO_2 emissions from the cement industry, it is imperative to minimise the calcination of limestone. Replacing PC clinker with supplementary cementitious materials (SCMs) such as ground granulated blast furnace slag (GGBS), fly ash, limestone fillers, and calcined clay [18–21], has been an effective way of reducing the total CO_2-footprint of modern construction materials. According to the Cement Sustainability Initiative (CSI) report of the World Business Council for Sustainable Development in 2009 [10], the average PC clinker ratio in European nations was found to be around 78 %, and is expected go down further.

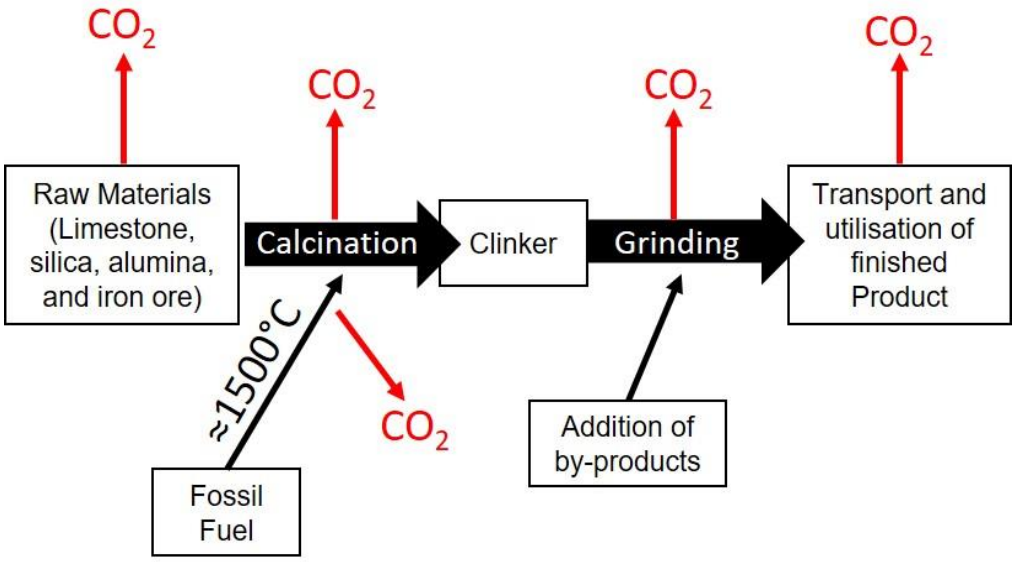

Figure 1-2: A schematic of the cement manufacturing process and the processes that are responsible for CO_2 emissions, adapted from [22]. The raw materials such as limestone, and other mineral species are mined and transported to a cement plant where they are calcined in a kiln to temperatures of approximately 1500°C. The clinker from the kiln is then cooled and ground, and other mineral additives are incorporated into the mix, making it ready for use.

Another relatively recent technology that has garnered significant academic and industrial attention is the sole use of various SCMs with alkaline solutions and avoiding any use of PC clinker. These materials are termed as alkali-activated materials (AAMs) and are the products of the reaction between an aluminosilicate source (usually industrial by-products such as slags from the iron and steel industry, coal fly ashes from thermoelectric plants, among others) and an aqueous 'activator', which supplies alkaline constituents, usually alkali-metal hydroxide, silicate, carbonate or sulfate [23–25]. It is important to mention that the feasibility of AAMs as a 'greener' alternative to PC depends strongly on the local availability of the precursors required for their production. There exist other alternative strategies and roadmaps for the development of sustainable construction materials, however they are not discussed here and the focus of this thesis is primarily on AAMs.

Figure 1-3 shows the major influencing factors that determine the service life of steel reinforced alkali-activated concrete. In the presence of chloride, the durability of steel reinforced alkali-activated materials can be broadly categorised into the transport process, which is primarily a function of the chemistry of the hydration products and their ability to

bind chloride ions, the pore structure of the cement matrix, the pore solution chemistry and its ionic strength; and the breakdown of steel passivity, which is governed by the local characteristics of the steel-concrete interface – pore solution chemistry and its pH, the chloride concentration and the chemical composition of the passive film [26].

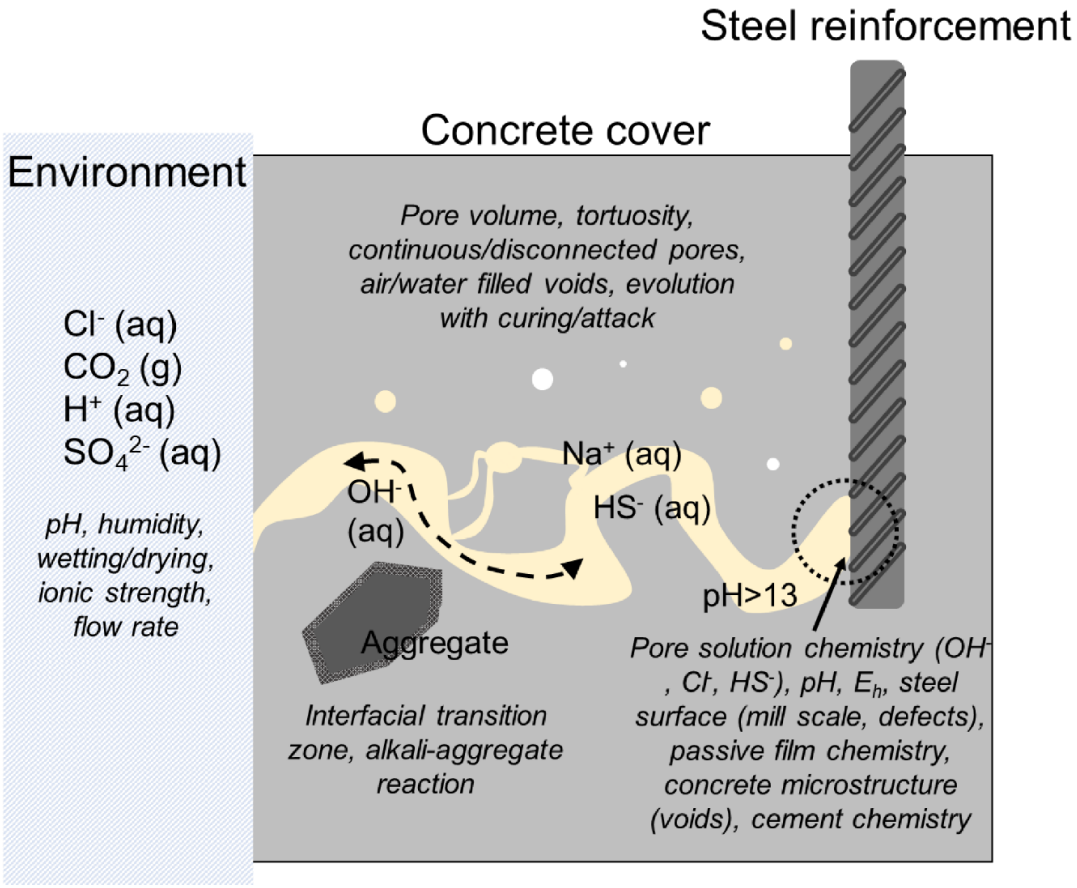

Figure 1-3: A schematic of steel reinforced alkali-activated concrete, highlighting various factors that could affect the long-term durability of structures made using AAMs. Adapted from [26].

The development of AAMs as an alternative to PC has seen significant progress in the past decades. However, there still remains significant uncertainty regarding their long-term performance when used in steel-reinforced structures. Studies concerning durability of AAMs in the presence of chlorides have mainly centred on determining transport properties such as water and chloride permeability parameters, but the focus of this thesis is based on three much-less answered questions:

- how does the chemistry of the AAMs influence the surface of the steel?

- what are the conditions required for the onset of chloride-induced steel corrosion in AAMs, once the chloride has passed through the cover concrete and begun to increase in concentration at the steel-concrete interface (SCI)?
- and can the service life of steel reinforced alkali-activated concretes be estimated using the answers to the first two objectives?

A thorough discussion of the literature is presented in Chapter 2, with a particular focus on the factors that influence the durability of steel reinforced AAMs. The chapter is broadly divided into three sections, where the first section is an overview of the chemistry and the microstructure of the concrete cover (made out of various AAMs). The second section introduces the fundamentals of steel corrosion in concrete and service life of reinforced concrete structures. The third section is a detailed description of the two major mechanisms of corrosion responsible for the premature failure of steel reinforced concretes.

Chapter 3 presents an overview of the materials and experimental methods used in this thesis. The materials used in this thesis are presented in detail. This chapter also provides the reader a brief background of each technique used in this thesis. However, detailed experimental parameters used in the thesis are specific to each of the results chapters and are discussed in Chapters 4-6.

Chapter 4 presents an electrochemical investigation into the passivation and chloride-induced depassivation of steel rebars immersed in varying alkaline environments (0.80 M, 1.12 M and 1.36 M NaOH solutions), simulating the pore solutions of low-Ca alkali-activated concretes (CaO content in the precursor $\leq$ 10 wt. % [27]). The passive film on the steel rebars was complex in chemical makeup, composed of Fe–hydroxides, oxy-hydroxides and oxides. An increased degree of passivation of the rebars was observed when exposed to solutions with higher hydroxide concentrations. The critical chloride level ($[Cl^-]/[OH^-]$ ratio) required to induce depassivation of steel was strongly dependent on the alkalinity of the pore solution, and was found to be 0.90, 1.70 and 2.40 for 0.80 M, 1.12 M and 1.36 M NaOH solutions, respectively. These values all correspond to a constant value of $[Cl^-]/[OH^-]^3 = 1.25$, which is a novel relationship to predict the onset of pitting, interlinking chloride concentration and the solubility of the passive film.

Chapter 5 presents an investigation on the passivation and chloride-induced depassivation of steel rebars exposed to simulated pore solutions representative of high-Ca alkali-activated concretes (CaO content in the precursor $\geq$ 20 wt. % [27]) such as alkali-activated slags (AAS).

The simulated pore solutions of AAS are synthesised using various concentrations of alkalinity (0.80 M, 1.12 M and 1.36 M NaOH) and 0.45 M HS^-. In addition, a detailed examination on the influence of sulfide on the passivity of steel in alkaline solutions was carried out. The passive film formed on the steel reinforcement was found to be a complex assemblage of $Fe(OH)_2$ and $Fe^{II}S_{1+x}$, instead of the conventional Fe (III) oxide film formed in low-Ca AAMs, as illustrated in Chapter 4. In highly alkaline, sulfide-containing solutions, the critical chloride concentration was found to be dependent on the concentration of sulfide in the simulated pore solutions (i.e. the reducing capability of the electrolyte), and the time that steel specimens were exposed to the electrolyte.

Chapter 6 presents a comprehensive model to understand the diffusion of chloride in slag-based binders activated using various activators (NaOH, Na_2SiO_3, $Na_2Si_2O_5$, Na_2CO_3 and Na_2SO_4). Generally speaking, the model incorporates the chemistry of the binder chemistry and the resulting diffusion of chloride through such a binder. The model allows the user to input data regarding the chemistry of the slag, the kind of activator used, the thickness of the concrete cover, and the exposure solution. Thermodynamic modelling of the simulated solid phase assemblage and the aqueous chemistry was used to quantify the maximum and minimum chloride binding capacity of a particular AAS concrete cover, and to calculate the chloride diffusion coefficient. An explicit finite element numerical method was used to estimate the concentration of chloride as a function of distance within the concrete cover and time.

The results and discussions of Chapters 4-6 are summarised in Chapter 7 and a new classification of cements is proposed based on the oxidising capability of the binder used. Recommendations for future work are also discussed in detail.

Chapter 2: Literature review

2.1 Alkali-activated materials

Alkali-activated materials (AAMs) are a group of cementitious materials that have garnered significant attention both academically and industrially as alternatives to Portland cements (PC), primarily due to their potential in reducing 'greenhouse' emissions when compared to PC [23,24,26]. AAMs are a product of the reaction between solid aluminosilicate sources (commonly referred to as 'precursors') and a highly alkaline solution (or 'activators') [23,24,26]. The aluminosilicate sources are generally industrial by-products such as fly ash, and blast furnace slags; and processed clays such as metakaolin [23]. The activators used in the production of AAMs have traditionally been concentrated alkali-metal silicate or hydroxide solutions. In addition, alkali-carbonate and sulfate solutions have also been used as activators [23].

The reaction mechanism involved in alkali activation of aluminosilicates can be described as a process of dissolution, rearrangement, condensation and re-solidification [23,28,29]. Naturally, the reaction products formed depend on the aluminosilicate source and the activating solution and given the number of variables, the materials classified as AAMs are significantly diverse in structure and chemistry. AAMs are, therefore, broadly categorised on the basis of the calcium content in the aluminosilicate source. Figure 2-1 provides a detailed schematic of the various stages involved in the process of alkali-activation of different aluminosilicate sources.

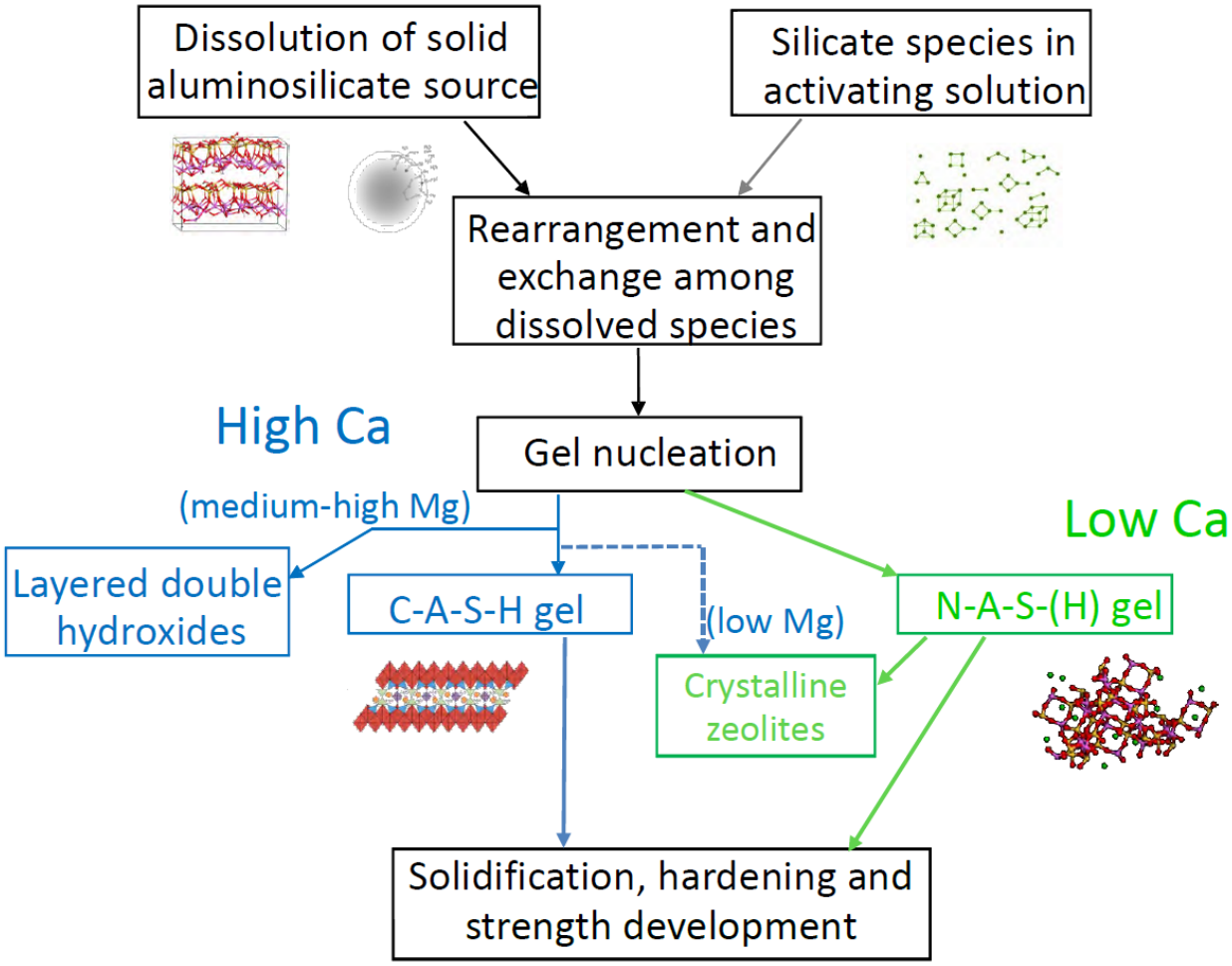

Figure 2-1: Process and reaction products of alkaline activation of a solid aluminosilicate precursor. High-calcium systems react according to the left-hand (blue) pathway, with the nature of secondary products determined by Mg content, whereas low-Ca systems react according to the right-hand (green) pathway. For each type of precursor, hydroxide activation tends to increase the ratio of crystalline to disordered products compared with silicate activation (Adapted from [30])

2.1.1 Low-Ca alkali-activated materials

Alkali activation of low-calcium aluminosilicate sources such as fly ash and metakaolin results in the formation of a highly cross-linked alkali aluminosilicate N-A-S-H gel [31] or 'geopolymeric gel', where the structural units are chemically similar to aluminosilicate zeolites but do not exhibit long range order [23,30]. Secondary reaction products are crystalline zeolites such as faujasite-type, chabazite-Na, gismondine-type, and hydrosodalites [30,32]. It can therefore be inferred that the local structures of these geopolymeric gels are in some sense

similar to the local structures of these zeolites [33]. Studies conducted by Bell et al. [34] and Provis et al. [35] using X-ray and neutron scattering techniques have confirmed the above theory. Figure 2-2 is an example of the X-ray pair distribution data showing significant local ordering in geopolymer binders below the length scale of 10Å, but highly disordered above that length scale. Bell et al. [34] also found that heating the material beyond 1100°C resulted in crystallisation of the geopolymer to a zeolite-like phase called pollucite, but did not alter the local structure below 10Å. According to "Loewenstein's principle" [36], the local ordering of Si and Al is due in part to the fact that Al-O-Al linkages in tetrahedral structures are thermodynamically not favourable [23].

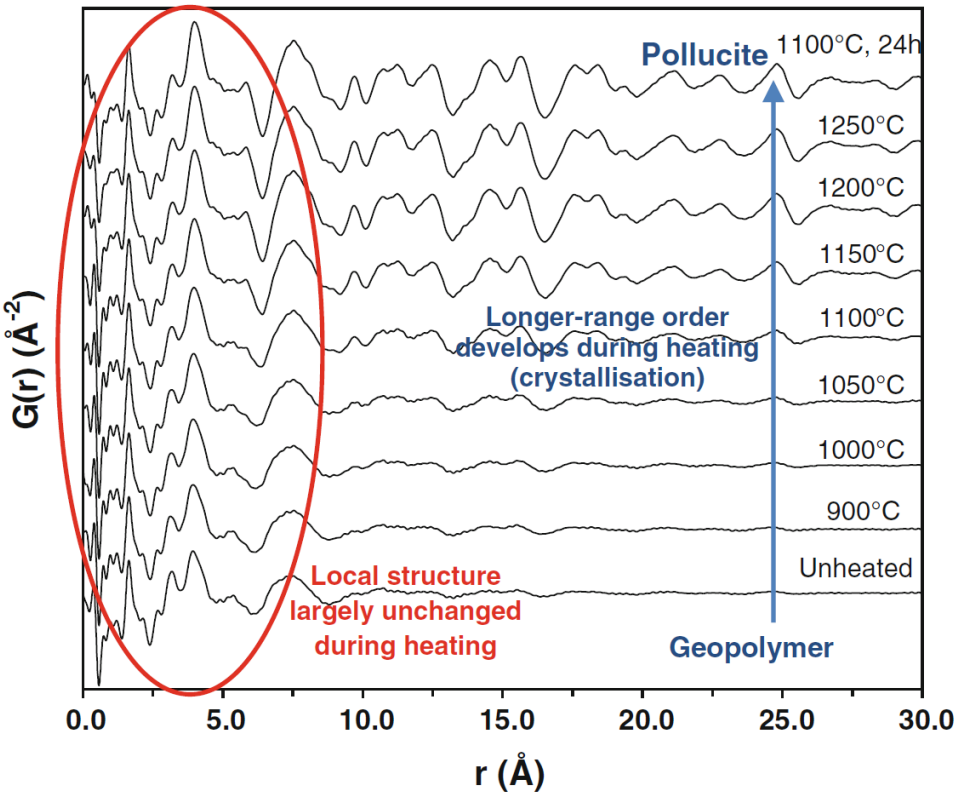

Figure 2-2: Example of X-ray pair distribution function data for a geopolymer of composition $Cs_2O{\cdot}Al_2O_3{\cdot}4SiO_2{\cdot}nH_2O$, both as-synthesised (bottom), and heated to temperatures as marked at a heating rate of 10°C/min, with no hold time for all samples other than the 1100°C, 24 h sample. Data from Bell et al [34].

Another key aspect of the structures of low-Ca AAMs is the presence of alkali cations in non-framework sites that compensate the net negative framework charge caused by the

substitution of tetrahedral Al for Si. These alkali cations are generally bound to the framework oxygen atoms, with a higher preference for larger alkali cations. Hence, Na cations are found to be more exchangeable than K cations in AAMs produced with a high-water content, raising concerns of alkali leaching from these materials [37].

2.1.2 High-Ca alkali-activated materials

High calcium alkali-activated systems where the Ca/(Si + Al) ratio is approximately equal to 1, such as alkali-activated blast furnace slag (AAS), result in the formation of an aluminium substituted calcium silicate hydrate (C-A-S-H) gel possessing a disordered tobermorite-like structure [38–40]. The degree of polymerisation and cross-linking between tobermorite chains in such gels is much higher than that observed in PC hydration, due to higher substitution of Al into tetrahedral sites (presence of Q^3 sites). This is consistent with the thermodynamic model calculations conducted by Myers et al. [38]. Figure 2-3 shows a schematic of the tobermorite-like C-A-S-H gel structure, where silicate chains are tetrahedrally coordinated in a dreierketten type chain structure [41]. Al substitution in tetrahedral sites generates a net negative charge, which is balanced by the some of the interlayer Ca^{2+} and alkalis [38,41]. In addition to that, the interlayer region also contains the water of hydration.

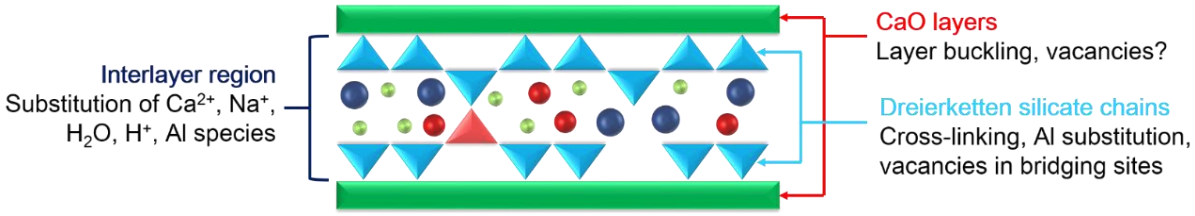

Figure 2-3: Tobermorite-like C-A-S-H gel structure. The triangles denote tetrahedral Si sites (the red triangle denotes Al substitution into one bridging site), the green rectangles denote CaO layers, and the circles denote various interlayer species (Adapted from [38]).

Magnesium present in blast furnace slags cannot be incorporated into the C-A-S-H structure due to the lower ionic radius of Mg^{2+}, when compared to Ca^{2+} [42]. Therefore, Mg is observed to react with the Al resulting in secondary hydration products that are hydrotalcite-type [30,43,44]. Additional common secondary products include AFm-group layered hydrous calcium aluminates [30]. Instead of hydrotalcite, formation of zeolites such as gismondine and

garronite is evidenced when the Mg content in ground granulated blast furnace slags (GGBS) is low.

In addition to the different aluminosilicate sources, the type and dosage of alkali activator used during the synthesis of AAMs also have an impact on the hydration chemistry and microstructure development. Alkali-metal hydroxides and silicates are the most commonly used activators. The use of alkali metal carbonates and sulfates has also been reported for specific applications, but concerns regarding the degree of reaction and the pH within these binders still exist [25].

2.1.3 Pore network of alkali-activated materials

Hardened PC and AAMs are porous materials and their microstructure is characterised by a complex pore structure that determines its strength, permeability, fluid transport mechanisms and durability. Porosity in hardened cement systems can be defined as the spaces occupied by evaporable water [45]. When cement is mixed with water, the spaces between cement particles are occupied by water, but upon hydration, these spaces are filled with the hydration products that reduce the volume of the interconnected pore network [45–48]. The pore network in cements exhibit pores with diameters varying from a few nanometres to several millimetres and therefore, can be classified into three categories, namely gel pores, capillary pores and macroscopic air voids [49]. Gel pores are nm-sized pores (0.5 to 2.5 nm) that can be defined as interstices in the hydration products and do not permit the movement of fluid [50,51]. Capillary pores vary from several nanometres to several micrometres and are defined as the spaces that have not been occupied by solid reaction products. Factors such as water/binder (w/b) ratio, degree of hydration, temperature and fineness of the binder play an important role in determining the connectivity of the capillary system and therefore, greatly influencing the permeability of concrete [47,50,52,53]. Macroscopic pores and air voids, of sizes that can go up to several millimetres, are generally dependent on how well the cement systems are compacted and can greatly affect the durability of concrete [14,54]. However, for concretes that are likely to be freeze-thaw cycled, macroscopic voids are induced intentionally in order to account for expansion of water when it freezes.

In the case of alkali-activated systems, a complete understanding of the pore structure has not been established yet, and limited research has been conducted to study key microstructural parameters such as tortuosity and extent of percolation. Literature suggests that the pore structure of alkali-activated binders depends on a number of factors such as aluminosilicate

source, alkali activator-type and dosage, w/b ratio, temperature, and curing time [53,55–65]. In general, binders formed by activation with alkali hydroxides tend to have much more porosity and less compact microstructures than alkali-silicate-activated ones [55,58]. Smaller pore size distribution and lower porosity are generally observed for alkali silicate-activated slag binders when compared with alkali silicate-activated fly ash binders [58]. Shi and Day [66] compared the porosity and cumulative pore volumes of PC and sodium silicate-activated slag binders after 28 days of curing at 25°C using mercury intrusion, and observed not only a lower porosity but also a finer pore structure for the latter.

Provis et al. [67] studied the relationship between the pore structure and the tortuosity of alkali-activated binders using X-ray microtomography. With increasing curing time, an inverse relationship between segmented porosity and diffusion tortuosity was observed for slag-rich and fly ash-rich binders. On comparing slag-rich binders and fly ash-rich binders, the former were found to have a much lower segmented porosity and a higher diffusion tortuosity. The tortuosity of the pore network has a significant influence on the resistance to diffusion and consequentially the durability of alkali-activated binders. Therefore, slag-rich binders with a higher tortuosity and a lower porosity than the fly ash-rich binders can therefore be inferred to have a much higher resistance to diffusion (of aggressive species, and/or of alkalis) and protection of the embedded steel reinforcement.

Here, it is noteworthy that pore structures and the features mentioned above are a description for cement pastes and not concretes. The pore structure of concretes differs considerably from cement pastes. This is mainly due to the addition of aggregates and other additives in concrete that result in variation of properties at the paste-aggregate interfaces or the interfacial transition zone (ITZ) [68]. The ITZ is characterised by a much higher capillary porosity than the bulk cement pastes and therefore, can have a drastic influence on the diffusion behaviour of different species in the pore solution [50,69–71]. However, several studies have indicated that the net influence of the ITZ on chloride diffusivity is small, even though its local porosity and local diffusivity are much higher when compared to the bulk cement paste [72,73].

2.1.4 Pore solution composition

As mentioned above, the porosity in hardened cement pastes is defined as the space that may be occupied by evaporable water. Therefore, water in cement pastes can be categorised according to the pore volume it occupies (and the difficulty associated with its removal) into capillary water – held in capillaries, interlayer water – held in gel pores, physically adsorbed

water – held on the pore walls, chemically bound water – combined with hydration products, and water in macro pores and air voids [48,55]. According to Powers [45,47], capillary water usually accounts for the greatest proportion of water in hardened Portland cement pastes and is primarily responsible for influencing transport properties such as permeability in cement systems. In the case of AAMs, larger capillary pores have been observed to be accessible through smaller gel pores and therefore, permeability in AAMs depends on both gel pores as well the interconnectivity between capillary pores [74]. Like the pore structure, the chemistry of the pore solution can also influence the transport properties of AAMs [75] and depends on aluminosilicate source, alkali activator type and dosage, w/b ratio, ambient humidity, curing conditions, and hydration products.

Song and Jennings [76] studied the pore solution chemistry of different alkali-activated slag pastes and the influence of pH and hydration time on the concentration of different cations present in the pore solutions. They found that the concentration of Na^+ in NaOH-activated pastes remained constant through 56 days of hydration. The pH of the pore solution predominantly depends on the concentration of the alkali activator and remained constant during the entire course of the study. They observed that an increased pH of the pore solution resulted in higher concentrations of Si and Al ions, but decreased levels of Ca and Mg ions [76]. The relationship between pH and the dissolution of different ionic species is governed by the thermodynamic stability of different species (according to the Gibbs free energy of dissolution).

Puertas et al. [77] investigated the compositions of pore solutions of alkali-activated Spanish blast furnace slag pastes activated using NaOH and waterglass solutions at different times. Unlike Song and Jennings [76], they found that the concentration of Na^+ decreases with increasing reaction times for both waterglass and NaOH-activated slags, with a higher degree of reduction in the latter. For NaOH-activated slags, the concentration of Na^+ decreased from 2.60 M to 1.80 M, compared to a reduction from 2.10 M to 1.20 M for waterglass-activated slags, measured after 3 hours and 7 days of curing respectively [77]. They observed that the concentration of Si ions in the pore solutions is related to the type of activator used, and therefore, the Si concentration in pore solutions of waterglass-activated slags during the early stages of hydration was significantly higher when compared to the NaOH-activated pastes [77]. For both activators, the decrease in concentrations of Na^+ and Si progresses with time. In the case of Al, Song and Jennings [76] found that the concentration of Al decreased with increasing reaction time and was less than 0.30 mM after 28 and 56 days of hydration. Puertas et al. [77]

observed positive and negative parabolic trends with respect to hydration time, for Al concentrations in the pore solutions of Na_2SiO_3 (minimum: 1.10 mM) and NaOH (maximum: 8.80 mM) activated slag pastes respectively.

Gruskovnjak et al. [78] made a detailed comparison between the hydration of sodium metasilicate-activated slags and PC, and characterised the chemical evolution of the pore solutions over a period of 180 days. They found that the alkali-activated slag systems were dominated by a high pH (~13.7) with high concentrations of Na^+ (>1 M) and S (~ 0.45 M), and relatively low concentrations of K, Al and Si. As in the study of Song and Jennings [76], the concentration of Al decreased over time from 7 to 3.20 mM. In contrast to the study conducted by Puertas et al., [77] the Si concentration was found to be 30 times lower after 24 hours of curing, but a similar decrease in concentration over time was observed. Both studies related the decrease in concentrations of Na and Si over time to the precipitation of C-A-S-H.

Lloyd et al. [79] characterised the pore solutions of different types of inorganic polymer cements, such as Na_2SiO_3-activated fly ash and ground granulated blast furnace slag, extracted using the technique defined by Barneyback and Diamond (application of 550 MPa to 250 g samples and extraction of pore solution) [48], after 90 days of curing. They observed concentrations of alkali cations to be greater than 0.50 M or in some cases, greater than 1 M. In the case of alkali-activated ground granulated blast furnace slag pastes, the Na^+ concentration was found to be 3.617 M and was significantly higher than that observed by Gruskovnjak et al. [78] and Puertas et al. [77], mainly due to the higher concentration of the activator, indicating an almost linear relationship between the concentration of the activator and the concentration of alkali in the pore solution [79]. They also observed that negative correlations exist between the alkali concentration in the pore solution and the w/b ratio, and dissolved silica in the activating solution. The effect of binder chemistry on the alkali content present in the pore solution indicated that with increasing Ca content, there exists a higher preference of Ca incorporation into the gel when compared to monovalent cations [79]. The concentration of Al and Ca^{2+} in the pore solution were found to be <1 mM in alkali-activated ground granulated blast furnace slag. This was confirmed through thermodynamic calculations by Myers et al. [80]. Unlike the studies (Song and Jennings [76], Gruskovnjak et al. [78]) where the Al concentration was observed to decrease over time, Lloyd et al. [79] did not observe a decreasing trend, and instead found that the Al incorporation into the gel structure increased with increasing activator concentration.

The chemistry of the pore solution determines its pH, and consequently impacts the durability of reinforcement. As literature, e.g. [78], suggests, pore solutions of AAMs have higher concentrations of soluble alkalis when compared to that of PC, primarily due to the nature of the activator and hydration mechanisms. With concentrations of counter-ion species such as aluminate and silicate being low, it can be inferred that the electro-neutrality of the pore solution is preserved by the presence of hydroxyl ions, therefore providing the pore solution with significant alkalinity to maintain the passivity of the reinforcement [79]. Myers et al. [80] calculated the pH of various alkali-activated blast furnace slags to be between 13.5 and 14.2 based on simulated phase assemblages, and found that an increase in the silica content in the precursor from 30 to 40 wt.% leads to a reduction in the pH of the pore solution.

Figure 2-4 summarises the concentration of various elements in pore solutions of AAS, calculated using thermodynamic simulations [81] and measured experimentally [76–79].

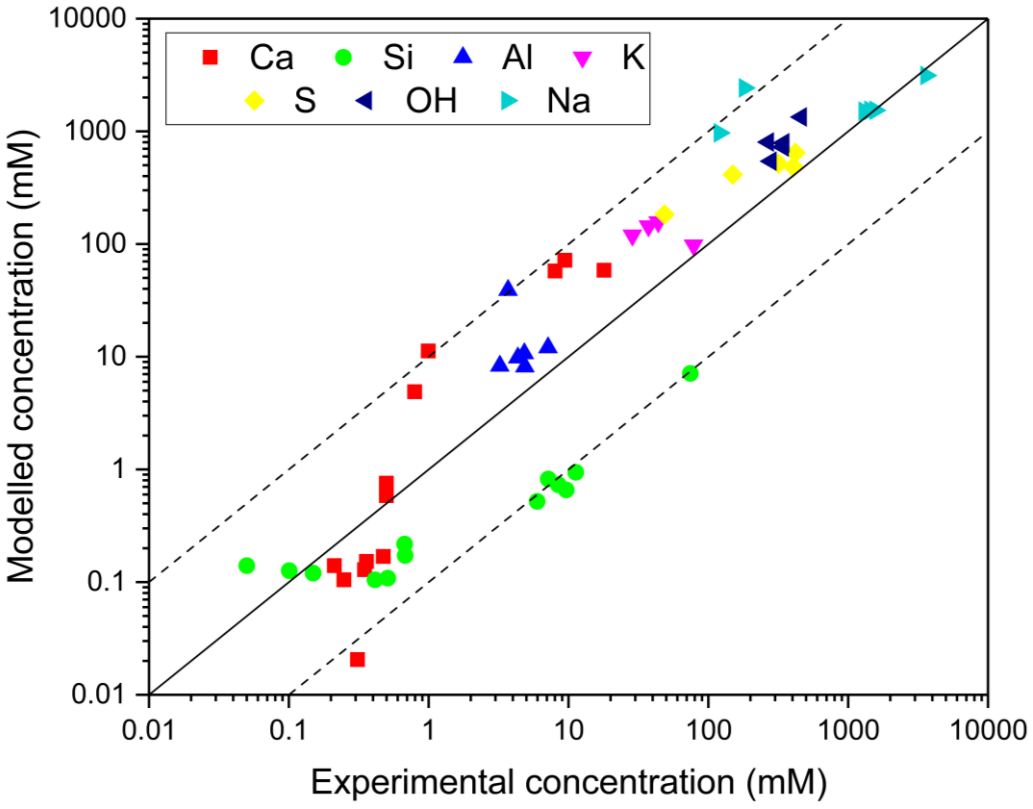

Figure 2-4: Simulated [81] and experimental concentrations [76–79] of elements in pore solutions of AAS. Experimental details regarding each data point from [76–79] can be found in [81]. Adapted from [81].

One of the major differences between the pore solutions of low-Ca AAMs and high-Ca AAMs (alkali-activated blast furnace slags in particular) arises due to the presence of reduced sulfur species in the pore solution of the latter. Blast furnace slag is a by-product of the iron making process and retains the reducing nature of the furnace, containing approximately 1 to 3 wt.% sulfur. The sulfur present in blast furnace slags readily dissolves into various aqueous sulfur species, with majority of them being in the reduced state (as HS^- or S^{2-} or S_n^{2-} - depending on the pH of the system). In highly alkaline systems such as AAMs, the majority of the sulfur is expected to exist primarily as HS^- and minor quantities of SO_3^{2-}, SO_4^{2-} and $S_2O_3^{2-}$, giving the alkali-activated blast furnace slags a reducing characteristic. Figure 2-5 shows the E_h-pH diagram for the sulfur-water system, showing the stability regime of various aqueous sulfur species and their relevance in high-Ca AAMs such as alkali-activated slags (denoted by the red circle).

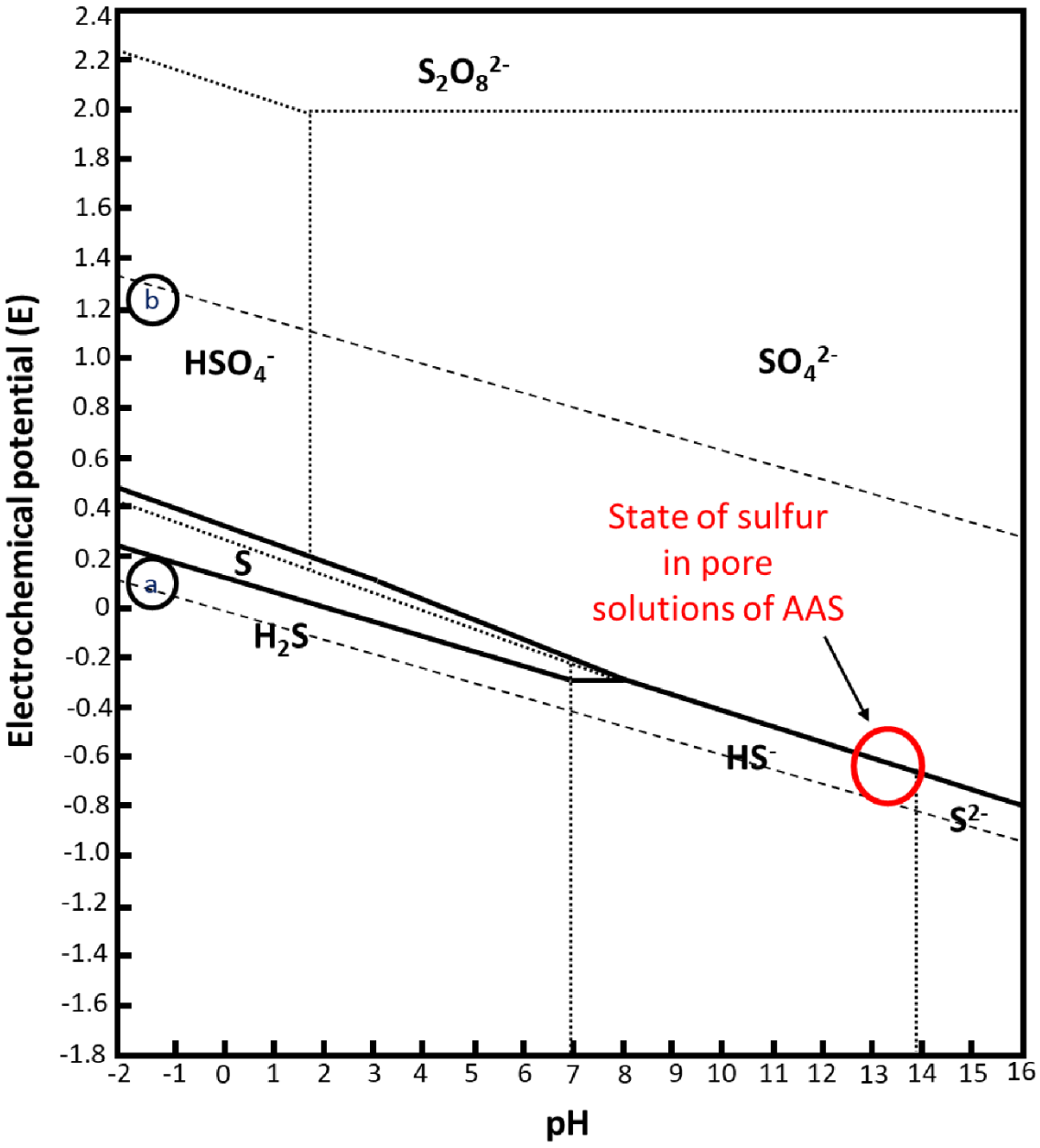

Figure 2-5: Potential (vs. standard hydrogen electrode (SHE))–pH equilibrium diagram for the system sulfur-water at 25°C, 1 atm, showing the dominance of various aqueous sulfur species. The region encompassed by the red circle shows the state of sulfur in pore solutions of AAS. It is noteworthy to mention that this figure does not show the formation of metastable sulfur species such as S_n^{2-}, SO_3^{2-}, and $S_2O_3^{2-}$. The dashed lines 'a' and 'b' mark the stability range of water. Adapted from [82].

2.2 Fundamentals of steel corrosion

Corrosion of the reinforcement is one of the primary causes of premature deterioration of reinforced concrete structures. The reinforcement in structures is generally mild steel, an alloy of iron and carbon with trace quantities of Mn, Cu and Si. The degradation process of the reinforcement can be characterised as the oxidation of metallic Fe, in the presence of moisture and oxygen, into Fe oxides and hydroxides that are commonly referred to as rust [83,84]. The process of reinforcement corrosion is redox in nature and comprises the anodic dissolution of iron and the reduction of oxygen. The electrons generated during the oxidation reaction, i.e. dissolution of iron, are transported to the cathode, where they are consumed by the electrolyte components, forming hydroxyl ions. The combination of iron ions with the hydroxyl ions results in the formation of ferrous hydroxide which then converts to rust [85]. Hence, it is important to note the pre-requisites for corrosion of steel reinforcement in concrete - (a) anode-cathode couple, with part of the steel acting as the anode; (b) flow of electric charge; (c) presence of oxygen and moisture [50]. The aforementioned redox process can be described by the following reactions (Eq. 2.1 to Eq. 2.3):

Oxidation reaction (anodic dissolution of iron):

$$Fe \rightarrow Fe^{2+} + 2e^{-} \qquad \text{(Eq. 2.1)}$$

Reduction reaction (oxygen reduction):

$$H_2O + \frac{1}{2}O_2 + 2e^{-} \rightarrow 2OH^{-} \qquad \text{(Eq. 2.2)}$$

The net redox reaction can be written as a combination of the two half-cell reactions occurring at the same rate:

$$Fe + H_2O + \frac{1}{2}O_2 \rightarrow Fe(OH)_2 \qquad \text{(Eq. 2.3)}$$

In general, the corrosion product $Fe(OH)_2$ further oxidises into Fe_3O_4 and $Fe_2O_3/Fe(OH)_3$ [84]. The damage due to corrosion of the reinforcement is firstly in the form of reduction in the cross-sectional area of the reinforcement, which reduces the load bearing capacity of the concrete structure [50]. Secondly, the corrosion products formed have a larger volume compared to the steel itself, which induces tensile stresses in the concrete, initiating cracks parallel to the reinforcement and eventually leading to spalling of the concrete cover [50,86].

2.2.1 Electrode potentials

As corrosion of reinforcement steel is principally an electrochemical process, it is important to understand different electrochemical concepts involved.

When a metal (M) surface comes into contact with a solution, an interfacial phase boundary is established that can lead to the dissolution of metallic ions (M^{z+}) into the electrolyte; and is represented by the following reaction (Eq. 2.4):

$$M \leftrightarrow M^{z+} + ze^{-} \qquad \text{(Eq. 2.4)}$$

The electrolyte, forms an electrical double layer or an interfacial region (at the metal surface and the aqueous environment) where the positively charged ions are spatially separated from the negatively charged ions, creating a non-homogeneous distribution of ions close to the metal surface [50,87]. This charge separation creates a potential difference within the layer, and its magnitude determines the rate at which reactions and movement of charges across the interface occur, thereby affecting the kinetics of corrosion processes.

For a redox process to occur, a potential difference between the two half-cell reactions, namely oxidation and reduction, needs to be present [50]. For a given half-cell reaction, such as the one given in Eq. 2.4, the potential can be measured against a given reference electrode. When the temperature and pressure are 25 °C and 1 bar respectively, and the metal ions in the electrolyte have a concentration of 1 mol/L, the measured potentials are termed as standard electrode potentials (denoted as $E°_{M/M^{z+}}$). For conditions deviating from the standard conditions (mentioned above), the electrode potentials can be calculated using the Nernst equation (Eq. 2.5):

$$E_{M/M^{z+}} = E^{\circ}_{M/M^{z+}} + \frac{RT}{zF}\ln([M^{z+}]) \qquad \text{(Eq. 2.5)}$$

where R is the gas constant, T is the temperature, F is Faraday's constant, E° is the standard electrode potential, $[M^{z+}]$ is the concentration of M ions in the electrolyte, and z is the number of electrons involved in the redox reaction [50,85].

2.2.2 Pourbaix diagram and passivation

As the redox process of corrosion involves the reduction of oxygen to hydroxide ions, it is evident that corrosion of the reinforcement depends on the pH of the aqueous environment (in

the case of reinforcement, the pore solution). The thermodynamic stability of an electrochemical system can therefore be predicted using the Nernst equation and can be expressed as a function of electrode potential, pH, and the concentration of metal ions in the electrolyte [85]. Pourbaix used electrochemical thermodynamics to graphically represent the influence of electrode potentials and pH on electrochemical equilibria (as shown in Figure 2-6, for the case of Fe) for various systems [84].

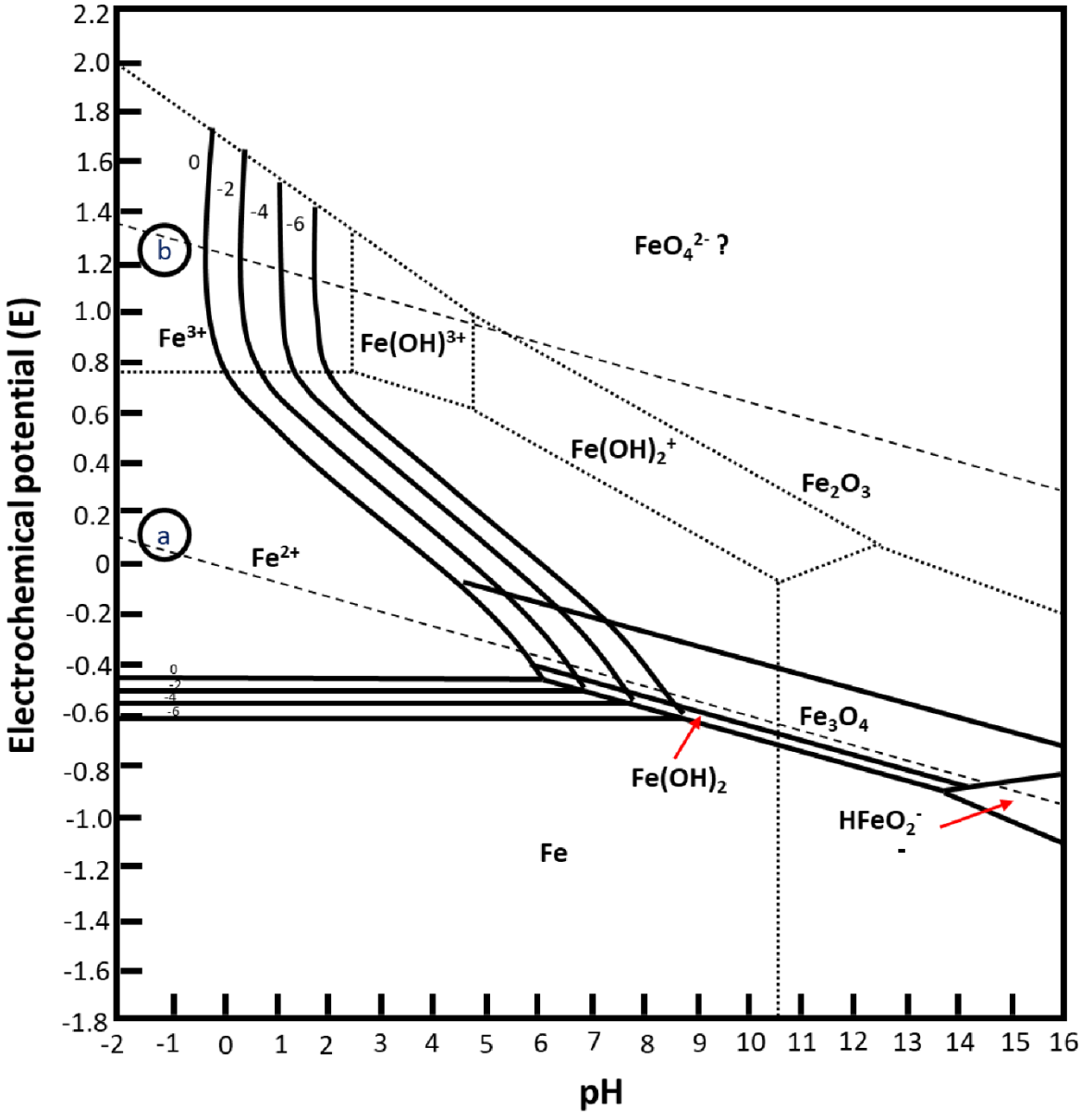

Figure 2-6: Potential (vs. standard hydrogen electrode (SHE))–pH equilibrium diagram for the system iron-water at 25°C, 1 atm (considering solid substances as only iron, iron (II, III) oxide (Fe_3O_4) and iron (III) oxide (Fe_2O_3)). Boundaries between the fields in which iron (Fe) and iron (II) (Fe^{2+}) are the most prominent species, and between soluble iron and various

solids, are shown as a function of log concentration (marked as numerical values) of soluble iron. The dashed lines 'a' and 'b' mark the stability range of water. Adapted from [84].

As shown in Figure 2-6, the region below line 'a' represents conditions where water may be reduced to gaseous hydrogen; whereas the region above line 'b' represents conditions where water may be oxidised to oxygen [85]. The area between these two lines represents the region where water is thermodynamically stable, as both the aforementioned oxidation and reduction reactions are disfavoured. The region of thermodynamic stability for metallic iron lies completely below the region of stability for water and therefore, irrespective of the pH at normal atmospheric conditions (25°C and 1 atm), simultaneous thermodynamic stability of iron and water is not possible. Their simultaneous stability at 25°C is only possible when pressures are high enough (approximately 725 atm) to suppress line 'a' below the equilibrium of the Fe-Fe_3O_4 system and the pH values lie between 10 and 12; or the potentials are low enough (i.e. cathodic protection) [84,85,88]. The oxidation of iron can give rise to a number of soluble and insoluble products, such as Fe^{2+}, Fe^{3+}, $HFeO_2^-$; and $Fe(OH)_2$, Fe_3O_4, Fe_2O_3 respectively, depending on pH and electrode potential. The following chemical reactions (Eq. 2.6 - Eq. 2.12) [84,87] represent different transformations depicted in the Pourbaix diagram (Figure 2-7).

$$Fe + 2H^+ \rightarrow Fe^{2+} + H_2 \quad \text{(Eq. 2.6)}$$

$$Fe + 2H_2O \rightarrow FeO_2H^- + H^+ + H_2 \quad \text{(Eq. 2.7)}$$

$$3Fe^{2+} + 4H_2O \rightarrow Fe_3O_4 + 6H^+ + H_2 \quad \text{(Eq. 2.8)}$$

$$Fe^{2+} + 2H_2O \rightarrow Fe(OH)_2 + 2H^+ \quad \text{(Eq. 2.9)}$$

$$3Fe(OH)_2 \rightarrow Fe_3O_4 + H_2O + H_2 \quad \text{(Eq. 2.10)}$$

$$Fe^{2+} + O_2 + 10H_2O \rightarrow 4Fe(OH)_3 + 8H^+ \quad \text{(Eq. 2.11)}$$

$$4Fe_3O_4 + O_2 \rightarrow 6Fe_2O_3 \quad \text{(Eq. 2.12)}$$

As seen in the Pourbaix diagram for Fe (Figure 2-7), the stability region for $Fe(OH)_2$ is very small and is partially overlapped by the stability region for Fe_3O_4, and this compound will therefore tend to be transformed to the latter (depicted by Eq. 2.10) [85]. The formation of insoluble oxides, such as Fe_2O_3 and Fe_3O_4, leads to the protection of the underlying metallic

iron from further dissolution and iron can be considered to be in the passive state with very low corrosion rates. This process of forming dense, thermodynamically stable oxide films of nanoscale thickness is called passivation [85]. As shown in in Figure 2-7, the Pourbaix diagram for Fe can be theoretically categorised into two major regions – where corrosion is likely (areas of corrosion) and regions where corrosion is unlikely (regions of passivation and regions of immunity) [85]. In other words, depending on the electrode potentials of the metal and the pH of the aqueous solution (and also the presence of other ions such as Cl^-), the metal can be in a state of localised/pitting corrosion (due to imperfect passivation), or generalised corrosion (region of corrosion), or in a state of total protection (regions of immunity and perfect passivation).

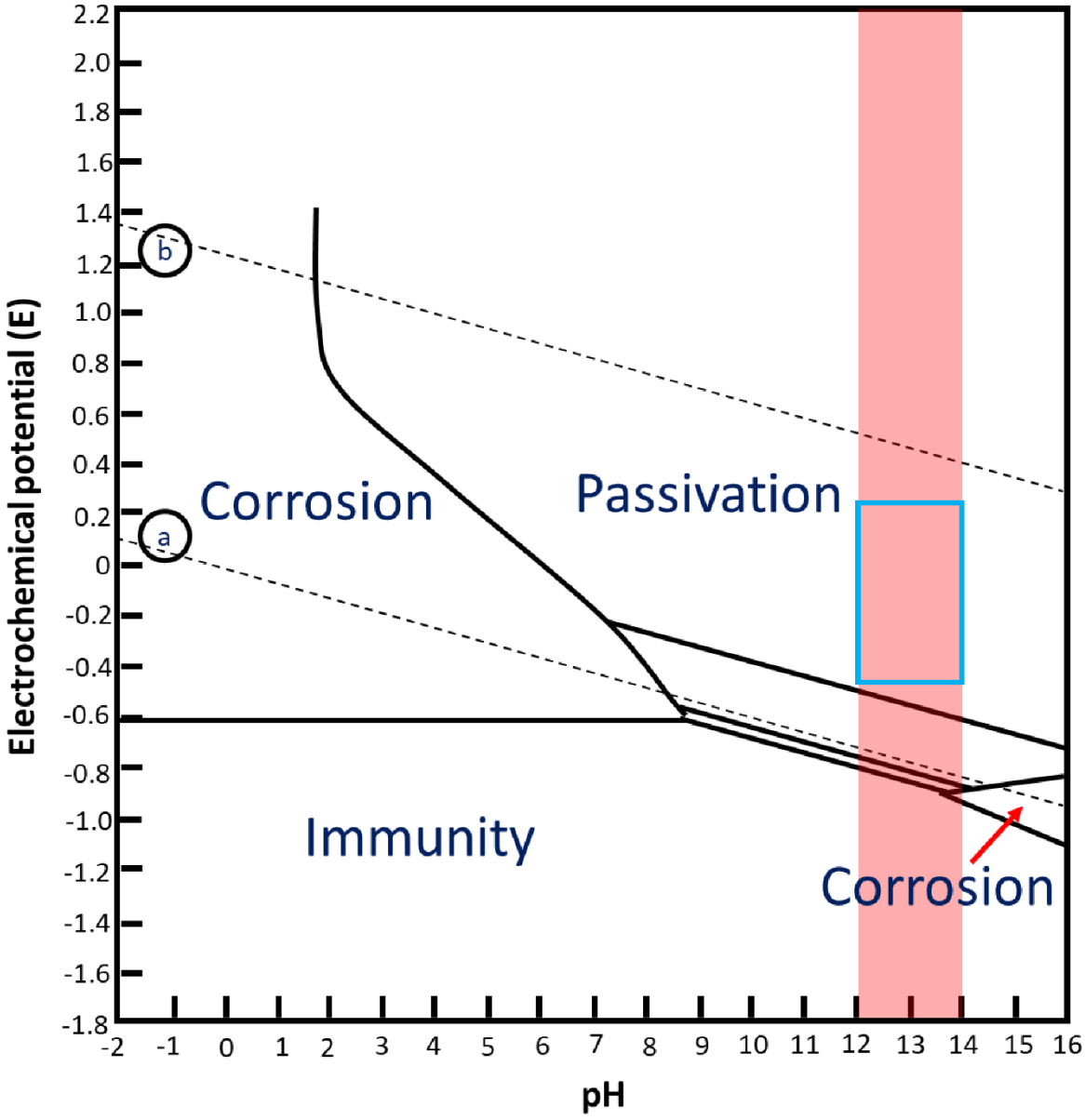

Figure 2-7: Theoretical conditions of corrosion, immunity and passivation of iron depicted through the Pourbaix diagram, at 25°C. The red area and the blue box denote normal pH values and electrode potentials (vs. SHE) in reinforced-concretes (in the absence of aggressive species) respectively [84,88]. Adapted from [84].

In addition to the dependence of passivity on the chemistry (including pH) of the concrete pore solution, electrode potentials and oxygen contents also play an important role in determining the precise nature of the passive film. In hydrated cement pastes, steel is never thermodynamically stable, but the alkaline nature of the concrete pore solution (pH values typically between 12.5 and 13.8, due to the high amounts of alkalis) has the capability to provide protection to the reinforcing steel from corrosive processes by the formation of thermodynamically stable passive oxide films (as seen from the passivation domain in the Pourbaix diagram – Figure 2-7) that slow down the growth rate of corrosion products. It is to be noted that the steel used in the majority of concrete structures around the world is of mild steel or carbon steel grade, and not stainless steel. Therefore, the chemistry of the passive film and the surface condition of the reinforcement is particularly important, and literature pertaining only to mild/carbon steel has been discussed here.

According to Figure 2-6 and Figure 2-7, the region of passivation is characterised by the formation of iron (II, III) oxide (Fe_3O_4) at conditions of high pH and low electrochemical potentials, whereas the formation of iron (III) oxide (Fe_2O_3) can be witnessed at conditions of high pH and high electrochemical potentials. Many authors have argued regarding the compositions and structures of passive films formed on the reinforcement when immersed in simulated pore solutions as well as when placed in mortars. Glasser and Sagoe-Crentsil [89] analysed the microstructure of the passive film formed when steel reinforced concrete is exposed to atmospheric conditions. They found that the passive layer possesses a bi-layered structure comprising an inner layer made up of a dense spinel $Fe_3O_4/\gamma–Fe_2O_3$ solid solution, and a porous outer layer composed mainly of poorly crystallised α–FeOOH interspersed with crystalline nodules of spinel and portlandite. Haupt and Strehblow [90], Ghods et al. [91] and Freire et al. [92] found similar results. Joiret et al. [93] confirmed the bi-layered characteristics of the passive film and concluded that the inner layer of the passive film was based on the three-dimensional spinel structure of magnetite (Fe_3O_4). They also observed that the outer layers were formed as a result of oxidation or reduction depending on the electrode potentials and availability of oxygen. Haupt and Strehblow [90] characterised the growth of iron (III)

oxide to be linearly correlated with log time and the electrode potential, and this was in agreement with the oxide growth model for high fields developed by Deal and Grove [94]. Similar conclusions were drawn by Freire et al. [92], who also found that the growth of the outer layer was topotactic and was directly proportional to the increase in the electrode potential.

Gouda [95] investigated the corrosion behaviour of reinforcement steel in aerated and de-aerated lime water, and in NaOH solutions with different pH values, using electrochemical techniques, and found that the oxidation processes depended on the dissolved oxygen and were characterised by formation of different intermediate oxidation products. In the case of aerated solutions, Fe first oxidised to Fe_3O_4 and this was evidenced by a step in the electrode potential vs. time curve. Before oxygen evolution, Fe_3O_4 was found to further oxidise to Fe (III) oxide, characterised by another step. In the case of de-aerated solutions, instead of Fe_3O_4, $Fe(OH)_2$ was found to be the intermediate oxidation product, probably due to the hydrolysis of the FeO_2H^- anion. The second step in the potential vs time curve, before oxygen evolution, was characteristic of the oxidation of $Fe(OH)_2$ to $Fe(OH)_3$. For the case of immersion in NaOH solutions, similar potential curves were observed. Therefore, the passivation of iron does not depend on the cation (Ca or Na) in the aqueous environment; and the chemistry of the passivation layer formed on the surface of the steel depends primarily on the availability of oxygen and the pH of the aqueous solution. In a subsequent paper, Gouda and Halaka [96] investigated the corrosion behaviour of reinforcement steel when embedded in PC based concrete mixed with distilled or tap water, and found that passivation followed an oxidation procedure that was exactly the same as in the case of steel immersed in aerated lime water [95].

Several studies have also reported the formation of iron hydroxides in addition to magnetite (Fe_3O_4) and maghemite (Fe_2O_3). Oranowska and Szklarska-Smialowska [97] measured the optical properties of the passivation layer formed on Armco iron in de-aerated saturated calcium hydroxide solutions (of pH 12.5) under open circuit conditions and at anodic potentials. They observed that the refractive index of the first layer adherent to the metal was 1.43 under open circuit conditions and 1.7 at anodic potentials. They attributed these refractive indices of 1.43 and 1.7 to $Fe(OH)_2$ and to a mixture of FeOOH-$Ca(OH)_2$ respectively, and their observations were in agreement with the findings of Glasser and Sagoe-Crentsil [89]. Hugot-Le Goff et al. [98] used Raman spectroscopy and a rotating slit ring disk electrode to characterise the passive film formed on iron exposed to 1 M NaOH solution, and observed the formation of iron oxyhydroxides such as goethite (α –FeOOH), lepidocrocite (γ –FeOOH) and

akaganeite (β –FeOOH) above protective forms of iron oxides such as magnetite (Fe_3O_4), maghemite (γ –Fe_2O_3) and hematite (α –Fe_2O_3). Figure 2-8 represents a simple schematic of the passive film formed in PC, with an inner layer of iron (II, III) oxide and an outer layer of a hydrated iron (III) oxide or a polymorph of hydrate iron oxyhydroxide.

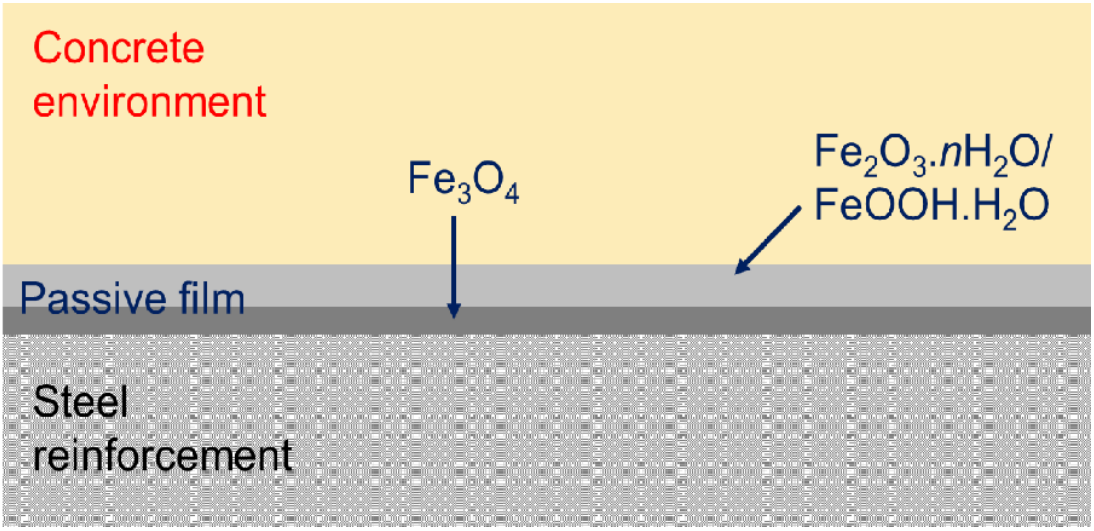

Figure 2-8: A schematic of the complex phase assemblage of the passive film formed on the surface of mild steel reinforcement when exposed to alkaline environments (adapted from conclusions of Chapter 4)

2.2.3 Service life of reinforced structures

Tuutti [14] proposed a macroscopic service life model for reinforced concrete structures, taking into account exposure to a corrosive environment, and suggested that the service life can be subdivided into three stages: an initiation time, the onset of corrosion, and a propagation period (as shown in Figure 2-9):

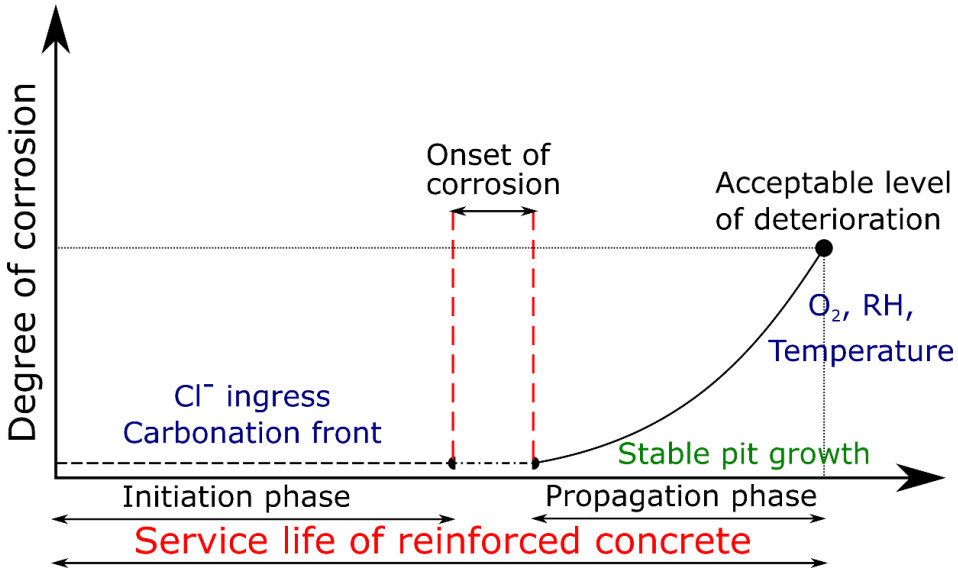

Figure 2-9: Service life model for reinforced concrete exposed in a corrosive environment, as proposed by Tuutti (adapted from [14,54]). This model depicts the service life of reinforced concrete structures when corrosion of the reinforcement is either chloride-induced or due to the effects of carbonation of the concrete cover.

- The *initiation stage* can be regarded as the time taken by aggressive species to penetrate the concrete cover and reach the surface of the reinforcement, until a sufficient concentration for depassivation/corrosion of steel is attained [14]. The concrete cover acts as a physical barrier and provides protection to the embedded reinforcement. The *initiation stage* is an inherent property of the concrete cover that controls the transport of aggressive species. The transport mechanisms are a function of the nature of the binder and the hydration products, the exposure conditions, extent of saturation, the pore network and the pore solution, and age of the concrete. In the case of chloride-induced corrosion, the *initiation stage* is the time it takes for the concentration of chloride to build up to a critical level at the steel-concrete interface (SCI) [99]. The *initiation stage* for corrosion due to carbonation of the concrete matrix is based on the time it takes for the pH of the pore solution at the SCI to drop below approximately 9 [100].

- The *onset of corrosion* can be defined as the point in time when the passive layer is broken down (depassivation) by the action of aggressive species. The *onset of corrosion* is influenced by the local properties of the SCI, such as the hydration products at the

SCI, the alkalinity of the pore solution, the presence of voids, bleed water zones, the chemistry of the passive film and the presence of defects on the steel surface. The *onset of corrosion* is characterised by either a drop in the pH at the SCI to approximately 9 or below, or the formation of a pit.

- Post depassivation, the steel corrodes until failure of serviceability (for a particular application) takes place, and this is termed the *propagation stage* [14]. The *propagation stage* depends on the alkalinity of the pore solution, the availability of oxygen, and the relative humidity at the SCI. The temperature also influences the rate at which steel corrodes, and therefore could affect the propagation phase. Irrespective of the corrosion mechanism, the propagation phase is characterised by the thinning of the steel reinforcement and the growth of corrosion products away from the surface of the reinforcements, towards the concrete cover, until the appearance of a crack, spalling, or structural failure. In addition to the thinning of the reinforcement, growth of pits formed due to the action of chloride causes a reduction in the local cross-sectional area of the reinforcement. The growth of pits is one of the most dangerous forms of cross-sectional thinning, particularly in the case of load-bearing sections in a concrete structure, due to the difficulty associated with predicting and locating them.

2.3 Mechanisms of steel corrosion in concrete

Corrosion of steel in concrete is generally induced through the ingress of chloride ions or the action of carbon dioxide on the cement matrix [101]. Chloride ions cause breakdown of the passive layer locally, whereas carbon dioxide decreases the alkalinity of the cementitious binder and its pore solution, and therefore leads to dissolution of the passive layer over the entire surface of the steel reinforcement [50,102].

2.3.1 Chloride-induced corrosion

2.3.1.1 Chloride ingress

The view of the role of chloride in concrete has changed with time; in the past chloride was used to accelerate cement hydration and strength development [13,103], whereas in recent times, it is considered to be the primary factor that leads to the breakdown of the protective passive film formed on embedded steel [99], and so its use as an addition is now very restricted.

The presence of chloride in the concrete cover can be due to several reasons, such as the use of de-icing salts, marine environments, and the use of contaminated water, aggregates or admixtures. Corrosion induced by the action of chlorides in reinforced structures has been one of the most important concerns over the last few decades and has led to significant amount of research to understand the complex corrosion processes due to ingress of chloride. The process of chloride-induced corrosion can be considered to follow the service life model proposed by Tuutti [14], as mentioned above. In simplistic terms, chloride has to penetrate the concrete cover in order to reach the concrete/steel interface, where the concentration of chloride needs to be above a certain critical value (initiation stage) for local depassivation to occur. Post local depassivation, corrosion of the rebar in the local environment (called pitting corrosion) occurs until it reaches a certain level when cracking and spalling of the concrete cover are witnessed (propagation stage).

The transport of chloride [13,55,69,104–106] within the concrete cover is not a simple phenomenon, but is governed by several mechanisms such as:

- Diffusion (under the influence of concentration gradients),
- Capillary suction (capillary action inside capillary pores of the concrete cover),
- Permeation (due to pressure gradients), and
- Migration (due to electrical potential gradients).

Transport of chloride occurs only in the form of aqueous ions in the pore solution and therefore, the kinetics of different transport mechanisms are controlled by microstructural properties of the concrete (w/b ratio, pore features – pore structure, porosity, interconnectivity etc.) and the environmental conditions (humidity, temperature, wet-dry cycles etc.) to which the structure is exposed.

The transport of chloride in PC has been studied thoroughly by many researchers. According to the literature, chloride ingress across the depth of the concrete cover is assumed to primarily occur due to the action of capillary suction; and due to the influence of a concentration gradient, following Fick's second law (non-steady state) of diffusion [13]. Capillary suction in concrete is defined as the uptake of water due to the action of capillary forces (surface tension and adhesive forces), without the influence of external forces such as gravity [46]. The rate of transport through capillary suction depends predominantly on the amount of capillary pores and their interconnectivity in the concrete specimen. The effect of capillary action is clearly witnessed by the wetting and drying of concrete, characterised by the uptake of water during

the wetting regime, and the partial release of water during the drying regime [46]. Powers et al. [45,47] identified that the capillary porosity in the cement matrix directly influences the permeability of the concrete and therefore, the rate of water uptake. In water-saturated concrete, diffusion is the dominant mechanism controlling chloride transport and therefore, the concentration gradient becomes the driving force for movement of oxygen and chloride across the depth of the concrete [50]. Under non-steady state conditions (concentration depending on time), Fick's second law of diffusion (Eq. 2.13) can be represented by the following equation for one-dimensional ingress [49]:

$$\frac{\delta C}{\delta t} = D\frac{\delta^2 C}{\delta^2 x} \qquad \text{(Eq. 2.13)}$$

where C is the concentration of the diffusing species and is a function of the distance x from the surface, and of time t, and D is the diffusion coefficient (m^2/s) which depends on the characteristics of the diffusing species, the characteristics of the concrete cover and temperature. The most commonly used solution for Eq. 2.13 is obtained by integration, assuming:

- The concentration of the diffusing species at the surface does not vary with time and is equal to C_s ($C = C_s$ for $x = 0$ and $t \geq 0$).
- The concrete cover is homogeneous in nature and the initial chloride content in the concrete is zero ($C = 0$ for $x > 0$ at $t = 0$).
- The diffusion coefficient is constant with respect to time and does not change as a function of position within the concrete (D = constant for $t \geq 0$ and $x \geq 0$).

The simplest form of the one-dimensional mathematical solution to Fick's second law of diffusion in a semi-infinite medium is represented by an error function (Eq. 2.14):

$$C(x,t) = C_s\left(1 - erf\left(\frac{x}{2\sqrt{Dt}}\right)\right) \qquad \text{(Eq. 2.14)}$$

where,

$$\text{erf}(z) = \frac{2}{\sqrt{\pi}}\int_0^z e^{-t^2}\,dt \qquad \text{(Eq. 2.15)}$$

Eq. 2.14 mathematically describes the transport of chloride to be dominated by the process of non-steady state diffusion and does not take into account the effects of chloride binding, or the roles of permeation and electric migration (caused by the presence of different charged species in the concrete) [13]. Another constraint of Eq. 2.14 is the assumption that the diffusion coefficient is constant with respect to time, which is not likely to be the case in reality as the

continuous hydration of the cement matrix may lead to changes in its porosity and permeability, thereby changing the diffusion coefficient to a time-dependent apparent diffusion coefficient ($D_a(t)$ instead of D) that primarily depends on the local conditions used [13,69]. Several models such as DuraCrete [107], ClinConc [107] and the *fib* model code [108] have taken into account the influence of time dependent diffusion coefficients, chloride binding capacity of PC-based concretes, and the interaction between various charged species in the pore solution [109]. In general, the movement of chloride across the depth of an unsaturated concrete cover is believed to be governed by capillary suction near the surface, whereas diffusion controls transport away from the surface of the concrete [110]. For a saturated concrete cover, diffusion is the main mode of chloride transport.

In the case of AAMs and blended cements containing GGBS, such a simple diffusion model would not accurately depict chloride transport as it does not take into account the differences in hydrate phase assemblage, the chloride binding capacity, the pore solution composition and the pore structure between PC and AAMs. Roy et al. [106] studied the effect of slag addition to alkali-activated PC systems on the chloride diffusion coefficients estimated using Fick's first law of diffusion, and found that diffusion coefficients for chloride decreased from 50×10^{-15} m^2/s to approximately 5×10^{-15} m^2/s with slag contents increasing from 0 to 100%. They related the decreasing diffusion coefficients to the overall reductions in porosity and decreasing permeability with addition of slag in the concrete mix. Similar trends of decreasing diffusion coefficient have been shown by studies conducted by others for addition of different supplementary cementitious materials [111–113]. Ismail et al. [114] found the diffusion of chloride in alkali-activated slags to be much slower than in PC, but in the case of alkali-activated fly ashes, the diffusion coefficient was found to be much higher than PC. They attributed such observations to the higher pore filling capabilities of the C-A-S-H gel (in alkali-activated slags) than the more porous N-A-S-H gel (in alkali-activated fly ashes and metakaolin). Similar observations were made by Tennakoon et al. [115] for alkali-activated slag/fly ash blends. Ma et al. [116] reported the chloride diffusion coefficients in alkali-activated slags to be much lower than PC, and the modulus of the activator and the concentration of Na_2O were found to have a great influence on the non-steady state diffusion coefficient. An increase in the Na_2O content in the activating solution has been found to lead to a lower porosity, and consequently a lower diffusion coefficient [116]. As mentioned in Section 2.1.3, the higher volume of permeable voids in NaOH-activated AAMs when compared to waterglass-activated AAMs would lead to faster chloride diffusion [58]. The higher alkalinity and the greater ionic strength of the pore solutions in AAMs when compared to the

pore solutions of PC could create a potential gradient leading to retardation of the transport of chloride [117]. In general, low-Ca AAMs show a lower resistance to chloride transport than high-Ca AAMs, and the diffusion coefficients in various cementitious systems can be ranked as: low-Ca AAMs > PC > PC-GGBS > high-Ca AAMs [67,118,119].

During the initiation stage, before the chloride reaches the steel, the chloride can exist in several states depending on the chemistry of the binder, the pore solution, the physico-chemical properties of each hydration product, and the binding energy. The total chloride content in the cement matrix can be expressed as the sum of 'free chloride' and 'bound chloride', depending on the extent of interaction between the chloride and the concrete. Ramachandran [103] analysed the different possible states in which chloride can be bound in the cement matrix and found that they can exist as being either physisorbed, chemisorbed on the surface; or substituted in the lattice of the hydration products.

Ramachandran [103] suggested that chloride binding through physical adsorption occurs through the formation of a surface chloro-complex, with almost all of the chloride leachable by water and alcohol. In the case of chemisorption, the chloride can exist either in the form of a surface complex or in the interlayers of the hydration products such as C-S-H due to the presence of electrostatic and Van der Waals forces, thus reducing the amount of leachable chloride [103]. In addition to this, after longer durations of hydration the chloride can also be incorporated through an ion exchange mechanism in the lattice of the hydration products. PC hydration products are generally characterised by high amounts of Ca, and therefore, the chloride binding tendency depends strongly on the dissolution of Ca-rich hydration products and their capability to maintain the alkalinity of the pore solution [13]. There is a general agreement in the literature that most of the bound chloride in hydrated PC exists in the form of a chloride-containing AFm phase called Friedel's salt ($Ca_2Al(OH)_6(Cl,OH)_2 \cdot H_2O$), through the reaction between sulfate or carbonate AFm phases, and chloride [13]. Depending on the concentrations of different anionic species and the thermodynamic stability, other chloride-containing AFm phases might also exist. Arya et al. [120] concluded that factors such as source of chloride, binder chemistry, hydration time, w/b ratio, chemistry and alkalinity of the pore solution, and the curing temperature, all play a major role in determining the degree of chloride binding in the cement matrix.

The chloride binding mechanism in alkali-activated systems is somewhat similar to PC, but due to differences in the composition of the binder material and hydration products, and the chemistry of the pore solution, dissimilarities in the extent of chloride binding and the

chemistry of the bound phases may arise. In alkali-activated fly ash and metakaolin systems, where the Ca content is relatively low, chloride binding has not yet been studied extensively, but it can be expected that the chloride ion would be physically adsorbed on the surface of the N-(A)-S-H gel, primarily due to the increased surface area of the highly porous binding gel [114,121]. In addition to the physical adsorption of chloride ions on the N-(A)-S-H gel, the free chloride could also react with the alkali metal cations in the pore solution and precipitate as halite upon drying/evaporation [114]. In high-Ca systems, where the major reaction product is an Al-substituted C-S-H gel, the positive charge on the surface of the C-S-H gel is minimised due to the substitution of Si by Al, therefore reducing the electrostatic interaction with chloride [122]. Therefore, the chloride binding capacity of the C-(A)-S-H gel might be much lower compared to C-S-H.

High calcium AAM systems are also characterised by the formation of secondary hydration products such as hydrotalcite-like (Mg, Al)-layered double hydroxides (LDH), and AFm-type (Ca, Al)-LDH, which can have significant roles in terms of chloride binding due to the presence of positively charged layers in their structures and their anion exchange property. As in the case of PC, AFm phases formed in high-Ca AAMs could convert to Friedel's salt in the presence of chloride through an ion-exchange mechanism. There is significant literature on the ion exchange property of hydrotalcite and its effect on protection of different surfaces. Kayali et al. [123,124] extensively analysed this behaviour in PC-GGBS concrete, where hydrotalcite is one of the key hydration products. They found that increasing the GGBS content in PC-GGBS bended systems led to a decrease in the ionic conductivity of the pore solution, and related lower corrosion rates to a decrease in the chloride ions in the pore solution. They attributed this reduction of free chloride to the anion exchange property of hydrotalcite, and concluded that increasing quantities of hydrotalcite in hydrated cement mixes lead to increased chloride binding capability [123,124]. In a detailed study, Ke et al. [125] reported the chloride binding capacity of secondary hydration products in alkali-activated slags to be dependent on the alkalinity of the pore solutions, and the free chloride content in the pore solution; the dominant mechanism of chloride binding was through surface adsorption rather than a direct ion-exchange process (for both hydrotalcite-like Mg-Al-LDH phases and AFm-type (Ca, Al) LDH). Though a chloride-containing hydrotalcite phase could exist in the cement matrix, the binding capacity of hydrotalcite is limited due to carbonation [125]. As chloride binding in hydrotalcite takes place through surface adsorption and ion exchange, the presence of carbonate ions in the pore solution (with low pH when compared to un-carbonated pore solutions) could

lead to the release of bound chloride ions (both physically adsorbed and chemically bound) and the incorporation of carbonate ions instead [125].

Chloride binding therefore has significant importance when considering chloride transport and its influence on the service life of concrete. The interaction of chloride with the cement matrix, in conjunction with different conditions of pH, temperature and humidity, may have a retarding effect on the diffusivity of chloride and therefore can alter the outcomes of models predicting service life.

2.3.1.2 Chloride-induced pitting

Unlike general corrosion, where the breakdown of passivity occurs globally, corrosion through the action of chloride is localised. Pitting corrosion is characterised by the loss of material through formation of cavities or pits, in the presence of aggressive ionic species such as chlorides and sulfates. The formation of these pits and associated material losses are considered to be more detrimental than general corrosion due to difficulties with their detection and the highly aggressive chemical environment within them [126]. In the case of pitting corrosion, the corrosion mechanism is determined primarily by the geometry of the pits that control the rate of mass transport for different species. Geometrical constraints of the pits make the rate of oxygen transport to the pits much slower than the rate of oxygen reduction [126], which results in the formation of a macro-cell due to the spatial segregation of the cathodic (surface of the metal surrounding the pit) and anodic sites (inside the deaerated pit) [127]. Figure 2-10 shows a schematic of the mechanism of chloride-induced pitting in steel reinforced concretes.

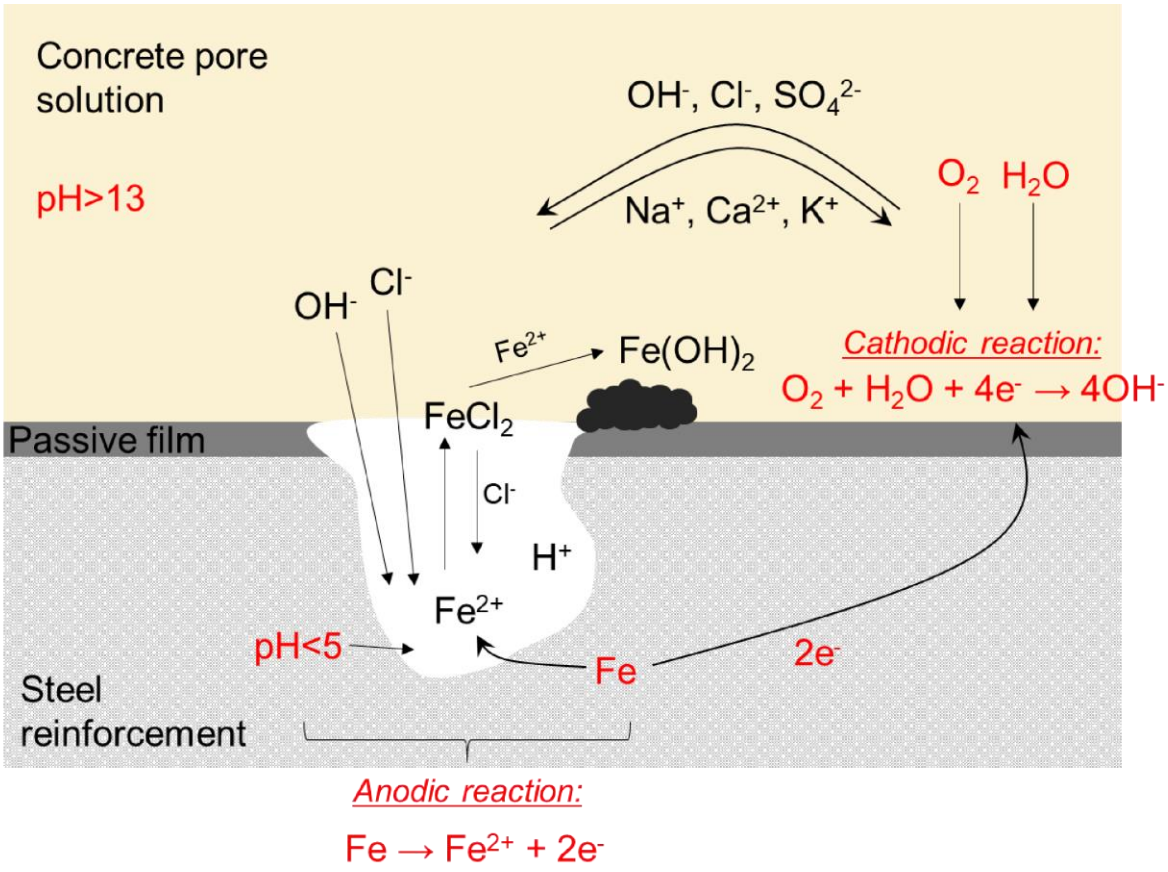

Figure 2-10: Schematic of chloride-induced pitting corrosion mechanism.

The dissolved iron ions in the pit hydrolyse by reacting with water to create a relatively acidic and an anodic environment within the pit and can be represented by the following reactions (Eq. 2.16 - Eq. 2.18) [126]:

$$Fe^{2+} + 2H_2O \rightarrow Fe(OH)_2 + 2H^+ \quad \text{(Eq. 2.16)}$$

$$2Fe^{2+} + 3H_2O \rightarrow Fe_2O_3 + 6H^+ + 2e^- \quad \text{(Eq. 2.17)}$$

$$3Fe^{2+} + 4H_2O \rightarrow Fe_3O_4 + 8H^+ + 2e^- \quad \text{(Eq. 2.18)}$$

As shown in Figure 2-10, in order to maintain charge neutrality in the pit, anions from the surrounding pore solution (such as chloride, sulfate, hydroxide etc.) of the concrete migrate inside the pit, whereas the cations (potassium, sodium, calcium, aluminium etc.) migrate in the opposite direction. In highly alkaline solutions surrounding the steel, as in the case of alkali-activated systems, hydroxide ions tend to migrate first in the pit to maintain the pH of the system and therefore, acidification occurs only when anionic species other than hydroxide

migrate into the pit. However, when the chloride concentration surrounding the pit increases, its tendency to migrate into the pit becomes much higher than that of the hydroxide ion and hence, an alkaline environment in the pit can no longer be maintained. In addition, the chloride ions can react with the dissolved iron ions to form iron chloride complexes that are thermodynamically stable in the acidic environment of the pit. However, the high local concentration of these species within the pit leads to the diffusion of iron chlorides towards the opening of the pit where, due to the high alkalinity, they readily dissolve, releasing iron and chloride ions. The chloride ions are released back into the pit enhancing chloride attack, whereas the iron ions react with the hydroxide ions at the cathodic sites outside the pit, resulting in the formation of various corrosion products composed of iron hydroxides and oxides at the cathodic sites next to the pit.

Several mechanisms have been postulated to describe the breakdown of passivity due to the presence of chloride, and Jovancicevic et al. [128] categorised different mechanism models into three classes: (i) adsorption-displacement, (ii) chemical-mechanical and (iii) migration-penetration.

The adsorption-displacement mechanism suggests that the breakdown of passivity is driven by the simultaneous adsorption of Cl^- and the displacement of anionic species such as O^{2-} and OH^- from a passive monolayer, therefore making it an instantaneous process upon the adsorption of chloride ions [128]. Such a model explains the concentration dependence of breakdown kinetics, but does not take into account the thickness and the compositional changes in the passive film. On the other hand, Hoar and Jacob [129] suggested that adsorption of chloride on the surface of the passive layer leads to the formation of thermodynamically unstable chloride complexes with iron cations, that dissolve readily in solution. Such a process would cause localised thinning of the film and a strong local anodic field on the surface, causing the diffusion (displacement) of cationic species to the surface, forming chloride complexes that dissolve readily, eventually leading to the breakdown of the passive film. The chemical-mechanical mechanism, proposed by Hoar [130], suggested that upon adsorption of chloride ions on the passive layer, repulsive forces acting between charged particles result in the lowering of interfacial surface tension between the pore solution and the oxide passivating film. When the repulsive forces become sufficiently large, cracks and splits are formed, increasing the capability of the system to adsorb more anions, and making the process incessant.

The theory of migration-penetration mechanisms has also been suggested by several authors in the literature. The penetration model, postulated by Kruger [131], considered the

incorporation of chloride ions in the passive layer and their subsequent migration to the metal/oxide interface. These ion migration models are fundamentally dependant on the exchange process via cation and O^{2-} (or OH^-) vacancies. Lin et al. [132,133] proposed a point defect model to mathematically describe the factors determining the initiation of chloride-induced corrosion at specific sites, or in other words, the reasons behind pitting corrosion. The model considers that the adsorbed chloride on the surface of the passive layer migrates to the metal-oxide interface via vacancies formerly occupied by O^{2-}, and the formation of Fe^{2+}/Cl^- complex leads to enhanced cation diffusion rates. The decreasing oxygen vacancies at the film/solution interface, due to occupation by Cl^-, lead to the formation of voids at the metal/film interface, primarily by the accelerated dissolution of iron in that particular local environment, leading to pitting.

2.3.1.3 Chloride threshold value

The concept of critical chloride content has been developed significantly over the last several decades and is one of the major factors considered while designing new and assessing already existing structures [99]. According to this concept, in non-carbonated reinforced concrete structures, the corrosion/depassivation of the reinforcement can only occur when the chloride concentration at the depth of the reinforcement has reached a certain critical value [134]. This value is termed the chloride threshold value, often referred to as C_{crit}. The critical chloride content is closely related to Tuutti's [14] model for corrosion initiation and propagation, and along the time scale can be described as the deterministic point of transition from the initiation to the propagation stage. The C_{crit} values are generally defined by the total chloride content with respect to the weight of cement, but are also quite often reported relating the free chloride ion concentration to the pH of the solution ($[Cl^-]/[OH^-]$), and this value represents the condition where the preference of the free chloride ion to migrate into the pit becomes greater than that of the hydroxide [99].

Numerous works have been published presenting values for C_{crit} for reinforced concrete, for steel immersed in simulated solutions as well as for steel embedded in concrete, and some of these are shown in Table 2-1. Hausmann [135] experimentally reported the value of C_{crit} ($[Cl^-]/[OH^-]$) to vary between 0.5 and 1.08, and statistically found the ratio of 0.63 as critical, for steel samples immersed in simulated pore solutions of concrete with chloride contamination. On the other hand, Gouda [95] related the chloride threshold to the pH of the pore solution and

found a linear relationship between the pH and the logarithm of the chloride concentration with a slope of 0.83, indicating a relationship based on ($[Cl^-]^{0.83}/[OH^-]$), thus implying that the chloride threshold value is highly dependent on the concentration of hydroxide ions. A similar observation was made by Li and Sagues [136], where the chloride threshold value increased with higher pH. As can be seen from Table 2-1 and other works in the literature, the values reported for chloride threshold vary not only from study to study, but also depending on the experimental conditions. These studies, however, represent the inhibitive property of the concrete only through the concentration of hydroxide ions present in the pore solution.

Table 2-1: Published C_{crit} values for conditions when steel is immersed in simulated pore solutions (assuming only free chloride content) – adapted from [99].

C_{crit} (Cl^-/OH^-)	**Remarks**	**Reference**
0.02-0.13	Aerated solution, pH 12.6	[137]
0.6	Aerated solution, pH 11.6-13.2	[135]
0.57; 0.48; 0.29; 0.27; 0.30	Solution with pH 11.8; 12.1; 12.6; 13.0; 13.3 respectively	[95,138]
0.25-0.8	Aerated solution, pH 13.8	[139]
0.26	Solution with pH 13.5	[140]
0.01-0.04; 0.2-0.8; 1-2.5	Solutions with pH 12.6; 13.3; 13.6 respectively	[136]
0.178; 0.313	Solutions with pH 12.5; 13.9 respectively	[141]

Glass and Buenfeld [142,143] argued that the representation of the chloride threshold value in terms of $[Cl^-]/[OH^-]$ considering only free chloride, does not take into account other factors that might play a role in determining the service life of concrete structures. They mainly argued that the representation of the chloride threshold value as $[Cl^-]/[OH^-]$ ignores the fact that a percentage of the total chloride bound to the hydration products in the concrete cover could be

released back into the pore solution (due to several factors), increasing the concentration of chloride locally and therefore posing a higher risk of corrosion. Therefore, the chloride threshold value should be represented in the form of total chloride content with respect to the weight of binder, and so the consideration of bound chloride is important in determining chloride threshold values. They also suggested that other properties such as the buffer capacity of the concrete and the SCI (i.e., control of local acidification) may also affect the chloride threshold value. Various studies have reported C_{crit} as a percentage of the total binder content to be between 0.04 wt.% and 8.34 wt.%. Table 2-2 lists various determinations of C_{crit} as a percentage of the binder content, found in the literature for PC, PC blended concretes and mortars exposed to chloride solutions.

Table 2-2: Published C_{crit} values (as a percentage of the total binder content) obtained from experiments with the steel embedded in cement based material (laboratory conditions) – adapted from [99]. PC: Portland cement; FA: Fly ash; SF: Silica fume; GGBS: Ground granulated blast furnace slag; SRPC: Sulfate resistant Portland cement; RHPC: Rapid hardening Portland cement

C_{crit} (wt. % of binder)	**Remarks**	**Reference**
0.20 – 0.68	PC, FA, SF, SRPC, RHPC	[144]
0.48 – 2.02	PC, FA, SF, GGBS, SRPC	[145]
1.50 – 2.50	PC, SRPC	[146,147]
0.50 – 1.80	PC, SF, FA	[148]
0.50 – 1.50	PC, GGBS, FA	[149]
0.25 – 0.75	PC, FA, SF, GGBS, SRPC	[150]
0.25 – 1.25	PC	[151]
0.735	PC, SRPC, FA	[152]
1.00 – 8.34	PC, SRPC, FA	[152]
0.62	SRPC	[153]

0.04 – 0.24	PC	[154]
0.45	SRPC	[154]
0.40 – 1.30	PC	[155,156]
0.52 – 0.75	PC	[157]
0.05 – 0.15	PC	[158]
0.40 – 0.80	PC	[159]

An extensive review conducted by Angst et al. [99] listed numerous factors that affect the chloride threshold value. The most dominant factors were found to be the SCI, the pH of the pore solution and the redox potential of the steel. As mentioned in Section 2.2, pore solutions of hydrated cement pastes are highly alkaline and maintain the embedded steel in a passive state. Considering the concentration of hydroxide ions as the only major inhibiting factor, the chloride threshold value ($[Cl^-]/[OH^-]$) has a direct relationship with the pH of the pore solution [95,135,136]. A recent review by RILEM TC 262-SCI [54] looked at the various characteristics of the SCI that could potentially influence the chloride threshold value (a schematic of all the features of the SCI is shown in Figure 2-11). From a metallurgical perspective, the type of steel reinforcement used [160,161], the presence of mill scale or pre-existing rust layers [162,163], the surface condition of the reinforcement [164], and the chemistry of the passive film [165] would possibly affect the susceptibility to chloride-induced corrosion. Microstructural features of the concrete cover at the SCI such as presence of air and water filled voids, cracks, and bleed water zones have been shown to influence chloride-induced corrosion [54,166,167]. The chemistry of the cement paste, the composition of the pore solution and the degree of saturation at the SCI impact the corrosion behaviour of the reinforcement [54]. The chloride threshold values also depends on the redox potential of the steel and has been found to be higher for conditions when the steel potential is more negative [152]. At this point, it would be noteworthy to mention that the parameters affecting the chloride threshold value are all interlinked and therefore, defining major influencing parameters independently in real structures is extremely difficult. Literature on the chloride threshold value for AAMs is very scattered and limited, and will be discussed in detail in Chapters 4 and 5.

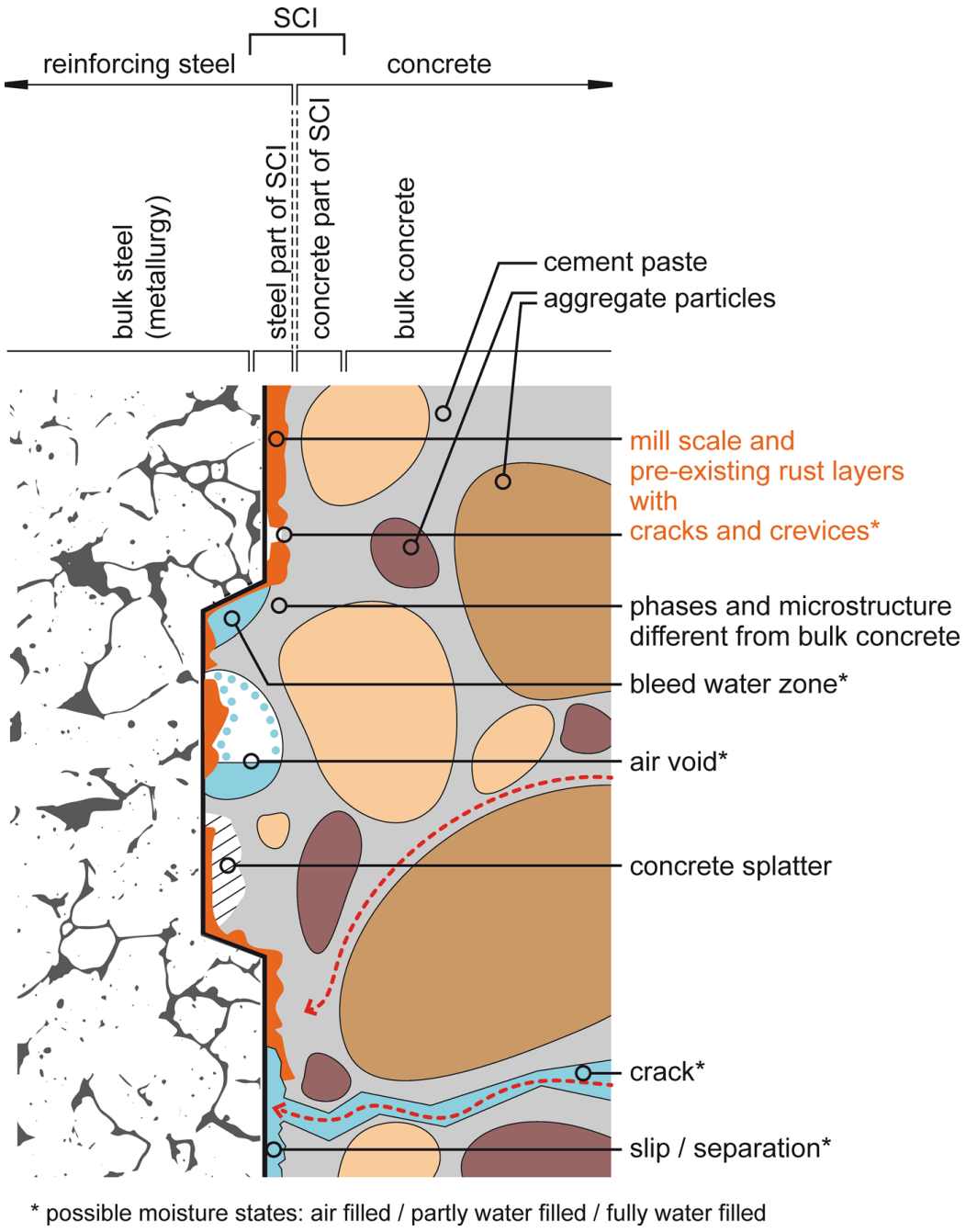

Figure 2-11: An illustration of the SCI and some of its characteristics features that could potentially influence the onset of chloride-induced corrosion. Preferential pathways for chloride ingress and adsorbed water are represented by red dashed lines and blue spaces, respectively. The water contained within cement is not shown here. From [54].

2.3.2 Carbonation induced corrosion

Carbonation of concrete, which is the chemical reaction between atmospheric carbon dioxide and the cement matrix, is one of the important degradation processes adversely impacting the long term durability of structures [168–170]. The carbonation of PC has been thoroughly studied in the literature. Gaseous carbon dioxide from the surrounding environment penetrates through the porous concrete structure and dissolves in the pore solution forming weak acidic ionic species of HCO_3^- and CO_3^{2-} [102]. The dissolution of gaseous carbon dioxide and formation of weak acids can be represented by the following reactions (Eq. 2.19 – Eq. 2.21) [171]:

$$CO_2(g) \rightarrow CO_2(aq) \quad \text{(Eq. 2.19)}$$

$$CO_2(aq) + H_2O \rightarrow H^+ + HCO_3^-(aq) \quad \text{(Eq. 2.20)}$$

$$HCO_3^-(aq) \rightarrow H^+ + CO_3^{2-}(aq) \quad \text{(Eq. 2.21)}$$

The release of acidic species such as H^+ leads to a reduction in the alkalinity of the pore solution which causes the dissolution of Ca-rich hydration products such as portlandite, calcium silicate hydrate gel, AFm and ettringite [172–174]. The dissolved calcium and carbonate ions react to precipitate various polymorphs of $CaCO_3$ – vaterite, aragonite, amorphous $CaCO_3$, or calcite (Eq. 2.22) [172].

$$Ca^{2+}(aq) + CO_3^{2-} \rightarrow CaCO_3(s) \quad \text{(Eq. 2.22)}$$

The reduction of alkalinity due to carbonation in reinforced structures can result in the breakdown of the passive film formed around steel. In the case of chemically bound chloride in the form of calcium chloroaluminate hydrates, or bound otherwise [13], carbonation may lead to the release of chloride ions in the pore solution, thereby increasing the concentration of chloride and the possibility of depassivation.

The mechanisms of carbonation in AAMs are significantly different from those observed in PC due to the differences in the pore solution composition and the hydrate phase assemblage. Depending on the calcium content in the binder, carbonation of AAMs can be described by two processes: carbonation of the pore solution and carbonation of the solid hydrate phases. In the case of high-Ca AAMs such as alkali-activated slags, the carbonation of the pore solution leads to the formation of alkali-metal carbonates and bicarbonates depending on the CO_2 exposure conditions [119]. Under natural exposure to carbon dioxide (0.03 - 0.04 % CO_2), natron

(Na_2CO_3) was found to be the major carbonate containing phase formed due to the reaction between dissolved alkalis in the pore solution and the carbonate ions [175]. However, exposure to CO_2 concentrations above 0.2 % led to the formation of nahcolite ($NaHCO_3$) [175]. The importance of exposure conditions is highlighted by the role of carbonate/bicarbonate ions on the pH of the pore solution. Under ambient conditions of CO_2 exposure, the CO_3^{2-}/HCO_3^- ratio was found to be >1, whereas for elevated CO_2 exposure conditions CO_3^{2-}/HCO_3^- was observed to be <0.1, and the pH of the pore solutions under natural exposure to CO_2 was two units higher than those exposed to accelerated testing conditions [175]. The concentrations of both of these species in the pore solution were in agreement with the nature of the solid phases predicted by a thermodynamic model [175]. Under ambient conditions, the pH of the pore solution did not fall below 10 [176] and therefore, according to the Pourbaix diagram the loss of steel passivity in AAMs seems to be unlikely.

In addition to carbonation of the pore solution, carbonation of the solid phase in high Ca-AAMs such as alkali-activated slags proceeds by the decalcification of C-A-S-H gel, resulting in an alumina-rich remnant silicate gel and the precipitation of various polymorphs of $CaCO_3$ [119,177]. Unlike in PC, where carbonation occurs through the reaction of dissolved CO_2 with portlandite to form $CaCO_3$ followed by reaction with the C-S-H gel, in the case of alkali-activated slags (which contain no portlandite) carbonation occurs by the direct decalcification of C-A-S-H gel [119]. Secondary hydrate products such as the hydrotalcite-type phases in alkali-activated slags also influence the rate of carbonation [178]. The formation of hydrotalcite-type phases is directly related to the MgO content in the slag [178]. Higher MgO contents in the slag were found to give higher carbonate binding capacities and henceforth, lead to lower carbonation rates.

The effect of carbonation on the alkalinity of pore solution is one of the most important factors when considering corrosion of the steel reinforcement. In addition, carbonation of AAMs has been found to adversely influence the porosity of the cement matrix as well as the strength [119,179,180]. However, further work is required to understand the mechanisms governing the influence of carbonation on the mechanical properties of AAMs.

2.3.3 Analysing steel corrosion in concrete – current state of the art

Various techniques have been used to detect the depassivation/corrosion of steel reinforcement in concrete. It is important to note that the methods used for assessing the severity of corrosion for structures in-service and the methods used for detecting the conditions/time required for

depassivation of the steel reinforcement in the laboratory are very similar. This section covers the current state of the art – based on the recommendations of [181] and [182,183] - in analysing the data obtained from various techniques, and is primarily valid for PC based concretes; applicability in the case of AAMs is discussed in Chapter 7. A detailed description of the various techniques used in this thesis can be found in Chapter 3.

The potential of a corroding steel specimen is much lower than that of passivated steel and measuring the steel potential with respect to a reference electrode is the most common technique employed to detect depassivation of the steel reinforcement. Figure 2-12A highlights the probability of corrosion as a function of the potential for PC based concretes, based on [181]. However, a lower potential does not necessarily indicate the corrosion state of the steel reinforcement, as this could be due to various factors such as oxygen availability, resistivity of the concrete, use of SCMs, and saturation state of the concrete. Therefore, in order to detect onset of steel corrosion a clear drop in the potential needs to be observed. The general criterion for detecting a transition from the passive to the active state has been experimentally observed to be a shift in the steel potential by around -250 mV [184], and this can be effectively used to measure the C_{crit}.

Another technique quite frequently used for detecting the onset of corrosion is calculation of the instantaneous corrosion current density using the method described by [182,183]. The corrosion current density is inversely proportional to the linear polarisation resistance, and can be calculated using the Stern-Geary relationship [185]. The Stern-Geary relationship is based on the theory put forward by Wagner and Traud [186] on the mixed potentials of electrodes subject to uniform corrosion. The Stern-Geary relationship also assumes the oxidation and reduction reactions occurring at the electrolyte-electrode interface to be activation controlled. Therefore, in the case of chloride-induced corrosion of steel-reinforced concrete, the applicability of the Stern-Geary relationship to determine the instantaneous corrosion current density or instantaneous corrosion rate has been debated [187]. Figure 2-12B indicates the level of corrosion as a function of the corrosion current density for PC based concretes. According to empirical observations [182,183], any specimen with an instantaneous corrosion current density above 0.1 and 0.2 $\mu A/cm^2$ can be considered to be actively corroding. The difficulties in using this technique to accurately assess the severity of corrosion have been described in more detail in Chapter 3. As in the case of analysing the steel potential, only a significant rise in the corrosion current density should be assumed to correspond to a transition from the passive to the active state of the steel reinforcement. Corresponding classifications have been

described for the risk of corrosion as a function of the resistivity of the concrete cover by RILEM TC-154 EMC [188].

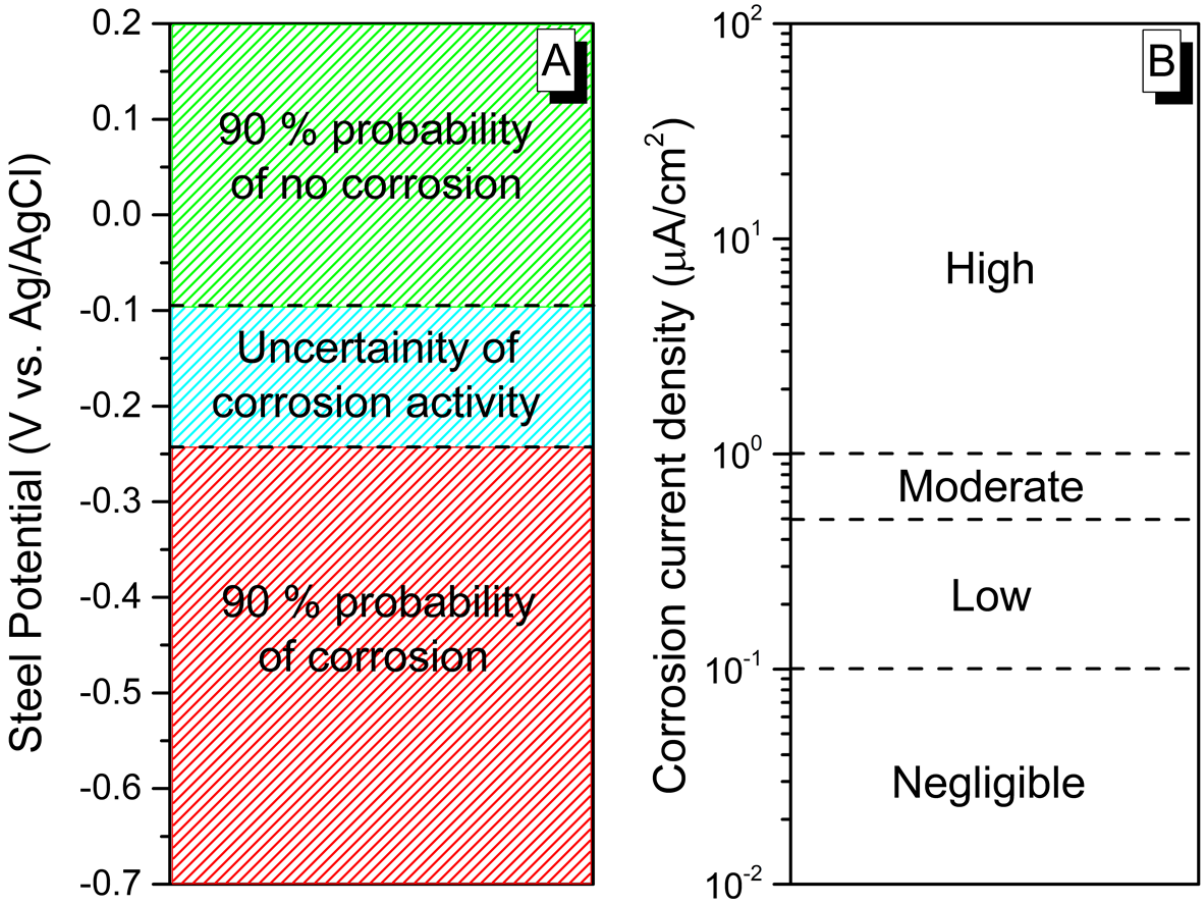

Figure 2-12: (A) Standard criterion described by [181] for assessing the probability of corrosion in steel reinforced concrete structures. The reference potential has been changed from $Cu/CuSO_4$ to Ag/AgCl according to ASTM G3 [189]. (B) The severity of corrosion in PC-based concretes as a function of the corrosion current density calculated using the Stern-Geary relationship (adapted from [182,183]).

Gravimetric weight loss is a common technique to assess the corrosion rate of the steel reinforcement, where the steel is weighed before and after corrosion is induced. The reinforcement needs to be extracted from the concrete and cleaned very carefully, ensuring the removal of remnant concrete but also without damaging the corrosion products. However, significant corrosion is required to record any noticeable weight loss, and therefore this technique is not very useful in detecting the onset of corrosion or pitting and C_{crit}.

Various other techniques such as electrochemical impedance spectroscopy, galvanostatic polarisation, and visual inspection, among others, have been used to detect the onset of steel corrosion in concrete.

Electrochemical impedance spectroscopy (EIS) is a non-destructive technique and has often been used to characterise the SCI and in particular to assess the resistance of the passive film on the reinforcement to chloride or carbonation induced corrosion. The fundamentals of EIS have been discussed in Chapter 3 and can also be found in an extensive review by Chang and Park [190]. Several authors have used EIS to quantify the stability of the passive film formed on the steel reinforcement by interpreting Nyquist plots (discussed in Chapter 3 in more detail) through modelling electrical circuits representative of the SCI [184,191–195]. As illustrated in [92,93,193,196], simulating the SCI as an electrical circuit, important information regarding the mechanism of passivation and depassivation could be obtained. However, there exist no standards or validated recommendations regarding the quantitative assessment of data from EIS, to detect depassivation and the severity of steel corrosion. Additionally, EIS has also been used to understand the mechanism of cement hydration and the pore structure, but this falls outside the scope of this thesis and can be found in [197,198].

Cyclic voltammetry is a common technique employed to understand the mechanisms of passivation of steel in various electrolytes. A detailed description of the technique has been highlighted in Chapter 3. The current response of the system upon cyclic polarisation in the anodic and the cathodic directions can be used to interpret the redox reactions occurring at the electrode-electrolyte interface and the reversible nature of redox reactions can be also be detected [199,200]. Cyclic voltammetry is an extremely useful technique to determine the state of the steel reinforcement in simulated pore solutions of various cementitious materials and therefore, can be used to gain insight into the mechanisms of steel corrosion as a function of the surface chemistry within cementitious matrices [194].

2.4 Conclusion

AAMs are very different from PC, both in chemistry and in microstructure, and this leads to differences in their performance. On both aforementioned fronts, there have been significant advances in the understanding of AAMs, however there still remains substantial uncertainty regarding their long-term durability. In particular, the performance of steel reinforced AAMs

in environments of CO_2 or chloride exposure is a matter of great concern. There exists very limited and inconsistent literature on the long-term durability of these materials.

In Europe, the degradation of majority of the concrete structures are due to chloride-induced corrosion of the embedded steel reinforcement and therefore, this thesis is aimed at understanding the long-term performance of various AAMs when exposed to chloride, through a simulated pore solution approach. The following chapters provide fundamental insight into the influence of the chemistry of the AAMs on the steel surface – and thus the mechanisms governing the passivation chemistry of the steel surface in various AAMs. This thesis analyses and details the conditions which induce the onset of chloride-induced steel corrosion in AAMs, once the chloride has passed through the cover concrete and begun to increase in concentration at the SCI. Finally, a model to predict the service life of steel reinforced AAMs when exposed to chloride is developed.

Chapter 3: Materials and Methods

3.1 Materials

The steel reinforcement bars used in this research were mild steel, conforming to B500 grade [201], with chemical composition (measured through X-ray fluorescence (XRF)) as listed in Table 3-1. The steel bars (φ = 12 mm) were obtained from a local supplier in Sheffield, UK. The rebars were sectioned into small pellets, thickness 5.5 - 6.5 mm, using an abrasive disc. Before electrochemical testing, the pellet surfaces were polished using SiC abrasive paper with 240 to 600 grit sizes and degreased using acetone, ensuring R_a = 0.14 μm (measured using ContourGT-X 3D Optical Profiler at the University of Sheffield). Additionally, the Fe $2p_{3/2}$ and S 2*p* spectra obtained using XPS on bare steel surfaces can be found in Chapter 8.

Table 3-1: Composition of mild steel rebar measured using XRF (standard deviation = ± 0.03 wt.%)

Elements	**Fe**	**C**	**Cr**	**Ni**	**Cu**	**Si**	**Mn**	**S**	**Mo**	**P**
Wt.%	97.91	0.21	0.13	0.20	0.47	0.23	0.76	0.03	0.02	0.04

3.1.1 Simulated pore solution compositions

Simulated pore solutions representative of AAMs were formulated primarily based on the work of Lloyd et al. [79] and Myers et al. [80,81]. Keeping in mind the variation in the chemistry of the aluminosilicate sources, the type and dosage of activators and the curing conditions, data from [76–78,202] were taken into account. Reagent grade chemicals: NaOH (Sigma Aldrich) and $Na_2S{\cdot}9H_2O$ (Alfa-Aesar) were used to synthesise simulated pore solutions representative of low-Ca AAMs and high-Ca AAMs. Chloride was introduced in the simulated pore solutions as NaCl (Santa Cruz Biotechnology). Simulated pore solutions of low-Ca AAMs were synthesised by mixing NaOH pellets of known quantities with 250 ml distilled water. In the case of high-Ca AAMs, known quantities of NaOH and $Na_2S{\cdot}9H_2O$ were dissolved in 250 ml distilled water. Detailed compositions of the simulated pore solutions used in this study can be found in Chapters 4 and 5. The pH of all simulated pore solutions were recorded within the

corrosion cell using a digital pH meter (Oakton Acorn Series), calibrated with reference standard pH buffer solutions of pH 4, 7 and 10. It is to be noted that accuracy of glass electrodes used to measure the pH of highly alkaline solutions, as is the case in this study, is questionable and is commonly referred to as the "alkaline error" [203]. Additionally, due to instrumental constraints the recorded pH values are representative of the bulk solution instead of the pH at steel/solution interface.

3.2 Electrochemical Techniques

All electrochemical tests were conducted in a 400 mL corrosion cell using a PGSTAT 204 potentiostat/galvanostat (Metrohm Autolab B.V.). Measurements were conducted using a conventional three electrode setup (electrolyte volume 250 mL), comprising a stainless steel counter electrode, an Ag/AgCl (saturated 3 M KCl) reference electrode and the steel surface (surface area: 0.287 cm^2) acting as the working electrode (Figure 3-1). The steel surface acting as the working electrode was the cut surface and not the actual (curved) rebar surface, primarily due to constraints of the corrosion cell (as shown in Figure 3-1 and Figure 8-1, Chapter 8). The reference electrode was positioned near the surface of the working electrode by means of a Luggin capillary. All measurements were conducted at room temperature (22 ± 2 °C) at least on two samples to ensure reproducibility.

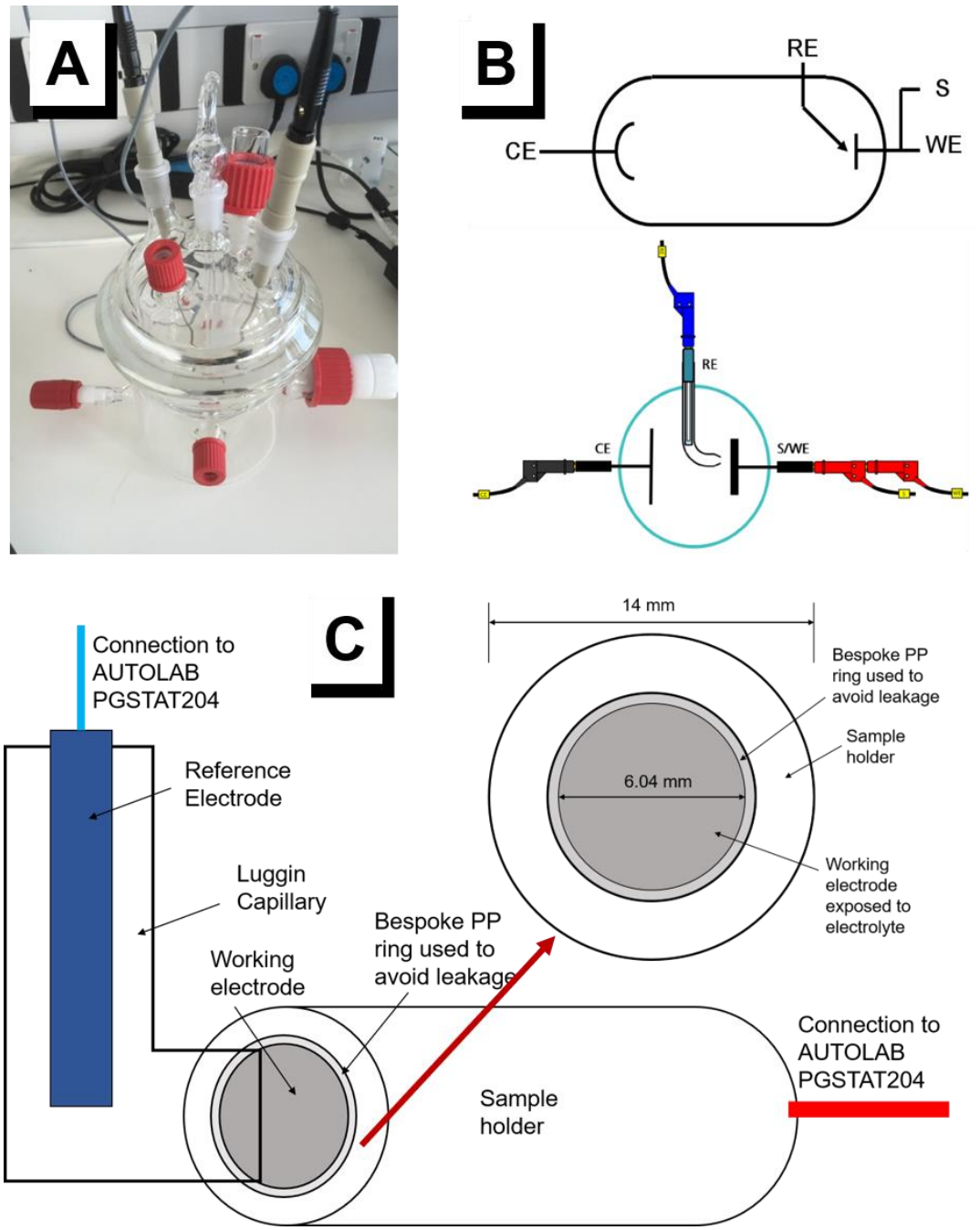

Figure 3-1: (A) 400 mL corrosion cell provided by Metrohm Autolab B.V., (B) schematic of the three-electrode cell, where RE = reference electrode, CE = counter electrode, WE = working electrode, S = sample. The RE is placed next to the sample (WE) by means of a Luggin capillary, and (C) schematic of the cell setup used for electrochemical testing. The Luggin capillary was positioned in front of the working electrode at a distance of 1-1.5 mm.

3.2.1 Open circuit potential

Open circuit potential (OCP), also commonly referred to as the corrosion potential (E_{corr}) or as the half-cell potential, can be described as the potential difference between the reference electrode and the working electrode in a particular electrolyte, when the cell is disconnected [83]. In electrochemical literature, the OCP is generally referred to as the zero-current potential, due to the cell being switched off and no external current/voltage being applied. In aqueous systems (at a given temperature), the OCP strongly depends on the chemistry of the working electrode, the chemistry of the electrolyte, and the nature of the reference electrode (Figure 3-2). The OCP of any particular system can yield qualitative thermodynamic data (through Pourbaix diagrams), where any potential above the OCP would be representative of the oxidation reactions occurring at the electrolyte/working electrode interface, and a potential lower than OCP would be representative of reducing conditions at the electrolyte/working electrode interface. The measurement of OCP is a non-destructive test, and therefore is done prior to almost all other electrochemical tests.

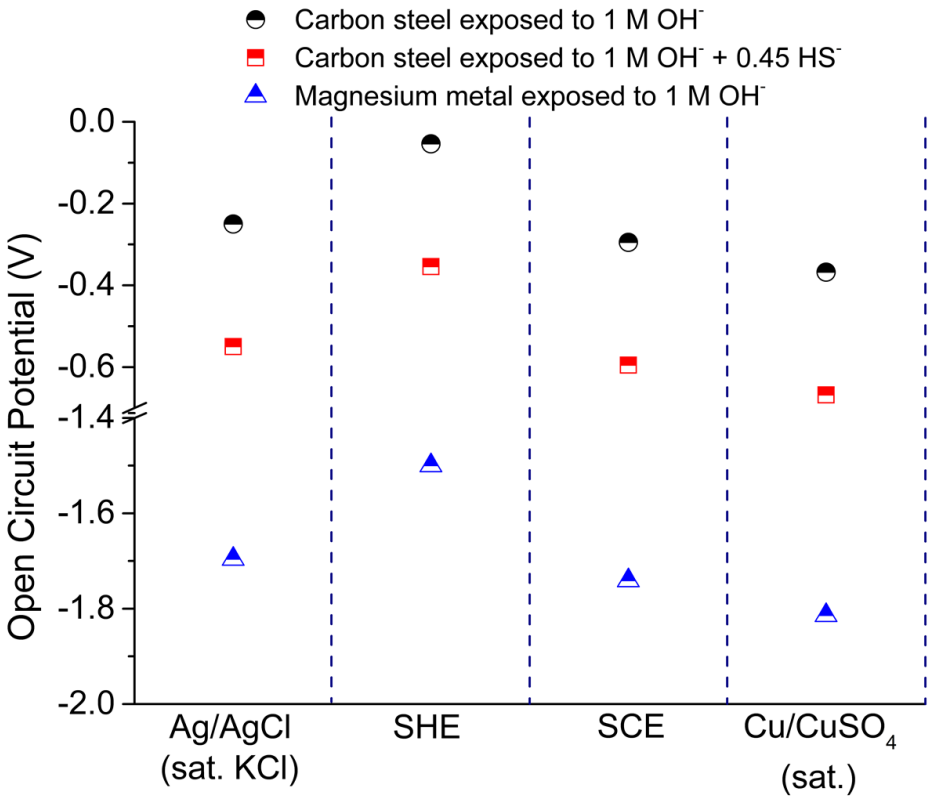

Figure 3-2: The influence of various aqueous electrolytes, chemistry of the working electrode and the reference electrode on the measured OCP values. SHE stands for standard hydrogen

electrode, SCE stands for standard calomel electrode, and sat. indicates a saturated solution. The offsets for various reference electrodes were calculated using ASTM C876-15 [181].

In the case of OCP or corrosion potential for steel embedded in concrete, other factors such as concrete resistivity, microstructure of the concrete cover, the humidity, oxygen availability and positioning of the reference electrode can greatly influence the measurements. Measurement of the corrosion potentials and their interpretations for steel embedded in mortar/concrete are described in great detail in ASTM C876-15 [181] and in the recommendations of RILEM TC-154 EMC [204].

In this study, each sample was allowed to stabilise in the electrolyte for 15 mins inside the corrosion cell prior to testing. The OCP was recorded for 30 mins in the beginning of each experiment unless the change in potential with time (dV/dt) reached ≤ 1 µV/s before 30 mins. The OCP value reported in each case is the mean potential recorded during the last 60 seconds of the test.

3.2.2 Electrochemical impedance spectroscopy

The impedance of a system is defined as the resistance or opposition to the flow of alternating current (AC) [190]. Electrochemical impedance spectroscopy (EIS) is conducted by applying a sinusoidal potential excitation (typically with an amplitude of 10 mV) at varying frequencies and the corresponding current response is recorded (as shown in Figure 3-3) [83,205]. EIS has become a very popular technique in characterising and quantifying passivation and depassivation of the steel reinforcement in concrete as well as in simulated pore solutions [193,194,206,207].

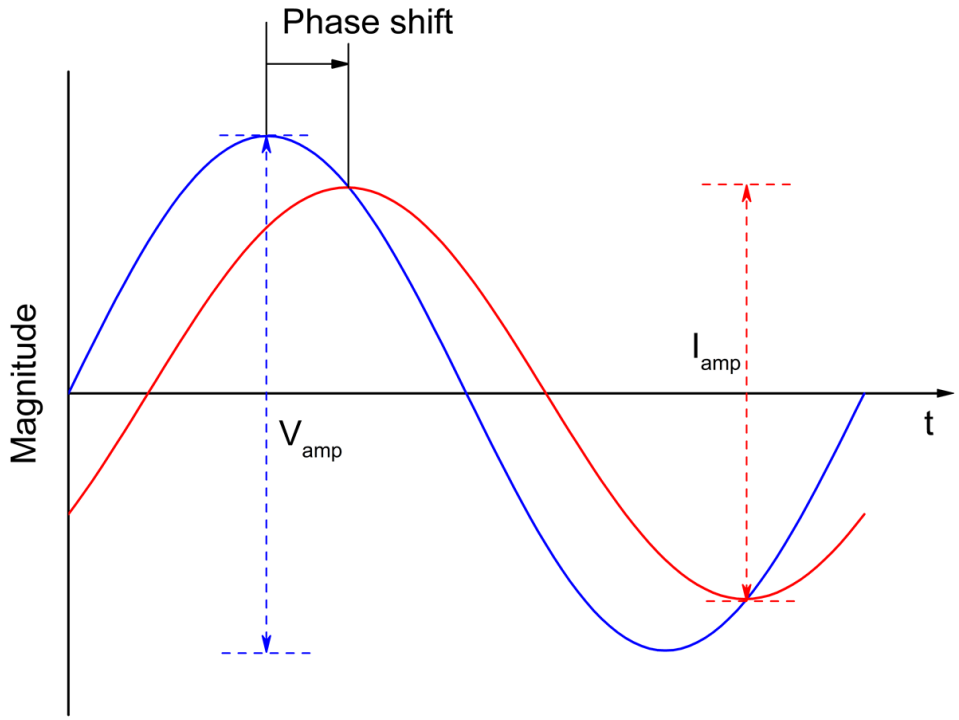

Figure 3-3: Schematic of the applied sinusoidal potential excitation (with an amplitude of V_{amp}) and the current response (amplitude of I_{amp}) of the system. The current response of the system is sinusoidal with the same frequency, but shifted in phase.

The impedance (Z) of the system can be calculated by Eq. 3.1, analogous to Ohm's law:

$$Z = \frac{E_t}{I_t} = \frac{E_o \sin(\omega t)}{I_o \sin(\omega t + \varphi)} \qquad \text{(Eq. 3.1)}$$

where E_t is the potential at time t, E_o is the amplitude of the potential signal, I_t is the amplitude of the current at time t, shifted in phase (φ) and different from the applied amplitude I_o, and ω is the angular frequency and is given by $\omega = 2\pi f$ (where f is the frequency in hertz). The impedance can be expressed in terms of the magnitude (Z_o) and a phase shift (φ), as:

$$Z = Z_o \frac{\sin(\omega t)}{\sin(\omega t + \varphi)} \qquad \text{(Eq. 3.2)}$$

On applying Euler's relationship, the impedance can be expressed in the complex plane as:

$$Z = \frac{E_t}{I_t} = \frac{E_o e^{i\omega t}}{I_o e^{i(\omega t - \varphi)}} = Z_o e^{i\varphi} = Z_o (\cos\varphi + i \sin\varphi) \qquad \text{(Eq. 3.3)}$$

The imaginary and the real parts of impedance from Eq. 3.3 can be used to plot the Nyquist plot (complex plane), to determine the electrical properties of the electrolyte/electrode interface [83]. Equivalent electrical circuits can be used to model and fit the Nyquist plots, in order to

quantify the resistance of the electrolyte, the double layer capacitance and the charge transfer resistance [83]. In this study, the Zview2 software was used to fit the Nyquist plots with the most appropriate equivalent circuit model.

EIS can be carried out in two modes, by a small excitation of the potential (potentiostatic) or by a small excitation of the current (galvanostatic) [83]. When EIS is conducted in the potentiostatic mode, the potential of the working electrode is excited with respect to the OCP (with an amplitude of ± 10 mV vs OCP) and the current response is measured. One of the limitations of the potentiostatic mode is that the potential of the system needs to be stable (*dE/dt = 0 V/s*) before conducting the test, and this is very difficult to achieve when the steel is passivating or corroding. Conversely, the current is fluctuated (with an amplitude of ± 10 µA) in the galvanostatic mode, and the net current of the system is maintained at 0.00 A before each excitation. The galvanostatic mode can address any variation in the OCP due to the interaction of hydroxide or chloride with steel during the course of EIS measurements. Detailed descriptions of conducting EIS in concretes and in simulated pore solutions can be found in [193,206,208–212].

The parameters used for carrying out EIS, and the equivalent circuit models used to fit the Nyquist plots, are described in detail within Chapter 4.

3.2.3 Polarisation

3.2.3.1 Linear polarisation resistance

Linear polarisation resistance (LPR) is one of the most common non-destructive techniques used for measuring the instantaneous corrosion rate of the steel-reinforcement embedded in concrete. The fundamentals of LPR are based on the observations of Stern and Geary [185], where the potential-current relationships were found to exhibit linearity for a small applied polarisation with respect to OCP (5-20 mV vs. OCP). Upon slight polarisation from OCP, the polarisation resistance (R_p) of the steel can be described as the ratio between the applied voltage (ΔE) and the corresponding current (ΔI), or as the slope of the polarisation curve (E vs. I) at the corrosion potential (Eq. 3.4):

$$R_p = \left(\frac{\Delta E}{\Delta I}\right)_{\Delta E \to 0} \qquad \text{(Eq. 3.4)}$$

R_p values are generally related to the surface area of the metal exposed to the electrolyte and can be expressed with the units $\Omega.cm^2$, as the term ΔI is normalised to the surface area. The relationship between the corrosion current density (i_{corr}) and R_p can be described by the classical Stern-Geary equation [185] (Eq. 3.5):

$$i_{corr} = \frac{B}{R_p} = \frac{\beta_a \beta_c}{2.3(\beta_a + \beta_c)} \cdot \frac{1}{R_p} \qquad \text{(Eq. 3.5)}$$

where, β_a and β_c are the anodic and cathodic Tafel constants, B is the proportionality constant derived from the Tafel constants, and i_{corr} has the units A/cm^2. In the case of PC and simulated pore solutions of PC, the value of B has conventionally been proposed to be 26 mV for corroding steel and 52 mV for passive steel [213]. These values of B are not necessarily true in the case of AAMs (discussed in Chapter 4 and Chapter 7) [21]. The reader is directed towards specific and detailed literature on the Stern-Geary equation [185] and the Tafel equation [83].

Though LPR is a quick and a non-destructive technique for steel embedded in concrete, conclusions about i_{corr} derived from its use in the case of localised corrosion may be questionable, particularly for steel embedded in concrete [187]. In most laboratory specimens where the surface area of the exposed specimen is known, it is easy to calculate R_p, but for in-service structures, the surface area of the steel reinforcement is effectively infinite and therefore, the R_p and i_{corr} cannot be calculated as a function of the area of the exposed steel. Moreover, unlike uniform corrosion where the corroding area is generally the entirety of the exposed surface, the corroding area in localised corrosion is generally unknown, smaller in area and can vary over time. This leads to both R_p and i_{corr} becoming average values over the entire surface area exposed to the electrolyte and therefore, not accurately depicting the corrosion rate of the reinforcement. Another drawback of the LPR technique is that the technique does not give reliable measurements for submerged concretes (that may be water saturated) or where the steel is in the passive state with restricted access to oxygen. As mentioned in Chapter 2, the presence of oxygen is a fundamental requirement for localised corrosion to occur. Therefore, the absence of oxygen would inhibit the cathodic reaction and hence, measurement of R_p and i_{corr} using LPR would be misleading (discussed in detail in Chapter 5).

In this study, LPR was used to measure R_p and i_{corr} for steel reinforcement exposed to various pore solutions. Prior to LPR measurements, the open circuit potential was measured once again to take into account any change in potential during EIS testing due to changes on the steel surface. The potential was varied from -20 mV to +20 mV vs. OCP (scan rate of 0.167

mV/s and step potential 0.244 mV) and the current response was recorded. R_p and i_{corr} were calculated using Eq. 3.4 and Eq. 3.5 respectively, and the values of B used in this study were those proposed in the literature [213,214].

3.2.3.2 Anodic and cathodic polarisation

As discussed in Section 2.2, corrosion of steel is a combination of two half-cell reactions: the anodic oxidation of the steel (Eq. 2.1) and the cathodic reduction of adsorbed oxygen on the surface of the metal (Eq. 2.2). To study the anodic and cathodic reactions occurring at the steel surface, the steel is polarised in both the anodic (positive) and the cathodic (negative) directions vs. OCP. However, the polarisation (> 20 mV vs. OCP) is much higher than that used in LPR, beyond the region where the applied potential and current exhibit linearity.

In this study, the specimens were polarised in the cathodic direction initially from the OCP to -0.25 V vs. the OCP, with the step potential and scan rate set at 0.244 mV and 0.167 mV/s respectively, and the corresponding current density was recorded. Upon the completion of cathodic polarisation, the steel was allowed to stabilise back to the OCP. Subsequently, the steel was polarised from the OCP to + 1.0 V vs. the OCP with the same step potential and scan rate, and the corresponding current density was recorded.

3.2.4 Cyclic voltammetry

Cyclic voltammetry (CV) is one of the most widely used electrochemical techniques to decipher reactions occurring at the working electrode/electrolyte interface [83]. The potential is linearly swept from a starting potential towards a predetermined potential (also referred to as the 'switching potential'), and then the direction of the scan is reversed until reaching another predetermined potential. The corresponding current density is recorded and plotted against the applied potential. Figure 3-4 shows a typical schematic of the experimental configuration used in cyclic voltammetry, where the potential is linearly swept from the cathodic limit ($E_{\lambda,c}$) to the anodic limit ($E_{\lambda,a}$) and reversed back to $E_{\lambda,c}$. The corresponding current density as a function of the applied potential yields information about the electrochemical reactions occurring at the interface of the working electrode and the electrolyte. The reader is directed towards [83] for an in-depth understanding of CV.

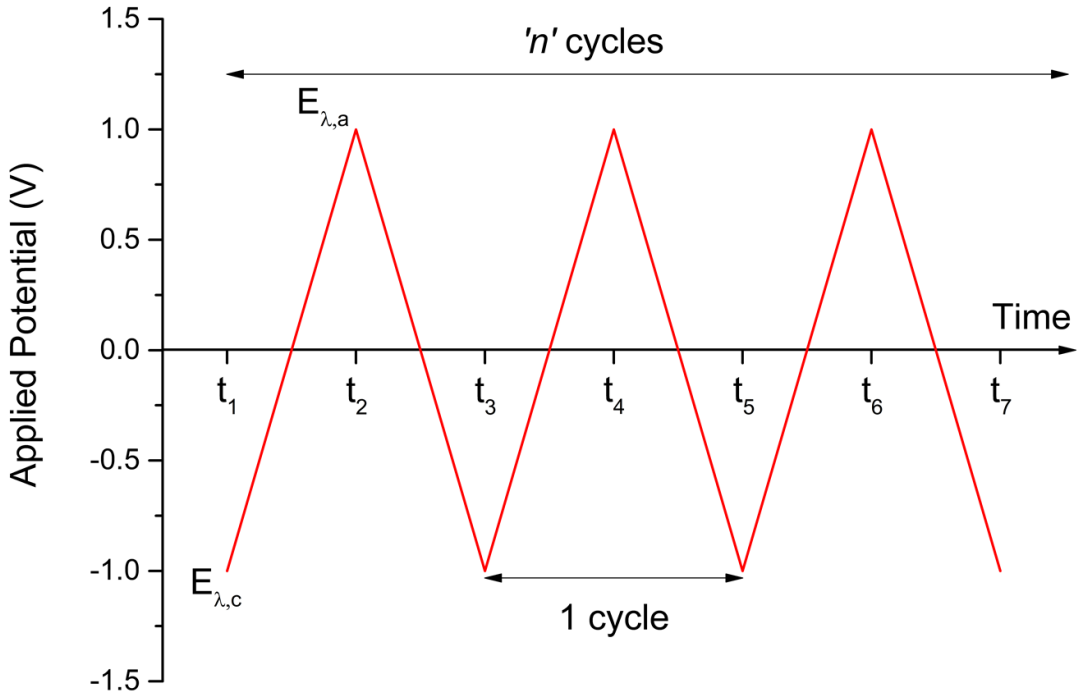

Figure 3-4: A typical schematic of the experimental configuration (commonly referred to as 'potential waveform') used in cyclic voltammetry. The potential is ramped up from the cathodic limit ($E_{\lambda,c}$) to the anodic limit ($E_{\lambda,a}$) and reversed back to $E_{\lambda,c}$, thereby completing one cycle. The corresponding current density is recorded to elucidate the oxidation and reduction reactions occurring at the working electrode/electrolyte interface.

In this study, CV was used to identify the mechanisms of passivation for steel immersed in highly alkaline solutions representative of the pore solutions of low Ca AAMs and high Ca AAMs. The reader is directed to Chapter 4 and Chapter 5 for a detailed discussion on the testing parameters used to conduct CV.

3.3 X-ray photoelectron spectroscopy

X-ray photoelectron spectroscopy (XPS), also known as electron spectroscopy for chemical analysis (ESCA), is an extremely powerful technique to characterise the surface chemistry of a material (in this case, mild steel exposed to simulated pore solutions of AAMs). XPS works on the principle of the photoelectric effect where X-rays with a known energy are directed towards a specimen, leading to the emission of photoelectrons from the surface. The number and kinetic energy of the emitted photoelectrons are measured by a detector and are

characteristic of the element from which the photoelectrons originated. Quantification of the chemical states of an element within a sample are obtained from the position and the intensity of the peaks in an energy spectrum. XPS has been used both qualitatively and quantitatively to characterise the surface chemistry of the steel reinforcement in simulated pore solutions of concrete [91].

In most modern XPS instruments, like the one used in this study (Kratos Supra instrument), a beam of high energy electrons is directed towards an Al anode generating Al characteristic X-rays including the Kα line and other wavelengths, Bremsstrahlung radiation, and satellite X-rays. Some of these X-rays reach a quartz crystal monochromator, which is curved so that the diffracted X-ray beams from a broader area are focussed on a smaller analysis area on the surface of the sample. Only the X-rays with the correct wavelength at the chosen incident angle are diffracted by quartz, and this effectively filters the incident X-rays so that only the Al Kα radiation at 1486.6 eV reaches the sample. This monochromatic X-ray illumination of the sample enables high energy resolution of chemical shifts as well as detailed study of line profiles and subtle bonding changes evident in the valence band.

The binding energy (*BE*) of a photoelectron depends strongly on the chemical state of an atom and results in a change in the kinetic energy (*KE*) measured by the instrument. The *BE* is related to the *KE* by the following equation (Eq. 3.6):

$$BE = h\nu - KE \qquad \text{(Eq. 3.6)}$$

where $h\nu$ is the photon energy. The chemical information about an element (e.g. oxidation state, bonding) can be derived from the chemical shift. The test parameters used to characterise the surface chemistry of steel exposed to various simulated pore solutions of AAMs through XPS can be found in Chapter 5.

3.4 Modelling

3.4.1 Thermodynamic modelling of alkali-activated slags

Thermodynamic modelling has often been used by various researchers to predict the phase assemblage and the aqueous chemistry of various cements, and has been experimentally validated for hydrated PC, PC with supplementary cementitious materials, and for the case of AAS. The reader is directed to [29,80,81,215–219] for an in-depth understanding of the thermodynamic modelling of AAS.

In this study, the phase assemblage and the aqueous chemistry of the pore solutions of slags activated using various alkaline solutions were predicted through simulations carried out in the Gibbs Energy Minimization software (GEM-Selektor version 3.2). Thermodynamic data for solid, aqueous and gas phases were acquired from the CEMDATA14 database, with the ideal solid solution end member models of C-(N-)A-S-H gel [81] and MA-OH-LDH [220]. A detailed description of all input parameters used in this study have been outlined in Chapter 6.

3.4.2 Modelling of chloride diffusion

As mentioned in Chapter 2, chloride diffusion though concrete cover is often described using the analytical solution of Fick's second law (Eq. 2.14 and Eq. 2.15) that generally provides a good fit to the chloride profiles using the empirically derived time-dependent apparent diffusion coefficient ($D_a\,(t)$) function (Eq. 3.7).

$$D_a(t) = D_o \cdot \left(\frac{t_o}{t}\right)^n \qquad \text{(Eq. 3.7)}$$

where D_o is the reference chloride diffusion coefficient at a reference time t_o, and n is the ageing factor that is a constant value defined by parameters such as binder type and w/b ratio. However, it is to be noted that the analytical solution of Fick's second law is based on a constant diffusion coefficient, and therefore substituting Eq. 3.7 directly in Eq. 2.14 would be mathematically erroneous. Therefore, in this study the use of the analytical solution of the Fick's second law was avoided and instead, an explicit finite difference method was used to calculate the chloride profiles in concretes made out of AAS.

The following paragraphs include the derivation of the explicit finite difference method, following [221]. Assuming a space, x (distance) vs. t (time) as shown in Figure 3-5, let the x and t coordinates be divided by intervals of the size δx and δt, respectively, allowing the space to be viewed as a grid of rectangles, each with dimensions ($\delta x \times \delta t$). The coordinates of a representative grid point are denoted as ($i\delta x$, $j\delta t$), where i and j are integers. The concentration of a species is given as $c_{i,\,j}$ at point ($i\delta x$, $j\delta t$) and the neighbouring values are highlighted in Figure 3-5. On expanding Eq. 2.13 into a Taylor's series in the t-direction and keeping x constant,

$$c_{i,j+1} = c_{i,j} + \delta t \left(\frac{\partial c}{\partial t}\right)_{i,j} + \frac{1}{2}(\delta t)^2 \left(\frac{\partial^2 c}{\partial t^2}\right)_{i,j} + \cdots \qquad \text{(Eq. 3.8)}$$

$$\left(\frac{\partial c}{\partial t}\right)_{i,j} = \frac{c_{i,j+1} - c_{i,j}}{\delta t} + O(\delta t) \qquad \text{(Eq. 3.9)}$$

where, $O(\delta t)$ represents the terms that have been neglected and are of the order of δt or higher, when both sides of right and left-hand sides of Eq. 3.8 have been divided by δt.

Similarly, the application of Taylor's series in the x-direction, and keeping t constant, one could write,

$$c_{i+1,j} = c_{i,j} + \delta x \left(\frac{\partial c}{\partial x}\right)_{i,j} + \frac{1}{2}(\delta x)^2 \left(\frac{\partial^2 c}{\partial x^2}\right)_{i,j} + \cdots \quad \text{(Eq. 3.10)}$$

$$c_{i-1,j} = c_{i,j} - \delta x \left(\frac{\partial c}{\partial x}\right)_{i,j} + \frac{1}{2}(\delta x)^2 \left(\frac{\partial^2 c}{\partial x^2}\right)_{i,j} + \cdots \quad \text{(Eq. 3.11)}$$

On adding Eq. 3.10 and Eq. 3.11,

$$\left(\frac{\partial^2 c}{\partial x^2}\right)_{i,j} = \frac{c_{i+1,j} - 2c_{i,j} + c_{i-1,j}}{(\delta x)^2} + O(\delta x)^2 \quad \text{(Eq. 3.12)}$$

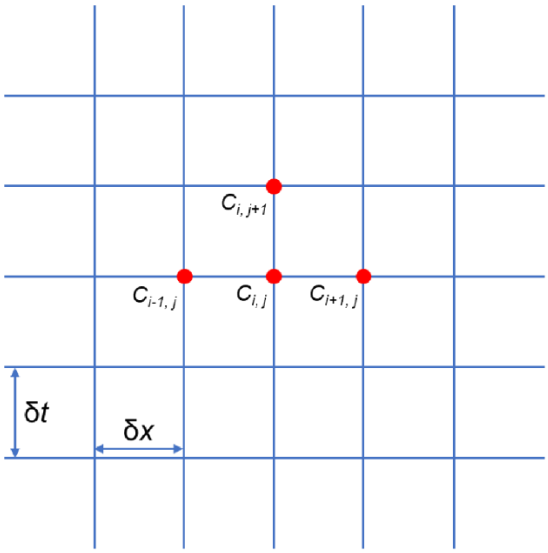

Figure 3-5: A graphical representation of the explicit finite difference method used to characterise the diffusion of chloride through AAMs

Upon neglecting the error terms and substituting Eq. 3.9 and Eq. 3.12 into Eq. 2.13 and rearranging, we get,

$$\frac{c_{i,j+1} - c_{i,j}}{\delta t} = D \cdot \frac{c_{i+1,j} - 2c_{i,j} + c_{i-1,j}}{(\delta x)^2} \quad \text{(Eq. 3.13)}$$

$$c_{i,j+1} = c_{i,j} + r(c_{i+1,j} - 2c_{i,j} + c_{i-1,j}) \quad \text{(Eq. 3.14)}$$

where, $r = D \cdot \frac{\delta t}{(\delta x)^2}$ (Eq. 3.15)

Based on the works of Smith et al. [222], one of the limitations of this method is that the value of r needs to be less than 0.5, thereby increasing the number of small time steps (δt) required for a given δx. However, in this study, the values of r were always ensured to be < 0.5. Further details regarding the quantification of parameter representing the chloride diffusion coefficient (D) and other considerations have been thoroughly discussed in Chapter 6.

Finally, a MATLAB script has been developed incorporating the simulated chemistry of the concrete cover and the diffusion of chloride for a simulated concrete cover. The MATLAB script works on user defined parameters such as slag composition, activator used, and exposure solution. A detailed description of the MATLAB script can be found in Chapter 6.

Chapter 4: Chloride-induced corrosion of steel in low-Ca alkali-activated materials

Note: This chapter is primarily based on the paper: Shishir Mundra, Maria Criado, Susan A. Bernal, John L. Provis. 'Chloride-induced corrosion of steel rebars in simulated pore solutions of alkali-activated concretes.' Cement and Concrete Research, 100 (2017), 385-397. The published paper represents the experimental work conducted by Shishir Mundra. Maria Criado, Susan A. Bernal, John L. Provis reviewed the manuscript prior to publication.

4.1 Introduction

As mentioned in Chapter 2, the passive film formed on the surface of steel reinforcement embedded in mortars or concretes comprises iron oxides such as α-Fe_2O_3, γ-Fe_2O_3, Fe_3O_4, and iron hydroxides and oxy-hydroxides such as $Fe(OH)_2$, $Fe(OH)_3$, α-FeOOH, γ-FeOOH and β-FeOOH, with a layered microstructure [89–91,93,95,96]. The chemistry of the passive film is governed by the oxygen availability, pH and chemistry of the surrounding environment, and the redox potential of the steel [89–91,93,95]. In a concrete environment, breakdown of the passive film or 'depassivation' can be initiated by two common mechanisms: the lowering of pH, e.g. due to carbonation, and by the localised attack of aggressive species such as chloride. The breakdown of passivation due to the action of chloride is often associated with the concept of critical chloride value, or chloride 'threshold' value (C_{crit}) [99]. The C_{crit} value is influenced by a large number of factors, including: the chemistry and alkalinity of the pore solution [95,139,148,164,165,223–225], chloride binding in the cement hydrates [142,143,226], the steel-concrete interface [227], the availability of oxygen at the steel-concrete interface [228] and the surface condition and chemical composition of the reinforcement [164,223]. Given the number of confounding variables, there exists no general consensus on a precise chloride 'threshold' value [99]. In an extensive review, Angst et al. [99] summarised the C_{crit} values obtained by several authors to be between 0.04 wt.% to 8.34 wt.% of the binder, and between 0.01 to 45 when defined in terms of the molar ratio $[Cl^-]/[OH^-]$. These values correspond to systems based primarily on Portland cement (PC) and were determined through electrochemical measurements conducted on in-service structures, simulated pore solutions and laboratory specimens.

Low-Ca AAMs such as alkali-activated fly-ash/metakaolin are characterised by a poorly crystalline three-dimensional alkali-aluminosilicate hydrate (N-A-S-H) gel as the main hydration product, and zeolites such as faujasite-type, chabazite-Na, gismondine-type, and hydrosodalites as secondary hydration products. In the pore solutions associated with neat PC hydrates [202], alkali and hydroxide concentrations are about 0.70 M, while concentrations of calcium and sulfate are around 2 mM and 7 mM respectively, with Si and Al each present at levels of less than 1 mM [202]. However, this composition would vary with time and composition of the precursors. The pore solutions of low-Ca AAMs are more alkaline than those of PC pore solutions. Lloyd et al. [79] measured the concentrations of different species in pore solutions extracted from alkali-activated fly ashes and observed concentrations of Na^+ and OH^- between 0.60 M and 1.60 M. Sulfate was not detected, and the concentrations of Ca, Si and Al were close to 1 mM [79,229]. These differences in the hydration products and pore solution of low-Ca AAMs in contact with the reinforcement, compared to PC based concretes, could lead to dissimilar mechanisms of passivation (and passivation breakdown) due to the ingress of chloride.

There are limited published data on the chloride-induced corrosion of reinforcement in low-Ca AAMs. Miranda et al. [230] and Bastidas et al. [231] reported similar passivation behaviours for alkali-activated fly ash and PC mortars, however upon addition of chloride (2 wt.% of binder), increased corrosion current density and lower corrosion resistance were observed for alkali-activated fly ash mortars compared to PC mortars. Criado et al. [232] indicated that depassivation of carbon steel rebar in alkali-activated fly ash mortars could be initiated at a chloride content of around 0.4 wt.% of binder, but this value depended on the activator used. However, Monticelli et al. [233] reported C_{crit} values for alkali-activated fly ash mortars to be about 1 – 1.7 wt.% of binder, much higher than previously reported. With such limited and varying data in the literature related to degradation of the reinforcement in AAMs, and considering the significant differences from reinforced PC concretes (as shown by Babaee and Castel [214]), it is important to gain an understanding of the mechanisms responsible for passivation of the reinforcement and its breakdown due to chloride.

This chapter focusses on the passivation behaviour of steel and the phenomena of localised corrosion due to chlorides in highly alkaline electrolyte solutions (0.80 M, 1.12 M and 1.36 M NaOH) representing the pore solutions of low-Ca AAMs, with the aim of probing the chloride 'threshold' values for such systems. This was achieved by employing electrochemical techniques such as cyclic voltammetry (CV), open circuit potential (OCP), alternating current

electrochemical impedance spectroscopy (EIS), linear polarisation resistance (LPR) and anodic polarisation.

4.2 Experimental methods

Mild steel rebars (φ = 12 mm) from a local supplier in Sheffield, UK with specifications and chemistry described in Section 3.1, Chapter 3 were used in this study.

The compositions of the simulated pore solutions were based on the work of Lloyd et al. [79] who analysed the pore solution chemistry of alkali-activated fly ashes. The concentrations of dissolved Al, Si, Ca and sulfur species in that study were close to or less than 1 mM, therefore were not considered here. In addition, preliminary tests with pore solutions containing Al, Si and Ca in concentrations of 3 mM, 0.9 mM and 0.45 mM respectively [81], showed negligible or no difference in the electrochemical response of the system (shown in Chapter 8). Alkali hydroxide solutions were used to simulate the pore solution chemistry of these binders: sodium hydroxide solutions with $[OH^-]$ concentrations of 0.80 M, 1.12 M and 1.36 M were prepared using ACS reagent grade NaOH pellets (Sigma Aldrich). To investigate the effect of chloride on corrosion initiation, commercial grade NaCl (EMD Chemicals) was added to the representative pore solutions; the molar ratio $[Cl^-]/[OH^-]$ was varied between 0 and 3 for each of the three NaOH concentrations assessed. Table 4-1 lists the aqueous compositions considered in this study.

Table 4-1. Simulated low-Ca AAM pore solutions with varying alkalinity and chloride concentrations ($[Cl^-]/[OH^-]$ ratio). All concentrations in mol/L.

[NaOH]	**Molar ratio $[Cl^-]/[OH^-]$**													
	0	0.25	0.50	0.75	0.80	0.90	1.00	1.50	1.60	1.70	2.00	2.30	2.40	3.00
	Concentration of chloride, mol/L													
0.80	0	0.20	0.40	0.60	0.64	0.72	0.80	1.20	--	--	1.60	--	--	2.40
1.12	0	0.28	0.56	0.84	--	--	1.12	1.68	1.79	1.90	2.24	--	--	3.36
1.36	0	0.34	0.68	1.02	--	--	1.36	2.04	--	--	2.72	3.13	3.26	4.08

4.2.1 Electrochemical techniques

All electrochemical tests were conducted as described in Section 3.2, Chapter 3.

4.2.1.1 Cyclic voltammetry

Potentiostatic cyclic voltammetry (CV) was conducted to electrochemically characterise the passive film formed on the steel surface when exposed to the three NaOH concentrations without chlorides (0.80 M, 1.12 M and 1.36 M NaOH solutions). Before starting each test, the steel was maintained at -1.50 V vs. Ag/AgCl (cathodic limit: $E_{\lambda,c}$) in the hydrogen evolution region for 10 mins to remove the pre-existing oxide layers on the surface of steel. The electrochemical response of the system was recorded when the potential was cycled from -1.50 V ($E_{\lambda,c}$) to 0.65 V (anodic limit: $E_{\lambda,a}$), at a scan rate of 2.5 mV/s over 10 cycles, taking into account hydrogen and oxygen evolution at the cathodic and anodic limits respectively.

4.2.1.2 Open circuit potential, electrochemical impedance spectroscopy, linear polarisation resistance and anodic polarisation

To investigate the influence of chloride on corrosion initiation, the following electrochemical techniques were employed (in the order described) on the same steel specimen, which was distinct from the specimen used for CV, in each of the solutions listed in Table 4-1: (i) OCP or E_{corr}; (ii) EIS; (iii) LPR; and (iv) anodic polarisation.

Prior to any electrochemical polarisation technique being applied, the OCP of the steel specimens were recorded using the parameters mentioned in Section 3.2.1, Chapter 3.

EIS measurements were conducted for selected specimens in galvanostatic mode, where the net current in the system was maintained at zero. The galvanostatic mode was chosen primarily to address any variation in the OCP due to the interaction of chloride with steel during the course of EIS measurements. The tests were carried out in the frequency range of 10^5 Hz – 10^{-2} Hz, with a logarithmic sweeping frequency of 5 points per decade and a current amplitude of 10^{-5} A (RMS), to ensure that the corresponding potential variation did not exceed 10 mV. The results were analysed only for impedance measurements in the frequency range of 10^4 Hz - 10^{-2} Hz, to eliminate the effects of the reference electrode and the Luggin capillary, which are observed at frequencies between 10^5 Hz and 10^4 Hz. The Nyquist plots obtained were

normalised to the exposed surface area and fitted with an equivalent electrical circuit using Zview2.

LPR measurements and anodic polarisation on the steel specimens were conducted as described in Section 3.2.3.1, Chapter 3.

4.3 Results and discussion

4.4 Passivation

4.4.1 Cyclic voltammetry

Figure 4-1 shows 10 cyclic voltammetric scans obtained for polished mild steel surfaces exposed to simulated pore solutions representative of low-Ca AAMs, as a function of the hydroxide concentration in the solution. The initial increase in the potential from $E_{\lambda,c}$ to -1.20 V was characterised by a sharp increase in the current, and the evolution of hydrogen bubbles from the steel surface (not shown in Figure 4-1). Moving from the active to the noble direction, four anodic current peaks were observed, at approximately -0.94 V (denoted Peak I), -0.89 V (Peak II), -0.72 V (Peak III) and -0.67 V (Peak III'). Sweeping in the reverse direction, three cathodic current peaks at about -0.96 V (Peak IV'), -1.05 V (Peak IV) and -1.14 V (Peak V) were noticeable. Less clearly defined peaks III' and IV' were present as broad shoulders on the positive potential sides of the asymmetric peaks III and IV, respectively. The potential sweep after peak III' (not shown in Figure 4-1) in the anodic direction up to $E_{\lambda,a}$ was characterised by a constant anodic current of a relatively low value until 0.55 V, where the current was observed to rise sharply due to the oxygen evolution reaction. A similar trend was observed in the cathodic direction (not shown in Figure 4-1) in approximately the same potential range after which a rise in the cathodic current was witnessed, leading to peaks IV' and IV. Cathodic and anodic peak potentials were approximately the same for all three concentrations of hydroxide assessed, and therefore the following discussion applied is general to Figure 4-1A, 1B and 1C.

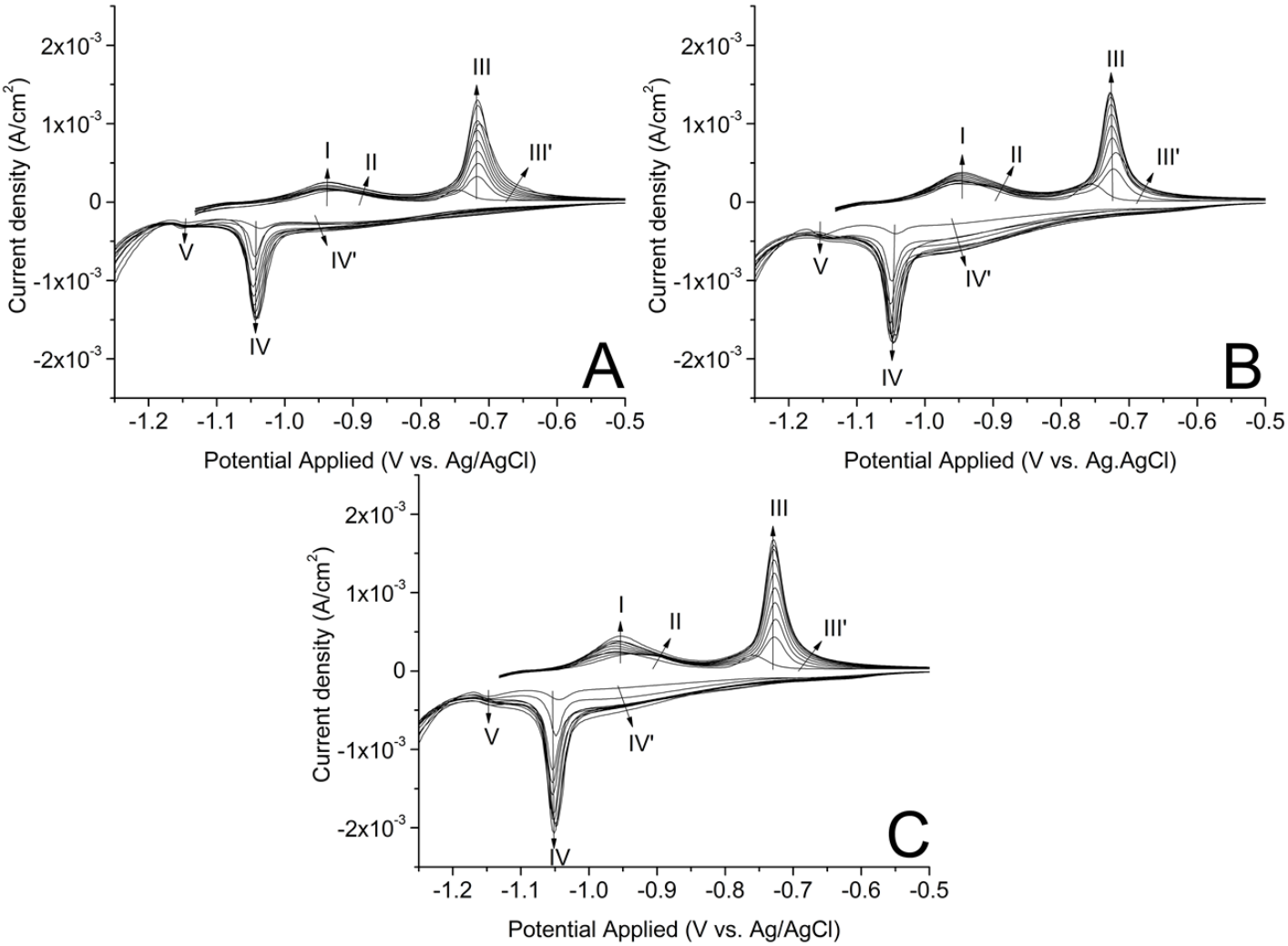

Figure 4-1. Cyclic voltammograms of steel immersed in simulated pore solution with NaOH concentrations of: (A) 0.80 M (B) 1.12 M and (C) 1.36 M. Data were collected at a sweep rate of 2.5 mV/s. Arrows indicate the current response from scan numbers 1 to 10. Data from -1.50 V to -1.13 V in the anodic sweeps are not presented to enable visibility of peak V. These cyclic voltammograms do not show the current response due to the oxidation/reduction of Cr and Mn, as the concentrations of Cr and Mn in the mild steel used are very low (shown in Table 3-1).

Peaks I and II occurred as a single broad peak centred at about -0.94 V in the first scan, however, a clear distinction between peak I (centred at -0.94 V) and peak II (centred at -0.89 V) was observed upon subsequent anodic potential sweeps. The current density of peak I increased from scan 1 to scan 10, and this was more pronounced with increasing hydroxide concentrations. Current densities for peak II remained fairly constant for all concentrations of

hydroxide; however, the overlapping nature of peaks I and II became more distinct at higher alkalinity.

The cyclic voltammograms shown in Figure 4-1 clearly indicate that passivation of the steel surface is a complex mechanism involving several oxidation processes, representing a chemical gradient in the composition of the passive film. Each current peak represents an individual oxidation/reduction process occurring on the surface of the steel. It can be assumed that the cathodic treatment of the steel for 10 mins in the hydrogen evolution region at $E_{\lambda,c}$ results in the removal of the pre-existing oxide scale from the specimen surface, so iron exists in the bare Fe^0 state prior to sweeping in the forward direction. A minor peak at -1.10 V is primarily attributed to the electrochemical displacement of hydrogen adsorbed on the electrode surface. The occurrence of anodic peaks I and II likely corresponds to the electro-oxidation of iron from Fe^0 to Fe^{2+} [200,234]. The direct dependency of current densities of peaks I and II on the alkalinity of the electrolyte, indicates the possible role of $[OH^-]$ in the appearance of these peaks. Therefore, it is likely that peaks I and II are associated with the formation of $Fe(OH)_2$. Such behaviour is expected in alkaline solutions, and several passivation mechanisms have been proposed since the early 20th century [235]. One possible reaction route for peaks I and II in the electrolytes used in this study, describing the initial formation of Fe^{2+}, could be represented by the reactions described in Eqs. 4.1 to 4.4, where the square brackets depict the intermediate species, and curly braces indicate species that may undergo changes with time.

$$Fe + OH^- = [Fe(OH)]_{ads} + e^- \quad \text{Eq. 4.1}$$

$$[Fe(OH)]_{ads} = [Fe(OH)]^+_{ads} + e^- \quad \text{Eq. 4.2}$$

$$[Fe(OH)]^+_{ads} + 2OH^- = HFeO_2^- + H_2O \quad \text{Eq. 4.3}$$

$$HFeO_2^- + H_2O = \{Fe(OH)_2\} + OH^- \quad \text{Eq. 4.4}$$

Peak I could therefore be attributed to the adsorption of $[Fe(OH)]^+_{ads}$ on the surface of the specimen through a two-step electron transfer process indicated in Eq. 4.1 and Eq. 4.2. Kabanov et al. [234] and Schrebler Guzmán et al. [236,237] reported the first stage of passivation to be the formation of an electrochemically active adsorbed layer of $[Fe(OH)]_{ads}$ through Eq. 4.1. A similar mechanism for the formation of $[Fe(OH)]_{ads}$ was suggested by Dražić and Hao [238].

The second step is characterised by the formation of $[Fe(OH)]^+_{ads}$ through an electron transfer process, occurring predominantly due to the labile nature of $[Fe(OH)]_{ads}$ [234,236–

239]. The amount of adsorbed species, therefore, depends on the concentration of OH^-, and is reflected by the increasing anodic current densities corresponding to peak I with increasing NaOH concentration. Peak II can be assigned to the formation of $Fe(OH)_2$ by the mechanisms indicated in Eq. 4.3 and Eq. 4.4. Thus, the fact that peak II is more distinct from peak I in 1.12 M (Figure 4-1B) and 1.36 M (Figure 4-1C) NaOH solutions than in 0.80 M (Figure 4-1A) NaOH solution could be explained by either the higher amounts of adsorbed $[Fe(OH)]^+_{ads}$ or by the increased tendency to form $HFeO_2^-$ ions in the potential range of peak II in concentrated alkaline solutions where pH > 14. According to the Pourbaix diagram for iron in water [85], it is reasonable to assume the formation of $HFeO_2^-$ as an intermediate product in highly alkaline solutions, as has been reported by several authors [234,237,240]. The subsequent hydrolysis of the intermediary species, as indicated in Eq. 4.4, results in the formation of $Fe(OH)_2$. Schrebler Guzmán et al. [237] also suggested the existence of a precipitation-dissolution equilibrium between $Fe(OH)_2$, $HFeO_2^-$ and FeO_2^-.

It is important to note here that several authors [92,194,200] have instead attributed peaks I and II to the formation of $Fe(OH)_2$ and Fe_3O_4 respectively. However, the clear dependency of peaks I and II on the hydroxide concentration for the systems assessed in this study indicates that a dehydroxylation mechanism is highly unlikely to arise here. In the reverse sweeping direction, the broad cathodic current Peak V can be assigned as the reduction couple of peaks I and II, indicating the reduction of the $Fe(OH)_2$ to Fe^0 through the reversible mechanisms listed in Eqs. 4.1 to 4.4. This is supported by the fact that the sum of the anodic charges associated with current peaks I and II is approximately equal to the charge associated with current peak V, at all concentrations of OH^-. Similar observations have been reported by Schrebler Guzmán et al. [237].

In the case of anodic current peak III and cathodic current peak IV, repeated cycling led to an increase in the peak currents in both directions. Similar trends were observed for shoulders III' and IV'. After the first scan, anodic and cathodic current peaks III and IV shifted slightly towards more positive and negative potentials respectively and occurred at relatively constant potentials during sweeps 2 to 10. The current densities of peaks III, III', IV and IV' increase with increasing NaOH concentration. Successive potential sweeps did not significantly alter the position or the current density of peak V. However, from being a distinct peak during the first scan, peak V changed into a less distinct and broader peak during subsequent sweeps. These observations are generally aligned with the literature describing the passivation behaviour of steel in highly alkaline electrolytes [236,237].

The appearance of peak III indicates the oxidation of the Fe^{2+} species to a Fe^{3+} species [235]. The current density of peak III during potential sweeps is much higher than those of peaks I and II, and could possibly be related to the expansion of the structure of the passivation layer arising from the lower densities associated with Fe^{3+} species when compared to Fe^{2+} species [237]. The oxidation product formed during the anodic current peak III has been argued extensively in the literature to be various polymorphs of either FeOOH or Fe_2O_3 [200,234,241–243]. The anodic current density associated with peak III at about -0.72 V was observed to rise with increasing OH^-, and therefore the species formed at peak III due to the oxidation of $Fe(OH)_2$ can be assigned to an iron species involving hydroxide. The anodic current contribution observed as shoulder III', located at the positive side of peak III, could possibly indicate the formation of a non-equilibrium species at peak III that undergoes either a structural transformation or a chemical change at shoulder III' to a more stable species.

Kabanov et al. [234] proposed that the passivation of iron is due to an adsorbed layer of FeOOH. However Schrebler Guzmán et al. [237] suggested that FeOOH transforms initially into $Fe_2O_3 \cdot H_2O$, and upon ageing takes on a structure similar to Fe_3O_4 or hydrated Fe_2O_3. Similarly, Tschinkel et al. [242] assigned the oxidation product at peak III as α-FeOOH or δ-FeOOH that later transformed into Fe_3O_4. Considering the different observations by several authors in the literature, the following Eq. 4.5, and then Eq. 4.6 or Eq. 4.7, could be possibly assigned to the anodic current peaks III and III' respectively:

$$\{Fe(OH)_2\} + OH^- = [FeOOH]_{ads} + H_2O + e^- \quad \text{Eq. 4.5}$$

$$2[FeOOH]_{ads} = \{Fe_2O_3 \cdot H_2O\} \quad \text{Eq. 4.6}$$

$$[FeOOH]_{ads} + H_2O = \{FeOOH \cdot H_2O\} \quad \text{Eq. 4.7}$$

It is evident that there still is no agreement in the literature on the oxidation reaction occurring at peaks III and III'. However, the formation of a hydrated oxide or oxy-hydroxide film that can undergo chemical changes upon ageing seems to be a reasonable supposition.

In the reverse sweep, the cathodic current peaks IV and IV' can be directly assigned to the reduction couples of the oxidation reactions associated to peaks III and III' respectively. As seen from Figure 4-1 the cathodic current contribution from peak IV is similar to that of the anodic current peak III, representing reduction of the Fe^{3+} species formed at peak III to $Fe(OH)_2$. This is however not the case for the current contributions in shoulders IV' and III', and it is rather difficult to accurately characterise the location of IV'. Additionally, the current

contribution in the forward sweep remains fairly constant at a relatively small non-zero value in the potential range -0.50 V to +0.55 V, which could possibly be due to further chemical changes in the oxidation product formed at peak III'. Therefore, on the reverse sweep, the cathodic contributions from the broad shoulder spanning from -0.50 V to -1.00 V could possibly represent the reduction of all the species formed in the forward sweep from -0.67 V (peak III') to 0.55V. Cyclic voltammograms obtained with different sweep rates (5 mV/s and 10 mV/s, shown in Chapter 8, Section 8.2) were consistent with the results and interpretations presented here.

4.4.2 Open circuit potential, electrochemical impedance spectroscopy, linear polarisation resistance and anodic polarisation

OCP values measured at the start of the experiments were -0.30 V, -0.32 V and -0.32 V (±15 mV) vs. Ag/AgCl for 0.80 M, 1.12 M and 1.36 M NaOH solutions respectively. According to the Pourbaix diagram [85], these potentials lie in the region where the steel is expected to be protected by a film containing Fe mainly as iron (III) oxides.

EIS was used to analyse the electrical properties of the passive film. Figure 4-2 shows the Nyquist plot obtained for all three NaOH concentrations considered in this study, and the electrical equivalent circuit model used for fitting. From the Nyquist plots, a clear change in the electrochemical response of the system with decreasing frequency is evident. The spectra are characterised by an incomplete depressed semicircle at higher frequencies (10^4 Hz to 10^{-1} Hz), followed by a linear diffusion tail at lower frequencies (10^{-1} Hz to 10^{-2} Hz). Such behaviour is similar to that depicted by the classical Randles circuit [196], which was used to fit EIS data (Figure 4-2). The equivalent circuit model was composed of:

- the electrolyte resistance (R_e),
- A constant phase element (CPE_{dl}) representing the imperfect capacitive nature of the double layer,
- A charge transfer resistance (R_{ct}) representing the resistance of the passive film to charge transfer, and
- A semi-infinite Warburg diffusion element (W_o) representing the mass transport processes occurring at the passive film/metal interface.

The use of a Warburg element in this model is related to the fact that the growth of the passive film on a metallic surface is primarily driven by the diffusion of oxygen vacancies from the solution/passive film interface to the passive film/metal interface [132,193]. Parameters in the high frequency region, R_e, R_{ct} and CPE_{dl}, were determined separately without the use of the Warburg element, primarily because of the underestimation of these parameters by direct fitting of the full electrical equivalent circuit in this range.

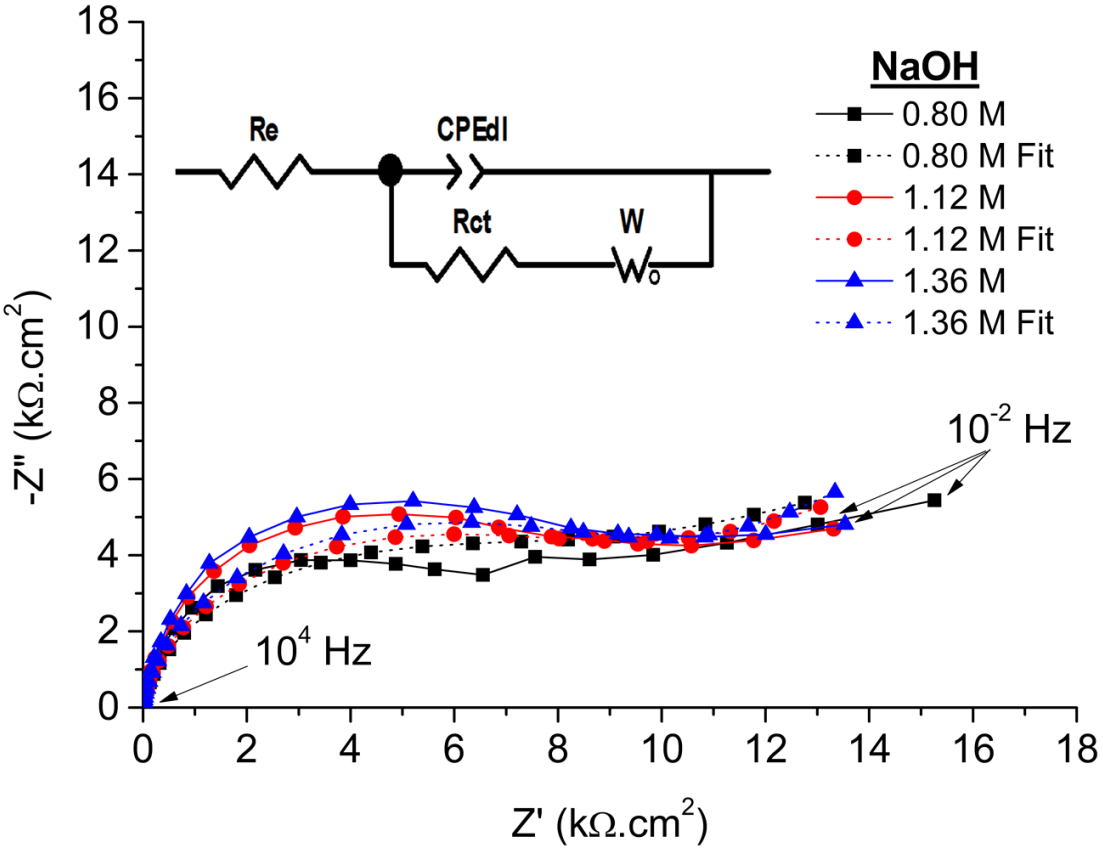

Figure 4-2. Nyquist data and fitting plots for steel exposed to simulated pore solutions with varying NaOH concentrations. The equivalent circuit fitting model (modified Randles circuit) used to generate the fitting curve is also shown.

Table 4-2 shows the fitting parameters obtained for the electrical equivalent circuit model. The electrolyte resistance (R_e) was found to be between 1.72 and 1.06 $\Omega.cm^2$ for the three NaOH concentrations, and reduces at increased alkalinity and conductivities of the simulated pore solutions. The capacitance values of the CPE_{dl} element were almost independent of NaOH concentration, between 76 and 80 $\mu F.cm^{-2}$. The parameter α corresponds to CPE_{dl}, and the properties of the CPE are determined by the value of α ($0 \leq \alpha \leq 1$) [193]. When α is 1, the element is a capacitor, whereas the behaviour is governed by diffusion/mass transfer when α

approaches 0.50 [193]. The value of α in this study was 0.93 for all electrolyte concentrations, indicating the non-ideal but mainly capacitive nature of the solution/passive film interface. This deviation from ideal behaviour can be attributed to the non-homogeneous distribution of ions at the solution and the roughness of the electrode surface.

Table 4-2. Fitting results obtained for equivalent circuit model components related to EIS data shown in Figure 4-2. All values are reported after surface area normalisation. The values reported in parenthesis are standard deviations.

$[OH^-]$	R_e ($\Omega.cm^2$)	CPE_{dl} ($\mu F.cm^{-2}$)	α	R_{ct} ($k\Omega.cm^2$)	Y_o ($\mu S.s^n.cm^{-2}$)	χ^2
0.80 M	1.72 (0.01)	80.0 (1.17)	0.93	9.51 (0.21)	16.34 (2.40)	0.009
1.12 M	1.21 (0.05)	78.0 (2.10)	0.93	11.88 (0.12)	0.040 (0.009)	0.013
1.36 M	1.06 (0.08)	76.7 (1.77)	0.93	12.80 (0.22)	0.003 (0.000)	0.014

The resistance to charge transfer (R_{ct}) of the passive film increased from 9.51 to 12.80 $k\Omega.cm^2$ with a rise in $[OH^-]$. The admittance values (Y_o) associated with semi-infinite diffusion processes at the passive film/metal interface decreased from 16.34 to 0.003 $\mu S.s^n.cm^{-2}$, with increasing $[OH^-]$. Higher admittance values indicate an increased mass transport through the film, as this parameter is directly related to the diffusivity of ionic species through the film [244]. Such trends in R_{ct} and Y_o can be attributed to the existence of a proportional relationship between the concentration of hydroxide in the electrolyte and the protective nature of the passive film. Therefore, a rise in the R_{ct} value, and consequently reduction in Y_o, with increasing alkalinity, is associated with an increased concentration of passivating species on the surface of the electrode.

The Nyquist plots (Figure 4-2) show the non-conventional nature of the diffusion tail, where at low frequencies the slope between the imaginary and real components of impedance was much lower than 45°. This indicates a slow transition from the capacitive behaviour of the solution passive/film interface to the diffusional behaviour of the passive film/metal interface, and could be a result of the mass transfer resistance of the passive film and the consequentially low diffusivity of ions through the passive film. Therefore, if the frequency domain used in this study was extended to even lower frequencies, the appearance of a conventional diffusional tail would be anticipated.

R_p values calculated from linear polarisation measurements were analogous to the trend for R_{ct} observed through EIS, and were found to be 45.5, 67.6 and 88.2 kΩ.cm^2 for 0.80 M, 1.12 M and 1.36 NaOH solutions, respectively.

Anodic polarisation curves obtained for the three NaOH concentrations are shown in Figure 4-3. All three polarisation curves follow the same trend with clearly defined active, passive and trans-passive regions. On increasing the potential in the positive direction from the OCP, the current density was observed to increase steadily until the potential reached about 0.10 V, representing the active region where the electrode surface reacts with the electrolyte to form a passive film. The current density remained fairly constant when the potential was increased from 0.10 V to about 0.55 V, indicating that the steel (electrode) was being protected against corrosion by the passive film. A sharp rise in the current density was evidenced when the potential was increased from 0.55 V onwards, typical of the oxygen evolution reaction.

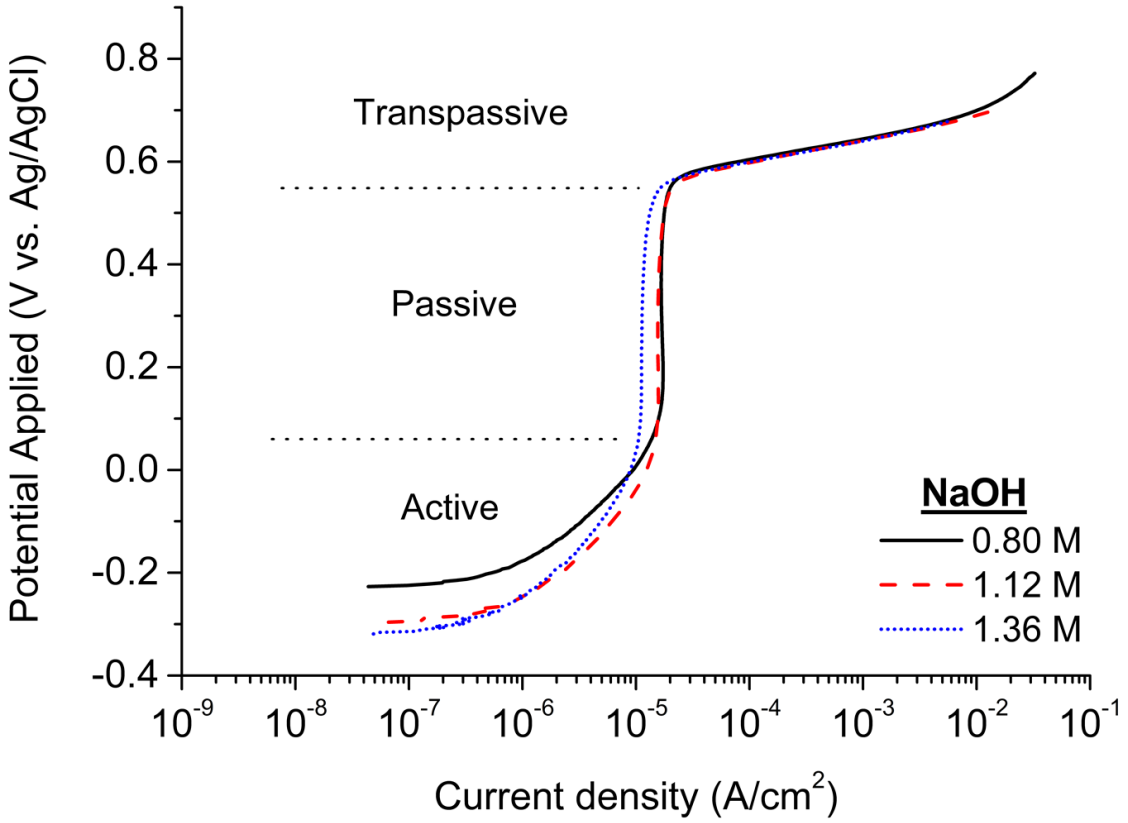

Figure 4-3. Anodic polarisation curves obtained for steel rebars immersed in chloride-free simulated pore solutions, as a function of the NaOH concentration

The current densities recorded in the passive region decreased with increasing [OH^-] in the electrolyte, indicating a direct relationship between the degree of passivation and the alkalinity

of the solution. This is consistent with EIS and LPR measurements, where an increased alkalinity results in a higher resistance and a reduction in the admittance of the passive film.

4.5 Depassivation

4.5.1 Open circuit potential

Figure 4-4 shows the measured open circuit potentials for steel immersed in simulated pore solutions with different concentrations of hydroxide (0.80, 1.12 and 1.36 M) and chlorides. In the case of 0.80 M NaOH solutions, the steel rebars (working electrode) exhibited fairly constant OCP values for chloride additions from zero up to 0.64 M, followed by a sudden drop in the potential for chloride concentrations greater than 0.64 M. A similar trend was observed for 1.12 M and 1.36 M NaOH solutions, where the sudden drop in OCP values was identified at chloride concentrations greater than 1.79 M and 3.13 M, respectively. When expressed in terms of $[Cl^-]/[OH^-]$ ratios, the sharp decrease in OCP was observed when the $[Cl^-]/[OH^-]$ was greater than 0.80, 1.60 and 2.30, for 0.80 M, 1.12 M and 1.36 M NaOH solutions respectively.

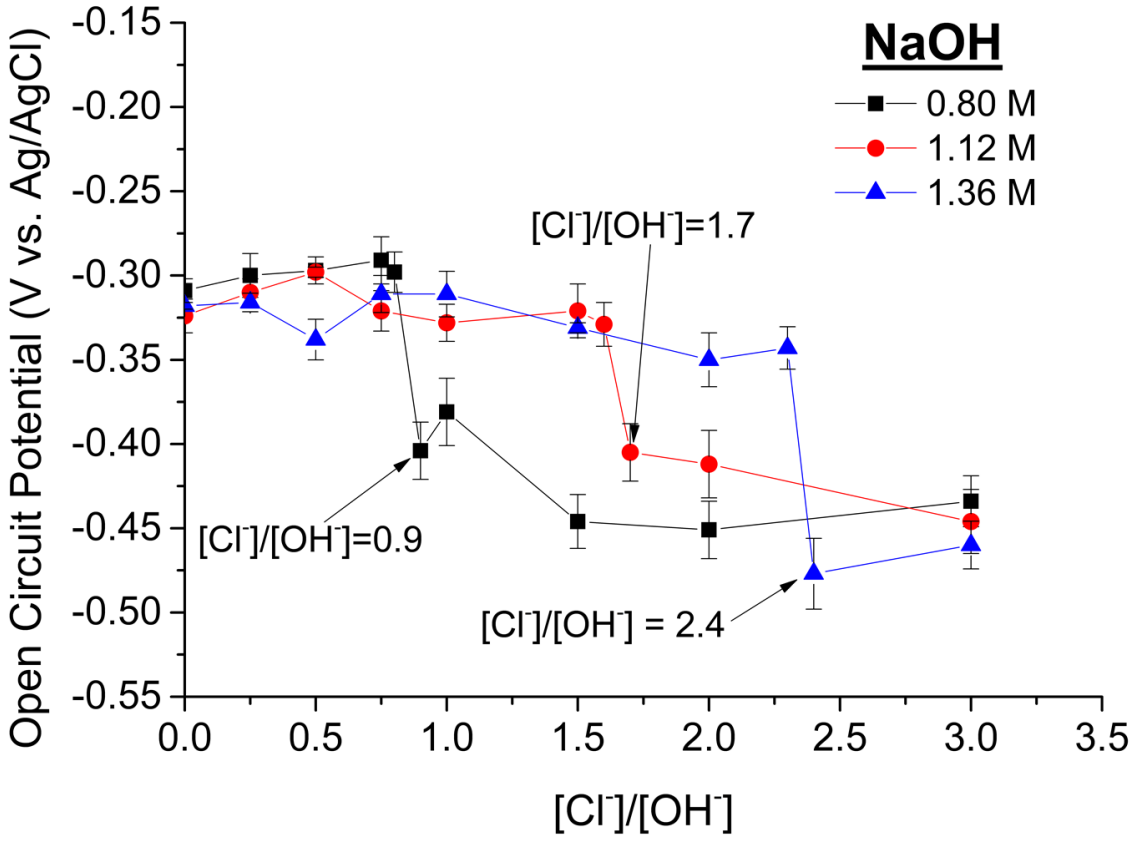

Figure 4-4: Measured open circuit potential values (V vs. Ag/AgCl) for steel immersed in chloride-contaminated NaOH solutions. OCP values are plotted against the ratio $[Cl^-]/[OH^-]$.

All of the OCP values shown Figure 4-4 lie in the range of potential values where the steel is protected by a passive film [85], with a complex chemical and phase composition that includes species containing iron in (II) and (III) oxidation states. However, the notable reduction in the potentials at particular concentrations of chloride (which are different for each $[OH^-]$) indicates the interaction of chloride with the passive film.

From the OCP values, it is possible to conclude that depassivation of the steel does not occur until the chloride concentration reaches a critical value (C_{crit} or $[Cl^-]/[OH^-]$ ratio) which depends on the amount of hydroxide present in the vicinity of the electrode surface. The C_{crit} value (in terms of chloride concentration) for the assessed steel immersed in a 1.36 M NaOH was approximately 1.91 and 3.62 times higher than that detected in rebars immersed in 1.12 M and 0.80 M NaOH solutions respectively. In terms of $[Cl^-]/[OH^-]$ ratios, the above C_{crit} values can be represented as 0.90, 1.70 and 2.40, for 0.80 M, 1.12 M and 1.36 M NaOH solutions respectively. This result is consistent with earlier observations indicating a rise in C_{crit} with an increase in the pH of the electrolyte [95,164,184,223]. This relationship will be revisited below,

with input also from additional characterisation methods to provide deeper insight into the factors which control C_{crit}.

4.5.2 Linear polarisation resistance

Figure 4-5 shows the polarisation resistance (R_p) values obtained via LPR analysis, as a function of the $[Cl^-]/[OH^-]$ ratio. R_p values were determined from the slope of the voltage vs. current plot obtained by varying the potential from -20 to +20 mV vs. OCP. The R_p values of the steel exhibited a sharp decrease when the chloride concentration was equivalent to the same $[Cl^-]/[OH^-]$ (C_{crit}) ratios of 0.90, 1.70 and 2.40 determined via OCP analysis (Figure 4-4), for 0.80 M, 1.12 M and 1.36 M NaOH solutions, respectively. The findings from LPR measurements clearly demonstrate that the passive film on the steel surface remains intact until the chloride concentration reaches a critical value to induce depassivation. This critical value of chloride required for depassivation depends strongly on the hydroxide concentration in the pore solution. Ghods et al. [184] reported a similar trend for R_p values when investigating chloride-induced depassivation of black steel reinforcement.

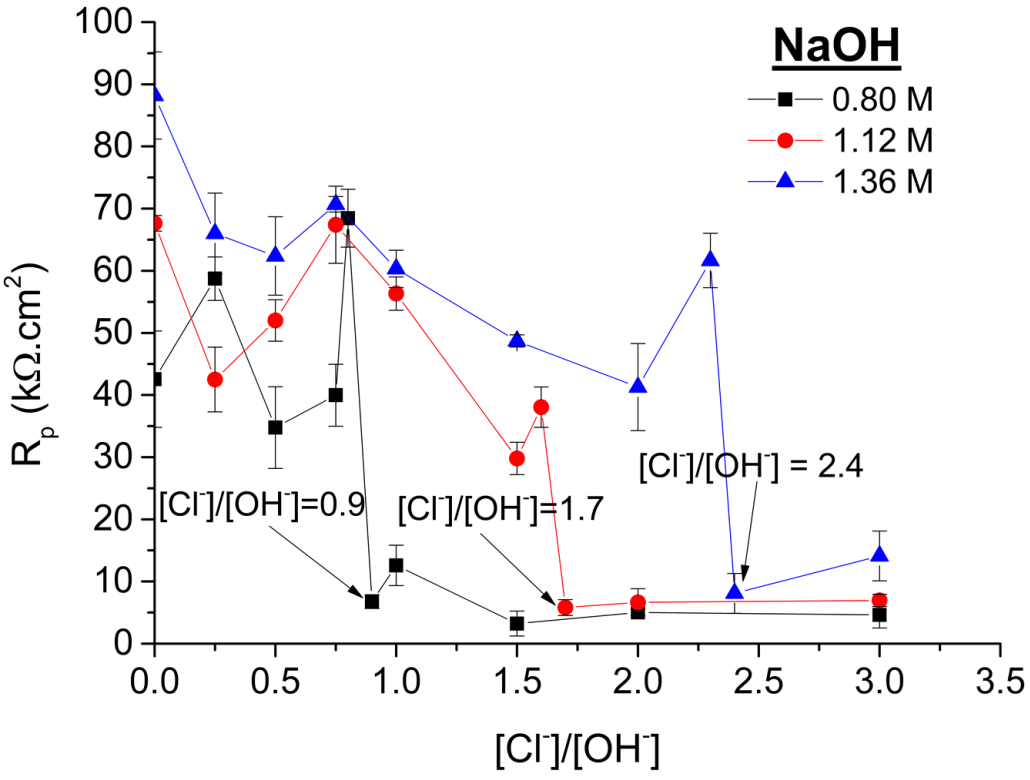

Figure 4-5: Linear polarisation resistance measurements for steel rebars immersed simulated pore solutions with different concentrations of NaOH, as a function of the $[Cl^-]/[OH^-]$ ratios

Corrosion current densities (i_{corr}) were calculated using the Stern-Geary relationship (Eq. 2) and are shown in Figure 4-6, as a function of $[Cl^-]/[OH^-]$ ratio. Corrosion rate determinations

in reinforced PC concretes generally use 26 mV and 52 mV as the values of the proportionality constant 'B' for active and passive samples, respectively [182]. The applicability of the aforementioned 'B' values for reinforced low-Ca alkali-activated concretes was assessed by Babaee and Castel [214], and were found to diverge significantly from these values. They found that B was between 13 mV and 20 mV for passive alkali-activated samples, and between 45 mV and 58 mV for active samples. Three sets of i_{corr} values were thus calculated in this study, using the B values suggested by Andrade et al. [182], and the lower and the upper limits from the work of Babaee and Castel [214]. The choice of B values is clearly seen to influence the magnitude, but not the trend, of the values obtained. As seen in Figure 4-6, sudden changes in the i_{corr} values are observed for the three pore solutions when the chloride concentration reaches the same $[Cl^-]/[OH^-]$ (C_{crit}) ratios defined through OCP and R_p measurements, and accordingly the active and passive conditions of steel as a function of chloride concentration can be defined.

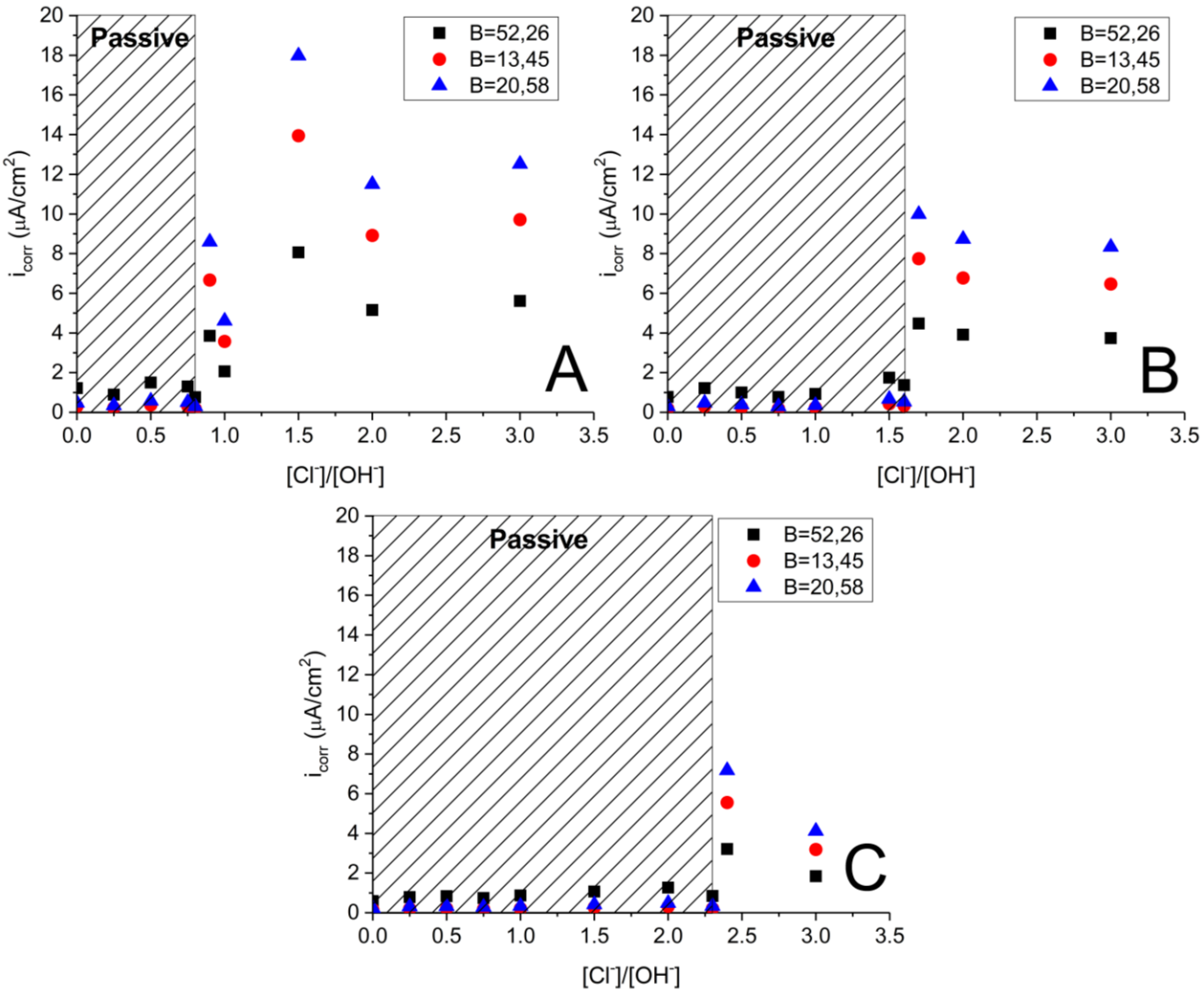

Figure 4-6: Variations of i_{corr} (µA/cm^2) of steel rebars immersed in simulated pore solutions with a [NaOH] of (A) 0.80 M, (B) 1.12 M and (C) 1.36 M, as a function of [Cl^-]/[OH^-] ratio. Legend entries represent the values of B used in the Stern-Geary equation for active and passive samples: $B = i,j;$ where i = value of B for passive samples, and j = value of B for active samples. B values taken from [182,214]. Shaded regions shows the region where the steel is in a passive state

When the steel is in its passive state, the i_{corr} values remain fairly constant for each set of B values, and is lower for solutions with increased alkalinity, consistent with the higher degree of passivation of steel in pore solutions with higher [OH^-]. In comparison to the current density of 0.1 µA/cm^2 or lower, proposed by Andrade et al. [182] as the criterion for steel to exhibit a passive nature in PC concretes, the calculated i_{corr} values in this study for steel in the passive state are 5 – 10 times higher when using the value of B from [182], and 2 – 3 times higher when the value of B is taken according to [214]. Even though the i_{corr} values in the passive region are much higher than 0.1 µA/cm^2, no active corrosion was observed for chloride concentrations less than the respective [Cl^-]/[OH^-] (C_{crit}) ratios for these solutions. The differences in the i_{corr} values can be attributed to several possible reasons, including the measurements being conducted in simulated pore solutions rather than concrete specimens, and the differences in the chemistry and alkalinity of the simulated pore solutions for low-Ca alkali-activated binders compared to PC.

When the concentration of chloride is higher than C_{crit} for different pore solutions, the values of i_{corr} are much higher when compared to those in the passive region, indicative of active pitting corrosion. The observations of lower corrosion current densities for solutions with increased alkalinity were also true for the active corrosion region (Figure 4-6). In contrast to the situation for the passive region, the corrosion current densities of steel calculated using the B values accepted for PC systems in the active region are much lower when compared to those proposed for low-Ca alkali-activated binders.

4.5.3 Anodic polarisation

Figure 4-7 shows anodic polarisation curves obtained for steel rebars immersed solutions with varying concentrations of NaOH and chloride. In all three NaOH concentrations, the

anodic polarisation curves were similar to that observed for steel in its passive state (Figure 4-3) until chloride concentrations in each electrolyte reaches the corresponding C_{crit} values identified in Section 4.5.1 and 4.5.2. Such an observation clearly complements the conclusions from OCP and LPR measurements as discussed above and signifies the fact that depassivation of steel does not initiate unless the concentration of chloride reaches a critical value, which is strongly correlated to the alkalinity of the pore solution. Upon reaching the C_{crit} concentrations for different pore solutions, the anodic polarisation curves presented a smaller passivation region, or in some cases did not exhibit a passivation region at all. Instead, on attaining specific anodic potentials (the pitting potential, E_{pit}), abrupt increases in the current densities were observed, indicative of either pit nucleation, metastable pitting, or stable pit growth.

It could be reasonably expected that an increase in the concentration of chloride higher than C_{crit} would result in increased current densities. However, this was not the case at all three NaOH concentrations, primarily because of the number of variables (e.g. microstructure and surface features of different steel specimens, the presence of defects and inclusions, and the location of pitting and the local chemistry of the pore solution around the pit) associated with pitting. Therefore, the current densities observed in the anodic polarisation curves cannot be used as the sole determining factor in quantitatively ranking the degree of pitting corrosion for various steel specimens in the presence of an aggressive species. However, anodic polarisation can be successfully employed to predict the chloride concentration required for initiation of depassivation and stable pit growth.

Chloride-induced corrosion initiates through the localised breakdown of the passive film (more likely at grain boundaries, or defect sites) and propagates by the nucleation and growth of pits [245,246]. The breakdown of the passive film at highly localised sites only occurs when the local concentration of chloride reaches a critical value, leading to the formation of a pit. Once a pit nucleates, pit growth is only possible when the solution in the pit cavity maintains an aggressive environment compared to the bulk electrolyte surrounding it [247]. To fulfil this requirement, a sustained anodic dissolution of iron and subsequent hydrolysis of iron ions to form H^+ inside the pit cavity is essential [141]. Such a process decreases the relative alkalinity inside the pit cavity and leads to the growth of pits. The process of stable pit growth ceases when the anions in the surrounding environment, such as OH^-, migrate into the pit cavity to maintain charge neutrality, resulting in the re-passivation of the steel surface [247,248]. The migration of anions into the pit cavity is directly dependent on the local availability/reservoir of anions and the pit geometry. The mechanism by which some of the nucleated pits fail to

achieve stability and re-passivate due to the surrounding chemistry has been termed 'metastable pitting' [247].

When the ratio $[Cl^-]/[OH^-]$ was either 0.90 or 1.00 in 0.80 M NaOH solution (Figure 4-7A), apparently random fluctuations (increments and decrements) in the current density were observed as the potential increased from 0.22 V or 0.13 V respectively. Given the high alkalinity in the electrolytes used in this study, and that this behaviour is only observed at chloride concentrations close to C_{crit}, this phenomenon can be explained by the formation of metastable pits. Therefore, it could be concluded that the amount of chloride required to initiate pit nucleation may not necessarily be the same that is required for stable pit growth. For the same electrolyte, stable pitting was observed for $[Cl^-]/[OH^-]$ ratios above 1.00.

From the anodic polarisation curves for steel immersed in 1.12 M (Figure 4-7B) and 1.36 M (Figure 4-7C) NaOH solutions, distinct transitions from the passive condition to metastable pitting to stable pit growth is not observed for the concentrations of chloride tested. However, it could be assumed that such a transition occurs at some $[Cl^-]/[OH^-]$ ratio lying between 1.60 and 1.70 when the concentration of OH^- is 1.12 M, and between 2.30 and 2.40 when the OH^- concentration is 1.36 M.

Similar observations of repassivation have been reported [226,247,249,250] for steel embedded in PC concrete, as well as immersed in simulated pore solutions representative of PC systems. PC binders are characterised by the formation of large amounts of portlandite ($Ca(OH)_2$) during the hydration of calcium silicates [79]. Portlandite present at the steel-concrete interface plays an important role in determining the mechanism of corrosion initiation of the embedded steel, as it acts as a reservoir of soluble Ca^{2+} and OH^- ions [79]. The dissolution of portlandite around the pit nucleation site acts as a buffer ensuring sufficient availability of OH^- to neutralise the aggressive environment in the pit cavity, resulting in repassivation of the pit. Once the local reservoir of portlandite has been exhausted, stable pit growth will occur. However, unlike PC binders, low-Ca AAMs do not contain any observable portlandite that could provide a buffer effect, meaning that repassivation of a nucleated pit in such systems will primarily be influenced by other factors such as the diffusivity of hydroxide ions from the bulk solution.

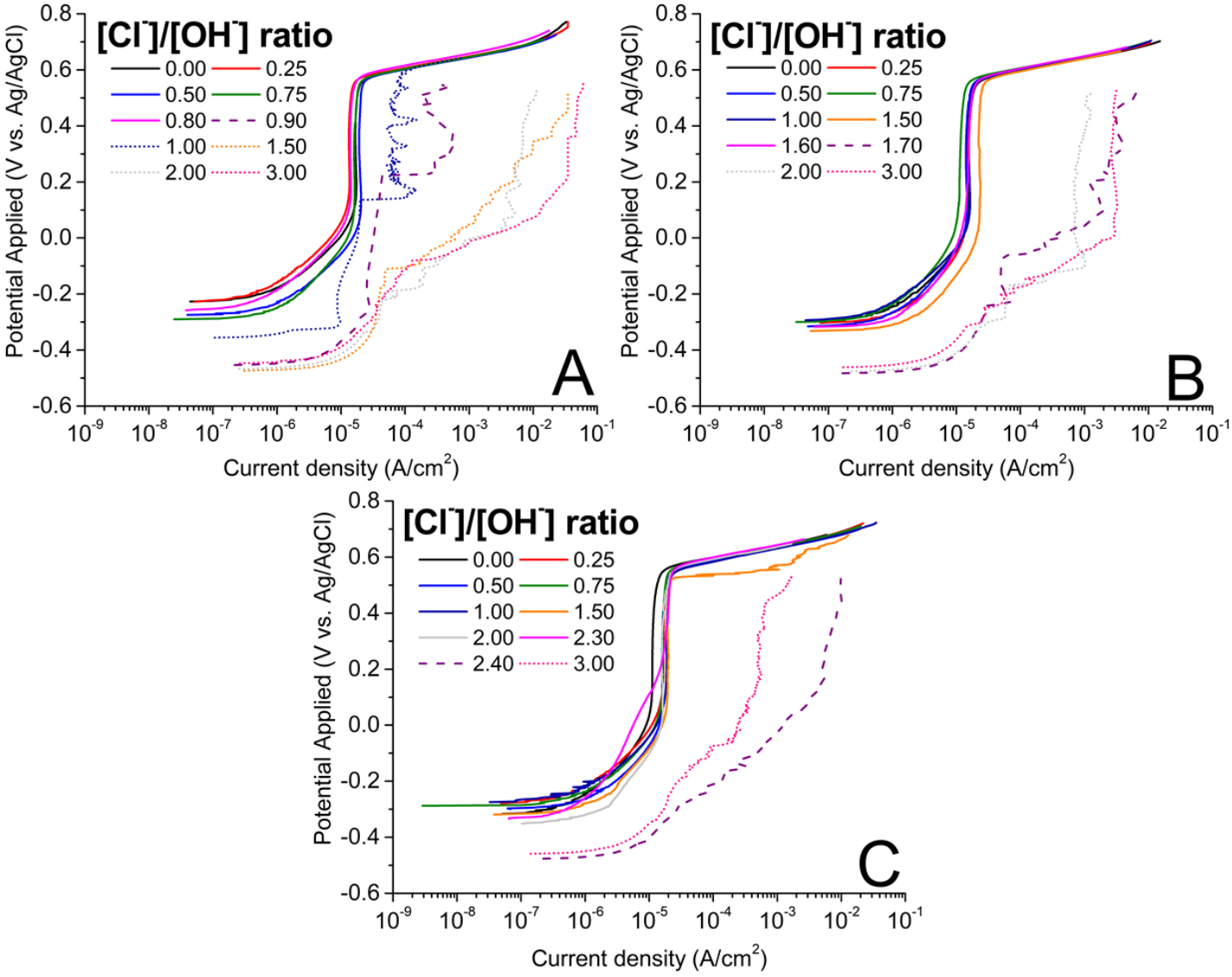

Figure 4-7: Anodic polarisation curves obtained for steel immersed in (A) 0.80 M, (B) 1.12 M and (C) 1.36 M NaOH solutions with varying concentrations of chloride. Solid lines (—) represent data for passive samples, dashed lines (- - -) represent data collected at the respective chloride threshold values for each OH^- concentration, and dotted lines (·····) represent data for chloride concentrations above the chloride threshold value.

4.5.4 Electrochemical impedance spectroscopy

Figure 4-8 shows the Nyquist data and fitting plots obtained for steel specimens immersed in solutions with varying concentrations of NaOH and chloride. Based on the OCP and LPR measurements, EIS analysis was conducted on steel exposed to selected concentrations of chloride (with $[Cl^-]/[OH^-]$ ratios = 0, 1.00, 3.00 and their corresponding C_{crit} values). The

equivalent circuit model used was similar to the classical Randles circuit, as shown in Figure 4-2. As discussed in Section 4.4.2, pitting corrosion is primarily driven by the diffusion of anionic species inside and outside the pit cavity, so the use of a Warburg diffusion element is justified. However, as in the analysis of passivation discussed in Section 4.4.2, the high frequency regions were characterised separately without the Warburg element.

Upon introduction of chloride, the general characteristics of the Nyquist plots did not change significantly when compared to steel in passivated conditions, where the higher frequencies reflected the non-ideal capacitive nature of the solution/passive film interface, and the lower frequencies showed a linear diffusion tail representing semi-infinite diffusion at the passive film/metal interface. Table 4-3 shows the fitting parameters obtained for the equivalent circuit model in the presence of chloride.

With increasing ionic strength or increasing chloride concentrations, the electrolyte resistance (R_e) decreases; this was consistent for all the three NaOH concentrations assessed. The capacitance associated with the CPE_{dl} varied only slightly, remaining between 72 and 95 $\mu F.cm^{-2}$, and the value of α was constant at 0.93 ± 0.01 for all solutions, demonstrating minimal changes of the double layer at the solution/passive film interface. The charge transfer resistance of the passive film (R_{ct}) did not exhibit any specific trend with increasing chloride concentrations for all the pore solutions; however, the values are consistent with the observations of anodic polarisation.

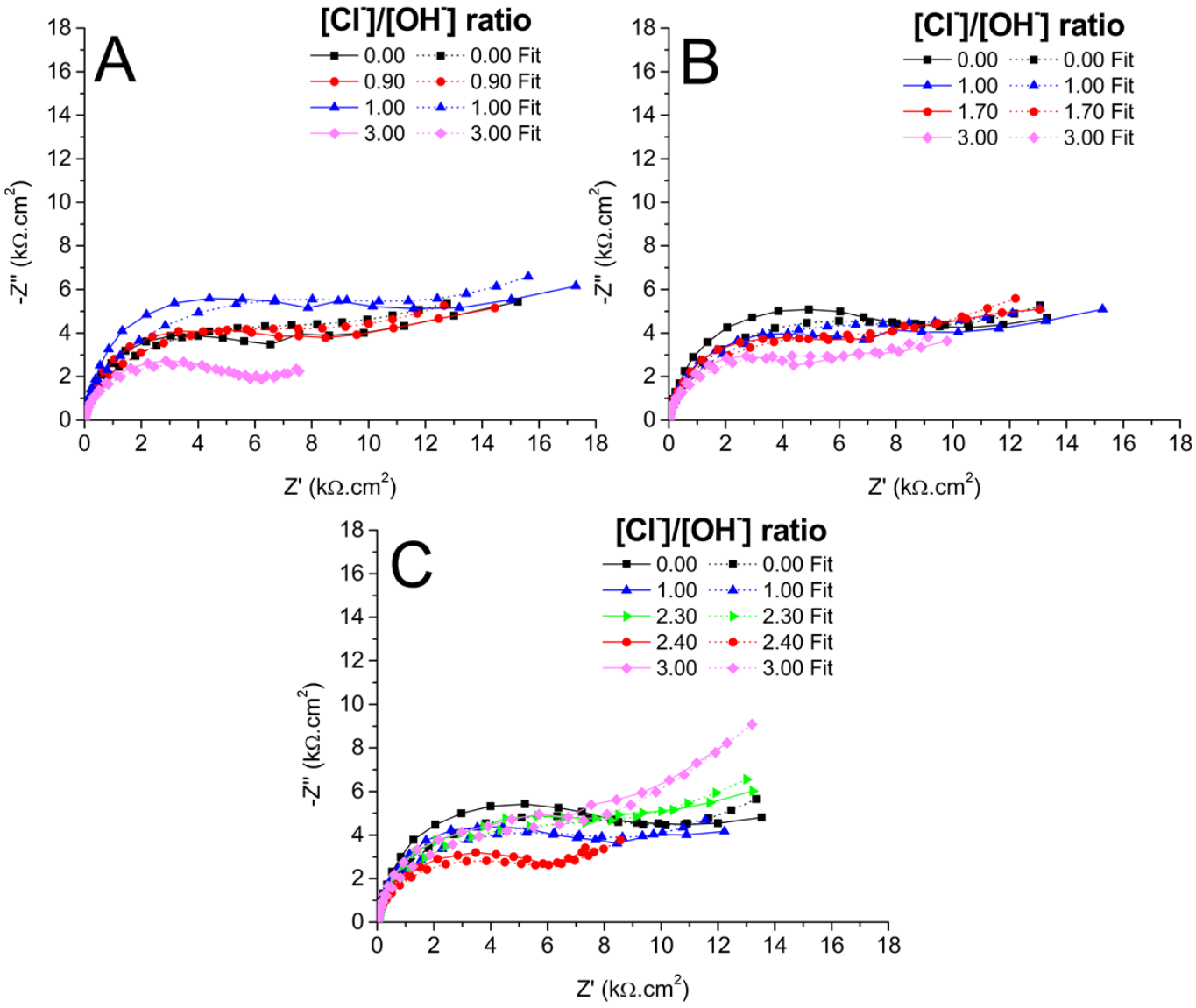

Figure 4-8: Nyquist data and fitting plots for steel exposed to (A) 0.80 M, (B) 1.12 M and (C) 1.36 M NaOH solutions with varying chloride concentrations. Solid lines such as —●— represent the impedance data collected at the respective chloride threshold values for each OH^- concentration, and dashed lines with the same markers, e.g. --●--, represent the corresponding fits.

Table 4-3. Fitting results obtained for equivalent circuit model components relating to EIS data shown in Figure 4-8. The values reported in parenthesis are standard deviations.

0.80 M NaOH						
$[Cl^-]/[OH^-]$	**R_e ($\Omega.cm^2$)**	**CPE_{dl} ($\mu F.cm^{-2}$)**	**α**	**R_{ct} ($k\Omega.cm^2$)**	**Y_o ($\mu S.s^n.cm^{-2}$)**	**χ^2**
0.00	1.72 (0.01)	80.0 (1.17)	0.93	9.5 (0.21)	16.3 (2.40)	0.009
0.90	1.43 (0.01)	75.9 (2.13)	0.93	9.5 (1.03)	85.9 (5.20)	0.008
1.00	1.40 (0.03)	72.2 (2.02)	0.93	12.8 (1.27)	263.7 (7.22)	0.013
3.00	0.95 (0.07))	89.4 (3.20)	0.93	6.0 (0.57)	5420.3 (121.7)	0.002
1.12M NaOH						
$[Cl^-]/[OH^-]$	**R_e ($\Omega.cm^2$)**	**CPE_{dl} ($\mu F.cm^{-2}$)**	**α**	**R_{ct} ($k\Omega.cm^2$)**	**Y_o ($\mu S.s^n.cm^{-2}$)**	**χ^2**
0.00	1.21 (0.05)	78.0 (2.10)	0.93	11.9 (0.12)	0.04 (0.009)	0.013
1.00	1.00 (0.07)	76.4 (0.12)	0.93	8.9 (1.11)	0.03 (0.005)	0.007
1.70	0.93 (0.01)	73.8 (2.11)	0.93	8.6 (1.76)	46.3 (4.33)	0.006
3.00	0.91 (0.02)	95.4 (2.79)	0.93	6.5 (0.37)	4349.5 (321.6)	0.005
1.36 M NaOH						
$[Cl^-]/[OH^-]$	**R_e ($\Omega.cm^2$)**	**CPE_{dl} ($\mu F.cm^{-2}$)**	**α**	**R_{ct} ($k\Omega.cm^2$)**	**Y_o ($\mu S.s^n.cm^{-2}$)**	**χ^2**
0.00	1.06 (0.08)	76.7 (1.77)	0.93	12.8 (0.22)	0.003 (0.000)	0.014
1.00	1.02 (0.03)	92.7 (1.56)	0.93	9.9 (0.02)	0.002 (0.000)	0.011
2.30	0.95 (0.05)	87.5 (2.11)	0.92	10.9 (0.13)	0.004 (0.000)	0.006
2.40	0.98 (0.05)	91.7 (1.85)	0.92	7.0 (0.21)	62.07 (3.100)	0.005
3.00	0.96 (0.02)	80.5 (1.99)	0.92	10.7 (0.30)	3247.5 (55.76)	0.008

As seen in Figure 4-7A for 0.80 M NaOH, the current density was much higher for a $[Cl^-]/[OH^-]$ ratio of 0.90 than 1.00. Correspondingly, the R_{ct} values mentioned in Table 4-3 were lower for $[Cl^-]/[OH^-]$ ratio of 0.90, than for $[Cl^-]/[OH^-] = 1.00$. Similar correlations between measured R_{ct} values obtained through EIS and current density determined through anodic polarisation could be made in the case of 1.36 M NaOH solutions, when the $[Cl^-]/[OH^-]$ ratios were 2.40 and 3.00. It is important to mention that, although the timescales allowed in this study for the passive film to stabilise in the simulated pore solutions were much less than has been suggested by other studies [184,251,252], the chemical nature of the film could be considered to be representative of what would exist after the suggested stabilisation timescales but with a lesser thickness. As shown by several authors [193,194], both the R_{ct} and CPE_{dl} parameters of the passive film are related to the time of exposure and are somewhat dependent on its physical nature. Therefore, variation in the values of R_{ct} and CPE_{dl} could be expected at longer times of exposure, but the electrical properties of the system would remain unaffected.

A substantial rise in the admittance (Y_o), characterising diffusion at the passive film/metal interface, was observed when the chloride concentration exceeded the respective C_{crit} values for the three pore solutions. As in the EIS study of passivation discussed in Section 4.4.2, non-conventional diffusion tails in the low frequency region were also observed upon addition of chloride, for all three NaOH concentrations. However, the slope between the real and imaginary components of impedance at lower frequencies approached its conventional 45° for all $[Cl^-]/[OH^-]$ ratios where the steel specimens underwent pitting.

The admittance can be physically interpreted as the ease of transport of chloride ions through the passive film to the metal, and is described as a function of the stability of the passive film. When the concentration of chloride is lower than C_{crit}, the steel is maintained in its passive state and consequently the admittance is fairly constant at a relatively low value, similar to that observed for chloride-free solutions. Hence, the diffusion of ions through the passive film to the metal surface can be considered to be not rapid enough to be detected at frequencies as low as 10^{-2} Hz, leading to the non-conventional diffusion tail. Breakdown of the passive film by the action of chloride would lead to easier transport of ions and a rise in the admittance value (Table 4-3). Thus, on increasing the chloride concentrations to C_{crit} and above, the diffusivity associated with the passive film would significantly increase due to the action of chloride on the passive film, and would lead the slope between real and imaginary components of impedance to approach 45°.

4.6 Observations on passivation and the chloride threshold value

Several relationships between C_{crit} and $[OH^-]$ have been reported in studies conducted in simulated concrete pore solutions. Hausmann [135] experimentally reported the value of $[Cl^-]/[OH^-]$ ratio to vary between 0.5 and 1.08, and statistically found the ratio of 0.63 as critical. Gouda [95] suggested a linear relationship between pH and the logarithm of the critical chloride concentration with a slope of 0.83, implying a constant value of $[Cl^-]^{0.83}/[OH^-]$. Goni and Andrade [139] found a linear relationship between the logarithm of corrosion current density and the logarithm of $[Cl^-]/[OH^-]$, and on assuming the boundary condition for active corrosion in the range of 0.1 – 0.2 μA/cm^2 suggested a threshold value between 0.25 and 0.8. Similar observations have been made in other studies including [165,223], where the critical chloride content for depassivation were witnessed to increase with higher pH.

Measurements from all of the techniques used in this study to analyse chloride-induced depassivation of the steel in simulated pore solutions representative of low-Ca AAMs, confirm a strong correlation between the concentration of hydroxide and the chloride threshold value. The C_{crit} values were found to be 0.72 M, 1.90 M and 3.26 M for pore solutions with $[OH^-]$ concentrations of 0.80 M, 1.12 M and 1.36 M respectively. Contrary to the observation of diverging C_{crit} values for a particular electrolyte obtained through different techniques in [184], the same C_{crit} value has been identified through several electrochemical techniques for a given electrolyte.

To develop a relationship between the measured C_{crit} values and the OH^- concentration of the simulated pore solution, C_{crit} values were plotted against $[OH^-]$, as shown in Figure 4-9. A linear correlation between the logarithm of C_{crit} and logarithm of $[OH^-]$ with a slope of 2.83 was fitted, implying an increased inhibition effect with an increase in $[OH^-]$. Given the heterogeneous nature of the steel-concrete interface (generally due to macroscopic and microscopic voids, varying hydration products and pore solution alkalinity, bleed-water zones) and the possible carbonation of pore solution, the derived relationship was used to extrapolate for values of $[OH^-]$ ranging between 0.5 and 1.43 M. The C_{crit} values obtained through the above-mentioned extrapolation method (as shown in Figure 4-9) show that even a chloride concentration as low as about 0.18 M, in regions at the steel-concrete interface where $[OH^-]$ is 0.5 M, could possibly initiate pitting of the embedded steel rebar. Here it is important to highlight that this relationship is possibly valid only when the binder does not contain any buffering agent (like portlandite in PC based concretes), as is in the case of low-Ca AAMs, and the alkalinity of the pore solution is primarily dependent on the concentration of hydroxides

present in the pore solution. For example, if the relationship was extrapolated to pH 13 or 10^{-1} M [OH^-], the resulting C_{crit} would be around 10^{-3} M. This would deviate from the C_{crit} values already reported in the literature (can be found in the review by Angst et al. [99]).

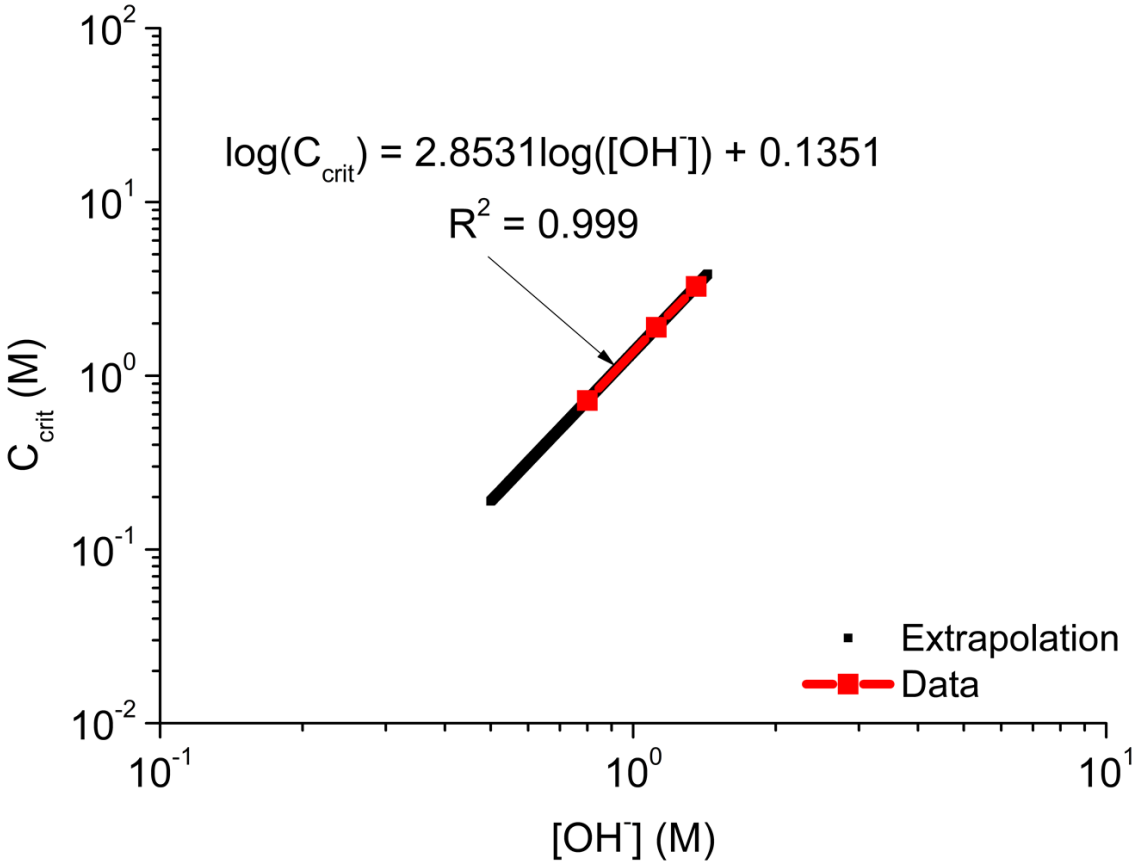

Figure 4-9: Relationship between C_{crit} and [OH^-]. Red points and the regression equation correspond to the experimental data. Black data points represent extrapolated values

The localised phenomena of depassivation by the action of chloride is primarily governed by the dissolution of the passive film, and therefore it can be hypothesised that the onset of pitting would be directly proportional to the concentration of chloride and inversely related to the solubility of the passive film for a particular electrolyte. For a given composition of the passive film, all electrochemical parameters should reflect the onset of pitting at a similar values of $[Cl^-]/[OH^-]^n$, where *n* is the stoichiometric coefficient of [OH^-] in the hydrated outer layer of the passive film. According to the results of cyclic voltammetry in Section 4.4.1, the passive film is composed of an outer layer of hydrated FeOOH or Fe_2O_3 for all three electrolytes. Therefore, considering a monohydrate layer of $Fe(OH)_3$ as the outer layer of the

passive film, the value of *n* could be taken to be 3; this value is also the nearest integer value to the 2.85 fitted above.

Figure 4-10 shows the variation of different electrochemical parameters (OCP, R_p and i_{corr}) as a function of the ratio $[Cl^-]/[OH^-]^3$, for all three pore solutions assessed. The three parameters OCP, R_p and i_{corr} were observed to be close to constant for $0 \leq [Cl^-]/[OH^-]^3 \leq 1.25$; these values of $[Cl^-]/[OH^-]^3$ correspond to chloride concentrations less than the measured C_{crit} values for the three pore solutions, and thus not high enough to cause depassivation. Above the value of $[Cl^-]/[OH^-]^3 = 1.25$, OCP and R_p showed a sharp decline whereas i_{corr} values increased suddenly, indicating active corrosion. The sharp transition from the passive to the active region was found to occur very close to $[Cl^-]/[OH^-]^3 = 1.25$ for all three pore solutions, and the respective C_{crit} values aligned at this value. This confirms the existence of a hydrated FeOOH or Fe_2O_3 as the outer layer of the passive film on all the steel specimens tested. The relationship thus appears to provide a powerful and novel means of characterising the likely onset of steel corrosion in low-calcium alkali-activated binders, at least as far as can be predicted through experimental work in simulated pore solutions.

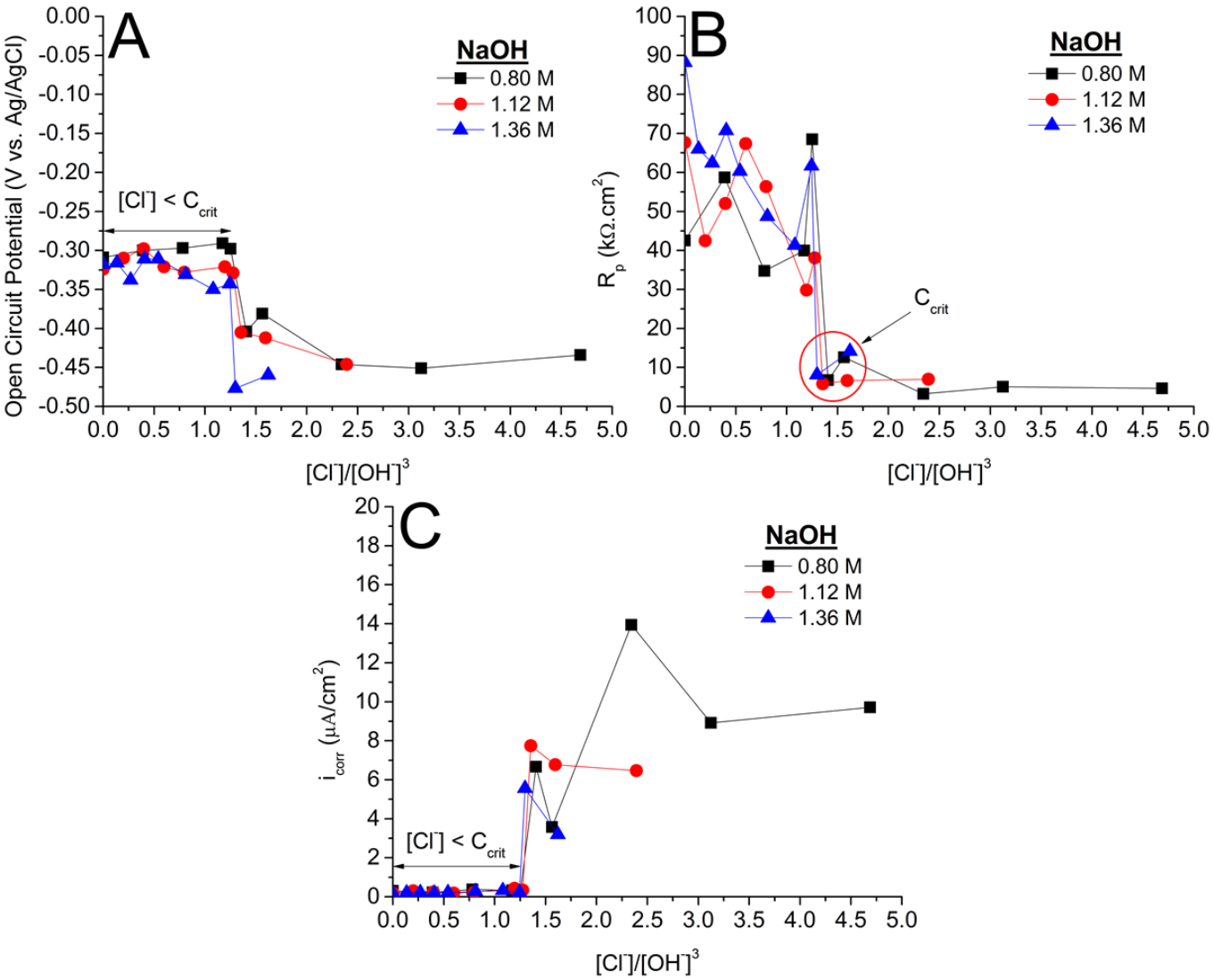

Figure 4-10: Representation of (A) OCP, (B) R_p and (C) i_{corr} as a function of $[Cl^-]/[OH]^3$, for steel rebars immersed in simulated pore solutions with varying NaOH concentrations

4.7 Conclusions

It is demonstrated through the analysis of the anodic and cathodic current peaks from cyclic voltammetry, that in highly alkaline solutions the mechanism of passive film formation can be hypothesised as:

$$Fe \rightarrow Fe(OH)_{ads} \rightarrow Fe(OH)^{+}_{ads} \rightarrow HFeO_2^{-} \rightarrow Fe(OH)_2 \rightarrow FeOOH \rightarrow \text{hydrated } FeOOH \text{ or } Fe_2O_3$$

This implies that the passive film is composed of an inner dense layer rich in iron (II) species and the outer layer is rich in a less dense iron (III) species. The amounts of passivating species

formed on the surface of the steel specimen are directly proportional to the alkalinity of the solution. This is consistent with results of EIS, LPR and anodic polarisation, revealing a higher degree of the passivation at increased concentrations of OH^- in the pore solution.

The C_{crit} values (in terms of $[Cl^-]/[OH^-]$ ratios) obtained from OCP, EIS, LPR and anodic polarisation are comparable and within 0.90 ± 0.10, 1.70 ± 0.10 and 2.40 ± 0.10 for NaOH concentrations of 0.80 M, 1.12 M and 1.36 M, respectively. It is clearly seen that an increased concentration of OH^- in the system, results in a rise in the chloride threshold value, as a consequence of improved passivation of the steel. Given the high alkalinity of the simulated pore solutions representative of low-Ca alkali-activated binders, the amounts of chloride at the steel-concrete interface required for pit nucleation and the amounts required for sustained pit growth might differ, and this led to observations of metastable pitting in some cases.

A novel relationship of depicting the onset of pitting as a function of the composition of the outer layer of the passive film, in terms of the ratio $[Cl^-]/[OH^-]^3$ was developed, where $[Cl^-]/[OH^-]^3 = 1.25$ was found to define the critical chloride concentration C_{crit} within the very highly alkaline range of solutions assessed. Rather than the simple ratio between chloride and hydroxide concentrations that is often used to define C_{crit}, this power law relationship provides improved descriptive power for solutions representative of the pore solution chemistry of low-calcium alkali-activated binders. The functional form used, with a third power relationship to hydroxide concentration, is also consistent with the passive film being composed of a hydrated FeOOH or Fe_2O_3 outer layer that plays an important part in the initiation of pitting corrosion. However, further research related to different passivation products needs to be done to confirm such a relationship for pit initiation, and particularly to understand its validity in actual concrete specimens, and also in pore solutions which are not as extremely alkaline as those studied here.

Chapter 5: Passivation and chloride-induced corrosion of steel in high-Ca alkali-activated materials

Note: This chapter is primarily based on: Shishir Mundra, John L. Provis. 'Influence of sulfide on the passivation and chloride-induced corrosion of steel in highly alkaline solutions.' (*under preparation*), and Shishir Mundra, Susan A. Bernal, Maria Criado, Petr Hlaváček, Gino Ebell, Steffi Reinemann, Gregor J. G. Gluth, John L. Provis. 'Steel corrosion in reinforced alkali-activated materials.' RILEM Technical Letters, 2 (2017), 33-39. (*Invited Publication*). Only work conducted by Shishir Mundra in the abovementioned manuscripts have been included in this Chapter.

5.1 Introduction

As mentioned in Chapter 2, high-Ca alkali-activated materials (AAMs) are most commonly produced by the reaction between blast furnace slags, a by-product of the iron making process, and an alkaline solution [23]. The resulting solid reaction products and the aqueous pore solution chemistry are significantly different from Portland cement (PC) binders as well as low-Ca AAMs. High-Ca AAMs or alkali-activated slags (AAS) are characterised by a C-(N-)A-S-H gel as the main reaction product along with secondary reaction products such as hydrotalcite-like phases and AFm type phases being formed [30,253]. Depending on the composition of the slag and the type of activator used to formulate AAS, additional phases such as Ca-heulandite, natrolite, monosulfoaluminate, monocarboaluminate may also precipitate in minor or trace quantities [80]. As stated in Chapter 2, one of the major differences in the chemistries of low-Ca AAMs and high-Ca AAMs, relevant to the corrosion of steel reinforcement, is the composition of the pore solution. The reducing nature of the blast furnace is retained by the slag, containing approximately 1-3 wt. % SO_3 that readily dissolves when mixed with PC and water [78]. Similarly, in the case of AAS, where the slag is the main precursor (along with a highly alkaline solution), the sulfur exists primarily in the reduced state (HS^-) creating a highly reducing environment at the steel-concrete interface that is depleted in dissolved oxygen [78,81,254]. The total HS^- concentration has been measured to be around 0.45 M [78], and also estimated be around the same value through thermodynamic simulations

of AAS [81]. Owing to the differences in the chemistry of the aqueous and solid phases in low-Ca and high-Ca AAMs, it is imperative that mechanisms of passivation and chloride induced corrosion of the embedded steel reinforcements are thoroughly investigated in the binders.

As highlighted in Chapter 4, the passive film formed on the steel reinforcement embedded in low-Ca AAMs is composed of an inner layer of ferrous hydroxide ($Fe(OH)_2$) that could readily oxidise to form magnetite (Fe_3O_4), and an outer layer composed of $Fe(OH)_3$ or hydrated Fe (III) oxide ($Fe_2O_3.nH_2O$). However, the exact composition of the passive film formed on steel reinforcements in alkaline conditions has been a subject of constant debate throughout the literature [235] and depends on the environmental conditions such as chemistry and pH of the electrolyte, the availability of oxygen and the redox potential of the steel [88]. Unlike low-Ca AAMs and PC, where OH^- in the pore solution is the major anion influencing the chemistry of the passive film formed on the steel reinforcement and the chloride threshold value (as shown in Chapter 4), blended cements containing steel slag have shown to influence electrochemical nature of the passive film and the chloride threshold value to initiate pitting [14,255,256]. Macphee and Cao [254] reported Fe in the passive film to be in the 2+ oxidation state for slag-PC blends rather than in the commonly observed 3+ oxidation state in plain PC. Based on the observations of higher porosity of the Fe (II) oxides in comparison to Fe (III) oxides by Lorenz and Heusler [257], Macphee and Cao [254] suggested that cements with replacement of PC with slags were incapable of forming a passive film on the steel reinforcement, thus giving lower protectiveness to aggressive ions such as Cl. In addition, they [254] showed the release of reduced sulfur species in blended cement with 75 and 85 % replacement of PC with slag lead to a significant decrease in the electrochemical potential of the steel reinforcement, when compared to cements with 50 % slag replacement. Similar results of reduced redox potentials of the steel reinforcement were obtained by Angus and Glasser [258] for slag-PC blends with > 75 % replacement of PC with slag. A recent study [255] (also highlighted in [254,258,259]), shows that the highly reducing nature of the slag results in reduced levels of dissolved oxygen and consequently significantly lower electrochemical potentials of the steel reinforcement embedded in slag-PC blends when compared to plain PC. In the case of high-Ca AAMs, it would be plausible to assume that a highly reducing environment, due to the high concentration of HS^-, would alter the passivation chemistry and the electrochemical nature of the steel-concrete interface.

The chloride threshold value for the corrosion initiation of the steel reinforcement in high-Ca AAMs such as AAS do not exist in the literature. However, few studies have investigated

the chloride threshold values when steel is immersed in simulated pore solutions of slag-PC blended systems. The presence of anions such as HS^- and $S_2O_3^{2-}$ in the pore solution of slag-PC blends and their influence on the chloride threshold value is important to discuss here as they are also likely to be found in the pore solutions of AAS. Published data on the chloride threshold values for steel reinforcements embedded in slag-PC bends in comparison to plain PC are contradictory and are scattered [99]. Some studies have indicated the chloride threshold value to be much higher in the case of slag-PC blends [149,260], whereas some studies have reported the contrary [14,96,261]. Oh et al. [262] suggested that the influence of PC replacement by slag did not significantly alter the chloride threshold value. A similar scenario of mixed conclusions exists for tests conducted in simulated pore solutions of slag-PC bends [255,263] as well. In the case of AAMs, Babaee and Castel [264] measured the chloride threshold values for Na_2SiO_3 activated fly ash/slag blends, and found that the chloride threshold was the lowest for binders produced with higher amounts of slag. Holloway and Sykes [265] investigated the electrochemical behaviour of steel reinforcement in AAS with admixed chloride levels of up to 8 wt. % of binder, and observed no pitting for very high levels of chloride concentrations. They suggested that the oxidation of HS^- present in the pore solution of AAS plays a critical role in the mechanisms of passivation/depassivation and the long term-performance of these binders [265].

This chapter focusses on the influence of reduced sulfur species on mechanisms of passivation of steel and the phenomena of localised corrosion due to chlorides in highly alkaline electrolyte solutions (0.80 M, 1.12 M and 1.36 M NaOH) containing varying concentrations of HS^- (0.01 M, 0.09 M and 0.45 M). The influence of reduced sulfur species on the passivity of steel is relevant not only for the durability of steel embedded in AAS/slag-PC blends, but also in various natural and industrial environments such as the Kraft process used for manufacturing pulp from wood chips, geological areas where sulfate reducing bacteria are predominant, waste from hydrocarbon processing plants.

5.2 Experimental Programme

5.2.1 Materials

Mild steel rebars (φ = 12 mm) from a local supplier in Sheffield, UK with specifications and chemistry described in Section 3.1, Chapter 3 were used in this study.

ACS reagent grade NaOH pellets (from Sigma Aldrich), $Na_2S.9H_2O$ (from Alfa Aesar) and commercial grade NaCl (from EMD Chemicals) were used to synthesise alkaline solutions (in 250 mL distilled water) with specific concentrations of HS^-, to understand the influence of sulfide on the passivity of steel and the mechanisms of chloride induced corrosion in alkaline solutions. It is to be noted that sulfur was assumed to only exist as HS^- (aq.) in all the synthesised alkaline solutions. Given the high affinity of sulfur to oxidation, it would be reasonable to expect minor/trace quantities of sulfur as S_n^{2-} (aq.), SO_3^{2-} (aq.), $S_2O_3^{2-}$ (aq.), and SO_4^{2-} (aq.) due to the dissolved oxygen within the electrolyte (as shown in the Pourbaix diagram for the system sulfur-water in Figure 2-5). Similar speciation of sulfur is seen in the pore solutions of AAS [78]. The precise compositions of the solutions used in this study are shown in Sections 5.2.2 and 5.2.3.

All electrochemical tests were conducted as described in Section 3.2, Chapter 3.

5.2.2 Passivation

Table 5-1 gives the detailed chemical composition of each of the electrolytes used to investigate the passivation of steel in alkaline sulfide containing solutions. The upper limit of $[HS^-]$ was set to 0.45 M, to be representative of pore solutions of AAS [78,81].

Table 5-1: Chemical composition of electrolytes synthesised in this study using NaOH and $Na_2S{\cdot}9H_2O$ to investigate the influence of HS^- on the passivity of mild steel. The concentrations of hydroxide $[OH^-]$ and sulfide $[HS^-]$ are represented in mol/L (M).

$[OH^-]$ (M)	$[HS^-]$ (M)
0.80	0
0.80	0.01
0.80	0.45

1.12	0.01
1.36	0.01

5.2.2.1 Cyclic voltammetry

Potentiostatic cyclic voltammetry (CV) was conducted to characterise the passive film formed on the steel surface when exposed to solutions containing 0.80 M OH^- and varying concentration of HS^- (0 M, 0.01 M and 0.45 M). Additionally, to understand the influence of OH^- in sulfide containing electrolytes, CV was also conducted on mild steels exposed to solutions with increased concentrations of OH^- (1.12 M and 1.36 M) with 0.01 M HS^-. Before starting each test, the steel was maintained at -1.50 V vs. Ag/AgCl (cathodic limit: $E_{\lambda,c}$) in the hydrogen evolution region for 10 mins to ensure electrochemical clean-up of the surface of steel. The electrochemical response of the system was recorded when the potential was cycled from -1.50 V ($E_{\lambda,c}$) to 0.65 V (anodic limit: $E_{\lambda,a}$), at a scan rate of 2.5 mV/s over 5 cycles, taking into account hydrogen and oxygen evolution at the cathodic and anodic limits respectively.

5.2.2.2 Open circuit potential, Linear polarisation resistance and Anodic polarisation

Steel specimens were exposed to each of the test solutions (mentioned in Table 5-1) in plastic vials in a vacuum desiccator, for 0, 5, 12 and 28 days prior to electrochemical testing. Additional sealing of all the plastic vials was done using parafilm. After each of the exposure time, the steel specimens were taken out from the vacuum desiccator and immediately transferred to the cell for electrochemical testing in fresh electrolytes prepared with a chemical composition matching the respective exposure solution.

The following electrochemical techniques were employed to each of the steel specimens at each of the exposure times in the following order: (i) Open circuit potential (OCP), (ii) linear polarisation resistance (LPR), and (iii) anodic polarisation.

Prior to any electrochemical polarisation technique being applied, the OCP of the steel specimens were recorded using the parameters mentioned in Section 3.2.1, Chapter 3.

LPR measurements and anodic polarisation on the steel specimens were conducted as described in Section 3.2.3.1, Chapter 3.

5.2.2.3 X-ray photoelectron spectroscopy

Steel specimens were exposed to solutions with compositions 0.80 M OH^- + 0.01 M HS^-, 0.80 M, 0.80 M OH^- + 0.09 M HS^-, and 0.80 M OH^- + 0.45 M HS^-, in plastic vials and were kept in a vacuum desiccator to avoid any interaction of the solution and the steel with air, for 5, 12 and 28 days. After each of the exposure times considered in this study, the steel specimens were taken out of the exposure solutions and dried in a nitrogen atmosphere. Dried specimens were then wrapped in parafilm and transferred to an airtight container to transport the specimens to the X-ray photoelectron spectroscopy (XPS) facility at the University of Sheffield. The specimens were unwrapped, and were mounted onto the sample holder using double sided sticky conducting tape, and placed in the fore chamber of the Kratos AXIS Supra spectrometer for the measurements to be carried out. Prior to the measurement, the chamber was evacuated by creating an ultra-high vacuum environment.

All measurements were carried out by using an achromatic Al Kα X-ray source and data were acquired from three points (each with diameter 800 μm) per specimen. Survey scans were collected between the binding energy range: 1200 to 0 eV, with a pass energy of 160 eV, a step size of 1 eV, and an acquisition time of 5 minutes for each measurement. High-resolution XPS spectra were collected for the following elements: iron (Fe 2*p*), oxygen (O 1*s*), carbon (C 1*s*) and sulfur (S 2*p*), with a pass energy of 20 eV and a step size of 0.1 eV for each measurement point over the appropriate energy range. The O 1*s* and C 1*s* spectra were collected with 5 minutes acquisition time, whilst S 2*p* spectra was collected as two sweeps of 5 minutes each and averaged, due to its lower sensitivity. The Fe 2*p* spectra were also collected as two sweeps of 5 minutes each and averaged, due to the broader energy range of this peak. The intensity of the acquired data was calibrated using a transmission function characteristic of the spectrometer (determined using software from NPL) to ensure the acquired data is instrument specific. Casa-XPS software (version 2.3.18PR1.0) was used to deconvolute and curve-fit the spectra and the following constraints were employed:

- All high-resolution spectra were first calibrated to the C 1*s* signal at 284.8 eV.
- Optimal spectral basal line and peaks were determined using the Shirley background correction algorithm provided within the software [91].
- The 2*p* spectrum of Fe consists of two peaks (a doublet structure) due to multiplets splitting, Fe $2p_{3/2}$ and Fe $2p_{1/2}$, separated by approximately 13.8 eV [91]. Due to the occurrence of satellite peaks between the two peaks, only the Fe $2p_{3/2}$ peak was

deconvoluted and curve fitted. A 80 % Gaussian, 20 % Lorentzian peak model was used to fit the Fe $2p_{3/2}$ spectra as adopted by [266].

- The S 2*p* spectrum also consists of a doublet structure, however, the separation between the S $2p_{3/2}$ and S $2p_{1/2}$ is much smaller (~ 1.18 eV) [267], and therefore, both the peaks were analysed in this study. The full width at half maximum (FWHM) of the S $2p_{1/2}$ peak was constrained to be half of the S $2p_{3/2}$ and the position of the S $2p_{1/2}$ peak was constrained to be 1.18 eV greater than the S $2p_{3/2}$ peak. Similar to the Fe $2p_{3/2}$ spectra, the S 2*p* spectra were analysed by the method adopted by [266,267].

5.2.3 Depassivation

A similar exposure scheme as used in Section 5.2.2, was employed to understand the mechanism of chloride-induced corrosion in sulfide containing alkaline solutions. Steel specimens were exposed to each of the test solutions without chloride (mentioned in Table 5-2) in plastic vials in a vacuum desiccator, for 0, 5, 12 and 28 days prior to electrochemical testing. After each exposure time, fresh electrolytes with the same composition of the exposure solution were prepared and to electrochemically investigate the chloride threshold value, NaCl was added in the freshly prepared electrolytes and the molar ratio $[Cl^-]/[OH^-]$ was varied between 0 and 4, 0 and 3.5, and 0 and 3.5 for solutions 0.80 M OH^-, 1.12 M OH^-, and 1.36 M OH^-, respectively.

Table 5-2: Chemical compositions of electrolytes synthesised using NaOH, $Na_2S{\cdot}9H_2O$ and NaCl used to investigate the mechanism of chloride induced corrosion in sulfide containing alkaline solutions. The concentrations of hydroxide $[OH^-]$, sulfide $[HS^-]$ and chloride $[Cl^-]$ are represented in mol/L (M).

$[OH^-]$ (M)	**$[HS^-]$ (M)**	**$[HS^-]$ (M)**	**$[HS^-]$ (M)**	**$[HS^-]$ (M)**	**$[Cl^-]$ (M)**
0.80	0.001	0.01	0.09	0.45	0 to 3.2
1.12	--	0.01	--	0.45	0 to 3.92
1.36	--	0.01	--	0.45	0 to 4.76

5.2.3.1 Open circuit potential, Linear polarisation resistance and Anodic polarisation

The following electrochemical techniques were employed to each of the steel specimens at each of the exposure times in the following order: (i) Open circuit potential (OCP), (ii) linear polarisation resistance (LPR), and (iii) anodic polarisation.

Prior to any electrochemical polarisation technique being applied, the OCP of the steel specimens were recorded using the parameters mentioned in Section 3.2.1, Chapter 3.

LPR measurements and anodic polarisation on the steel specimens were conducted as described in Section 3.2.3.1, Chapter 3.

5.3 Results and discussion

5.3.1 Passivation

5.3.1.1 Cyclic voltammetry

Figure 5-1 shows 5 cyclic voltammetry scans obtained for polished mild steel surfaces exposed to highly alkaline solutions (0.80 M NaOH), as a function of the sulfide concentration (0 M, 0.01 M and 0.45 M HS^-) in the electrolyte. Data from $E_{\lambda,c}$ to -1.20 V in the anodic sweeps are not presented to enable visibility of all peaks. An increase in the potential in the positive direction from $E_{\lambda,c}$ to -1.20 V resulted in significant increase in the current density of the steel related to the evolution of hydrogen bubbles at the steel surface and in the solution (not shown in Figure 5-1). The passivation mechanism in alkaline solution without HS^- (shown in Figure 5-1A) has already been discussed in Chapter 4, and therefore will only be briefly revisited in this Chapter.

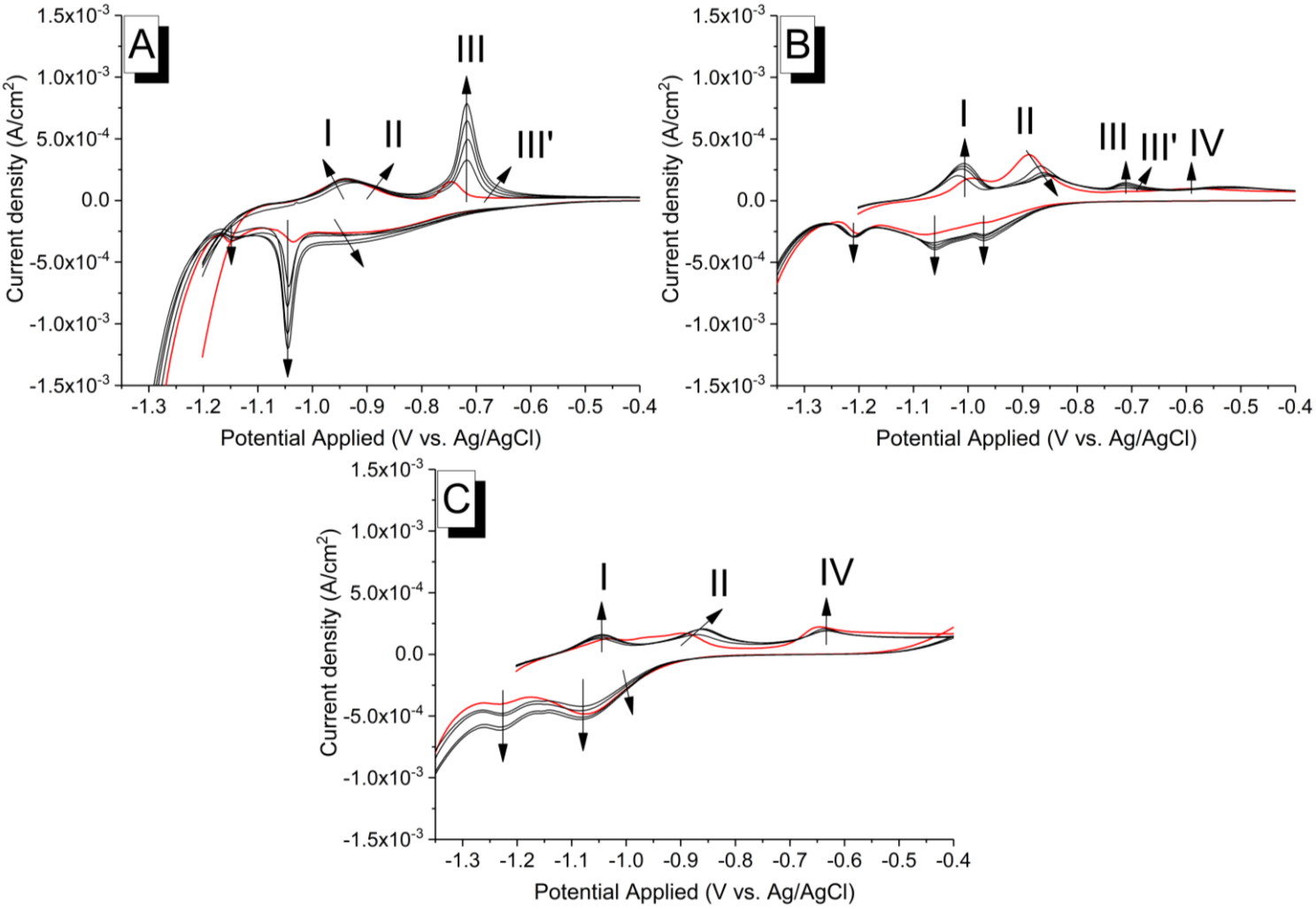

Figure 5-1: Cyclic voltammograms obtained for mild steel exposed to (A) 0.80 M OH^-, (B) 0.80 M OH^- + 0.01 M HS^-, and (C) 0.80 M OH^- + 0.45 M HS^-. Data were collected at a sweep rate of 2.5 mV/s. Arrows indicate the current response from scan numbers 1 to 5. Data from -1.50 V to -1.20 V in the anodic sweeps are not presented to enable visibility of all peaks. The red line indicates the first scan, and subsequent scans are represented by black lines.

As mentioned in Chapter 4, in the case of mild steel immersed in alkaline solutions without HS^- (Figure 5-1A), four anodic current peaks were observed on increasing the potential from -1.20 V towards $E_{\lambda,a}$, at approximately -0.94 V (denoted Peak I), -0.89 V (Peak II), -0.72 V (Peak III) and -0.67 V (Peak III'), and on reversing the potential, cathodic current peaks were observed at about -0.96 V, -1.05 V and -1.14 V. The oxidation and reduction reactions corresponding to these peaks have already been described in Chapter 4, and the mechanism of passivation can be described by the following reaction (Eq. 5.1.):

$$Fe \rightarrow Fe(OH)_{ads} \rightarrow Fe(OH)^{+}_{ads} \rightarrow HFeO^{-}_{2} \rightarrow Fe(OH)_2 \rightarrow FeOOH \rightarrow hydrated\ FeOOH\ or\ Fe_2O_3 \quad \text{(Eq. 5.1)}$$

As seen from Figure 5-1, the current response of mild steel in the anodic and cathodic directions was observed to be significantly different when the electrolyte contained HS^-, in comparison to steel immersed in electrolytes without HS^-. Similar cyclic voltammograms for steel exposed to alkaline solutions containing sulfide have been observed by Shoesmith et al. [268]. In the presence of HS^- in the electrolyte (Figure 5-1B and Figure 5-1C), the broad anodic current peak denoted as peaks I and II observed at -0.94 V and -0.89 V, respectively, in Figure 5-1A converted to a doublet. Peak I was observed to be shifted to lower potentials of approximately -1.00 V when the concentration of HS^- in the electrolyte was 0.01 M; and to an even lower potential of approximately -1.05 V when [HS^-] was 0.45 M. The position of the peak I did not change upon subsequent anodic sweeps, however the current density associated with the peak was observed to increase in both electrolytes containing HS^- (Figure 5-1B and Figure 5-1C). Peak II, however, was observed to shift towards more positive potentials with increasing anodic sweeps (Peak II was found to be cantered at -0.89 V in the first anodic sweep, and at around -0.85 V in the 5th scan) for electrolytes containing HS^- (Figure 5-1B and Figure 5-1C). The current density associated with peak II in Figure 5-1B and Figure 5-1C decreased and increased, respectively upon subsequent anodic sweeps and were observed to be of the same value after the 5th scan in both the cases.

With increasing concentration of HS^-, the anodic current peaks (Peak III and Peak III') observed at -0.72 V and -0.67 V were found to decrease in peak current in the case of 0.01 M HS^- containing solutions and completely disappear in the case of steel immersed in electrolytes containing 0.45 M HS^-. Additionally, in alkaline sulfide containing solutions, an anodic current peak (Peak IV) was observed to be present at -0.60 V and -0.63 V in Figure 5-1B and Figure 5-1C, respectively. As mentioned in Chapter 4, the potential sweep after peak III' (not shown in Figure 5-1A) in the anodic direction up to $E_{\lambda,a}$ was characterised by a constant anodic current of a relatively low value until 0.55 V, where the current was observed to rise sharply due to the oxygen evolution reaction. In sulfide containing electrolytes (Figure 5-1B and Figure 5-1C), the current response of the steel-solution interface due to polarisation above -0.40 V was significantly different from that observed in alkaline solutions without sulfide, and this will be discussed in the following paragraphs in detail.

In the case of the cathodic (or reverse) sweep from $E_{\lambda,a}$ to $E_{\lambda,c}$, the influence of sulfide on the current response of the system is much complex than those witnessed in sulfide free alkaline

solutions, as in Chapter 4 (and Figure 5-1A) and will be addressed in more detail in the following paragraphs and Figure 5-2B and Figure 5-2C. For data presented in Figure 5-1B and Figure 5-1C, i.e. the current response of the system for potentials lower than -0.4 V, three reduction peaks can be observed. In the case of solutions with 0.01 M HS^- (Figure 5-1B), two broad reduction peaks are observed at approximately -0.97 V and -1.06 V, and a distinct peak is observed at approximately -1.21 V, and upon subsequent cathodic sweeps the broad peaks cantered at -0.97 V and -1.06 V become more distinct. When the concentration of HS^- is 0.45 M in the electrolyte (Figure 5-1C), the cathodic sweep is characterised by three broad and convoluted peaks cantered at approximately -0.99 V, -1.08 V and -1.23 V. Another major difference observed between the current response of the steel in sulfide containing solutions and sulfide free solutions is the current density in the cathodic sweep at potentials < -1.25 V, being much lower in the former, suggesting a depressed release of hydrogen due to the breakdown of water. The nature and the position of these peaks are most probably related to the current response of the system at potentials > -0.40 V, and therefore are addressed later.

Based on the anodic current response of the mild steel in alkaline solutions containing 0.01 M and 0.45 M HS^-, the oxidation reactions occurring at the steel-solution interface can be postulated and the nature of the passive film can be determined. One of the major differences in the current response of steel in electrolytes with sulfide (Figure 5-1B and Figure 5-1C) and in sulfide free electrolytes (Figure 5-1A), is the disappearance or diminishing of anodic peaks III and III' in the former. As mentioned in Chapter 4 and indicated in Eq. 5.1, peaks III and III' are associated with the formation of FeOOH due to the oxidation of $Fe(OH)_2$. This indicates the tendency of Fe at the steel-solution interface to be in an oxidation state of 2+ (Fe^{2+}) in the presence of HS^- in alkaline solutions, rather than conventionally observed Fe^{3+} state. The lower current density of anodic peak III and III' in Figure 5-1B and its absence in Figure 5-1C suggest that the presence of HS^- in alkaline electrolytes inhibits the formation of FeOOH and its hydrated form $Fe(OH)_3$ or hydrated Fe (III) oxide ($Fe_2O_3 \cdot nH_2O$) on the surface of the steel – as is the case in alkaline solutions without HS^- - and due to its reducing nature instead forms a surface layer composed of Fe^{2+} species. Similar observations have been made by several authors [268–271]. Based on the observation on peaks III and III', it is highly likely that occurrence of peak I at more negative potentials with increasing [HS^-] is due to the competitive adsorption of OH^- and HS^- species on the steel surface. Shoesmith et al. [268] also concluded that the formation of Fe^{2+} species instead of Fe^{3+} oxide species indicate the adsorption of HS^-, in addition to OH^-, on the steel surface. They also associated this phenomenon to the lower current density observed in the cathodic current density at potential values where hydrogen is

released from the water, during the cathodic sweep [268]. Another possible reason for the shift of peak I to more negative potentials could be the increase in the ionic strength of the electrolyte [272] with increasing [HS^-].

In the case of the broad anodic peak II, subsequent anodic sweep led to a decrease and increase in the current density and the peak potential, respectively when the concentration of HS^- in the electrolyte was 0.01 M. However, when the concentration of HS^- in the electrolyte was 0.45 M, both the current density and the peak potential were observed to increase upon subsequent anodic sweeps. As the anodic peak II in Figure 5-1B and Figure 5-1C is observed to form at the same potential of -0.89 V in the first anodic scan as that seen in sulfide free electrolytes (Figure 5-1A), it is most likely that the it is characteristic of the formation of $Fe(OH)_2$ species on the steel surface. Additionally, the stabilisation of the peak current and the peak potential after the 5th scan in both Figure 5-1B and Figure 5-1C (with dissimilar concentrations of [HS^-]) to very similar values suggests that the occurrence of peak II is only related to the OH^- species in the electrolyte. Similar to the reaction route observed in sulfide free solutions described in Chapter 4, peaks I and II in the case of sulfide containing alkaline solutions can possibly be described as (Eq. 5.2 – 5.7):

$$Fe + OH^- = [Fe(OH)]_{ads} + e^- \quad \text{(Eq. 5.2)}$$

$$[Fe(OH)]_{ads} = [Fe(OH)]^+_{ads} + e^- \quad \text{(Eq. 5.3)}$$

$$Fe + HS^- = [Fe(HS)]_{ads} + e^- \quad \text{(Eq. 5.4)}$$

$$[Fe(HS)]_{ads} = [Fe(HS)]^+_{ads} + e^- \quad \text{(Eq. 5.5)}$$

$$[Fe(OH)]^+_{ads} + 2OH^- = HFeO_2^- + H_2O \quad \text{(Eq. 5.6)}$$

$$HFeO_2^- + H_2O = \{Fe(OH)_2\} + OH^- \quad \text{(Eq. 5.7)}$$

The reactions occurring at peak I can be described by Eq. 5.2 – 5.5, where the competitive adsorption of OH^- and HS^- on the steel surface forming an adsorbed layer of $Fe[OH]^+_{ads}$ and $Fe[HS]^+_{ads}$ due to a double electron transfer process is most likely. Based on the evolution of current density w.r.t to the anodic sweep, it can be assumed that the amount of $Fe[HS]^+_{ads}$ and $Fe[OH]^+_{ads}$ adsorbed on the surface are dependent on the concentration of HS^- in the electrolyte solution. Upon increasing the concentration of HS^- in the electrolyte from 0.01 M to 0.45 M, the current density at peak I was observed to slightly decrease, possibly due to an increased likelihood of $Fe[HS]^+_{ads}$ adsorbing on the surface. Similar observations have been described by

various authors [268,271], where the adsorption of $Fe[HS]^{+}_{ads}$ is favoured more than $Fe[OH]^{+}_{ads}$ with increasing concentrations of HS^-. Therefore, it can be postulated that when the $[HS^-]/[OH^-]$ ratio increases, the amounts of $Fe[HS]^{+}_{ads}$ adsorbed on the surface increased with respect to $Fe[OH]^{+}_{ads}$. This is also confirmed by the current density at peak I observed for cyclic voltammograms obtained for electrolyte with 1.12 M OH^- + 0.01 M HS^-, and 1.36 M OH^- and 0.01 M HS^- (provided in the Chapter 8, Section 8.2). As mentioned earlier and in Chapter 4, peak II is primarily related to the $[OH^-]$ in the electrolyte, and therefore can be attributed to adsorbed $Fe[OH]^{+}_{ads}$ species to $Fe(OH)_2$ (as indicated by Eq. 5.5 – 5.7) irrespective of whether the alkaline solution contains HS^- or not (Figure 5-1A, B and C).

There has been a constant debate in the literature about the designation of peaks I and II and several authors have indicated the peaks I and II correspond to the formation of $Fe(OH)_2$ and Fe_3O_4 [200,237,268,269,271], respectively. However, as seen in Figure 5-1B and Figure 5-1C, the current density at peaks I depend on the concentration of HS^- (and also $[OH^-]$, for a given concentration of HS^-), whereas the current density at peak II depends on OH^-, and also independent of the concentration of HS^- upon subsequent anodic sweeps. Therefore, it is reasonable to assume that peak I corresponds to the competitive adsorption of HS^- and OH^- on the steel surface, and peak II corresponds to the formation of $Fe(OH)_2$ via the formation of $HFeO_2^-$ in these alkaline solutions. In addition, it is highly unlikely that at such alkalinity, the dehydroxylation of $Fe(OH)_2$ to yield Fe_3O_4 would occur.

As mentioned earlier, the anodic peak III and III' diminishes and disappears with increasing HS^- in the electrolyte due to the highly reducing nature of HS^-. In the case of alkaline solutions without electrolyte (Figure 5-1A), peak III is associated with the formation of FeOOH and peak III' is associated with the hydration of FeOOH ($Fe(OH)_3$) or the formation of a hydrated Fe_2O_3 ($Fe_2O_3{\cdot}nH_2O$), and the amount of Fe^{3+} species formed increases with increasing $[OH^-]$ in the electrolyte (discussed in detail in Chapter 4). In the case of electrolytes containing 0.01 M HS^- (Figure 5-1B), a smaller current density is recorded at -0.72 V and -0.67 V when compared to Figure 5-1A, and like sulfide free electrolytes, the current density of peaks III and III' in electrolytes with 0.01 M HS^- was observed to increase with increasing $[OH^-]$ in the solution (shown in Chapter 8). Therefore, peak III and III' in Figure 5-1B can be described by the same reaction described by Eq. 5.8 – 5.10 (same reactions as Eq. 4.5 – 4.7 in Chapter 4):

$$\{Fe(OH)_2\} + OH^- = [FeOOH]_{ads} + H_2O + e^- \quad \text{(Eq. 5.8)}$$

$$2[FeOOH]_{ads} = \{Fe_2O_3 \cdot H_2O\} \quad \text{(Eq. 5.9)}$$

$$[FeOOH]_{ads} + H_2O = \{FeOOH \cdot H_2O\} \quad \text{(Eq. 5.10)}$$

In the case of the relatively broad anodic current peak IV observed in Figure 5-1B and Figure 5-1C, the current density is observed to increase with increasing [HS^-] in the electrolyte, however did not change with the alkalinity of the electrolyte (Chapter 8), indicating that its occurrence was related to the HS^- in the electrolyte. This peak could possibly be related to the formation of an Fe-S complex on the steel surface and the following reaction route (Eq. 5.11 and Eq. 5.12) could be proposed [268,271]:

$$[Fe(HS)]^+_{ads} + HS^- = \{Fe(HS)_2\}_{ads} \quad \text{(Eq. 5.11)}$$

$$Fe(HS)_{2\,ads} + OH^- = \{FeS\ complex\} + H_2O + e^- \quad \text{(Eq. 5.12)}$$

Based on Eq. 5.11 and Eq. 5.12, it could be postulated that the adsorbed $[Fe(HS)]^+_{ads}$ reacts with the HS^- in the electrolyte to form an adsorbed layer of $[Fe(HS)_2]_{ads}$ [268] which then reacts with the OH^- in the electrolyte resulting in an Fe-S complex [271], which could transform upon polarisation. Contrary to the reaction route proposed here for anodic peak IV, Tromans [273] suggested that the surface film formed on mild steel in hot alkaline solutions containing sulfide was composed of complex γ-Fe_3O_4 with sulfide substituting for the oxygen in the lattice (γ-$Fe_3O_{4-x}S_x$). Shoesmith et al. [268], on the other hand, proposed the formation of an iron oxide film (attributed to peak I in their study), irrespective of the concentration of HS^- in the electrolyte, and attributed the occurrence of peak IV to the oxidation of HS^- to elemental sulfur and the deposition of the latter. Similar conclusions about the deposition of elemental sulfur have been proposed earlier without conclusive evidence [274]. Shoesmith et al. [268] claimed that the growth of iron sulfide (mackinawite) species occurs at more anodic potentials (in comparison to peak IV) and at defect sites in the iron oxide film formed, leading to pitting corrosion [268,275]. However, the oxidation of HS^- to elemental S involves the release of H^+, which would decrease the pH of the electrolyte. In this study, the pH of the electrolyte before and after the occurrence of peak IV was maintained at 13.85, and therefore it is highly unlikely that the peak can be attributed to the oxidation of HS^- to elemental S and the deposition of the latter on the surface. Therefore, in the case of electrolyte containing 0.01 M HS^-, the identification that peak IV represents the formation of a Fe-S complex on a FeOOH film could probably be assumed. However, when the concentration of HS^- is 0.45 M, peak IV denotes that the surface of the steel is essentially an Fe-S complex on a relatively less stable $Fe(OH)_2$ film, and the oxidation of Fe to the 3+ state is not possible. Upon increasing the [HS^-] from 0.01 M

to 0.45 M, the position of the anodic peak IV was observed at lower potential values of -0.63 V (Figure 5-1C) instead of at -0.60 V (Figure 5-1B) probably due to higher availability of HS^- at the steel-solution interface for solutions containing 0.45 M HS^- and the much higher polarisability of the HS^- when compared to OH^-, thereby displacing the OH^- from the steel-solution interface. A similar shift has been observed by Shoesmith et al. [268] when the electrolyte contained 0.50 M HS^-.

As mentioned earlier, upon moving from the $E_{\lambda,a}$ towards $E_{\lambda,c}$ in sulfide containing solutions, several broad cathodic current peaks were observed (as shown in Figure 5-1B and C) related to the reduction reactions occurring at steel-solution interface, and are much complex and convoluted than those observed in Figure 5-1A. Prior to attributing the cathodic peaks to reduction reactions (shown in Figure 5-1B and Figure 5-1C) it is however necessary to understand the anodic response of the steel-solution interface at potentials > -0.40 V in sulfide containing solutions and this is highlighted by the 1st cyclic voltammetry scan shown in Figure 5-2.

Figure 5-2 shows only the 1st cyclic voltammetry scan obtained for mid steel exposed to solutions with chemistries (A) 0.80 M OH^-, (B) 0.80 M OH^- + 0.01 M HS^- and (C) 0.80 M OH + 0.45 M HS^-. For the purpose of visibility, data from $E_{\lambda,c}$ (-1.50 V vs. Ag/AgCl) to -1.20 V have been removed in Figure 5-2. As mentioned earlier, one of the major differences between Figure 5-2A, B and C, is the current response of the steel-solution interface at potentials > -0.40 V. From Figure 5-2A, B and C, it can be clearly seen that at potentials between -0.40 V and -0.35 V, the anodic current density is much higher for solutions with a higher [HS^-] (~2.2 × 10^{-5} A/cm^2, ~7.7 × 10^{-5} A/cm^2, and ~1.9 × 10^{-4} A/cm^2 in the case of Figure 5-2A, B and C, respectively), thereby indicating a lower extent of passivation in sulfide containing solutions. The anodic sweep from -0.35 V towards $E_{\lambda,a}$ in Figure 5-2B and Figure 5-2C is characterised by a broad peak centred at potentials close to ~ -0.05 V and a sharp rise in the current density at ~ 0.30 V, occurring as shoulder at ~ 0.45 V with the anodic peak typical of oxygen evolution at 0.55 V. The absence of these peaks at Figure 5-2A, where the electrolyte did not contain any HS^-, indicates that they are primarily related to the presence of HS^- in the electrolyte solution. The anodic peaks at -0.05 V and the subsequent shoulder at 0.45 V are therefore, associated to the oxidation of soluble HS^- in the electrolyte, however, due to the complex nature of sulfide oxidation and the broad nature of these anodic current peaks, it is difficult to explicitly identify the reactions occurring at these anodic peaks.

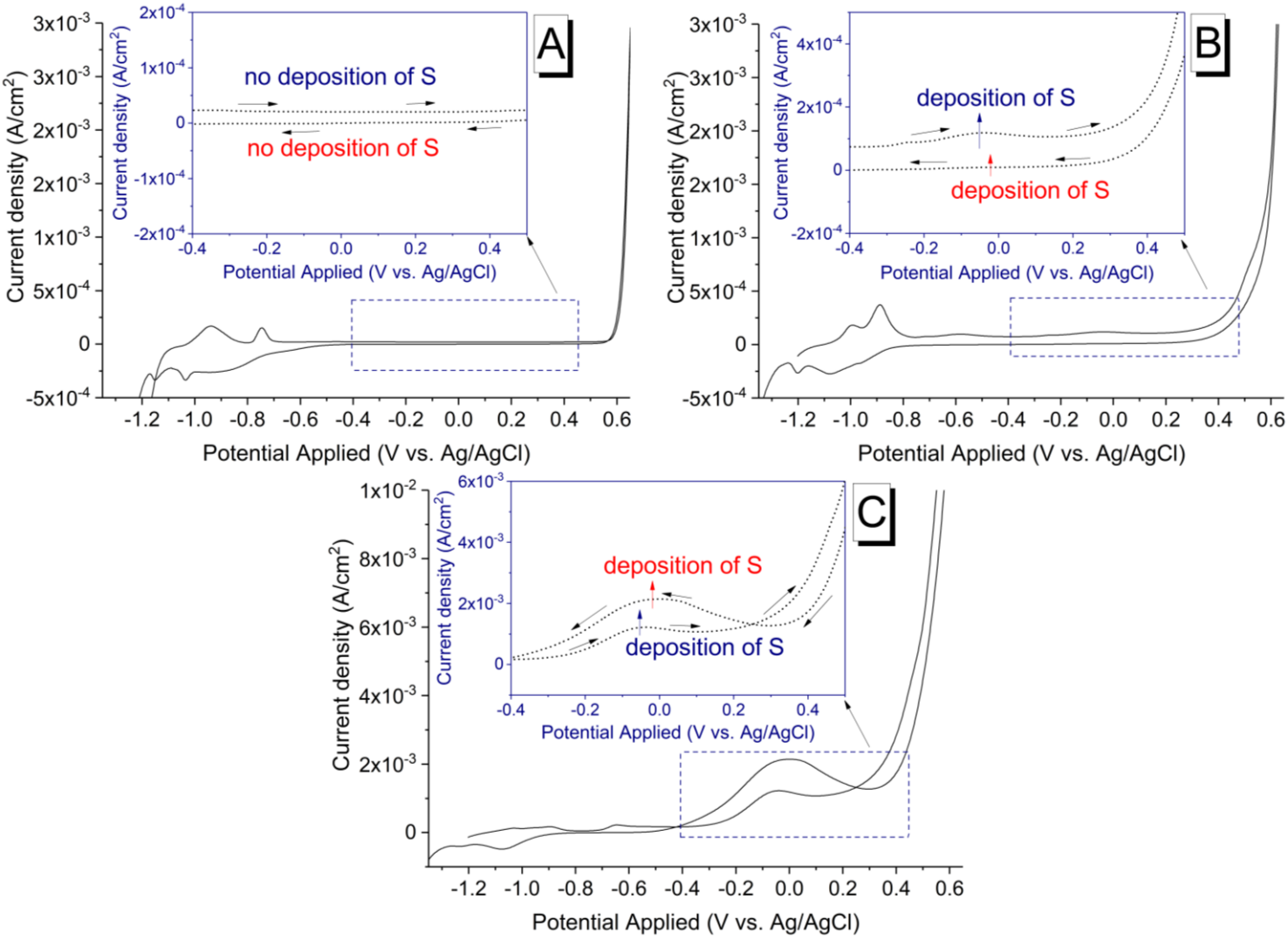

Figure 5-2: 1st scan obtained using cyclic voltammetry for mild steel exposed to (A) 0.80 M OH^-, (B) 0.80 M OH^- + 0.01 M HS^- and (C) 0.80 M OH + 0.45 M HS^-, highlighting the oxidation reactions associated with anodic peaks at -0.05 V and 0.45 V.

Based on the observations in Figure 5-2B and Figure 5-2C, several oxidation reactions could be assumed to be associated with anodic peaks at -0.05 V and 0.45 V and a plausible reaction route can be described (Eq. 5.13 – 5.17) [268,276,277]:

$$xHS^- = S_x^{2-} + xH^+ + (2x-2)e^- \quad \text{(Eq. 5.13)}$$

$$S_x^{2-} + 6OH^- = SO_3^{2-} + (x-1)S^0 + 3H_2O + 6e^- \quad \text{(Eq. 5.14)}$$

$$SO_3^{2-} + OH^- + HS^- = S_2O_3^{2-} + H_2O + 2e^- \quad \text{(Eq. 5.15)}$$

$$SO_3^{2-} + OH^- = SO_4^{2-} + 2e^- + H^+ \quad \text{(Eq. 5.16)}$$

$$S_2O_3^{2-} + OH^- + HS^- = SO_4^{2-} + H_2S + 2e^- \quad \text{(Eq. 5.17)}$$

The pH of the bulk solution dropped significantly from 13.85 to 12.97 upon moving in the anodic direction from -0.35 V towards $E_{\lambda,a}$, possibly due to the formation of hydrogen ions during the occurrence of anodic current peaks at -0.05 V and 0.45 V. The formation of hydrogen ions in the sulfide containing alkaline solutions, can therefore be likely associated with the conversion of HS^- to S_x^{2-}, as given by (Eq. 5.13) [268,278]. The polysulfide ions formed in the system are oxidised to SO_3^{2-} and elemental S (Eq. 5.14) [279,280]. Conversely, Chen and Morris [276] argued that the conversion of HS^- to elemental S and to polysulfide species occurs sequentially ($HS^- \rightarrow S^0 \rightarrow S_x^{2-}$) and due to slow rates of HS^- oxidation to elemental S in alkaline solutions with pH > 9, the formation of elemental S and polysulfide in these alkaline solutions is rather unlikely. However, Shoesmith et al. [268] showed that the current density and the potential of the anodic peak were dependent on the sweep rate and is most likely due to the deposition of a film [281], and in this case is due to the deposition of elemental sulfur on the steel surface. In alkaline solutions, Avrahami and Golding [280] observed that the oxidation of SO_3^{2-} to either thiosulfate ($S_2O_3^{2-}$) (Eq. 5.15) or sulfate (SO_4^{2-}) (Eq. 5.16) is almost instantaneous, and the therefore, the rate determining step is the oxidation of HS^- to SO_3^{2-}. Subsequent oxidation of $S_2O_3^{2-}$ to SO_4^{2-}, as described by Eq. 5.17, could also occur at potentials prior to oxygen evolution and would be characterised by the evolution of H_2S. Eq. 5.17 is primarily proposed due to observation of foul odour (due to the evolution of H_2S) particularly when the potential was increased from 0.40 V to 0.6 V.

Here it is important to note that the release of H^+ ions during the oxidation of HS^- (Eq. 5.13) in the electrolyte at the steel-solution interface possibly leads to the breakdown of the surface film formed due to the oxidation reactions (Eq. 5.2 – Eq. 5.12) discussed for the anodic peaks particularly in solutions where concentration of HS^- was 0.45 M. Another major difference in the cyclic voltammograms of steel immersed in sulfide containing (Figure 5-2B and Figure 5-2C) and sulfide free solutions (Figure 5-2A) is the current density associated with the evolution of oxygen at 0.55 V. The current density observed due to oxygen evolution is significantly higher in solutions containing sulfide than that in sulfide free solutions, and is proportional to the concentration of HS^- in the solution. This is probably due to oxidation of reduced sulfur species at the steel-solution interface and the removal of any deposited elemental S on the surface of the steel during the evolution of oxygen.

In sulfide containing solutions (Figure 5-2B and Figure 5-2C), the cathodic sweep from $E_{\lambda,a}$ towards $E_{\lambda,c}$ is characterised by an unusual current density peak at -0.02 V representing an oxidation reaction rather than the usual reduction reactions seen during the cathodic sweep (as seen in Chapter 4 and Figure 5-2A). The occurrence of this unusual oxidation peak is probably due to the oxidation of HS^- at the steel-solution interface as well as in the bulk solution. As seen from Figure 5-2B and Figure 5-2C, the occurrence of this peak is primarily influenced by the concentration of HS^- in the electrolyte. In addition, the pH of the bulk solution measured after the occurrence of this peak (particularly in Figure 5-2C) is around 12.4 (much lower than that observed during the anodic sweep), indicative of the release of H^+ ions in the electrolyte. Therefore, in the case of Figure 5-2C, the electrolyte solution is altered during the reverse cathodic sweep, and the cathodic current peaks observed in Figure 5-1C, cannot accurately be attributed to the corresponding oxidation reactions mentioned in Eq. 5.2 – 5.12. However, in the case of electrolytes containing 0.01 M HS^- (Figure 5-2B, and Figure 5-1B), where the current density of the unusual peak at -0.02 V is almost zero, the cathodic peaks seen in Figure 5-1B can be attributed the oxidation reactions occurring in the anodic sweep described for Figure 5-1B. Therefore, the cathodic peak observed in Figure 5-1B centred at -1.21 V corresponds to the reduction of the species formed at peak I (-1.00 V), the reduction peak at -1.06 V corresponds to the reduction of the species formed at peak II, III and III' (-0.89 V, 0.72 V and -0.67 V), and the broad cathodic peak at -0.97 V corresponds to the anodic product formed at -0.60 V.

Based on the above discussion, it is important to highlight that in the case of sulfide containing electrolytes and particularly those representing the pore solution of AAS, the composition of the surface of the steel can be determined only using the anodic response of the 1st scan in the cyclic voltammetry test, as the chemistry of the solution alters significantly upon the reverse cathodic sweep. Therefore, for steel immersed in simulated pore solutions representative of AAS, the high concentration of HS^- in the pore solution clearly alters the chemistry of the surface film, which in this case is primarily composed of Fe^{2+} species, with the inner layer being $Fe(OH)_2$ (that could potentially oxidise to a hydrated Fe^{3+} oxide if sufficient oxygen is available at later stages) and the outer layer being a Fe-S complex, possibly resembling disordered mackinawite.

5.3.1.2 Open circuit potential, linear polarisation resistance and anodic polarisation

Figure 5-3 shows the influence of varying concentrations of HS^- in an alkaline solution on the evolution of the OCP of mild steel over a period of 28 days. With an increase in the [HS^-] in the electrolyte solution, the OCP of mild was observed to decrease. In the case of sulfide free solution (0.80 M NaOH), the OCP was observed to be around -0.32 V at 0 days and was observed to increase to ~ -0.12 V after 12 days of immersion and stabilised around ~ -0.12 V. In solutions containing very low concentrations of HS^- (0.001 M), the OCP was found to be ~ -0.32 V, and stabilised at around ~ -0.22 V after 12 days. The OCP values obtained for solutions containing no HS^- and 0.001 M HS^- are indicative of the development of a passive film composed of layer of ferrous hydroxide ($Fe(OH)_2$) that could readily oxidise to form magnetite (Fe_3O_4), and an outer layer composed of $Fe(OH)_3$ or hydrated Fe (III) oxide ($Fe_2O_3 \cdot nH_2O$), as described above for Figure 5-1A.

In the case of steel immersed in solutions containing intermediate (0.01 M and 0.09 M) and high concentrations (0.45 M) of HS^-, the OCP was observed to be lower than < -0.40 V. As shown for PC-slag blends [255,258,282] and alkali-activated fly ash/slag blends [115,264], an increase in the amount of total reduced sulfur in the pore solution led to a significant decrease in the amount of dissolved oxygen in the electrolyte [255] and the OCP of the steel reinforcement. These observations from the literature have been confirmed by the findings of this study presented in Figure 5-3. The OCP of mild steel was observed to be around -0.44 V, -0.59 V and -0.71 V, when exposed to alkaline solutions containing 0.01 M, 0.09 M and 0.45 M HS^-, respectively, and much lower than those seen for solutions with no and 0.001 M HS^-. These observations are in line with Figure 5-1 and Figure 5-2, where the formation of a passive film based on iron oxides is retarded and inhibited due to the highly reducing nature of HS^-, and instead the precipitation of a Fe-S complex is promoted. In the case of solutions representing the pore solution of AAS (0.80 M OH^- + 0.45 M HS^-), the OCP was found to be very similar to those obtained by studies conducted in steel reinforced AAS mortars [265,283,284].

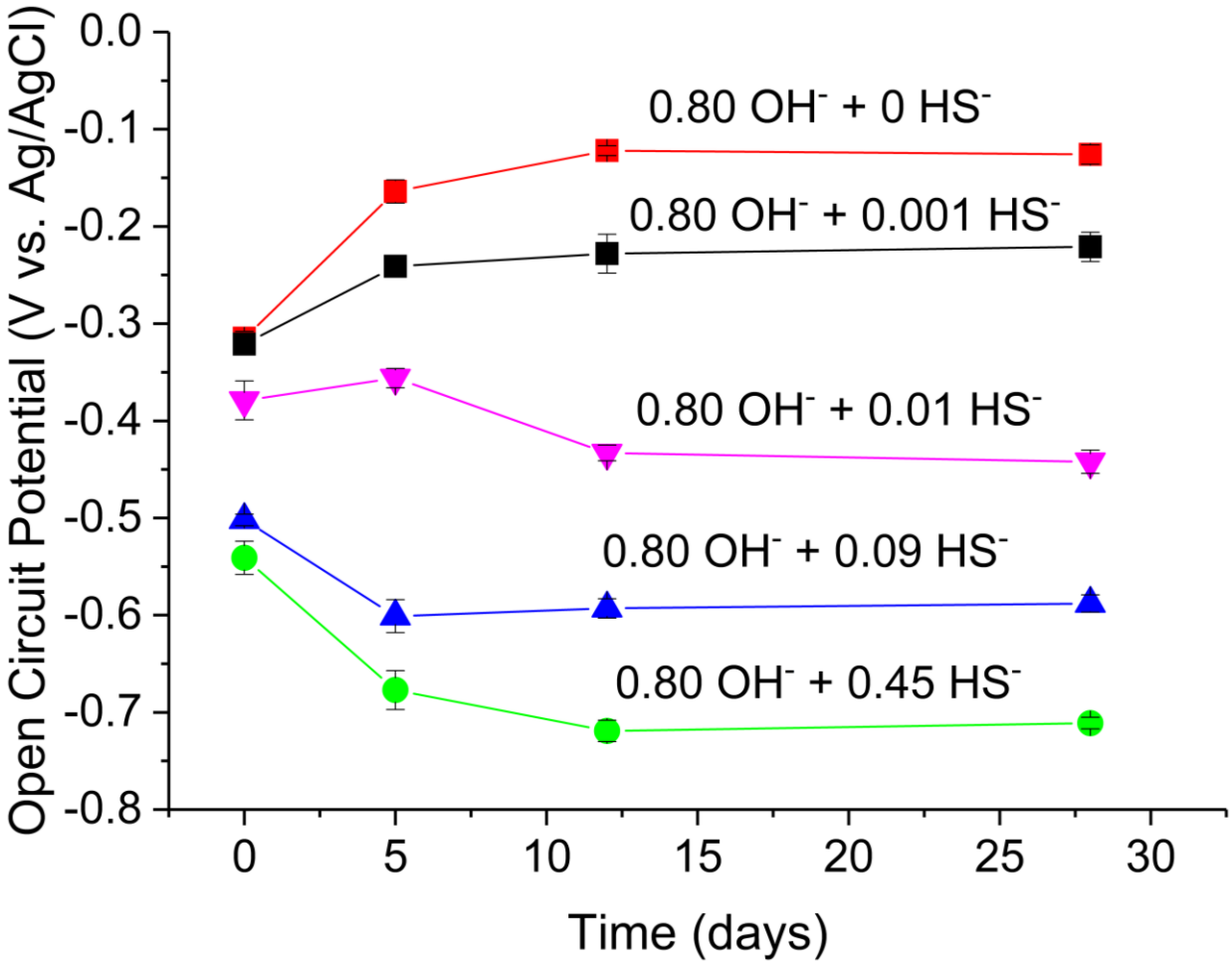

Figure 5-3: The evolution of the open circuit potential of steel immersed in alkaline solutions (0.80 M OH^-) with varying concentrations of HS^- (0 M, 0.001 M, 0.01 M, 0.09 M, 0.45 M) over a period of 28 days. The pH of the electrolytes was recorded using a digital pH meter (Oakton Acorn Series) and has been reported in Table 8-2.

Figure 5-4 shows the influence of sulfide in alkaline solutions on the resistance to polarisation (R_p) of mild steel, obtained using the LPR test method as described in Section 5.2. In solutions where the passive film on the steel surface is based on a complex assemblage of iron oxides, as is the case in solutions with no and 0.001 M HS^-, the resistance to polarisation is relatively stable between 45 and 60 $k\Omega \cdot cm^2$. As seen in Figure 5-4, in the case of solutions containing intermediate (0.01 M and 0.09 M) and high concentrations (0.45 M) of HS^-, the R_p values were observed to be significantly lower. In the case of solutions containing 0.09 M and 0.45 M HS^-, the R_p values stabilise after almost 5 days at around 4 $k\Omega \cdot cm^2$ and 2 $k\Omega \cdot cm^2$, respectively. It can be clearly seen from Figure 5-4, that the resistance to polarisation for mild steel in alkaline solutions decreases with an increase in the concentration of HS^- in the electrolyte. Based on the

modified Stern-Geary equation (described in Chapter 3) and using the value of B of 52 for steel in the passive state, the corrosion current density (i_{corr}) would be expected to increase with increasing [HS^-]. Similar results have been obtained by Scott and Alexander [255], where they observed higher corrosion current densities for steel reinforcements immersed in electrolytes containing reduced sulfur species (representative of PC-slag blends) compared to their counterparts (representative of plain PC). Criado and Provis [283] observed much lower R_p values for steel embedded in AAS mortars when compared to those in PC mortars.

The observation of a lower R_p for mild steel in sulfide containing alkaline solutions is also in line with the observations of the cyclic voltammetry results described in Section 5.3.1.1, where the current density was found to be much higher for steel exposed to electrolytes with HS^- when compared to those immersed in solutions without HS^-. However, the reason for such low R_p values in solutions with high [HS^-] could also be related to the aqueous chemistry of the electrolyte, and this will be revisited in detail a bit later.

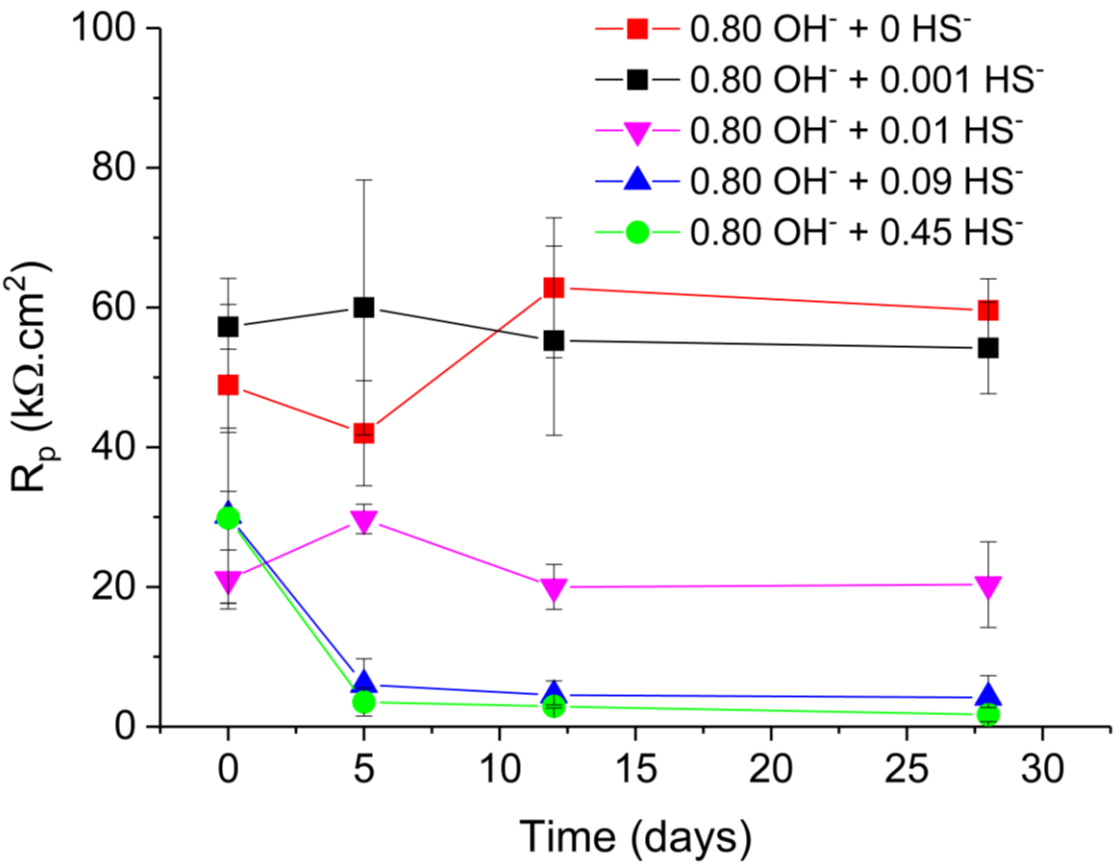

Figure 5-4: Resistance to polarisation (R_p) values obtained using the LPR test, for steel immersed in an alkaline solution (0.80 M OH^-) with varying concentrations of sulfide (0 M, 0.001 M, 0.01 M, 0.09 M, and 0.45 M) over a period of 28 days.

Figure 5-5 shows the influence of sulfide in alkaline solutions on the anodic behaviour of mild steel. As shown in Chapter 4, the anodic polarisation of mild steel in alkaline solutions without sulfide and with 0.001 M HS^- is characterised by a clear transition from the active to the passive and to the trans-passive regions (denoted by the red line in Figure 5-5). Upon an increase in the [HS^-] in the electrolyte, a clear reduction in the OCP and a significant increase in the current density can be observed. This observation is in line with the findings from Figure 5-3 and Figure 5-4. In addition, for solutions where [HS^-] ≥ 0.01 M, the active and the passive regions are unidentifiable, and instead, the polarisation of steel in the anodic direction (> OCP) resulted in a sharp rise in the current density until an anodic peak around -0.05 V was observed. Similar anodic polarisation curves characterised by high current densities were observed by Tromans for steel immersed in hot alkaline sulfide solutions [273] but no direct passivation was seen in these systems. The presence of the anodic peak at ~ -0.05 V and a subsequent drop in the current density at potentials > -0.05 V, confirm the deposition of S (in Figure 5-2B and Figure 5-2C) through the reaction pathway described in Eq. 5.13 and Eq. 5.14.

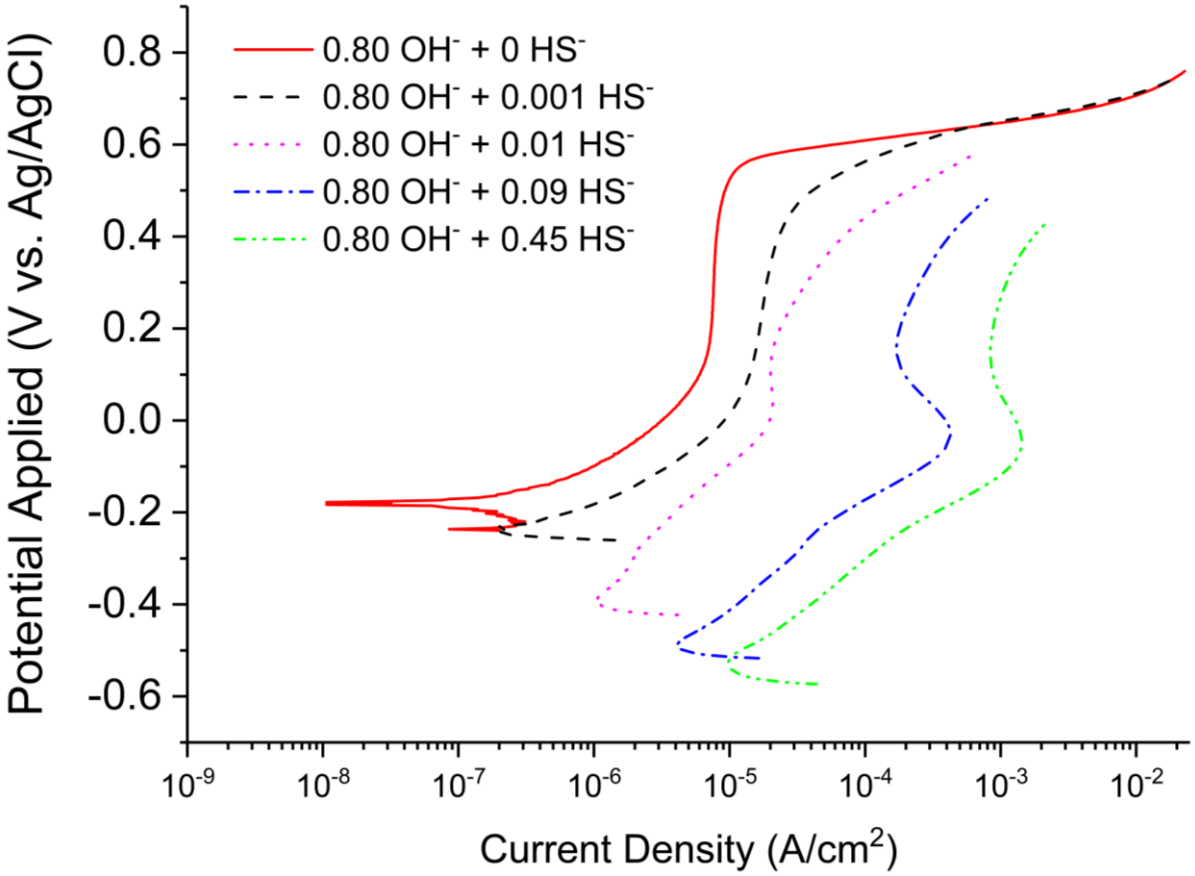

Figure 5-5: Influence of sulfide (0 M, 0.001 M, 0.01 M, 0.09 M, and 0.45 M HS^-) on the anodic polarisation behaviour of obtained mild steel immersed in an alkaline solution (0.80 M OH^-).

As mentioned in Chapter 2, passivation/corrosion is described by two half-cell reactions: a) the anodic dissolution or oxidation of Fe ($\rightarrow Fe^{2+}$/ Fe^{3+}), and b) the cathodic reduction of O_2 ($\rightarrow OH^-$), and the formation of a passive film/corrosion products depends on kinetics of both the half-cell reactions. In the case of steel in alkaline solutions without sulfide (as shown by the red line in Figure 5-5), the anodic polarisation of the steel specimen leads to the anodic dissolution of Fe, forming Fe^{2+}, when the potential is increased from the OCP to approximately 0.15 V (called the active region), and a region of constant current density indicative of the formation of an Fe^{3+} passive film between 0.15 V and 0.55 V (called the passive region). The strong similarities between the anodic polarisation of steel in solutions containing [HS^-] ≥ 0.01 M and the current response in the anodic sweep of the 1st cyclic voltammetry scan seen in Figure 5-2B and Figure 5-2C at potentials > -0.6 V, indicate that the increase in the current density in Figure 5-5 at potentials > OCP is primarily due to the oxidation of HS^- species within

the electrolyte (as discussed in Section 5.3.1.1). This suggests that the anode in these electrochemical systems is the HS^- present in the alkaline solutions that could readily oxidise due to an applied potential and not Fe, and hence explains the absence of Fe dissolution in the anodic polarisation curves. The HS^- being the anode in these electrochemical systems is of high significance when considering the formation of a macro-cell to initiate chloride-induced corrosion of the steel reinforcement, and has been addressed in detail later.

5.3.1.3 X-ray photoelectron spectroscopy

Figure 5-6, Figure 5-7, and Figure 5-8 show the chemistry of the steel surface when exposed to solutions containing 0.80 M OH^- + 0.01 M HS^-, 0.80 M OH^- + 0.09 M HS^-, 0.80 M OH^- + 0.45 M HS^- for 5, 12 and 28 days, through deconvoluted Fe $2p_{3/2}$ and S $2p$ spectra obtained using high-resolution XPS. Figure 5-6, Figure 5-7, and Figure 5-8 need to be looked in conjunction as they represent the exposure time scales of 5, 12 and 28 days respectively. When steel is exposed to solutions containing 0.80 M OH^- + 0.01 M HS^- for 5 days (Figure 5-6B), the S $2p$ spectra is characterised by numerous S $2p_{3/2}$ peaks representing $Fe^{2+}S$, $Fe^{2+}S/Fe^{3+}S$, $FeSO_3$ and FeS_2O_3 centred at ~160.98 eV, ~162 eV, ~164.6 eV and ~166.4 eV, respectively [267,285–288]. However, in the case of steel exposed to 0.80 M OH^- + 0.09 M HS^- and 0.80 M OH^- + 0.45 M HS^- (Figure 5-6D and Figure 5-6F), the S $2p$ spectra exhibits S $2p_{3/2}$ peaks centred at ~160.98 eV and ~162 eV indicating the presence of only $Fe^{2+}S$, and $Fe^{2+}S/Fe^{3+}S$ species on the surface of the steel [267,285–288]. This observation is in line with fact that an increase in the HS^- concentration creates a highly reducing environment (Figure 5-3) around the steel surface and due to the extremely low amount of dissolved oxygen at the steel-solution interface [255], the presence of any oxidised sulfur species is not observed. Purely based on comparing the intensities of the S $2p_{3/2}$ peaks associated with $Fe^{2+}S$ and $Fe^{2+}S/Fe^{3+}S$ in Figure 5-6B, D and F, one can clearly see that the formation of $Fe^{2+}S$ is much preferred with an increase in the HS^- concentration in the electrolyte. This confirms the hypothesis made earlier from the cyclic voltammograms (presented in Figure 5-1), where the formation of any oxygen containing Fe species was proposed to be heavily suppressed by the high concentrations of HS^- at the steel-solution interface and instead the formation of a Fe-S complex was much likely. The formation of $Fe^{2+}S/Fe^{3+}S$ in solutions containing 0.09 M and 0.45 M HS^- could possibly be due to the oxidation of $Fe^{2+}S$ species during experimentation [267,285–288].

Upon an increase in the exposure time to 12 days and 28 days, negligible or almost no changes were observed in the S $2p_{3/2}$ peaks for each of the exposure solutions and $Fe^{2+}S$ was found to be stable throughout the duration of exposure in solutions containing 0.09 M and 0.45

M HS^-. Holloway and Sykes [265] suggested that the oxidation of HS^- to elemental sulfur could be possible in AAS and its precipitation on the passive film play a major role in inhibiting pitting corrosion. However, Figure 5-6F, Figure 5-7F, and Figure 5-8F, provides irrefutable evidence that the surface film formed on steel exposed to simulated pore solutions of AAS (0.80 M OH^- + 0.45 M HS^-) contained sulfur only in the form of Fe-S complexes and the deposition of elemental sulfur was not observed. This observation is supported by the cyclic voltammograms (Figure 5-2C) and the anodic polarisation curves (Figure 5-5), where the deposition of sulfur occurs at around -0.05 V vs. Ag/AgCl and not when the OCP of steel is between -0.40 and -0.70 V.

The deconvolution of the Fe $2p_{3/2}$ (as shown in Figure 5-6A, C, E; Figure 5-7A, C, E; and Figure 5-8A, C, E) yielded in the observation of several peaks characteristic of Fe^0, $Fe^{2+}S/Fe^{3+}S$ species and FeOOH species for all exposure solutions and for all durations of exposure [267,285–288]. The deconvolution of the Fe $2p_{3/2}$ peak was much more complex primarily due to the broad nature of the Fe $2p_{3/2}$ and the very large background observed in these energy ranges. Based on the analysis of the S $2p_{3/2}$ peaks observed in all electrolytes and the OCP values observed in Figure 5-3, the precipitation of FeOOH species in these electrolytes is highly unlikely and the occurrence of Fe $2p_{3/2}$ associated to FeOOH species is primarily related to the oxidation of $Fe(OH)_2$ species during experimentation, and therefore the hypothesis of the inner layer of the surface film being comprised of $Fe(OH)_2$ is confirmed. Similar to the observations made by the S $2p_{3/2}$, Figure 5-6A, C, E; Figure 5-7A, C, E; and Figure 5-8A, C, E, clearly shows that on increasing the concentration of HS^- in the exposure solution results in the precipitation of a stable Fe-S species on the steel surface.

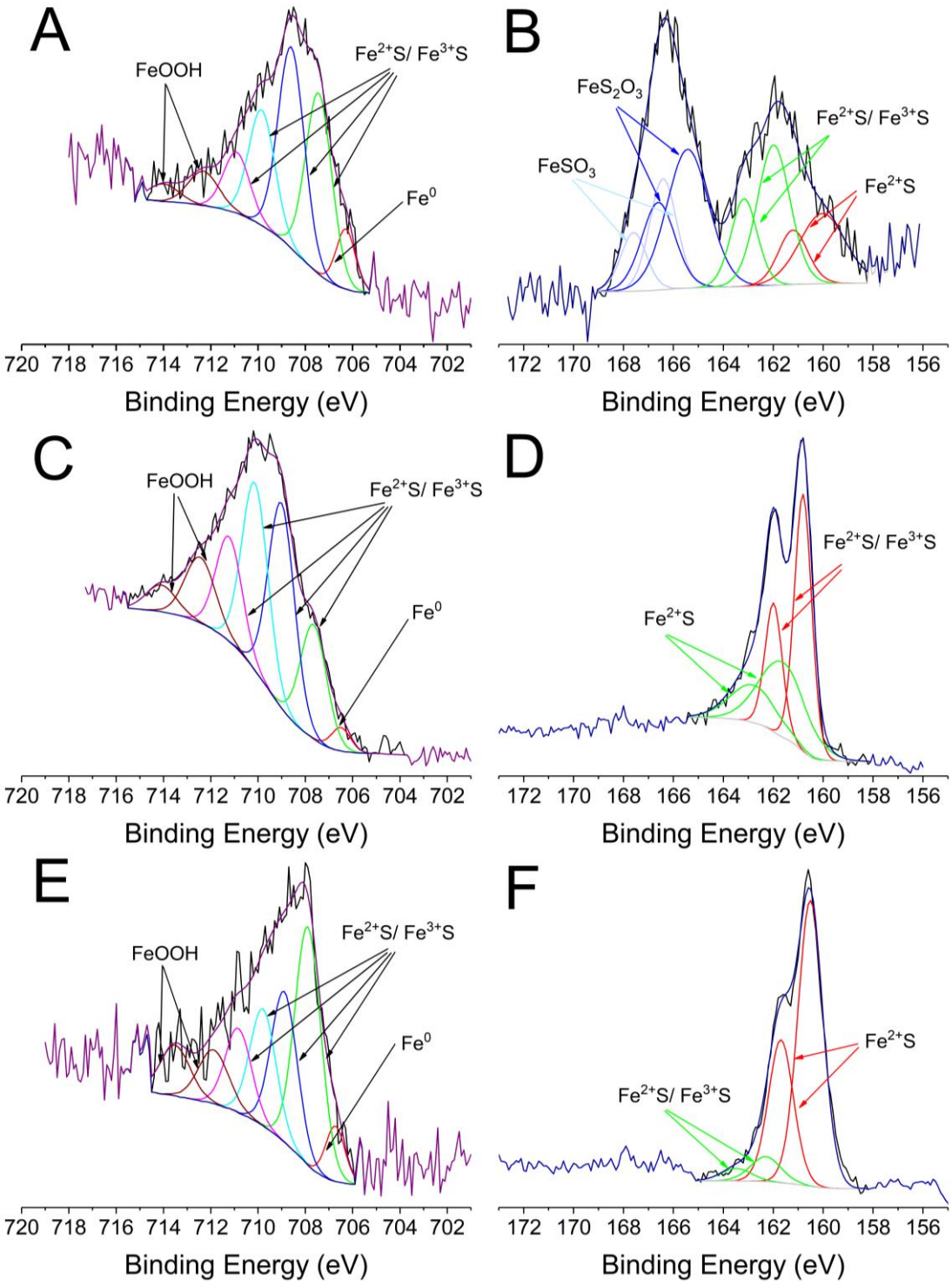

Figure 5-6: Fe $2p_{3/2}$ and S $2p$ spectra obtained using XPS on steel specimens exposed to alkaline solutions with varying concentrations of HS^- for 5 days. (A) and (B), show the Fe $2p_{3/2}$ and S $2p$ spectra, respectively for steel immersed in 0.80 M OH^- + 0.01 M HS^-, (C) and (D) show the Fe $2p_{3/2}$ and S $2p$ spectra, respectively for steel immersed in 0.80 M OH^- + 0.09 M HS^-, and (E) and (F) show the Fe $2p_{3/2}$ and S $2p$ spectra, respectively, for steel immersed in 0.80 M OH^- + 0.45 M HS^-.

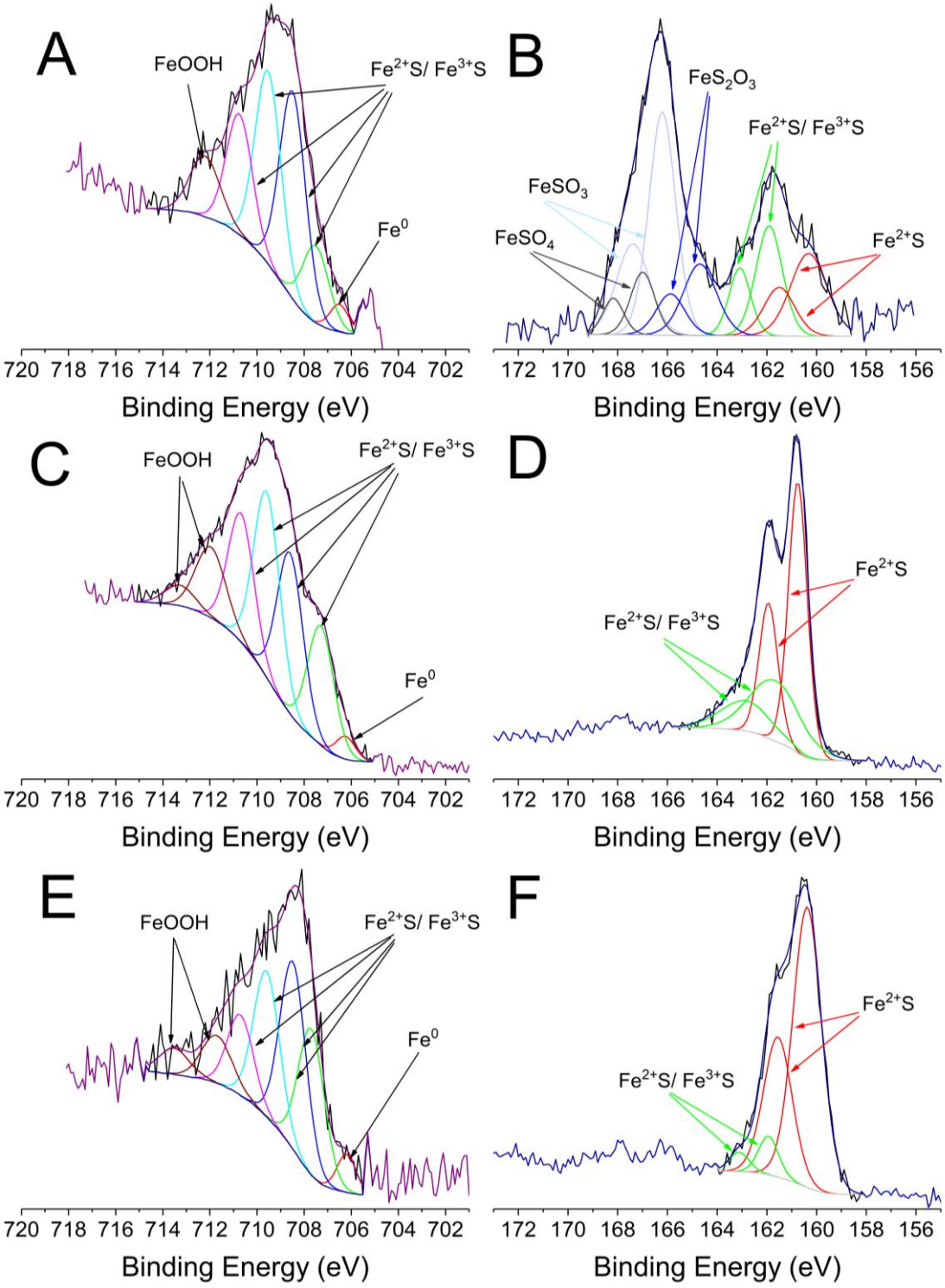

Figure 5-7: Fe $2p_{3/2}$ and S $2p$ spectra obtained using XPS on steel specimens exposed to alkaline solutions with varying concentrations of HS^- for 12 days. (A) and (B), show the Fe $2p_{3/2}$ and S $2p$ spectra, respectively for steel immersed in 0.80 M OH^- + 0.01 M HS^-, (C) and (D) show the Fe $2p_{3/2}$ and S $2p$ spectra, respectively for steel immersed in 0.80 M OH^- + 0.09

M HS^-, and (E) and (F) show the Fe $2p_{3/2}$ and S 2*p* spectra, respectively, for steel immersed in 0.80 M OH^- + 0.45 M HS^-.

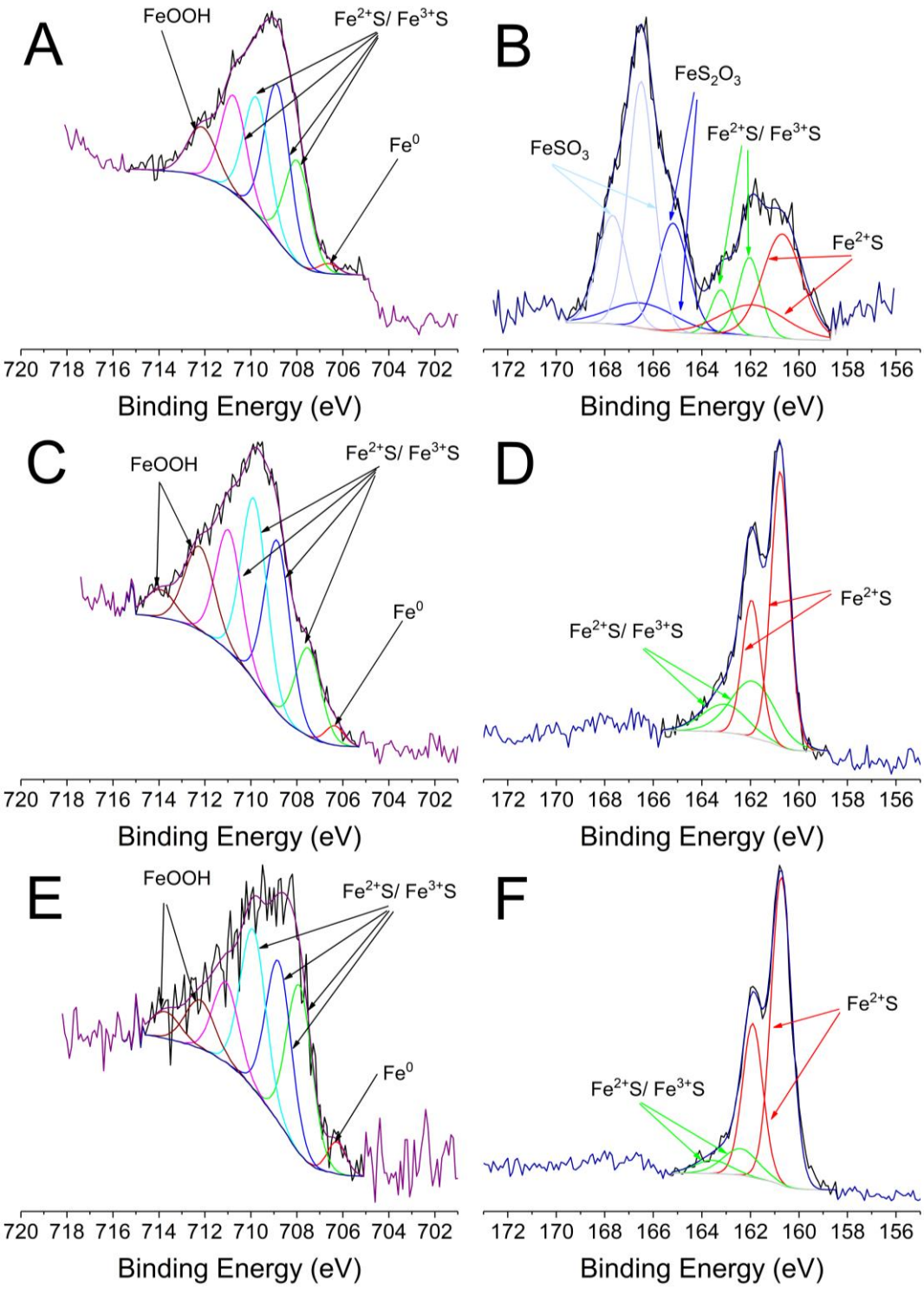

Figure 5-8: Fe $2p_{3/2}$ and S 2*p* spectra obtained using XPS on steel specimens exposed to alkaline solutions with varying concentrations of HS^- for 28 days. (A) and (B), show the Fe

$2p_{3/2}$ and S 2*p* spectra, respectively for steel immersed in 0.80 M OH^- + 0.01 M HS^-, (C) and (D) show the Fe $2p_{3/2}$ and S 2*p* spectra, respectively for steel immersed in 0.80 M OH^- + 0.09 M HS^-, and (E) and (F) show the Fe $2p_{3/2}$ and S 2*p* spectra, respectively, for steel immersed in 0.80 M OH^- + 0.45 M HS^-.

5.3.2 Depassivation

Based on the OCP and R_p of mild steel exposed to alkaline solutions containing sulfide (as shown in Figure 5-3 and Figure 5-4), one would likely interpret the data based on the guidelines by ASTM C876-15 [181] and recommendations by [183,213], and come to the conclusion that the increase in the HS^- concentration in the electrolyte leads to an increased susceptibility (of the steel) to chloride-induced corrosion. However, it must be considered that these guidelines [181,183,213] are based particularly for PC based concretes and mortars, and more importantly are applicable when the electrochemical system does not contain any additional redox active species other than Fe^{2+}. It is therefore very important to consider the influence of an additional redox active species (HS^-) in the electrochemical system on the onset of chloride-induced corrosion (commonly described by the chloride threshold value), and this has been addressed in detail in the following sections. As mentioned in Section 5.2, the influence of HS^- and exposure time on the chloride threshold value was investigated by exposing mild steel specimens to alkaline solutions (0.80 M OH^-) with varying concentrations of HS^- (0.001 M, 0.01 M, 0.09 M and 0.45 M HS^-) for 0, 5, 12 and 28 days, prior to electrochemical testing in a vacuum desiccator to avoid any interaction with air. After specific durations of exposure, electrochemical tests (OCP, LPR, anodic polarisation) were carried out on the steel specimens in freshly prepared electrolytes with the same composition of the exposure solution and varying chloride concentrations.

Table 5-3 shows the chloride threshold values of mild steel exposed to alkaline sulfide containing solutions for various timescales. As in Chapter 4, the chloride threshold values were considered to be the concentration of chloride in the electrolyte that causes a sudden rise in the current density upon the anodic polarisation of mild steel from OCP to 1.00 V vs. OCP. As seen from Table 5-3, the chloride threshold values for mild steel are dependent on the time of exposure as well as the $[HS^-]$ in the exposure solution. In the case of mild steel being exposed to electrolytes containing 0.80 OH^- + 0.001 M HS^-, the chloride threshold value (in terms of the molar ratio $[Cl^-]/[OH^-]$) was observed to increase significantly from 0.70 at 0 days to values

> 3.50 (the maximum $[Cl^-]/[OH^-]$ in the electrolyte considered in this study) with an increase in the duration of exposure. When the steel was exposed to electrolytes containing intermediate concentrations of HS^- (0.01 M and 0.09 M), the chloride threshold values were found to vary as a function of time, and no apparent relationship between exposure time and chloride threshold value was observed. Interestingly and surprisingly, chloride-induced corrosion or pitting was not observed on mild steels exposed to electrolytes contained 0.45 M HS^- with $[Cl^-]/[OH^-]$ as high as 4, and the exposure time had no influence on the chloride threshold value. These observations are not in line with the OCP and R_p values (shown in Figure 5-3 and Figure 5-4) for steel in solutions containing 0.01 M, 0.09 M and 0.45 M HS^- without chloride, as conventionally a lower OCP and R_p would indicate a higher susceptibility to corrosion.

Table 5-3: Influence of $[HS^-]$ and exposure time on the chloride 'threshold' value of mild steel determined using anodic polarisation. The chloride threshold values are represented as the molar ratio $[Cl^-]/[OH^-]$. Cases where chloride-induced corrosion was not observed for electrolytes with $[Cl^-]/[OH^-] = 3.5$ have been classified as 'No Pitting'.

Exposure time	**0.80 M OH^- + 0.001 M HS^-**	**0.80 M OH^- + 0.01 M HS^-**	**1.12 M OH^- + 0.01 M HS^-**	**1.36 M OH^- + 0.01 M HS^-**	**0.80 M OH^- + 0.09 M HS^-**	**0.80 M OH^- + 0.45 M HS^-**
0 days	0.7	2.5	2.7	2.8	3.1	No Pitting
5 days	No Pitting	3	2.9	3.1	3	No Pitting
12 days	No Pitting	2.8	2.3	2.8	3	No Pitting
28 days	No Pitting	2	2.2	2.6	3.2	No Pitting

Figure 5-9 shows the OCP of mild steel as a function of the HS^-, OH^-, Cl^- in the electrolyte and the time of exposure. In line with observations from Figure 5-3, the OCP was observed to decrease with an increase in the $[HS^-]/[OH^-]$, primarily because of the reducing nature of HS^-. However, the influence of Cl^- on the OCP, as is commonly seen in alkaline solutions, was not observed in sulfide containing alkaline solutions. In electrolytes containing 0.45 M HS^-, OCP measurements were found to be fairly constant in the range of -0.537 to -0.706 V, -0.546 to -0.700 V, and -0.562 to -0.635 V, for solutions with 0.80 M, 1.12 M and 1.36 M OH^- (for all chloride concentrations and exposure times), respectively. Similarly, in the case of electrolytes

with 0.01 M HS^-, the OCP of mild steel was found to be fairly constant in the range of -0.396 to -0.504 V, -0.454 to -0.613 V, and -0.478 to -0.527 V, for solutions with 0.80 M, 1.12 M and 1.36 M OH^- solutions (for all chloride concentrations and exposure times), respectively. In the case of solutions with 0.80 M OH^- + 0.09 M HS^-, the OCP ranged between -0.536 and -0.624 V. All the OCP values mentioned in the above text are very similar to those observed for steel immersed in solutions without chloride, as shown in Figure 5-3, indicating that unlike the behaviour of steel in alkaline sulfide free solutions (as seen in Chapter 4) where the OCP was observed to exhibit a sudden decrease upon the chloride concentration in the electrolyte reaching a threshold value, the chloride concentration in sulfide containing alkaline solutions (as shown in Figure 5-9) has negligible influence on the OCP. This is particularly clear from the very similar OCP values of steel that exhibit chloride-induced pitting and are passive when the [HS^-] in the electrolytes were 0.01 M and 0.09 M (shown by the transparent red region in Figure 5-9). Similar to observations made in Table 5-3, chloride-induced pitting was observed mostly in electrolytes with molar ratios [HS^-]/[OH^-] in the range of 0.007 and 0.1125, representing solutions with the compositions with 0.80 M + 0.01 M HS^-, 1.12 M + 0.01 M HS^-, 1.36 M OH^- + 0.01 M HS^-, and 0.80 M OH^- + 0.09 M HS^-, and therefore [HS^-]/[OH^-] in the range of 0.007 and 0.1125 has been denoted as the region where the probability of steel undergoing chloride-induced pitting is highest among all the electrolytes considered in this study.

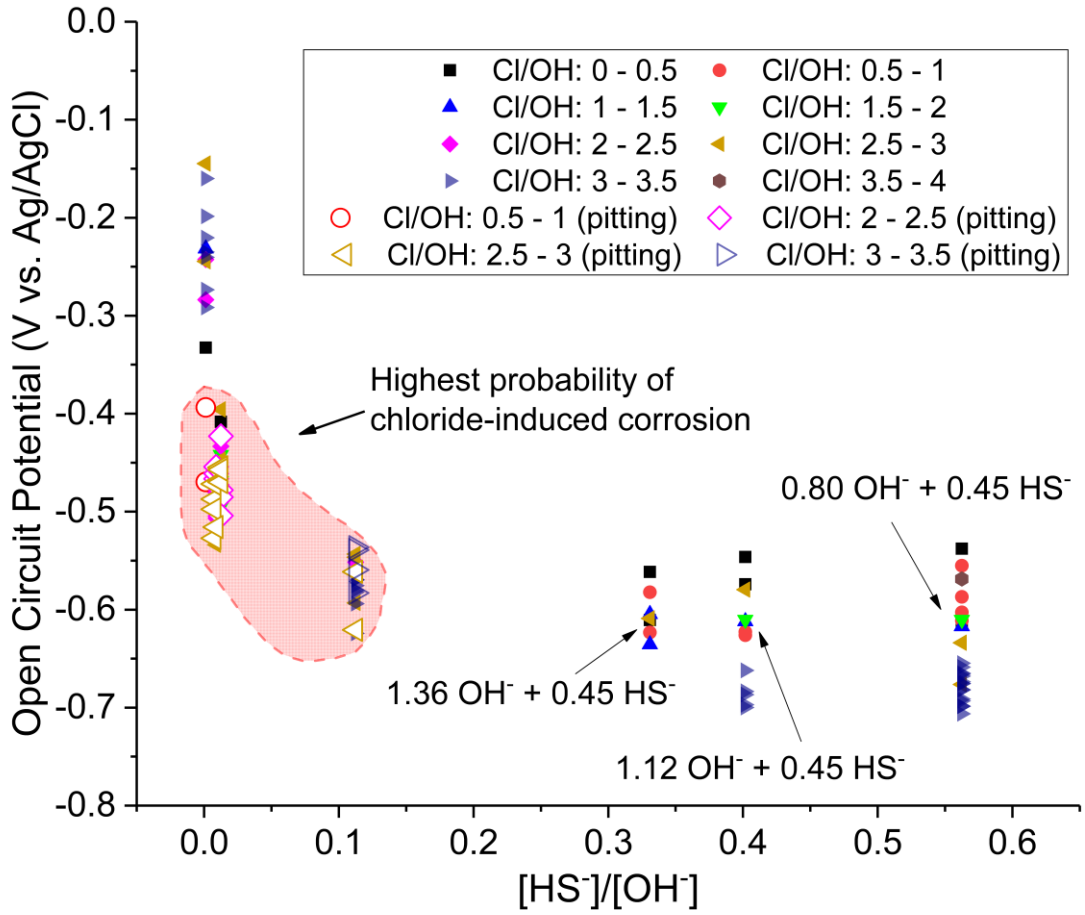

Figure 5-9: OCP of mild steel exposed to highly alkaline solutions (0.80 M, 1.12 M and 1.36 M OH^-), with varying concentrations of HS^- (0.001 M, 0.01 M, 0.09 M and 0.45 M) and Cl^- (0 - 4 in terms of $[Cl^-]/[OH^-]$), after 0, 5, 12 and 28 days exposure. The solid symbols denote the steel exhibiting no corrosion, whereas the hollow symbols indicate the steel undergoing stable/metastable chloride-induced pitting. The transparent red shaded area indicates the region in terms of $[HS^-]/[OH^-]$, where the susceptibility to chloride-induced corrosion is highest. This region should not be associated with the OCP data on the y-axis as no apparent correlation between the steel in the passive state or actively corroding and the OCP was observed in sulfide containing solutions.

Figure 5-10 shows the variation of R_p as a function of HS^-, OH^-, Cl^- in the electrolyte and the time of exposure. Similar to the observations of OCP in Figure 5-9, the resistance to polarisation of the steel in alkaline sulfide solutions was found to be scattered irrespective of the concentrations of HS^-, OH^-, Cl^- and duration of exposure and an apparent correlation between the different variables was not observed. Unlike the findings in Chapter 4 (in alkaline

sulfide free solutions), the R_p values did not exhibit a sudden drop when the chloride concentration in the electrolyte reach a threshold concentration.

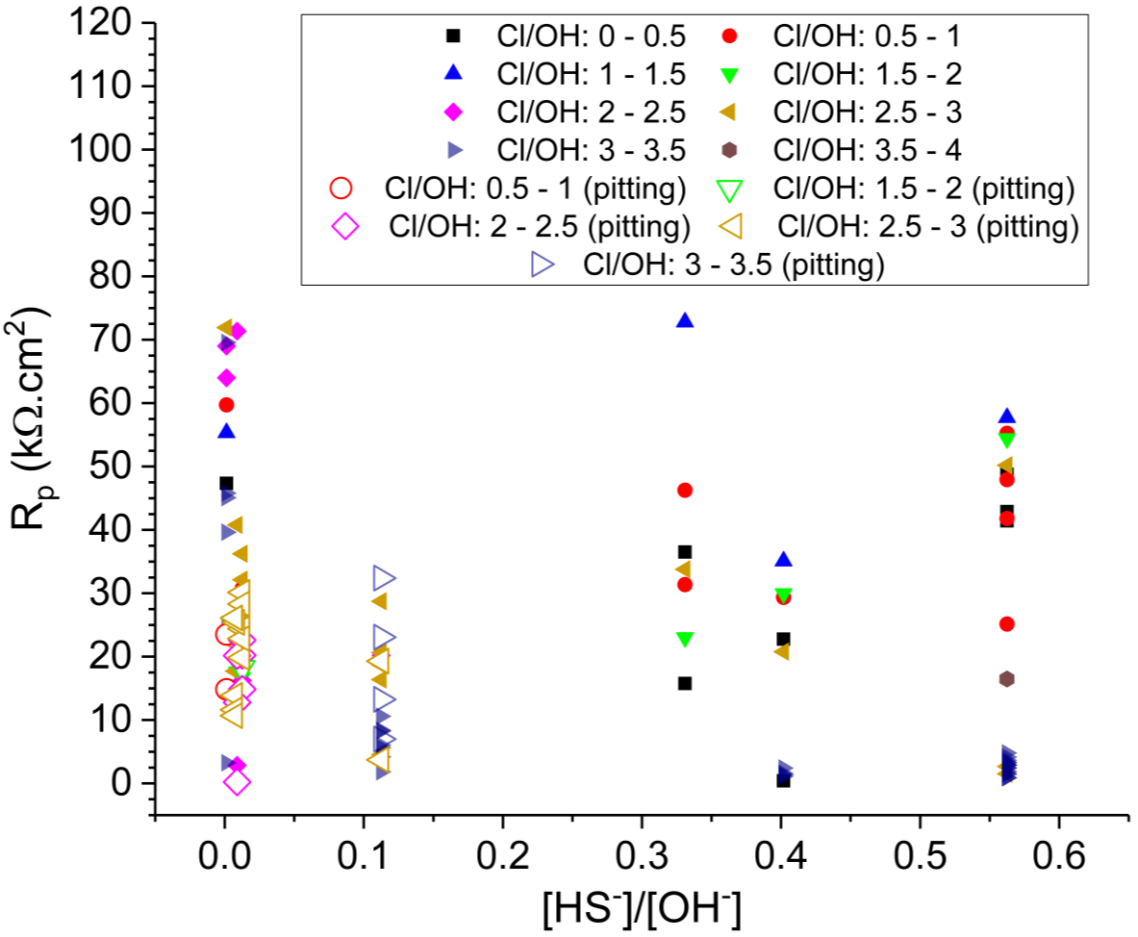

Figure 5-10: The resistance to polarisation (R_p), measured using LPR, of mild steel exposed to highly alkaline solutions (0.80 M, 1.12 M and 1.36 M OH^-), with varying concentrations of HS^- (0.001 M, 0.01 M, 0.09 M and 0.45 M) and Cl^- (0 - 4 in terms of $[Cl^-]/[OH^-]$), after 0, 5, 12 and 28 days exposure. The solid symbols denote the steel exhibiting no corrosion, whereas the hollow symbols indicate the steel undergoing stable/metastable chloride-induced pitting.

Similar observations have been made by several authors for steel embedded in AAS and PC. Holloway and Sykes [265] studied the corrosion behaviour of steel in AAS mortars containing admixed chloride, and did not observe well-defined trends for either i_{corr} and OCP as a function of the chloride concentration. The OCP values in AAS mortars with chloride concentrations as

high as 8 wt.% remained as low as those observed in mortars containing no chloride [265]. Similar observations were made by Criado et al. [284] for steel-reinforced AAS, where immersion of mortar specimens in alkaline solutions with and without chloride made no difference to the measured OCP values, which remained around -0.60 V vs Ag/AgCl. Higher apparent corrosion rates [116], higher i_{corr} and lower R_p values [115,284], without any visual evidence of corrosion have also been reported for steel-reinforced AAS exposed to chloride solutions in comparison to those observed in PC. The observation of R_p and i_{corr} being independent of the chloride concentration and whether the steel is in the passive and the active state, in this study as well as by other authors [115,116,265,283,284,289], indicate that under reducing conditions (due to the presence of HS^- in the electrolyte) measured values of R_p and i_{corr} are highly likely to be related to the aqueous chemistry of the electrolyte at the steel-solution interface, not necessarily the actual corrosion resistance of the steel. In particular, these values correspond mainly to the oxidation of the HS^- species in the electrolyte (and not to the oxidation/reduction couple of Fe/Fe^{2+}), which takes place because of the potential imposed in the electrochemical test procedure used to determine these parameters.

This has been confirmed by the anodic polarisation behaviour of steel in alkaline sulfide containing solutions shown in Figure 5-5, where the anodic polarisation curves were characterised by a continuous increase in the current density upon an increase in the potential in anodic direction from the OCP. As mentioned in Sections 5.3.1.1 and 5.3.1.2, this rise in the current density is primarily because the HS^- in the electrolyte, due to its high polarizability, become the anode and oxidises upon anodic polarisation, instead of the conventionally observed Fe as the anode. This phenomenon is analogous to the action of some bacteria that are capable of depleting the oxygen content in the electrolyte and create a highly reducing environment around the metal [290,291]. This leads to the suppression of the cathodic reduction of oxygen and a slowdown in the dissolution of metal ions; and in such systems the bacteria act as the anode [292].

From the results shown in Figure 5-9, and Figure 5-10 and those observed by [115,116,265,283,284,289], it is evident that in HS^- containing alkaline solutions the mechanisms of chloride-induced corrosion in alkaline solutions containing HS^- are much complex than those in sulfide free solutions, and the OCP measurements, or R_p values measured through LPR or i_{corr} calculated from the modified Stern-Geary equation (Eq. 3.5, Chapter 3), do not, in any case, give information about whether the steel is in the passive state or is actively undergoing chloride-induced pitting.

As shown by Scott and Alexander [255], an increase in the concentration of reduced sulfur in the electrolyte leads to a reduction in the amount of dissolved oxygen at the steel-solution interface and consequentially a reduction in the OCP (confirmed in Figure 5-3). The presence of HS^- in the electrolyte would therefore, inhibit or suppress the cathodic reduction of oxygen, leading to inhibition or retardation of the development of a passive film based on a complex assemblages of iron oxides, as conventionally observed in sulfide free alkaline solutions (shown in Sections 5.3.1.1 and 5.3.1.3). As shown in Figure 5-1, the presence of HS^- in the electrolyte forms a different 'surface' film consisting of a Fe-S complex. As mentioned in Chapter 2, the process of chloride-induced corrosion of steel or any metal is governed by two half-cell reactions (or the formation of a macro-cell), where the anodic reaction proceeds by the oxidation of Fe and the cathodic reaction is described the cathodic reduction of oxygen. Hence, the suppression of the cathodic reaction due to highly reducing conditions prevailing in HS^- containing solutions prevents the formation of macro-cell on the surface of the steel, and would restrict the onset of chloride induced corrosion. The inhibition of macro-cell formation is highly dependent on the concentration of HS^- in the electrolyte, and this is evident from the results shown above, where, for a given concentration of chloride, the susceptibility to chloride-induced corrosion is the highest when the molar ratio of $[HS^-]/[OH^-]$ in the electrolyte is between 0.007 and 0.1125 (mildly reducing), and the lowest for electrolytes with molar ratios of $[HS^-]/[OH^-] \geq 0.33$ (highly reducing).

Based on the works of [78,81,202], it would be reasonable to assume the mildly reducing electrolytes (molar ratio of $[HS^-]/[OH^-]$ between 0.007 and 0.1125) considered in this study to be representative of pore solutions of PC-slag blends/alkali-activated fly ash-slag blends, and highly reducing electrolytes (molar ratios of $[HS^-]/[OH^-] \geq 0.33$) considered in this study to be representative of the pore solutions of AAS. The results shown in this chapter elucidate that the highly reducing nature of HS^- in the pore solutions of AAS does not allow the steel to passivate in the conventional way, but also prevents the steel from undergoing chloride-induced pitting by suppressing the formation of a macro-cell. However, in the case of PC-slag blends/ alkali-activated fly ash-slag blends, the onset of pitting is much likely to occur when compared to AAS, due to the imperfect passivation capability of the binder as well as the ability of the system to sustain the cathodic reaction of oxygen reduction, leading to the formation of a macro-cell. Similar observations have been reported by various authors [255,264], indicating a higher susceptibility of steel to chloride-induced corrosion for binders with mildly reducing pore solutions when compared to binders with highly oxidising or highly reducing pore solutions. This indicates that the onset of chloride-induced corrosion in AAS is highly

dependent on the availability of dissolved oxygen at the steel-concrete interface, and the likelihood that the binder resists the onset chloride-induced pitting is directly proportional to the concentration of dissolved HS^- in the pore solutions of AAS and the ability of the binder to sustain the reducing environment at the steel-concrete interface (or the diffusion coefficient of oxygen).

5.4 Conclusions

The presence of HS^- in alkaline electrolytes alters not only the passivation behaviour of mild steel but also the mechanism of chloride-induced corrosion. By means of cyclic voltammetry, it has been shown that the in alkaline solutions containing sulfide, the competitive adsorption of $[OH^-]$ and $[HS^-]$ inhibits and retards the formation of a passive film composed of iron oxides, and instead forms an Fe-S complex, and in these solutions the mechanism of forming a surface film can be described as:

$$Fe + OH^- + HS^- \rightarrow Fe(OH)_{ads} + Fe(HS)_{ads} \rightarrow Fe(OH)^+_{ads} + Fe(HS)^+_{ads} \rightarrow Fe(OH)_2 + Fe(HS)_{2,ads} \rightarrow \text{hydrated FeOOH and Fe-S complex.}$$

The likelihood of precipitating a hydrated FeOOH layer is high when the concentration of HS^- in the electrolyte is ≤ 0.01 M. In the case of solutions containing $[HS^-] \geq 0.09$ M, the surface film is characterised by a stable Fe-S complex. This was confirmed by the Fe $2p_{3/2}$ and S $2p$ spectra obtained using XPS for steel immersed in alkaline sulfide containing solutions. Therefore, passivation in these electrolytes strongly depends on the availability of dissolved oxygen at the steel-solution interface.

Based on the measured values of OCP, R_p and anodic polarisation chloride induced corrosion was observed to occur only for steel exposed to solutions with $[HS^-]/[OH^-]$ between 0.007 and 0.1125, representative of pore solutions of binders based on PC-slag blends/alkali-activated fly ashes/slag blends. In solutions representative of the pore solutions of AAS with $[HS^-]/[OH^-] \geq 0.33$, chloride-induced corrosion was not evidenced. This was suggested to be due to the highly reducing environments created by the HS^- at the steel-solution interface and the restriction of the cathodic reaction, thereby inhibiting the formation of macro-cell to initiate pitting. Based on the XPS results for steel exposed to alkaline sulfide solutions without electrolytes and the OCP values measured for steel in chloride containing alkaline sulfide

solutions, it would be incorrect to say that under such reducing environments the deposition of elemental sulfur is responsible for the inhibition of chloride-induced corrosion.

Additionally, it has been shown that in pore solutions of AAS, the onset of chloride induced corrosion cannot be easily detected by the behaviour of the R_p or i_{corr}, as they tend to be highly influenced by the high affinity of the HS^- in the solution to lose electrons upon the application of a potential. Additionally, no apparent correlation between the concentration of chloride ions in the solution and the OCP was observed. Therefore, interpreting electrochemical data obtained for electrochemical systems containing a highly redox active species of HS^- based on the guidelines by ASTM C876-15 [181] and recommendations by [183,213] (that are valid only when Fe is the redox active species), would lead to misleading conclusions regarding whether the steel is in the passive or the active state.

Chapter 6: Developing a framework to model chloride ingress in alkali-activated slags

Note: This chapter is primarily based on: Shishir Mundra, Dale P. Prentice, Susan A. Bernal, John L. Provis. 'Developing a framework to model chloride ingress in alkali-activated slags' (*under preparation*). The framework to estimate the transport of chloride was modelled by Shishir Mundra. The 'GEMS calculated database' used within the MATLAB framework was provided by Dale P. Prentice.

6.1 Introduction

Figure 6-1 revisits (from Chapter 2, Section 2.2.3) the classical service life model for steel reinforced concrete structures in the presence of chlorides as proposed by Tuutti [14]. The model can be broadly categorised into the transport process *(initiation phase)*, which is primarily a function of the chemistry of the hydration products and their ability to bind chloride ions, the pore structure of the cement matrix, the pore solution chemistry and its ionic strength; and the breakdown of steel passivity *(onset of corrosion)*, which is governed by the local characteristics of the steel-concrete interface (SCI) – pore solution chemistry and its pH, the chloride concentration and the chemical composition of the steel surface. The time between the onset of corrosion and the end of serviceability *(propagation phase)* is determined by the ability of the local characteristics of the SCI to sustain stable pit growth and a reduction in the cross section of the steel reinforcement. The term 'acceptable level of deterioration' (as seen in Figure 6-1) characterising the duration of the propagation phase is not a constant, but is dissimilar for different application scenarios and depends on various parameters such as the load the corroding structure is subjected to, the criticality of the corroding concrete member, the location of the corroding structure, among others.

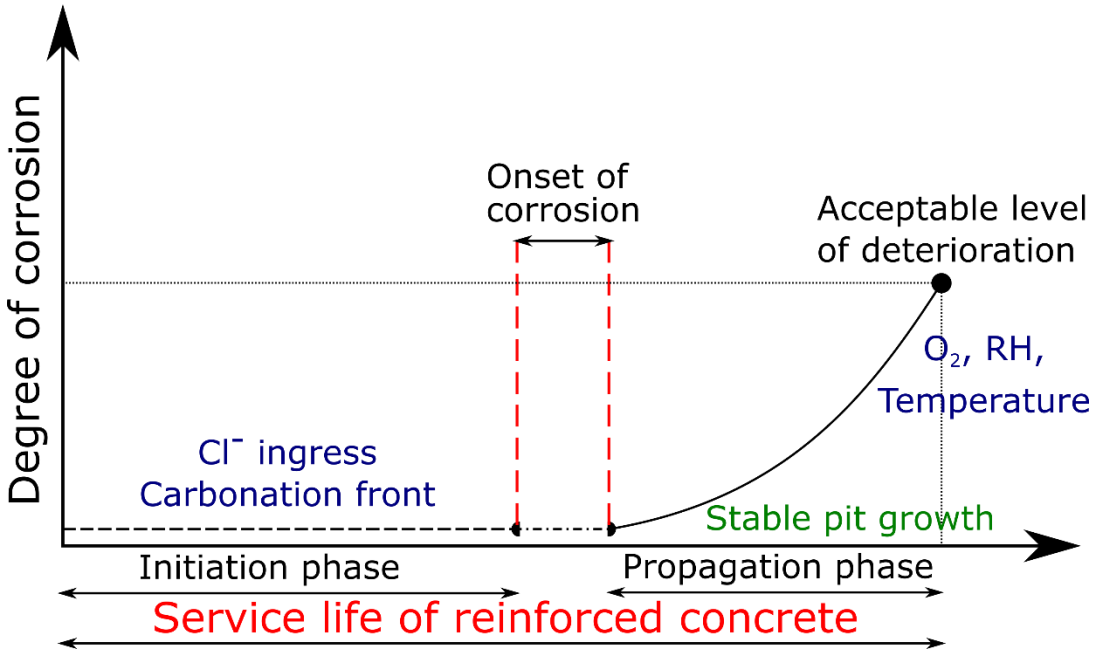

Figure 6-1 The service life model of a reinforced concrete structure based on the model proposed by Tuutti [14]. Adapted from [54].

In the case of Portland cement (PC) based steel-reinforced concretes, a significant amount of research has been carried out to gain an understanding of the initiation phase, the onset of corrosion and the propagation phase. However, some critical questions regarding the onset of corrosion in PC based systems remain unanswered, particularly those pertaining to the influence of the SCI [54].

Alkali-activated slags (AAS) are a much less understood system in comparison to PC, and there remains significant uncertainty regarding the long-term performance of AAS when used in steel-reinforced concrete structures. The initiation phase, or the time taken for chloride ingress through AAS cover, has been observed in some instances to be notably longer than in PC based systems, and this has been attributed to the denser microstructures, the higher chloride binding capacity and the higher ionic strength of the pore solutions in AAS [114,116,293]. The extent of chloride binding in AAS has been found to be highly dependent on the chemical composition of slag used, the phase assemblage and the alkalinity of the pore solution [125]. The pore solution chemistry in the bulk and at the SCI in AAS is different from in PC, and the pore solution is highly reducing due to the reducing nature of the slag. The presence of reduced sulfur species in the pore solution of AAS has been observed to alter the passivation capability and the surface chemistry of the steel reinforcement (shown in Chapter 5) from those encountered in PC based concretes. The breakdown of passivity and the subsequent propagation of steel corrosion in concrete structures has been associated with the

chloride ‘threshold’ value [99] and as is the case for PC, the available data on the chloride ‘threshold’ value for AAS are very scattered, which makes it very difficult to assertively draw conclusions regarding their likely duration of serviceability.

The various parameters pertaining to the initiation, onset of corrosion and propagation phases are highly convoluted and inter-dependent. Therefore, any service life model needs to consider the influence of concrete cover on the transport processes as well as the conditions prevailing at the SCI for corrosion to initiate and propagate. This study attempts to provide a framework that accounts for both of the above discussed points through thermodynamic simulations and numerical modelling.

6.2 Developing a modelling framework

A MATLAB script was created to develop a framework to model the ingress of chloride in AAS based concretes. The MATLAB script incorporates the thermodynamic data generated for various chemistries of slags and activators (discussed in detail in Section 2.1), the transport and chloride binding properties of AAS (discussed in detail in Section 2.2) and then calculates the chloride profiles for a particular AAS concrete for the first 70 years. The script works from input data provided by the user regarding the composition of the slag and the activator of interest, concentration of the exposure solution, and the concrete cover depth. To investigate the application of the proposed model, several slag compositions were selected from the literature [253,293] and are shown in Table 6-1.

Table 6-1: The chemical composition of various slags considered in this study, expressed as wt. % of oxides. Data for M01, M05, M06, and M14 were obtained from [293], and that of M08, M11, and M13 were obtained from [253].

	M01	**M05**	**M06**	**M08**	**M11**	**M13**	**M14**
CaO	42.9	42.3	41.3	35.8	34.6	33.4	33.9
SiO_2	31.6	32.3	36	38.2	37.1	36.4	37.4
Al_2O_3	14.6	13.3	11.3	12	11.5	11.3	9
Fe_2O_3	1.1	0.6	0.3	1.6	1.8	1.4	0.4
MgO	1.2	5.2	6.5	7.7	10.5	13.2	14.3
Na_2O	0.2	0	0.3	0.41	0.4	0.52	0.4
K_2O	0.3	0.3	0.4	1.2	1.1	1	0.5
MnO	0.3	0.2	0.3	1.5	1.5	1.4	1
SO_3	2	2.9	0.7	1.4	1.2	0.36	0.7

6.2.1 Chemistry of the concrete cover

Thermodynamic modelling simulations conducted in this study for slags activated using various activators (NaOH, Na_2SiO_3, $Na_2O{\cdot}2SiO_2$, Na_2CO_3 and Na_2SO_4) follow very similar procedures to those described by Myers et al. [80,81,220]. To set up a look-up database for use in further simulations, the masses and volumes of each stable solid phase and the chemical compositions of the aqueous solutions simulated by GEMS were tabulated and stored in MATLAB (referred as 'GEMS calculated database' hereafter) for a large number of slag compositions, to be used later for calculating the total chloride binding capacity of the binder and evaluating the ingress of chloride through concretes made out of these binders. Additionally, the properties of the modelled C-(N-)A-S-H gel such as, chemistry, density and molar volume are also included in the dataset. The full modelled dataset is presented in the electronic copy as an excel file called 'Gems calculated database.xlsx'.

To estimate the chemistry of the concrete cover for a given slag composition and activator, the MATLAB script developed in this study works on user defined input parameters. The MATLAB script calculates the molar fraction of each of the oxide species present in the slag inputted by the user, and normalises the molar fractions of CaO, MgO and Al_2O_3 ensuring CaO

+ MgO + Al_2O_3 = 1. This information is then used to find an appropriate hydrate phase assemblage in the calculated database.

To ensure that the range of chemistries studied here span those that are relevant to AAS, the SiO_2 contents within the simulated slags were fixed at 30 and 40 wt.%, and SO_3 was fixed at 2 wt.%. However, the sulfur in the slag was represented as sulfide; the SO_3 contained within each slag was actually specified as S^{2-} (0.025 mol/kg of slag) and H^+ (0.05 mol/kg of slag). The minor species Na, K and Mn were neglected, and given the passive nature of Fe within slags [294], Fe was excluded from the simulations and the remaining species were specified within the pseudo-ternary system CaO-Al_2O_3-MgO. For fixed quantities of SiO_2 and SO_3, the molar quantities of CaO, Al_2O_3, and MgO were calculated and normalised to ensure CaO + Al_2O_3 + MgO = 1, and only chemistries relevant to AAS with $0.5 \leq CaO \leq 1$, $0 \leq Al2O3 \leq 0.5$, and $0 \leq MgO \leq 0.5$ (molar basis) were considered in the simulation. The step size for each of the normalised molar quantities of CaO, MgO and Al_2O_3 was fixed at 0.02. The simulations were carried out using 100 g slag and the extent of reaction was varied from 10 to 60 % with a step size of 5 % to ensure coverage of early age and long-term characteristics of AAS. Unreacted slag at each extent of reaction was simply considered to be 'inert' and so was not included in the Gibbs energy minimisation protocol. The w/b ratio (water/solids + anhydrous components of activator) was fixed at 0.4, and is typical of AAS. The dosage of the activator was set to 8 g activator/100 g slag for Na_2CO_3 and Na_2SO_4 activated slags [80,295], 4.75 g activator/100 g slag for NaOH activated slags [296], 10.24 g activator/100 g slag for Na_2SiO_3 (modulus: SiO_2/Na_2O molar ratio = 1.00) activated slags [178], and 13.4 g activator/100 g slag for $Na_2O{\cdot}2SiO_2$ (modulus: SiO_2/Na_2O molar ratio = 2) activated slags [296]. The activator doses for NaOH, Na_2SiO_3 and $Na_2O{\cdot}2SiO_2$ activated slags are slightly higher than those used in the literature. A predominantly N_2 (g) atmosphere was used for the simulations to provide an oxygen-depleted environment to prevent sulfur oxidation, representing undamaged concrete.

Simulations were carried out through the Gibbs energy minimisation software GEM-Selektor version 3.2 [216,297] (http://gems.web.psi.ch/), using the CEMDATA14 database [298], with the addition of the CNASH_ss model to describe C-(N-)A-S-H chemistry, from ref. [81] Thermodynamic data for solid phases used in this study are listed in Table 6-2, and Table 6-3 and Table 6-4 represent the aqueous species/complexes and gases considered here. The aqueous and gas phase models were represented by the Truesdell-Jones version of the extended Debye-Hückel equation (Eq. 6.1) and the ideal gas equation of state, respectively.

$$log_{10}(\gamma_j) = \frac{-A_\gamma z_j^2 \sqrt{I}}{1+\dot{a}B_\gamma\sqrt{I}} + b_\gamma I + log_{10}\frac{x_{jw}}{X_w} \quad \text{(Eq. 6.1)}$$

where, γ_j and z_j are the activity coefficient and the charge of the j^{th} aqueous species, respectively, I is the ionic strength of the aqueous phase, A_γ ($kg^{0.5}mol^{-0.5}$) and B_γ ($kg^{0.5}mol^{-0.5}cm^{-1}$) are electrostatic parameters that depend on the temperature and pressure, and x_{jw} (mol) and X_w (mol) are the molar quantities of water and total aqueous phase, respectively. The average ionic radius ($\dot{a}$, Å) and the parameter for short-range interactions of charged species (b_γ, kg/mol) were specified according to [299], and set to 3.31 and 0.098 kg/mol respectively, thereby representing NaOH-dominated solutions.

Table 6-2: Thermodynamic properties of solid phases at 298.15 K and 1 bar. Cement chemistry notation is used: C = CaO; S = SiO_2; A = Al_2O_3; H = H_2O; N = Na_2O; M = MgO; $\underline{c}$ = CO_2; $\underline{s}$ = SO_3.

Phases	***V*°** **(cm^3/mol)**	**ΔH_f° (kJ/mol)**	**ΔG_f° (kJ/mol)**	***S*°** **(J/mol·K)**	***Cp*°** **(J/mol·K)**	**Reference**
AH_3 (microcrystalline)	32.0	−1265	−1148	140	93.1	[300]
Portlandite, CH	33.1	−985	−897	83.4	87.5	[301]
SiO_2 (amorphous)	29.0	−903	−849	41.3	44.5	[215,302]
C_2AH_8	90.1	−5278	−4696	450	521	[300]
Katoite, (C_3AH_6)	150	−5537	−5008	422	446	[300]
C_4AH_{19}	382	−1002	−8750	1120	1382	[300]
CAH_{10}	194	−5288	−4623	610	668	[300]
Strätlingite, C_2ASH_8	216	−6360	−5705	546	603	[218]
Calcium monocarboaluminate hydrate, $C_4A\underline{c}H_{11}$	262	−8250	−7337	657	881	[218]
Calcium hemicarboaluminate hydrate, $C_4A\underline{c}_{0.5}H_{12}$	285	−8270	−7336	713	906	[218]
Calcium tricarboaluminate hydrate, $C_6A\underline{c}_3H_{32}$	650	−16792	−14566	1858	2121	[218]
Ettringite, $C_6A\underline{s}_3H_{32}$	707	−17535	−15206	1900	2174	[303]
Gypsum, $C\underline{s}H_2$	74.7	−2023	−1798	194	186	[304,305]
Anhydrite, $C\underline{s}$	45.9	−1435	−1322	107	99.6	[304,305]

Lime, C	16.8	−635	−604	39.7	42.8	[302]
Brucite, MH	24.6	−923	−832	63.1	77.3	[302,304,305]
MA-c-LDH, M_4AcH_9	220	−7374	−6580	551	647	[303]
C–(N–)A–S–H gel ideal solid solution end-members, 'CNASH_ss' [81]						
5CA, $C_{1.25}A_{0.125}S_1H_{1.625}$	57.3	−2491	−2293	163	177	[81]
INFCA, $C_1A_{0.15625}S_{1.1875}H_{1.65625}$	59.3	−2551	−2343	154	181	[81]
5CNA, $C_{1.25}N_{0.25}A_{0.125}S_1H_{1.375}$	64.5	−2569	−2382	195	176	[81]
INFCNA, $C_1N_{0.34375}A_{0.15625}S_{1.1875}H_{1.3125}$	69.3	−2667	−2474	198	180	[81]
INFCN, $C_1N_{0.3125}S_{1.5}H_{1.1875}$	71.1	−2642	−2452	186	184	[81]
T2C*, $C_{1.5}S_1H_{2.5}$[a]	80.6	−2721	−2465	167	237	[81]
T5C*, $C_{1.25}S_{1.25}H_{2.5}$[a]	79.3	−2780	−2517	160	234	[81]
TobH*, $C_1S_{1.5}H_{2.5}$[a]	85.0	−2831	−2560	153	231	[81]
Calcium monosulfoaluminate–hydroxoaluminate hydrate non-ideal solid solution [218]						
Calcium monosulfoaluminate hydrate, C_4AsH_{12}	309	−8750	−7779	821	942	[218]
C_4AH_{13}	274	−8300	−7324	700	930	[300]
MA-OH-LDH ideal solid solution end-members, 'MA-OH-LDH_ss' [220]						
M_4AH_{10}	219	−7160	−6358	549	648	[306,307]
M_6AH_{12}	305	−9007	−8023	675	803	[220]
M_8AH_{14}	392	−10853	−9687	801	958	[220]
Carbonates						
Aragonite, Cc	34.2	−1207	−1128	90.2	81.3	[304,305]
Calcite, Cc	36.9	−1207	−1129	92.7	81.9	[304,305]
Magnesite, Mc	28.0	−1113	−1029	65.7	75.8	[304,305]
Zeolites						
Natrolite, $Na_{0.4}Al_{0.4}Si_{0.6}O_2{\cdot}0.4H_2O$	33.8[b]	−1144	−1063	71.9	60.4	[308]

Ca-heulandite, $Ca_{0.111}Al_{0.222}Si_{0.778}O_2 \cdot 0.667H_2O$	35.2[b]	−1179	−1090	87.1	82.9	[309]

[a]The asterisks for the T2C*, T5C*, and TobH* end-members indicate that these components have slightly modified thermodynamic properties [81] **but the same chemical compositions as the T2C, T5C and TobH end-members of the original downscaled CSH3T thermodynamic model** [310]**.**

[b]Molar volumes were taken from Myers et al. [220]**.**

The thermodynamic dataset for solid phases (as indicated in Table 6-2) considered in this study include the ideal solid solutions end member models of C-(N-)A-S-H_ss [81] and MA-OH-LDH_ss [220]. In addition, zeolites such as natrolite ($Na_{0.4}Al_{0.4}Si_{0.6}O_2 \cdot 0.4H_2O$) and Ca-heulandite ($Ca_{0.111}Al_{0.222}Si_{0.778}O_2 \cdot 0.667H_2O$) have been considered in the thermodynamic simulations and are consistent with experimentally determined phase assemblages in AAS. All other zeolites mentioned in [220] were supressed as they were not observed in initial trial simulations. It must be noted that the additional end-member models and the zeolites created in [220] have not been thoroughly assessed to be compatible with the CEMDATA14 database used in this study. Regions of phase transition where these phases are dominant may be less reliable than phases identified in the CEMDATA14 database, as was explained in [220].

Table 6-3: Thermodynamic properties of the aqueous species used in the thermodynamic simulations. The hydration reactions shown in parentheses indicate hydrated species/complexes represented by the simulated aqueous species/complexes.

Species/complex*	$V°$ **(cm^3/mol)**	$\Delta H_f°$ **(kJ/mol)**	$\Delta G_f°$ **(kJ/mol)**	$S°$ **(J/mol·K)**	$Cp°$ **(J/mol·K)**	**Reference**
Al^{3+}	−45.2	−530.6	−483.7	−325.1	−128.7	[311]
AlO^+ (+ H_2O = $Al(OH)_2^+$)	0.3	−713.6	−660.4	−113	−125.1	[311]
AlO_2^- (+ $2H_2O$ = $Al(OH)_4^-$)	9.5	−925.6	−827.5	−30.2	−49	[311]
$AlOOH^o$ (+ $2H_2O$ = $Al(OH)_3^o$)	13	−947.1	−864.3	20.9	−209.2	[311]
$AlOH^{2+}$	−2.7	−767.3	−692.6	−184.9	56	[311]
$AlHSiO_3^{2+}$ (+ H_2O = $AlSiO(OH)_3^{2+}$)	−40.7	−1718	−1541	−304.2	−215.9	[218]

$AlSiO_5^{3-}$ (+ $2H_2O = AlSiO_3(OH)_4^{3-}$)	-43.6	-2014.2	-1769	-66.3	-292.2	[304,305]
$AlSO_4^+$	−6.0	−1423	−1250	−172.4	−204.0	[218]
$Al(SO_4)_2^-$	31.1	−2338	−2006	−135.5	−268.4	[218]
Ca^{2+}	−18.4	−543.1	−552.8	−56.5	−30.9	[311]
$CaOH^+$	5.8	−751.6	−717	28	6	[311]
$CaHSiO_3^+$ (+ $H_2O = CaSiO(OH)_3^+$)	−6.7	−1687	−1574	−8.3	137.8	[312]
$CaSiO_3^o$ (+ $H_2O = CaSiO_2(OH)_2^o$)	15.7	−1668	−1518	−136.7	88.9	[218]
$CaSO_4^o$	4.7	−1448	−1310	20.9	−104.6	[312]
$CaCO_3^o$	−1.6	−1202	−1099	10.5	−123.9	[312]
$CaHCO_3^+$	13.3	−1232	−1146	66.9	233.7	[304,305]
Na^+	−1.2	−240.3	−261.9	58.4	38.1	[311]
$NaOH^o$	3.5	−470.1	−418.1	44.8	−13.4	[311]
$NaSO_4^-$	18.6	−1147	−1010	101.8	−30.1	[218]
$NaCO_3^-$	−0.4	−938.6	−797.1	−44.3	−51.3	[304,305]
$NaHCO_3^o$	32.3	−929.5	−847.4	154.7	200.3	[304,305]
$HSiO_3^-$ (+ $H_2O = SiO(OH)_3^-$)	4.5	−1145	−1014	20.9	−87.2	[312]
SiO_2^o (+ $2H_2O = Si(OH)_4^o$)	16.1	−887.9	−833.4	41.3	44.5	[215,313]
SiO_3^{2-} (+ $H_2O = SiO_2(OH)_2^{2-}$)	34.1	−1099	−938.5	−80.2	119.8	[218]
$S_2O_3^{2-}$	27.6	−649.9	−520.0	66.9	−238.5	[311]
HSO_3^-	33.0	−627.7	−529.1	139.7	−5.4	[311]
SO_3^{2-}	−4.1	−636.9	−487.9	−29.3	−281.0	[311]
HSO_4^-	34.8	−889.2	−755.8	125.5	22.7	[311]
SO_4^{2-}	12.9	−909.7	−744.5	18.8	−266.1	[311]
H_2S^o	35.0	−39.0	−27.9	125.5	179.2	[311]
HS^-	20.2	−16.2	12.0	68.2	−93.9	[311]
S^{2-}	20.2	92.2	120.4	68.2	−93.9	[311]
Mg^{2+}	−22.0	−465.9	−454.0	−138.1	−21.7	[311]

$MgOH^+$	1.6	−690.0	−625.9	−79.9	129.2	[311]
$MgHSiO_3^+$ (+ $H_2O = MgSiO(OH)_3^+$)	−10.9	−1614	−1477	−99.5	158.6	[311]
$MgSO_4^o$	1.8	−1369	−1212	−50.9	−90.3	[304,305,311]
$MgSiO_3^o$ (+ $H_2O = MgSiO_2(OH)_2^o$)	12.1	−1597	−1425	−218.3	98.2	[304,305]
$MgCO_3^o$	−16.7	−1132	−999.0	−100.4	−116.5	[304,305,312]
$MgHCO_3^+$	9.3	−1154.0	−1047	−12.6	254.4	[304,305]
CO_2^o	32.8	−413.8	−386.0	117.6	243.1	[304,305,313]
CO_3^{2-}	−6.1	−675.3	−528.0	−50.0	−289.3	[311]
HCO_3^-	24.2	−690.0	−586.9	98.5	−34.8	[311]
CH_4^o	37.4	−87.8	−34.4	87.8	277.3	[304,305,314]
OH^-	−4.7	−230	−157.3	−10.7	−136.3	[311]
H^+	0	0	0	0	0	[311]
H_2O^o	18.1	−285.9	−237.2	69.9	75.4	[315]
H_2^o	25.3	−4.0	17.7	57.7	166.9	[304,305,313]
N_2^o	33.4	−10.4	18.2	95.8	234.2	[313]
O_2^o	30.5	−12.2	16.4	109	234.1	[313]

***Note that nitrogen containing aqueous species were not included in the simulations. This was done to ensure that N_2 (g) remained in the gaseous state.**

Table 6-4: Thermodynamic properties of the gases used in the thermodynamic simulations

Gases*	***V*°** **(cm^3/mol)**	**ΔH_f°** **(kJ/mol)**	**ΔG_f°** **(kJ/mol)**	***S*°** **(J/mol·K)**	***Cp*°** **(J/mol·K)**	**Reference**
N_2	24790	0	0	191.6	29.1	[316]
O_2	24790	0	0	205.1	29.3	[316]
H_2	24790	0	0	130.7	28.8	[316]

CO_2	24790	−393.5	−394.4	213.7	37.1	[316]
CH_4	24790	−74.8	−50.7	186.2	35.7	[316]
H_2S	24790	−20.6	−33.8	205.8	34.2	[316]

***H_2O (g) was omitted from the simulations**

As mentioned earlier, thermodynamic simulations were conducted for slags either containing 30 wt. % or 40 wt. % SiO_2, and the MATLAB input script selects the type of slag to use from the database, initially based on the bulk SiO_2 content and the activator type inputted by the user. Therefore, slags with composition ≥ 35 wt. % SiO_2 were assumed to have similar chemistry to the database entries with 40 wt. % SiO_2, and slags with < 35 wt. % SiO_2 were assumed to be similar to those containing 30 wt. % SiO_2. Based on the molar fractions of CaO, MgO and Al_2O_3, the SiO_2 content and the activator, the MATLAB script pulls out data for the hydrate phase assemblage from the tabulated 'GEMS calculated database' at the selected degree of hydration. The SO_3 content of the slag and the w/b ratio used to formulate AAS were kept constant, as mentioned above. Figure 6-2 shows the process described above to estimate the chemistry of the concrete cover.

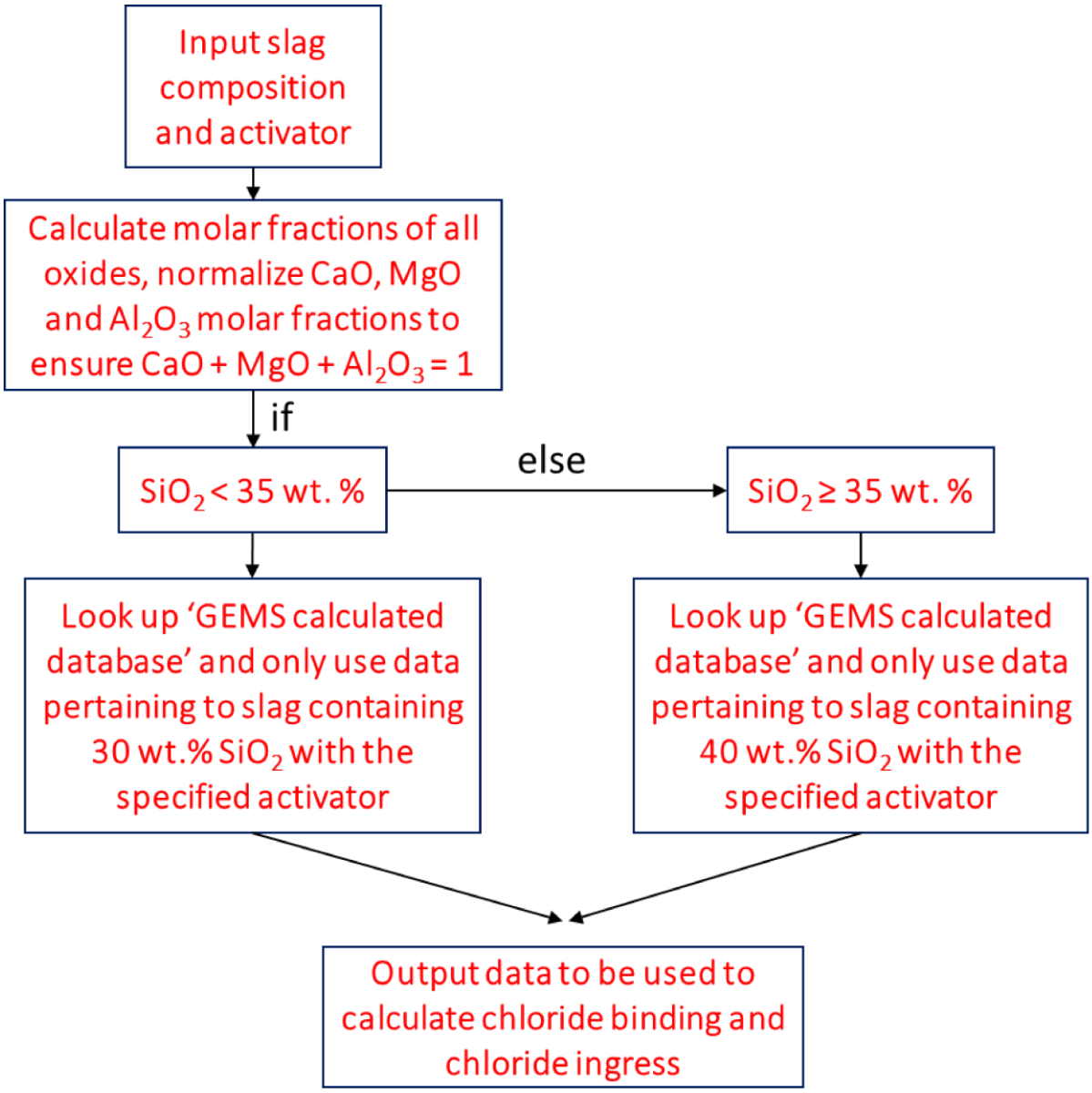

Figure 6-2: A schematic of the working of the MATLAB script developed to estimate the chemistry of the concrete cover based on user defined input parameters pertaining to the chemical composition of the precursors (slag and activator).

6.2.2 Chloride binding and diffusion

The transport of chloride within the concrete cover is not a simple phenomenon but under saturated conditions is primarily driven by diffusion (under the influence of concentration gradients), as stated in Chapter 2. This study is based solely on the diffusion of chloride through concrete cover, and hence other forms of transport such as migration and capillary suction are

not considered. Under saturated conditions, the transport of chloride ions [317] can be assumed to occur via the total evaporable water (w_e - dimensionless) in the concrete (considered to be the volume of water in the pore solution of the concrete), and so the flux (J_{Cl} in kg/m^2·s) of chloride ions through the concrete cover of depth x can be described by Fick's first law (Eq. 6.2):

$$J_{Cl} = -D_{Cl}^{*}\frac{\partial C_f}{\partial x} = -D_{Cl}\cdot w_e \cdot \frac{\partial C_f}{\partial x} \quad \text{(Eq. 6.2)}$$

where D_{Cl} (m^2/s) is the effective diffusion coefficient when the chloride concentration is expressed in terms of kg/m^3 of concrete, and D_{Cl}^{*} (m^2/s) is the effective diffusion coefficient when the chloride concentration is expressed as kg/m^3 of pore solution. The free chloride concentration is represented by C_f (kg/m^3) and the negative sign is indicating the difference between the direction of the concentration gradient and the direction of transport. By applying mass conservation in saturated concrete, and substituting Eq. 6.2 into Eq. 6.3, the change in the total chloride concentration (C_t in kg/m^3 of concrete) with respect to time (t) can be expressed as a function of the change in free chloride concentration as a function of the distance within the concrete cover, and is articulated as Fick's second law (Eq. 6.4) – similar to the form of Eq. 2.13 [318]:

$$\frac{\partial C_t}{\partial t} = -\frac{\partial J_{Cl}}{\partial x} \quad \text{(Eq. 6.3)}$$

$$\frac{\partial C_t}{\partial t} = \frac{\partial}{\partial x}\left(D_{Cl}\cdot w_e \cdot \frac{\partial C_f}{\partial x}\right) = D_{Cl}\cdot w_e \cdot \frac{\partial^2 C_f}{\partial x^2} \quad \text{(Eq. 6.4)}$$

The total chloride concentration can be expressed as a function of the free chloride concentration, bound chloride (C_b) and the total evaporable water as (Eq. 6.5) [319]:

$$C_t = C_b + w_e C_f \quad \text{(Eq. 6.5)}$$

Substitution of Eq. 6.5 into Eq. 6.4 allows consideration of the influence of chloride binding on the diffusion of free chloride ions within the concrete matrix, and the modified equation for Fick's second law can be expressed as (Eq. 6.6):

$$\frac{\partial C_f}{\partial t} = D_{app,Cl}\cdot \frac{\partial^2 C_f}{\partial x^2} \quad \text{(Eq. 6.6)}$$

and,

$$D_{app,Cl} = \frac{D_{Cl}}{1+\frac{1}{w_e}\cdot\frac{\partial C_b}{\partial C_f}} \quad \text{(Eq. 6.7)}$$

where $D_{app,Cl}$ is the apparent chloride diffusion coefficient (m^2/s) and $\partial C_b/\partial C_f$ is the chloride binding capacity of the binder in the concrete cover [317]. As highlighted in Eq. 6.7, $D_{app,Cl}$ can thus be described (shown in Figure 6-3) as function of the chloride binding capacity of the binder within the concrete cover. The chloride binding capacity of the binder is dependent on the hydrate phase assemblage, which in turn is a function of the chemistry of the precursors; and in the case of AAS, the precursors are slag and the activating solution. The evolution of pore structure (pore geometry, tortuosity, pore connectivity) of the concrete cover as a function of the hydration time can also have a significant influence on $D_{app,Cl}$, but falls out of the scope of this study.

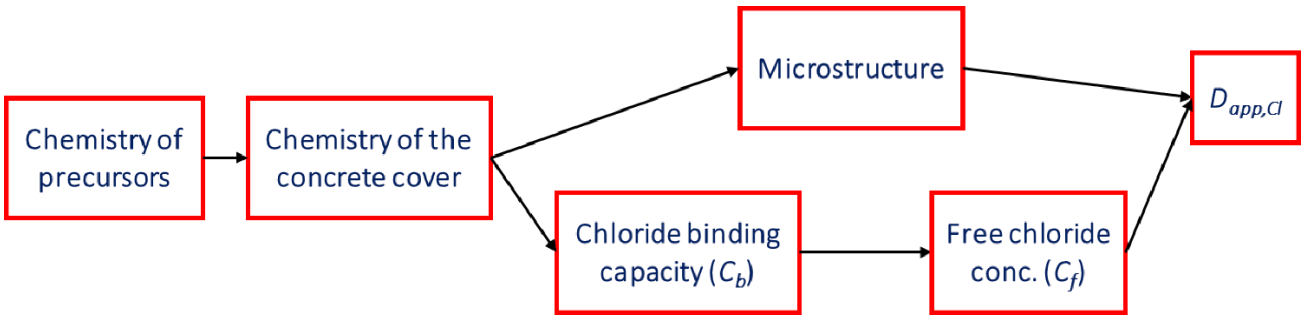

Figure 6-3: A simple schematic of the factors influencing the effective chloride diffusion coefficient in concrete under saturated conditions.

The extent of chloride binding for a particular binder can be described as a function of free chloride concentration (via relationships called 'chloride binding isotherms' when determined at a given temperature) and has been expressed by means of non-linear adsorption isotherms such as the Langmuir [318] and Freundlich isotherms (Eq. 8) [317,320]. Tang and Nilsson [319] observed that the use of Langmuir adsorption isotherm was only valid for free chloride concentrations less than 0.05 M (representing the formation of a monolayer at such low concentrations), however, for free chloride concentrations greater than 0.01 M, the use of a Freundlich isotherm would be more appropriate [319]. This is primarily due to the observation of binders exhibiting a binding capacity at high free chloride concentrations and the adsorption mechanism being more complex than the formation of a single monolayer [319]. Therefore, the Freundlich adsorption isotherm was used to fit experimental data [293] in this study, and to quantify the binding capacity and apparent chloride diffusion coefficient of AAS (Eq. 6.8, Eq. 6.9 and Eq. 6.10); this is revisited later.

$$C_b = \alpha C_f^{\beta} \quad \text{(Eq. 6.8)}$$

$$\frac{\partial C_b}{\partial C_f} = \alpha\beta C_f^{\beta-1} \quad \text{(Eq. 6.9)}$$

where, α and β are empirical constants and their values depend on the chemistry of the binder. On substituting Eq. 6.9 into Eq. 6.7,

$$D_{app,Cl} = \frac{D_{Cl}}{1+\frac{1}{w_e}\cdot\alpha\beta C_f^{\beta-1}} \quad \text{(Eq. 6.10)}$$

Both long- and short-term tests have been used to quantify chloride ingress within concrete structures, however, one of the most accepted methods is the accelerated test called NT Build 492 [321] or the rapid chloride migration (RCM) test, developed by Tang [322]. The RCM test is a short-term test and gives the value of non-steady state migration coefficient (D_{nssm} or D_{RCM}) and details of the test can be found in [321,322]. The DuraCrete guidelines [323,324] use $D_{RCM}(t)$ (defined as $D_a(t)$ in Eq. 3.7) as an input parameter to define the service life of concrete structures, and this therefore should be equivalent to $D_{app,Cl}$ values obtained using bulk diffusion tests. However, in the case of PC based concretes, several authors [322,325,326] have found the value of D_{RCM} to be slightly higher than $D_{app,Cl}$, and one of the primary reasons could be that the short-term RCM test underestimates the extent of chloride binding in cement matrices. This has been found to be true in the case of AAS as well [114], where the ratio of the non-steady state migration and apparent diffusion coefficients ($D_{RCM}/D_{app,Cl}$) was found to be approximately 100. Therefore, the value of D_{Cl} in Eq. 6.10 in this study was assumed to be the mean D_{nssm} (0.5×10^{-12} m^2/s) obtained using the NT Build 492 test on Na_2SiO_3-activated M6 mortars cured for 28 days, measured by [293] and [114]. The value of D_{Cl} was assumed to be the same for all AAS considered in this study. The experimentally observed D_{nssm} values for AAS mortars [293] were considered to be true for AAS concretes as well, on the assumption that the aggregate volume fraction (or the interfacial transition zone (ITZ)) has negligible influence on $D_{app,Cl}$ [73].

As mentioned in Chapter 2, AAS binders are characterised by the formation of C-(N-)A-S-H gel as the major reaction product, and secondary reaction products such as hydrotalcite-like Mg-Al-OH-LDH phases and strätlingite, among others. The total binding capacity of AAS can be assumed to be the sum of the individual binding capacities of various hydrate phases formed in AAS (Eq. 6.11).

$$\left(\frac{\partial C_b}{\partial C_f}\right)_{\substack{total\\binder}} = \left[\left(\frac{\partial C_b}{\partial C_f}\right)_{C\text{-}(N\text{-})A\text{-}S\text{-}H} + \left(\frac{\partial C_b}{\partial C_f}\right)_{Mg\text{-}Al\text{-}OH\text{-}LDH} + \left(\frac{\partial C_b}{\partial C_f}\right)_{str\ddot{a}tlingite} + \ldots\right] \quad \text{(Eq. 6.11)}$$

According to Eq. 6.11, if the amounts and the individual chloride binding capacity of each of the reaction products are known, a theoretical value for the total chloride binding capacity of AAS based concretes could be calculated. Ke [293] calculated the individual binding capacities of the C-(N-)A-S-H gel, hydrotalcite-like Mg-Al-OH-LDH phase and strätlingite. Substituting Eq. 6.11 into Eq. 6.7, $D_{app,\,Cl}$ can be represented as (Eq. 6.12):

$$D_{app,Cl} = \frac{D_{Cl}}{1+\frac{1}{w_e}\cdot\left[\left(\frac{\partial C_b}{\partial C_f}\right)_{C\text{-}(N\text{-})A\text{-}S\text{-}H}+\left(\frac{\partial C_b}{\partial C_f}\right)_{Mg\text{-}Al\text{-}OH\text{-}LDH}+\left(\frac{\partial C_b}{\partial C_f}\right)_{strätlingite}+\ldots\right]} \quad \text{(Eq. 6.12)}$$

Based on the individual binding isotherms obtained by Ke [293] (reproduced in Figure 6-4), the total chloride binding capacity of all AAS binders in this study were considered to be the sum of the individual binding capacity of only the C-(N-)A-S-H gel, hydrotalcite-like Mg-Al-OH-LDH phase and strätlingite. Additional phases formed in smaller quantities in AAS such as monocarboaluminate, monosulfoaluminate, ettringite, Ca-heulandite, natrolite, katoite and brucite were assumed to not contribute to chloride binding at all. Various authors have calculated the binding isotherms for synthetic monocarboaluminate and monosulfoaluminate phases [13,327,328], however, they were not considered in this study primarily because the experimental setup used to calculate the binding isotherms could neither represent the alkalinity nor the ionic strength of the pore solutions of AAS. The focus of this work was to understand the influence of chloride binding on the chloride ingress, and therefore the mechanisms of chloride binding are not considered here, and are discussed in a very limited capacity hereafter.

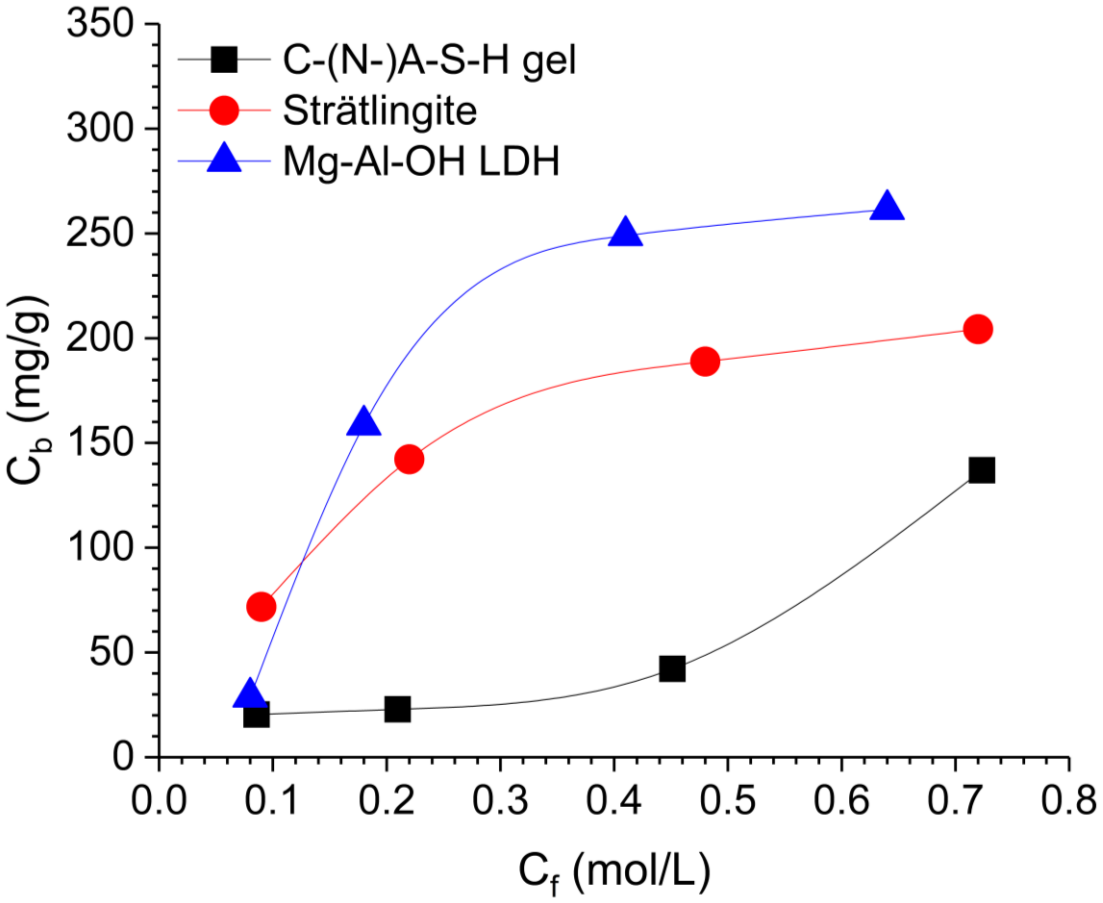

Figure 6-4: Chloride binding isotherms for synthetic phases formed in AAS, C-(N-)A-S-H gel, hydrotalcite-like Mg-Al-OH-LDH phase and strätlingite obtained by Ke [293] (reproduced from data in [293]).

Ke [293] reported the experimental chloride binding capacity of Na_2SiO_3 and Na_2CO_3-activated slag M6 (M6 composition in Table 6-1). In this study, the experimentally determined binding isotherm for Na_2SiO_3-activated M6 [293] was assumed to be true for slag M6 activated using NaOH, $Na_2O{\cdot}2SiO_2$, Na_2CO_3, and Na_2SO_4 as well, due to the lack of experimental binding isotherms in the literature for various AAS. In addition, Ke [293] compared the theoretical (calculated according to Eq. 6.11) and the experimental chloride binding isotherms, and observed the theoretical values to be 3 to 6 times higher than experimental observation. She attributed the overestimation to the higher crystallinity of the synthetic phases used for measuring the individual chloride binding isotherms [293]. Based on the quantities of C-(N-)A-S-H gel, hydrotalcite-like Mg-Al-OH-LDH phase and strätlingite obtained from the thermodynamic simulations as described in Section 6.2.1, the total chloride binding isotherms for each of activated slag considered in this study were calculated as the sum of the individual

chloride binding capacities of each of these phases (as shown in Figure 6-5A) when the extent of slag reaction was 60 %. This was followed by scaling down the theoretical binding isotherms of activated M6 binders to match the experimentally determined values. The theoretical binding isotherms for all other activated slags (M1, M5, M8, M11, M13 and M14) were also scaled down by the same factor (as shown in Figure 6-5B).

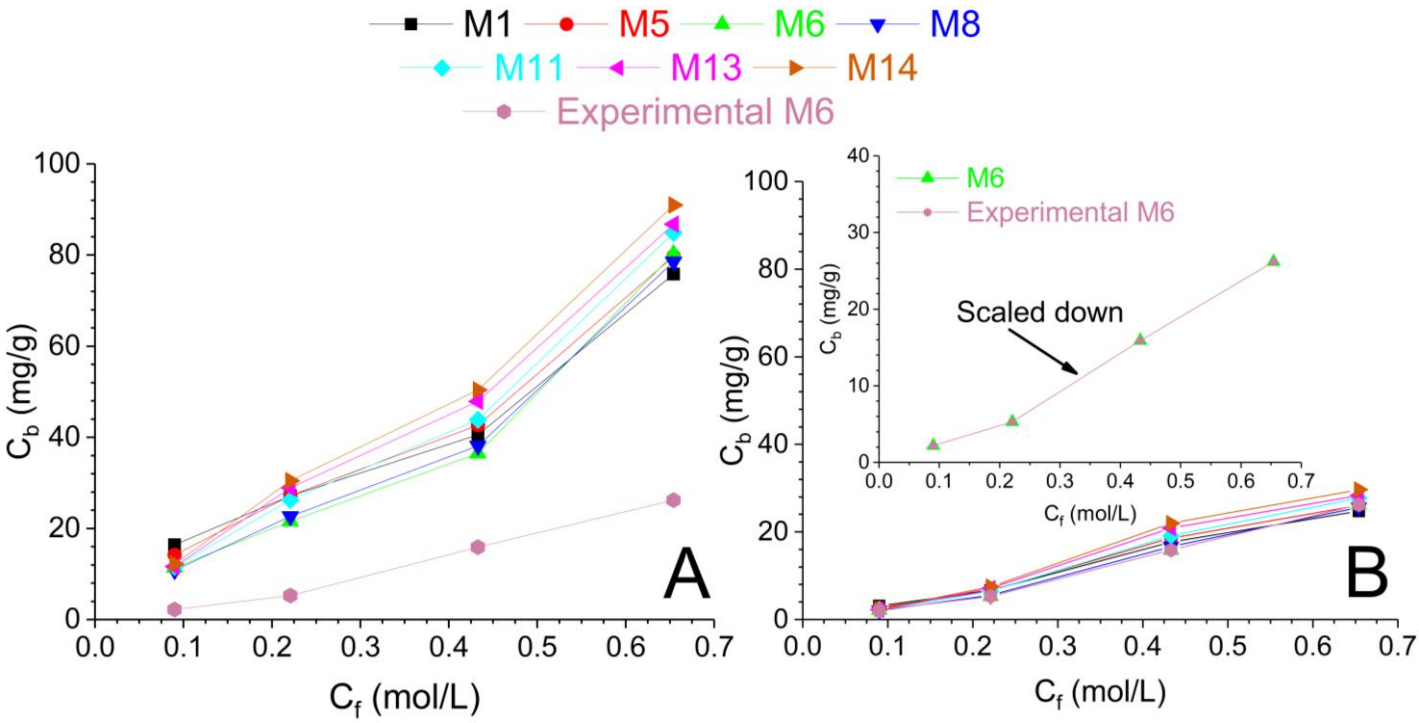

Figure 6-5: (A) Chloride binding isotherms calculated through the use of simulated solid phases for all alkali-activated slags considered in this study and the individual binding capacity of each of the reaction products; and compared with the experimental data from [293]. (B) Schematic of the scaling down of the theoretical chloride binding isotherms to match experimental data, used to define the apparent diffusion coefficients as a function of the free chloride concentration.

To model the diffusion of chloride in saturated concretes, governed by Eq. 6.7, considering $D_{app,Cl}$ as a function of C_f, Eq. 6.7 was solved numerically as a space-time problem using the explicit finite difference method, in one spatial dimension with time and space steps set to ~1 day and 1 mm, respectively. In order to take into account the non-linear nature of $D_{app,Cl}$ (C_f), the value of $D_{app,Cl}$ was set to be dependent on the free chloride concentration at the previous

space step for any given time step, and was calculated individually at each space-time step using the calculated binding parameters of the Freundlich adsorption isotherm for each AAS considered in this study. Figure 6-6 shows the modelling setup, based on Eq. 3.14, used in this study to estimate the ingress of chloride. It is important to note that the applicability of the calculated Freundlich adsorption isotherm, in this study, to estimate a relationship between $D_{app,Cl}$ and C_f is only validated for the free chloride concentration lower than 0.654 M, as binding isotherms [293] for higher free chloride concentrations do not exist in the literature. To reduce the computation time, the chloride profiles were calculated up to 70 years. For a concrete with thickness L, the initial and boundary conditions used to solve Eq. 6.7 numerically are described as (Eq. 6.13):

$$\begin{aligned} &\text{For } t \geq 0, && C_f = C_o && \text{at } x = L \\ & && C_f = C_s && \text{at } x = 0 \\ &\text{For } t = 0, && C_f = C_o && \text{at } x > 0 \end{aligned} \qquad \text{(Eq. 6.13)}$$

where C_o is the chloride concentration present in the concrete prior to exposure to a salt solution (wt.% of binder), and C_s is the concentration of chloride in the exposure salt solution. The value of C_o was set to zero, assuming that quantity of admixed chloride is zero and the exposure solution is the sole source of chlorides. The thickness (L) of the concrete was set to be 70 mm, much larger than the concrete covers recommended in BS 8500 [329] and the chloride penetration depth. It must be noted that the surface chloride concentration for each AAS was assumed to be constant (0.60 M Cl^-) as a function of time, and the influence of leaching [324] (or a reduction in the alkalinity) on the chloride binding capacity of various hydrate phase assemblage and chloride diffusion was not considered in this study. Based on the total amount of evaporable water content in each of the AAS, the surface chloride concentration was calculated as a function of the wt.% of binder.

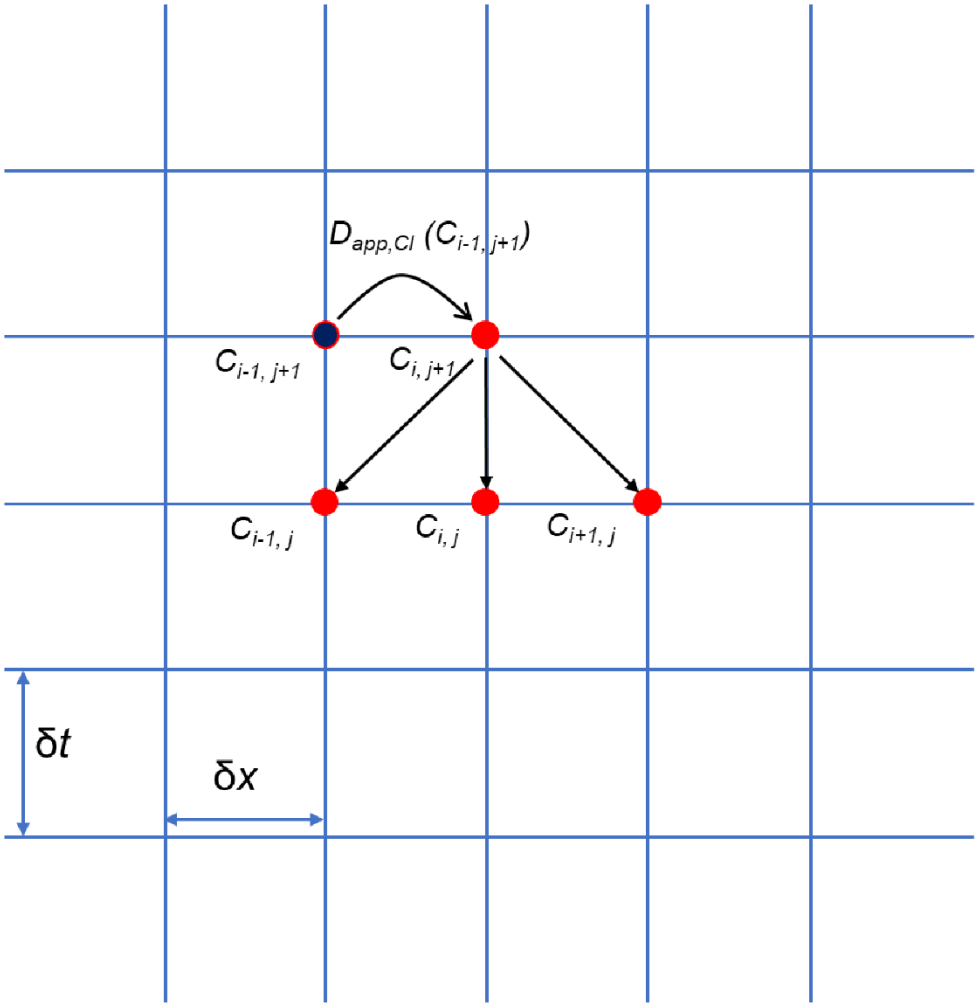

Figure 6-6: A schematic of the explicit fine difference method (based on Eq. 3.14) employed in this study to estimate the ingress of chloride as a space-time problem. The values of δx and δt were set to 1 mm and 0.9125 days (~1 day), respectively, making the grid (x vs. t) size 70 × 28,000, and representing a cover depth of 70 mm and 70 years of service-life. Eq. 3.14 was solved using a loop function over space and time, with the boundary conditions describe in Eq. 6.13. $D_{app,Cl}$ (or D, as expressed in Eq. 3.14) were calculated based on the Freundlich isotherms developed for each of the AAS and expressed as a function of the free chloride concentration ($\boldsymbol{c}_{i-1,j+1}$) of the previous space step $i - 1$. Based on the values of $D_{app,Cl}$, the free chloride concentration ($\boldsymbol{c}_{i,j+1}$) at time step ($j + 1$) was calculated on the basis of free chloride concentrations ($\boldsymbol{c}_{i,j}$, $\boldsymbol{c}_{i-1,j}$, and $\boldsymbol{c}_{i+1,j}$,) at the previous time step j at spaces i, $i - 1$ and $i + 1$.

This study also does not consider the influence of carbonation on the chloride binding capacity of AAS. Some authors have shown that the chloride binding capacity of a binder is reduced due to carbonation of the binder as some of the bound chloride could be released back into the

pore solution [142], which would in turn increase the availability of free chloride to diffuse through the concrete matrix. It must be mentioned that portlandite is generally not precipitated in AAMs [80], and therefore, unlike PC based binders, these binders do not possess a buffering capacity where portlandite could readily dissolve to maintain the pH of the pore solution. It could therefore be expected, that in the case of AAS, carbonation would significantly reduce the binding capacity of these materials. However, carbonation effects are beyond the scope of this study.

6.3 Results and Discussion

6.3.1 Chemistry of the concrete cover

Figure 6-7 shows the simulated evolution of solid phase assemblages for slag with composition M6, activated using various solutions. The composition of slag M6 was obtained from the literature [293], with the SiO_2 and SO_3 contents in this slag being 36 wt. % and 0.7 wt. %, respectively. As mentioned in Section 6.2.1, the first consideration used by the MATLAB script in extracting the simulated phase assemblage data is the SiO_2 content within the slag, and for any SiO_2 content $\geq$ 35 wt. % the script assumes the SiO_2 content in slag to be 40 wt. %. Therefore, the data plotted in Figure 6-7 correspond to thermodynamic calculations conducted on slag with 40 wt. % SiO_2 and 2 wt. % SO_3. However, it is it to be noted that the normalised CaO-MgO-Al_2O_3 molar ratios used to simulate the phase assemblages of M6 activated by various solutions correspond to the actual slag composition, which was calculated to be 0.74:0.16:0.10. The following discussion needs to be viewed in combination with Figure 6-8 which shows the influence of slag MgO content on the simulated solid phase assemblages when the extent of slag reaction is 60 % using different activators.

Irrespective of the kind of activator, the hydration products of AAS are dominated a by C-(N-)A-S-H gel (as shown in Figure 6-7 and Figure 6-8). The Ca/Si ratio in the C-(N-)A-S-H gel for all the activators, when the extent of reaction was 60 %, was estimated to be between 0.91 and 1.06 - much lower than the Ca-rich C-S-H gel observed in hydrated PC [41]. Similar

values have been reported in the literature [29,39,330] for NaOH and waterglass activated slags. The Ca/Si ratio was found to be the highest for NaOH-activated slags when compared to the other activators, as seen by other workers [29,39]. In the case of Na_2CO_3-activated M6, the Ca/Si ratio in the C-(N-)A-S-H gel was simulated to be around 0.95, within the range of values reported by Ke et al. [293]: between 0.8 and 1.6 (with an average value of 1.20 ± 0.02) after 180 d. In the case of slag M6 activated by NaOH, Na_2SiO_3 and Na_2CO_3, the Al/Si ratios were found to be 0.13, 0.11 and 0.10, respectively. The Al/Si ratios observed in this study are very similar to those simulated by Myers et al. [220], and experimental observations [178,331]. The Al/Si ratios in the case of Na_2SO_4 and $Na_2O{\cdot}2SiO_2$ activation of M6 were observed to be close to a lower value of ~0.08, due to much of the Al being consumed by the secondary hydration products in the former case, and the higher Si provided by the activator in the case of the latter.

Irrespective of the activator used, the bulk MgO content in the slag was found to have a significant influence on the chemistry of the simulated C-(N-)A-S-H gel when the extent of slag reaction was 60 % (as seen in Figure 6-8). As proposed by Bernal et al. [178], reduced bulk MgO contents in slags leads to a higher Al-uptake in the C-(N-)A-S-H gel, and this was confirmed for all activators by the simulated results shown in Figure 6-8. In reaction of MgO-rich slags, much of the Al is consumed in the formation of secondary hydration products such as hydrotalcite-like phases [178], therefore resulting in very low Al/Si ratios in C-(N-)A-S-H.

In NaOH-activated M6, the secondary reaction products were Mg-Al-OH-LDH, katoite (C_3AH_6) and strätlingite (C_2ASH_8), as shown in Figure 6-7A. The formation of a hydrotalcite-like Mg-Al-OH-LDH phase in AAS has been confirmed by various authors [29,43,125,178,220,332]. The quantity of hydrotalcite-like phase in the solid phase assemblage was found to be directly proportional to the extent of slag reaction (Figure 6-7A) and the amount of MgO in slag (as shown in Figure 6-8A). At low MgO contents, for example in slags M1 and M5, the secondary hydration products are dominated by the formation of katoite and strätlingite. However, at higher MgO contents in slags, as in the case of M6, M8, M11, M13 and M14, hydrotalcite-like Mg-Al-OH-LDH phase dominates the secondary hydration products with trace quantities of katoite and strätlingite. As observed in [178,332], reduced levels of MgO in slags resulted in a higher Al-uptake within the C-(N-)A-S-H gel. Katoite has been reported to be present as a minor secondary reaction product in NaOH-activated slags. The presence of katoite in this study was only observed for Ca-rich slags where the bulk C/S ≥ 1.14 (M1, M5 and M6) and this observation aligns well with those reported in [80,333,334]. Strätlingite is also a minor constituent observed in NaOH-activated slags with low MgO

contents [332]. The stability of strätlingite in C-(A-)S-H systems at low temperatures (around 20 °C) was confirmed by Okoronkwo and Glasser [335]. Trace quantities of natrolite ($Na_{0.4}Al_{0.4}Si_{0.6}O_2{\cdot}0.4H_2O$) and brucite (MH) were observed to form in slags containing high amounts of MgO; M13 and M14, respectively.

In Na_2SiO_3-activated and $Na_2O{\cdot}2SiO_2$-activated M6 (as shown in Figure 6-7B and Figure 6-7C, respectively), the secondary hydration products are characterised by the formation of hydrotalcite-like phase, natrolite, strätlingite, and brucite. In addition, trace quantities of Ca-heulandite are also seen to form in the case of $Na_2O{\cdot}2SiO_2$-activated M6. Hydrotalcite-like Mg-Al-OH-LDH phase was predicted to be the most dominant secondary reaction product in both Na_2SiO_3 and $Na_2O{\cdot}2SiO_2$-activated M6, and the quantity of hydrotalcite-like Mg-Al-OH-LDH phase formed was strongly dependent on the bulk MgO content in slag (as seen in Figure 6-8B and Figure 6-8C). Hydrotalcite-like Mg-Al-OH-LDH phases have often been reported to form in these systems in the literature [30]. Trace quantities of strätlingite were observed to precipitate in Na_2SiO_3-activated M6, however were absent in $Na_2O{\cdot}2SiO_2$-activated M6. The stability of strätlingite was found to be much higher in slags containing 30 wt. % SiO_2 and low MgO contents (M1 and M5) when compared to slags containing 40 wt. % SiO_2 (M6 to M14) for both activators. The formation of strätlingite in these systems is in fairly good agreement with experimentally determined solid phase assemblages of Na_2SiO_3 and $Na_2O{\cdot}2SiO_2$-activated slags with similar compositions to those discussed here [43,220,330,336].

Ca-heulandite was predicted to precipitate in trace quantities in $Na_2O{\cdot}2SiO_2$-activated M6, but was absent in the Na_2SiO_3-activated M6. Ca-heulandite was predicted to only form in slags containing 40 wt. % SiO_2 and high MgO contents (M6 to M14), and was more pronounced in $Na_2O{\cdot}2SiO_2$-activated slags (Figure 6-8B and Figure 6-8C), due to the higher Si content provided by the activator. Natrolite was predicted to form for both activators, with much higher quantities being precipitated in $Na_2O{\cdot}2SiO_2$-activated M6 due to the additional Si provided by the activator (Figure 6-7B and Figure 6-7C). The higher stability of natrolite in activation of high-SiO_2 slags has been reported previously [80], and this can be evidenced in Figure 6-8B and Figure 6-8C, where natrolite is only predicted to form in slags simulated with 40 wt. % SiO_2. The presence of zeolitic phases such as Ca-heulandite and natrolite aligns well with the experimental observations of gismondine in AAS activated using Na_2SiO_3 and $Na_2O{\cdot}2SiO_2$ [178].

Katoite is observed to form in minor and trace quantities only in slags containing 30 wt. % SiO_2 (M1 and M5) activated using Na_2SiO_3 and $Na_2O{\cdot}2SiO_2$, respectively. Brucite is also

predicted to form in trace quantities in Na_2SiO_3 and $Na_2O{\cdot}2SiO_2$-activated M6 when the extent of slag reaction is relatively low. However, in slags containing relatively high amounts of MgO (M6 to M14), brucite is found to be more stable at later stages of reaction. The prediction of brucite in the solid phase assemblages of slags activated using NaOH, Na_2SiO_3 and $Na_2O{\cdot}2SiO_2$ in this study is in contradiction with all experimental observations for AAS [30,39,41,253,296,334,336]. This could possibly be explained by the lack of thermodynamic data for MgO-SiO_2-H_2O (magnesium silicate hydrate or M-S-H) phases in the database. Recent experimental observations [42,337,338] indicate that brucite could stabilise in these systems, but their compatibility in AAS systems needs to be further understood.

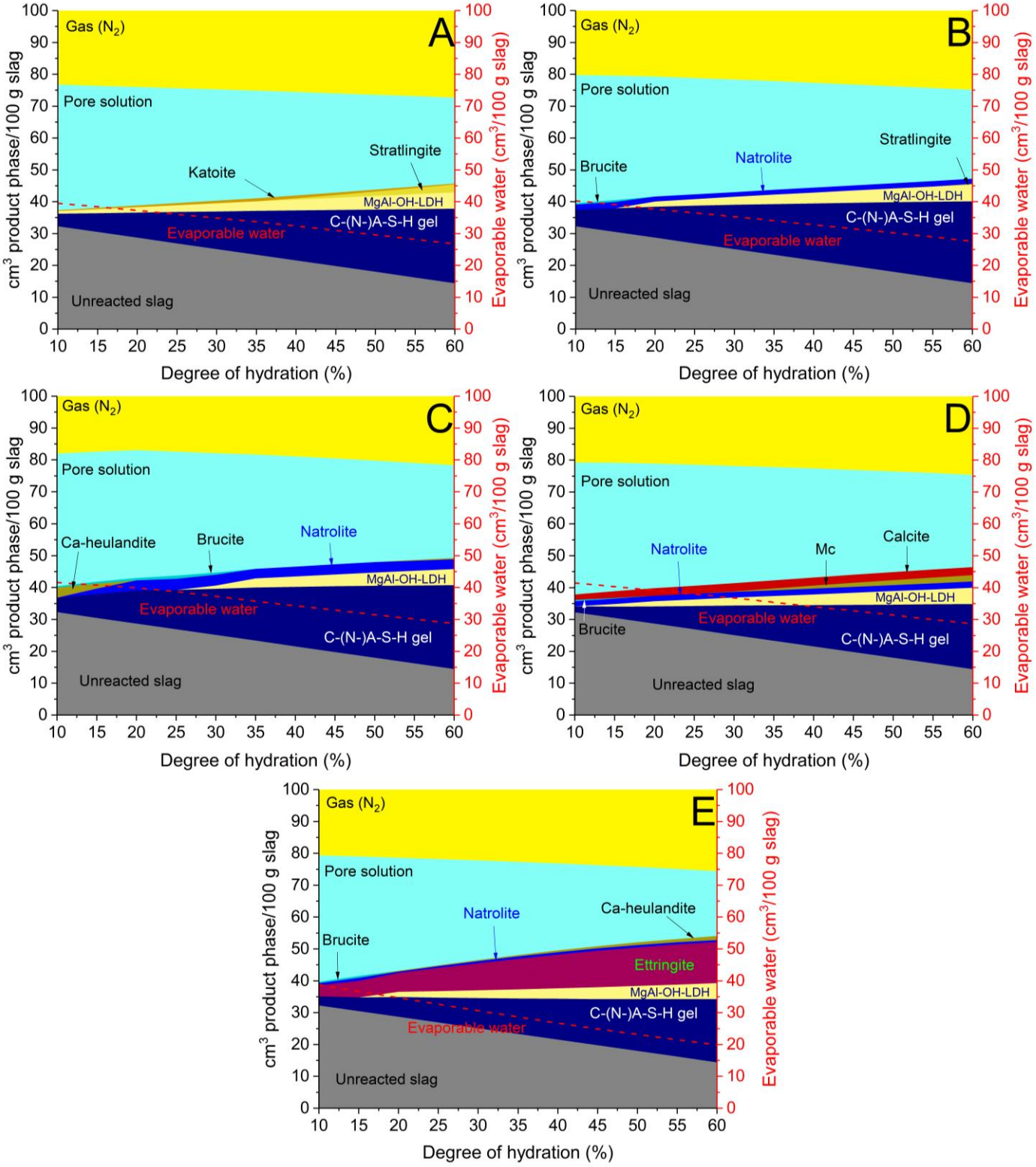

Figure 6-7: Simulated solid phase assemblages in slag (M6) activated using (A) NaOH, (B) Na_2SiO_3, (C) $Na_2O{\cdot}2SiO_2$, (D) Na_2CO_3, and (E) Na_2SO_4, plotted as a function of the extent of slag reaction. The evaporable water in each system is assumed to be the water content within the pore solution.

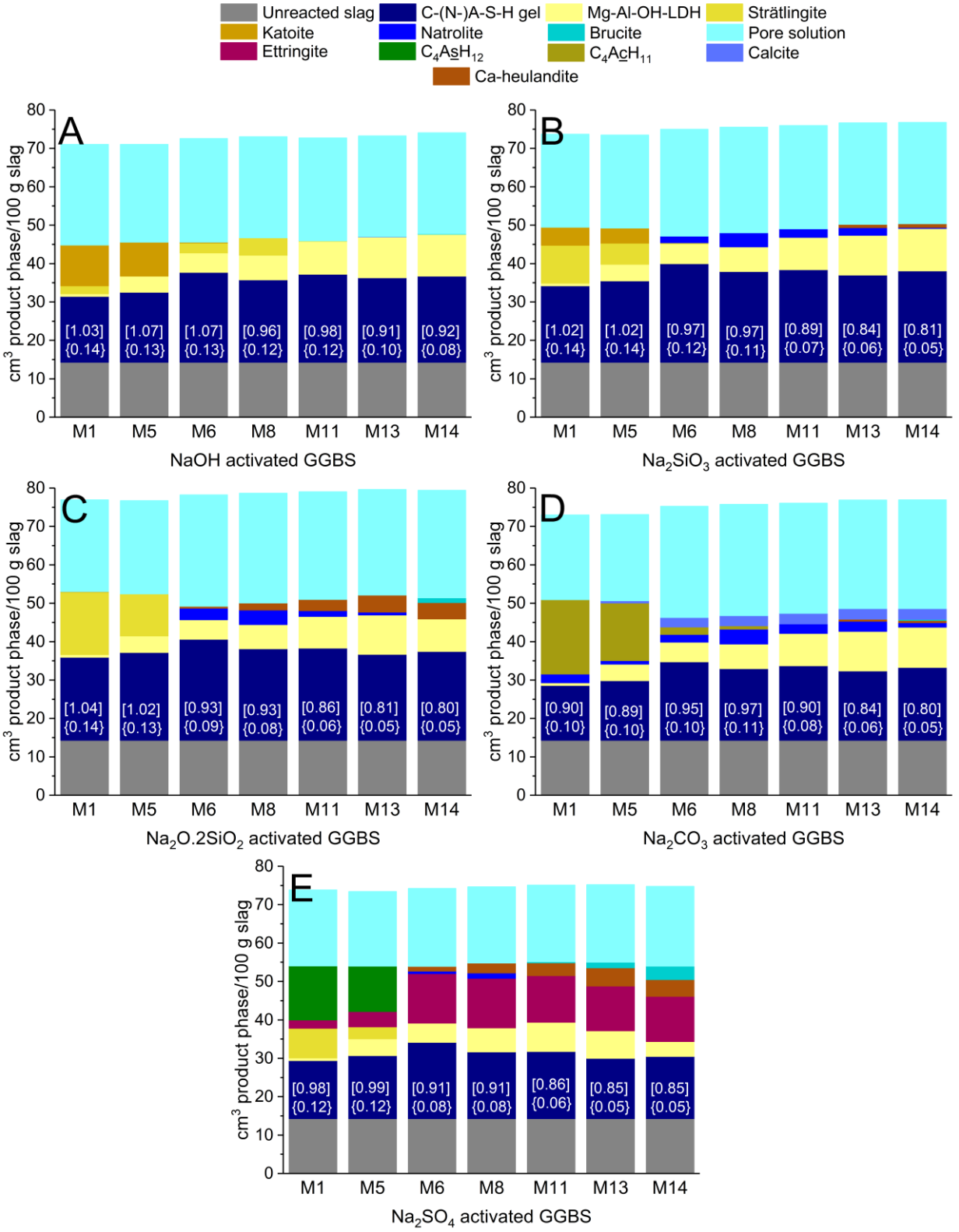

Figure 6-8: Influence of bulk MgO content in slags, and the type of activator in the simulated solid phases when the extent of slag reacted is 60 %. The values in square [] and

curly brackets {} within the navy-blue background indicate the calculated Ca/Si and Al/Si ratios in the C-(N-)A-S-H gel, respectively.

In Na_2CO_3-activated M6 (as shown in Figure 6-7D), hydrotalcite-like phase (Mg-Al-OH-LDH), natrolite, calcium monocarboaluminate hydrate ($C_4A\underline{c}H_{11}$; AFm structure type, and abbreviated Mc) and calcite ($CaCO_3$) were observed to form. Similar to NaOH, Na_2SiO_3, and $Na_2O{\cdot}2SiO_2$-activated M6, the formation of hydrotalcite-like phase was dependent on the extent of slag reaction and the bulk MgO content of the slag. As highlighted in [295,339], the MgO content within the slag plays a critical role in the kinetics of Na_2CO_3-activated slags, and higher bulk MgO contents lead to a higher rate of reaction and quicker setting times. The authors of those studies observed the consumption of aqueous CO_3^{2-} in the pore solution as the rate determining step, and higher amounts of hydrotalcite-type phase (capable of consuming carbonate species from the pore solution through ion-exchange) formed due to higher amounts of MgO is the primary reason for the increased kinetics of the system [295]. Given the high concentration of CO_3^{2-} present in the pore solution at the early stages of the reaction and the preference of Mg-Al-LDH to be intercalated with CO_3^{2-}, it would be reasonable to assume the presence of the carbonate containing hydrotalcite-like phase in Na_2CO_3-activated M6. However, simulated phase assemblages of these binders only indicate the formation of the carbonate-free counterpart. This is due to the lower solubility of Mg-Al-OH-LDH than Mg-Al-CO_2-LDH at pH >13, as assessed by the MA-OH-LDH_ss solid solution model [220], however more thermodynamic data pertaining to Mg-Al type LDH are required to thoroughly predict the stability of the hydrotalcite-like phases in these binders [80]. The occurrence of natrolite in Na_2CO_3-activated M6 is consistent with the presence of zeolite-A in X-ray diffractograms [339]. The formation of natrolite was predicted for all slags considered in this study and indicates the coexistence of C-(N-)A-S-H and N-A-S-H type gels, as put forward by Provis et al. [30].

The prediction of calcite is in-line with the experimental observations of various $CaCO_3$ polymorphs (vaterite, calcite, aragonite) in these binders cured for 180 days [339], 20 months [340] and aged concretes as well [341]. The thermodynamic stability of various polymorphs of $CaCO_3$ is very similar and their precipitation is kinetically controlled. Various authors have experimentally observed the formation of gaylussite ($Na_2Ca(CO_3)_2{\cdot}5H_2O$) in Na_2CO_3-activated slags at early ages [295,339], however, this was not observed in the predicted solid phase assemblage, and Myers et al. [220] suggested that formation of gaylussite in these binders cured at room temperature is due to kinetic factors.

Monocarboaluminate is predicted to form in trace quantities for Na_2CO_3-activated M6, similar to what has been observed experimentally [295] and predicted thermodynamically [220]. The formation of monocarboaluminate species in Na_2CO_3-activated slags is closely associated with the bulk MgO and SiO_2 content in the slag (as seen in Figure 6-8D) and this was found to be a major reaction product in slags with lower MgO and lower SiO_2 contents (M1, M5, or slags where the SiO_2 content was assumed to be 30 wt. %). Slags with higher SiO_2 and high MgO content (M6, M8, M11, M13 and M14, or slags where the SiO_2 content was assumed to be 40 wt. %) were observed to form monocarboaluminate in minor or trace quantities, indicative of an inverse relationship between its stability and the bulk SiO_2 content within the slag. Similar results have been observed in X-ray diffractograms obtained by Ke et al. [295], where M1 activated using Na_2CO_3 contained monocarboaluminate as a significant secondary reaction product, whereas for slag M14, hydrotalcite-like phase was the main secondary reaction product. For slags with intermediate MgO contents (M6), those authors [295] observed the precipitation of a less stable AFm type phase called calcium hemicarboaluminate hydrate ($C_4A\underline{C}_{0.5}H_{12}$) in conjunction with hydrotalcite-like phase and monocarboaluminate. The formation of hemicarboaluminate was not observed in the simulated phase assemblage for M6. Additionally (as seen in Figure 6-8D), in slags with high bulk MgO content and ~40 wt. % SiO_2 (M13 and M14), Ca-heulandite and brucite were predicted to form in trace quantities. Unlike NaOH, Na_2SiO_3 and $Na_2O{\cdot}2SiO_2$-activated slags, katoite and strätlingite were not predicted to form in Na_2CO_3 activation.

In Na_2SO_4-activated M6 (Figure 6-7E), ettringite ($C_6A\underline{S}_3H_{32}$) was predicted to be the dominant secondary reaction product with minor quantities of hydrotalcite-like phase and trace quantities natrolite, brucite and Ca-heulandite. Ettringite has been observed to the major secondary reaction product in Na_2SO_4-activated slags by various authors [342–345], and is primarily responsible for the higher solids volume of these binders than other activated slags. As seen in Figure 6-7E, and pointed out by Wang and Scrivener [118] and seen in X-ray diffractograms of 1 month cured Na_2SO_4-activated slags [343], the hydration of these binders at early stages was initiated by the formation of ettringite along with the C-(N-)A-S-H gel. Ettringite was estimated to be stable over the entire range of slags (M1 to M14) studied here (as shown in Figure 6-8E), but with a much higher stability for slags with higher bulk SiO_2 content (M6 to M14, or slags where SiO_2 content was assumed to be 40 wt. %). In contrast, for slags simulated with 30 wt. % SiO_2 (M1 and M5), calcium monosulfoaluminate hydrate ($C_4A\underline{S}H_{12}$) and strätlingite were observed to be the most stable secondary reaction products. Similar results were seen by Myers et al. [80] and Bernal et al. [345], where the formation of

monosulfoaluminate and strätlingite was predicted only for slags with 30 wt. % SiO_2 and intermediate to high Al_2O_3 content (M1 and M5). As expected, and seen in Figure 6-8, the hydrotalcite-like phase was found to have a much lower stability in slags with low MgO contents and with 30 wt. % SiO_2 (M1 and M5) when compared to their higher SiO_2 and higher MgO containing counterparts (M6 to M14). Both natrolite and Ca-heulandite were simulated to be formed in minor/trace quantities in the entire domain of extent of slag reaction for Na_2SO_4-activated M6. The presence of both these phases has been confirmed in [80] for slags with higher SiO_2 and Al_2O_3 contents, as in M6. Minor amounts of brucite was also predicted to form in slags with very high bulk MgO contents (M13 and M14).

6.3.2 Chloride diffusion

As mentioned in Section 6.2.2, based on the data from the simulated solid and aqueous phase assemblages when the extent of slag reaction was 60 %, chloride binding isotherms for each AAS were calculated, so they could be utilised to calculate the apparent chloride diffusion coefficient as a function of the free chloride concentration, and to estimate the ingress of chloride in each of these binders. Given that rate of slag reaction tends to be very slow after 60 % extent of reaction [220], chloride binding isotherms and chloride diffusion were modelled using simulated solid and aqueous phase assemblages when the extent of slag reaction was 60 %. The degree of slag reaction as a function of time in AAS is not available in the open literature and therefore, has not been incorporated in the modelling framework.

6.3.2.1 Influence of chloride binding

Figure 6-9 shows a representative example depicting the influence of chloride binding on the chloride ingress profiles calculated for concretes made from Na_2SiO_3-activated M6 at various ages of exposure. As mentioned in Section 6.2.2, it must also be noted that the migration coefficient (D_{nnsm}) obtained by [293] was assumed to underestimate chloride binding occurring within AAS, and therefore has been considered to be the value to be used when there is no chloride binding (as shown in Figure 6-9). Chloride binding significantly retards the transport of chloride towards the steel-concrete interface, and its importance can be clearly seen in chloride profiles modelled at later stages (Figure 6-9D). As seen by numerous researchers, chloride binding decreases the concentration of free chloride ions in the pore solution that are available to diffuse through the material [117,322,346]. Therefore, the use of D_{nssm} as a

parameter to characterise the ingress of chloride may significantly underestimate the service life of concrete structures based on AAS.

Figure 6-9 also compares the influence of using a constant value of $D_{app,Cl}$, calculated based on the maximum chloride binding capacity of a binder (denoted by a blue dotted line), and the $D_{app,Cl}$ dependent on the free chloride concentration, calculated based on the Freundlich adsorption isotherm (denoted by the red dashed line). As seen in Figure 6-9, using a fixed diffusion coefficient and assuming the highest chloride binding capacity (calculated using the Freundlich adsorption isotherm) to be true for all concentrations of free chloride and through the entire depth of the concrete cover overestimates the extent of chloride binding when the free chloride concentration is low, and also overestimates the service life. For example, it can be initially assumed, as a case study, that the cover depth and the chloride 'threshold' value for a steel-reinforced concrete structure based on Na_2SiO_3-activated M6 are around 20 mm and 0.2 wt. % of binder, respectively. The influence of chloride binding on the initiation time can be evidenced by the time it takes for the chloride concentration at the steel-concrete interface to build up to 0.2 wt.% of binder. In the case of no chloride binding and the $D_{app,Cl}$ being equal to D_{nnsm}, the initiation time was found to be ~15 years, whereas the initiation time was found to be ~70 years in the case of assuming the maximum binding capacity of the binder to be true for the entire depth of the concrete cover and using a fixed diffusion coefficient. However, when $D_{app,Cl}$ was related to the free chloride concentration (according to calculated binding isotherms), the initiation time was ~ 50 years. Hence, the most appropriate way of determining the ingress of chloride would be to relate the $D_{app,Cl}$ to the free chloride concentration by experimentally observed chloride binding isotherms. To the authors' best knowledge, experimental chloride profiles for AAS are not present in the literature, and therefore, the direct validation of the modelling results with experimental data was not possible.

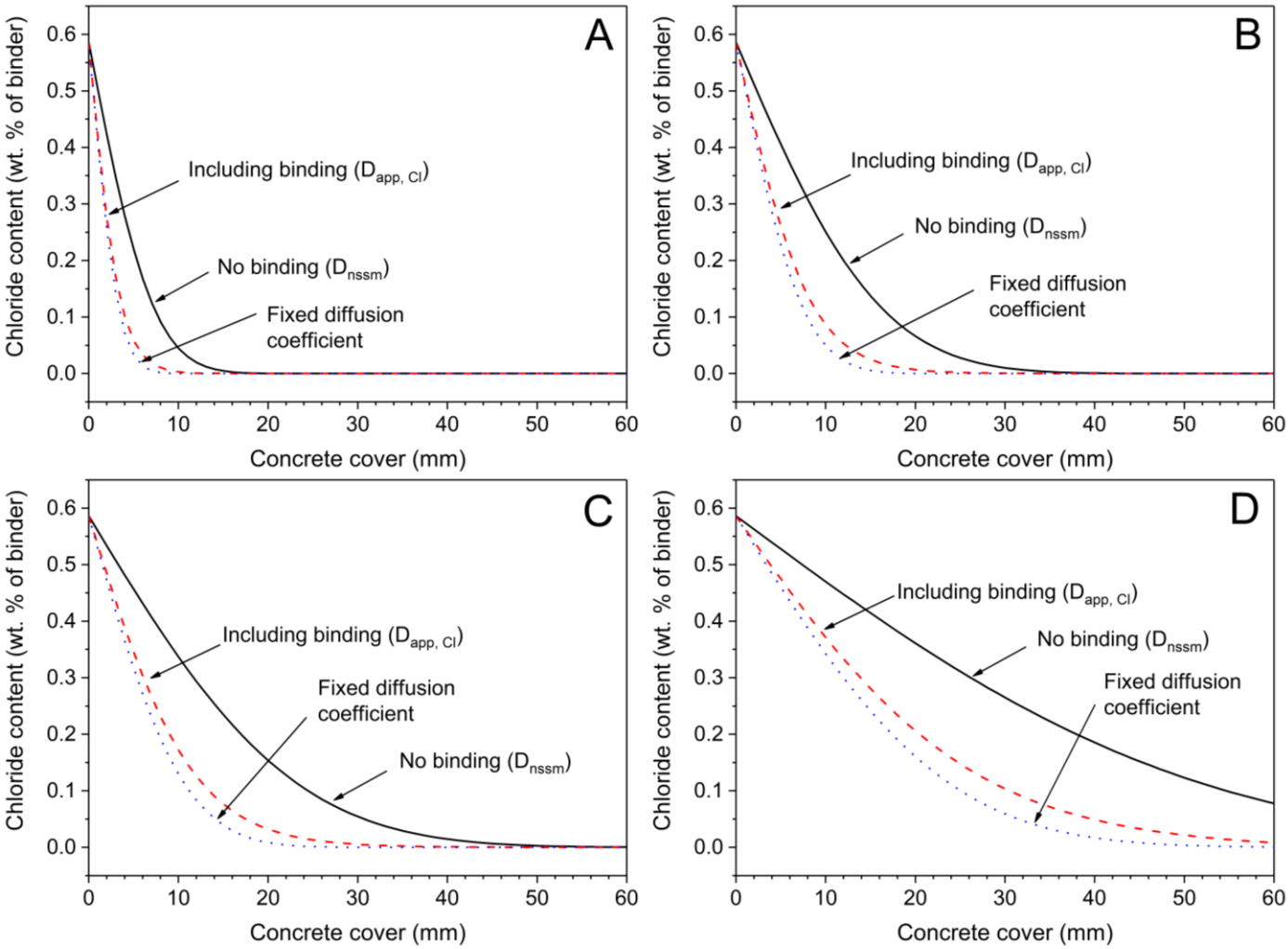

Figure 6-9: Influence of chloride binding on the chloride ingress profiles calculated for Na_2SiO_3-activated M6 at times (A) 1 year, (B) 5 years, (C) 10 years and (D) 50 years. The solid lines represent the case of no binding, and the apparent diffusion coefficient was assumed to be the value of the migration coefficient obtained from NT Build 492 [293]. The red dashed lines represent the case when the apparent diffusion coefficient was calculated using the free chloride concentration (based on the Freundlich adsorption isotherm) at the preceding space step for any given time step. The dotted blue lines represent the scenario when the apparent diffusion coefficient was kept constant and calculated using only the maximum chloride binding capacity of the binder.

One of the major advantages of relating the $D_{app,Cl}$ to the binding capacity of each of the hydrate phases present in a concrete structure, is the avoidance of the mathematically 'erroneous' usage of an empirically derived time-dependent diffusion coefficient (Eq. 3.7) in Eq. 2.14 – as is used by many service-life guidelines [323,324].

Table 6-5 shows the calculated binding constants of the Freundlich adsorption isotherm and the thermodynamically estimated evaporable water content expressed as volume % of the total binder (i.e., the volume % that is H_2O in the pore solution), used to derive a relationship between $D_{app,Cl}$ and the free chloride concentration for various AAS compositions when the extent of slag reaction is 60 %. The values of α and β Freundlich adsorption isotherm parameters obtained by fitting the chloride binding isotherms are only validated for free chloride concentrations up to 0.654 M, beyond which experimental data do not exist in the case of AAS, so any values at higher concentrations are extrapolations [293]. The binding parameter β calculated for all activated slags was greater than 1, which suggests that much of the chloride binding in AAS (for free chloride concentrations < 0.654 M) occurs via chemisorption rather than physical adsorption [347,348]. However, it can be assumed that at higher free chloride concentrations, the extent of binding becomes constant and the value of the β parameter would be < 1 [317,328,349]. Such behaviour has been reported in the literature in the case of PC based binders, as well as for individual binding capacity of various hydrate phases [13,317,319,325]. As stated in Section 6.2.2, the lack of experimental data in the case of AAS above a free chloride concentration > 0.654 M, makes the proposed model only applicable to exposure solutions < 0.654 M.

Table 6-5: Estimated values of binding constants and the evaporable water used to estimate the $D_{app,Cl}$ as a function of the concentration at each space and time step, for slags with varying compositions activated using NaOH, Na_2SiO_3, $Na_2O{\cdot}2SiO_2$, Na_2CO_3 and Na_2SO_4, when the chloride binding isotherms are described by the Freundlich adsorption isotherm (as shown in Eq. 6.8). The evaporable water content (volume %) relates to the total H_2O content in the pore solution of AAS, when the extent of slag reaction is 60 % and is obtained by the thermodynamic simulations.

	NaOH			**Na_2SiO_3**			**$Na_2O{\cdot}2SiO_2$**		
	α	***β***	**Evaporable water**	***α***	***β***	**Evaporable water**	***α***	***β***	**Evaporable water**
M1	0.29	1.22	36.55	0.85	1.08	32.50	1.32	1.03	30.76
M5	0.27	1.33	35.53	0.67	1.17	32.63	1.05	1.11	31.31
M6	0.46	1.28	36.83	0.46	1.28	36.74	0.46	1.28	36.68
M8	0.56	1.26	35.69	0.44	1.29	35.98	0.45	1.29	35.87
M11	0.40	1.36	36.46	0.48	1.31	34.99	0.48	1.30	35.04
M13	0.42	1.37	35.46	0.49	1.32	34.03	0.49	1.32	34.17
M14	0.41	1.37	35.21	0.51	1.32	33.90	0.47	1.31	34.78

	Na_2CO_3			**Na_2SO_4**		
	α	***β***	**Evaporable water**	***α***	***β***	**Evaporable water**
M1	0.25	1.22	29.83	0.85	1.06	26.41
M5	0.36	1.28	30.32	0.61	1.20	26.06
M6	0.46	1.28	38.05	0.46	1.28	26.85
M8	0.46	1.29	37.79	0.45	1.29	26.08

M11	0.51	1.31	37.26	0.51	1.30	26.03
M13	0.52	1.32	36.32	0.43	1.31	26.26
M14	0.53	1.32	36.39	0.36	1.27	27.26

6.3.2.2 Influence of slag composition

Figure 6-10 shows the influence of the slag composition on chloride ingress at 25 years of exposure to 3.5 wt.% (or 0.6 M) NaCl solution, calculated for NaOH (Figure 6-10A), Na_2SiO_3 (Figure 6-10B), $Na_2O{\cdot}2SiO_2$ (Figure 6-10C), Na_2CO_3 (Figure 6-10D) and Na_2SO_4 (Figure 6-10E) activated M1, M6, M11 and M14.

In the case of NaOH-activated slags (Figure 6-10A), an increase in the bulk MgO content of the slag leads to retardation in the chloride ingress, indicating a higher chloride binding capacity for NaOH-activated slags with higher MgO content. In slags with lower MgO content and higher CaO content, as in the case of NaOH-activated M1, the chloride binding capacity of the binder is primarily governed by the amounts of strätlingite and C-(N-)A-S-H gel formed. However, in the case of intermediate and high MgO slags, as in NaOH-activated M6, M11 and M14, the precipitation of higher amounts of hydrotalcite-like Mg-Al-OH LDH phase (as observed in Figure 6-10A) increases the total chloride binding capacity, thereby retarding the ingress of chloride in these binders.

According to the quantities of each reaction product (Figure 6-8A) and the individual binding isotherms of C-(N-)A-S-H gel, hydrotalcite-like Mg-Al-OH LDH phase and strätlingite obtained experimentally by Ke [293], as shown in Figure 6-4, at relatively high or low concentrations of free chloride, the total binding capacity of the binder would be primarily dominated by the C-(N-)A-S-H gel. However, at intermediate concentrations of free chloride, much of the chloride binding is due ion-exchange and physical adsorption to the secondary reaction products such as hydrotalcite-like Mg-Al-OH LDH phase and strätlingite (Figure 6-4). This is true for all the NaOH-activated slags. For constant exposure to 3.5 wt. % NaCl solution, the calculated surface concentration was found to only marginally change for all NaOH-activated slags shown in Figure 6-10A. This is primarily due to the similar amounts of

evaporable water calculated (as observed in Figure 6-10A) for each of the binders at 60 % extent of slag reaction.

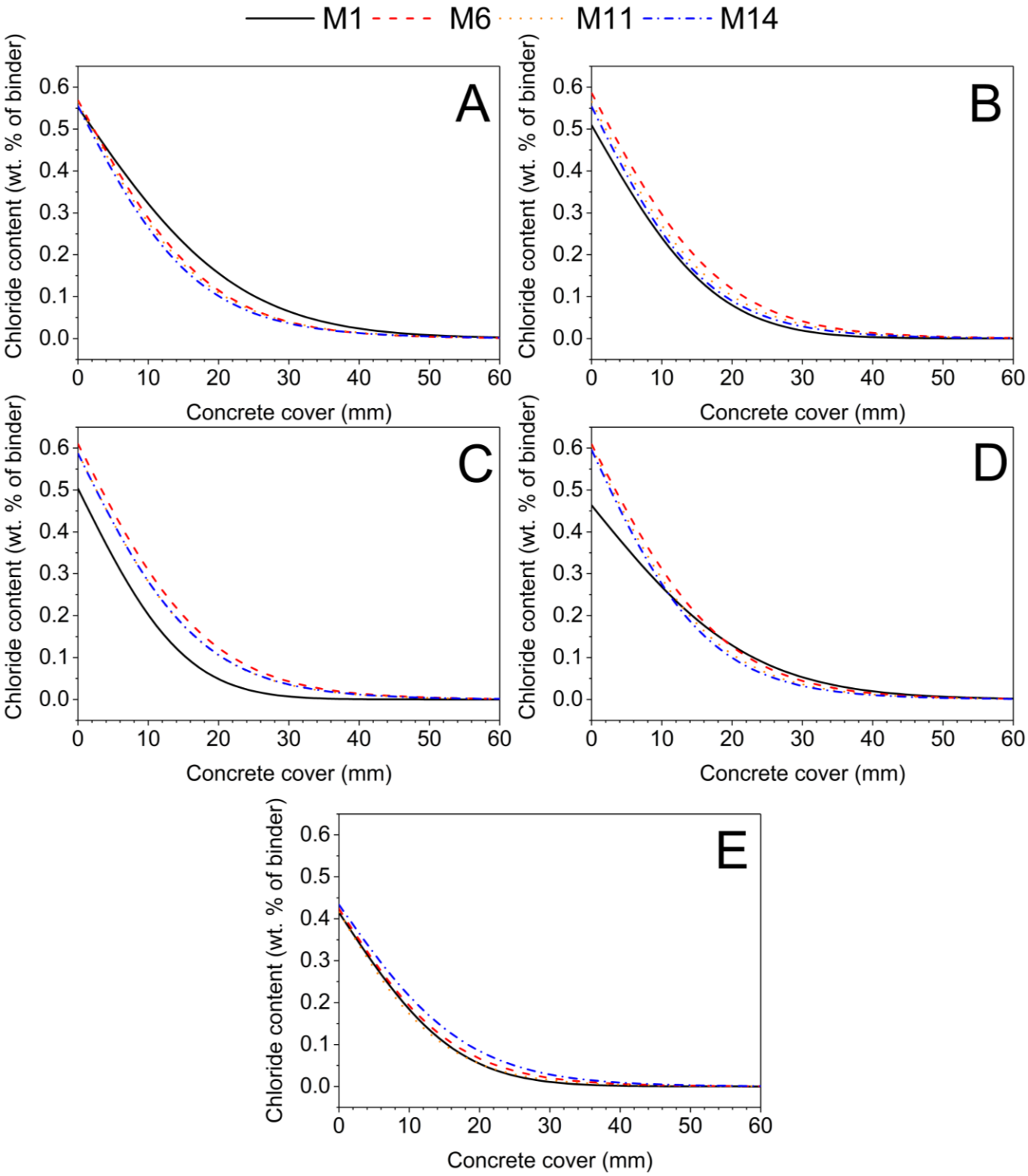

Figure 6-10: Influence of the slag composition on chloride ingress profiles calculated for (A) NaOH, (B) Na_2SiO_3, (C) $Na_2O{\cdot}2SiO_2$, (D) Na_2CO_3 and (E) Na_2SO_4 activated M1, M6, M11 and M14 at 25 years of exposure to 0.6 mol/L or 3.5 % NaCl solution.

Unlike NaOH-activated slags, in the case of Na_2SiO_3 and $Na_2O{\cdot}2SiO_2$-activated slags (Figure 6-10B and Figure 6-10C, respectively) chloride ingress was found to be the slowest in the case of slag M1, when compared to M6, M11 and M14. A closer look at Figure 6-10B reveals that at high concentrations of free chloride the extent of chloride binding (depending on the slope, $\Delta c/\Delta x$, of the chloride ingress profiles) is slightly higher in the case of Na_2SiO_3-activated M1 when compared to Na_2SiO_3-activated M6, M11 and M14, and the inverse being true at intermediate and low concentrations of free chloride. However, the binding capacity was found to be much higher at all concentrations of free chloride in the case of $Na_2O{\cdot}2SiO_2$-activated M1 (Figure 6-10C), when compared to $Na_2O{\cdot}2SiO_2$-activated M6, M11 and M14. In both Na_2SiO_3 and $Na_2O{\cdot}2SiO_2$-activated M1, the lower rates of chloride ingress could be attributed to the high amounts of secondary reaction product, strätlingite, formed in the binders (Figure 6-8B and Figure 6-8C). Therefore, in slags with low MgO content (as is the case in slag M1) activated using Na_2SiO_3 and $Na_2O{\cdot}2SiO_2$, the extent of chloride binding is strongly influenced by the chloride ion-exchange and chloride adsorption capabilities of the AFm-type structure of strätlingite. Much of the chloride binding in Na_2SiO_3 and $Na_2O{\cdot}2SiO_2$-activated M1 was due to the C-(N-)A-S-H gel and strätlingite, and only a small percentage of the total bound chloride was due to the hydrotalcite-like Mg-Al-OH LDH phase. In the cases of Na_2SiO_3 and $Na_2O{\cdot}2SiO_2$-activated M6, M11 and M14, chloride binding was only due to the presence of C-(N-)A-S-H gel and hydrotalcite-like Mg-Al-OH LDH phase, as no strätlingite was formed in these binders. Similar to the observations in Figure 6-10A, chloride binding was found to be the highest for slags (among M6, M11 and M14) containing higher bulk MgO contents, and consequentially slower chloride ingress. The surface chloride concentration was found to be much lower for Na_2SiO_3 and $Na_2O{\cdot}2SiO_2$-activated M1, when compared to the Na_2SiO_3 and $Na_2O{\cdot}2SiO_2$-activated M6, M11 and M14, primarily due to the lower volume of evaporable water (Figure 6-8B and Figure 6-8C).

In the case of Na_2CO_3-activated slags (Figure 6-10D), the extent of chloride binding was proportional to the bulk MgO content in the slag and thus the amount of hydrotalcite-like Mg-Al-OH-LDH phases. Na_2CO_3-activated M14 exhibited the slowest chloride ingress, followed by Na_2CO_3-activated M11, Na_2CO_3-activated M6 and Na_2CO_3-activated M1. In the case of Na_2CO_3-activated slags, chloride binding occurs only due to the presence of the C-(N-)A-S-H gel and the hydrotalcite-like Mg-Al-OH LDH phase, as no strätlingite was observed to precipitate during Na_2CO_3 activation of slags (Figure 6-8D). However, in the cases of Na_2CO_3-activated M1 and M6, where monocarboaluminate forms as a major and minor reaction product (Figure 6-8D) respectively, the total chloride binding capacity could be underestimated in these

calculations primarily because the chloride binding capacity of monocarboaluminate was not considered. Ke et al. [350] investigated the chloride binding capacity of Na_2CO_3-activated slags, and observed the transformation of monocarboaluminate to two polymorphs of Friedel's salt with structures very similar to rhombohedral and monoclinic hydrocalumite. This transformation has been attributed to the partial exchange of interlayer CO_3^{2-} by Cl^- in the AFm structured monocarboaluminate phase [350–352]. Therefore, chloride binding isotherms for monocarboaluminate in simulated pore solutions representative of Na_2CO_3-activated slags are required to accurately predict the chloride ingress in these binders. Additionally, in carbonate-bearing pore solutions, the binding capacity of the hydrotalcite-like phase Mg-Al-OH-LDH phase has been observed to be reduced due to the higher affinity of the hydrotalcite-like phase to incorporate divalent ions (CO_3^{2-}) instead of monovalent ions [125,353]. Therefore, in Na_2CO_3-activated slags where the pore solution contains CO_3^{2-}, the extent of chloride binding due to hydrotalcite-like Mg-Al-OH LDH phase is partially overestimated in these calculations.

In the case of Na_2SO_4-activated slags (Figure 6-10E), the amount of chloride binding decreases with increase in bulk MgO content in slag (except for Na_2SO_4-activated M11) due to the decreasing quantities of precipitated hydrotalcite like Mg-Al-OH-LDH phases and C-(N-)A-S-H gel (Figure 6-8E). Additionally, significant amounts of strätlingite are formed in Na_2SO_4-activated M1 (as seen in Figure 6-8E), that contribute to its higher chloride binding capacity when compared to Na_2SO_4-activated M6 and M14. As mentioned earlier for the case of monocarboaluminate, the chloride binding capacities of additional phases formed during Na_2SO_4 activation of slags, such as monosulfoaluminate and ettringite, have not been considered. The transformation of monosulfoaluminate to Friedel's salt in PC based binders is well known [13,328], but chloride binding isotherms in simulated pore solutions of AAS do not exist in the literature. The ability of ettringite to bind chloride ions has been debated in the literature [327,328,354]. Therefore, the calculations of the total chloride binding capacity of Na_2SO_4-activated M1 conducted in this study can be plausibly assumed to be underestimated. Na_2SO_4-activated slag M11 exhibited the slowest chloride ingress among all the Na_2SO_4-activated slags due to the higher amounts of hydrotalcite like Mg-Al-OH-LDH phases formed in these binders in comparison to Na_2SO_4-activated slags M1, M6, and M14, and consequentially leading to a higher chloride binding capacity. The surface chloride concentration in the case of Na_2SO_4-activated slags in Figure 6-10E is much lower than those observed for other activators in Figure 6-10A-D due to the lower amount of evaporable water within these binders, because of the precipitation of voluminous ettringite in these binders – as seen in Figure 6-8E.

6.3.2.3 Influence of activator

Figure 6-11 shows the influence of various activating solutions (NaOH, Na_2SiO_3, $Na_2O{\cdot}2SiO_2$, Na_2CO_3 and Na_2SO_4) on the chloride ingress profiles calculated for activated (A) M1, (B) M6 and (C) M14 slags, after 5 years of exposure to 0.6 mol/L (3.5 wt.%) NaCl solution.

For slag M1 (Figure 6-11A), the use of NaOH as the activator shows the lowest chloride binding, whereas $Na_2O{\cdot}2SiO_2$-activated M1 exhibits the highest chloride binding. Irrespective of the activator, only very minor quantities of hydrotalcite-like Mg-Al-OH-LDH is formed for slag M1 (relatively very similar quantities with all activators, as this is limited by the Mg content of the slag). Therefore, the majority of the chloride binding is due to the physical adsorption of chloride on the C-(N-)A-S-H gel and strätlingite, and also due to the transformation of strätlingite to various polymorphs of Friedel's salt. Hence, the extent of chloride binding can be described as a function of the amounts of C-(N-)A-S-H gel and strätlingite formed.

The amounts of C-(N-)A-S-H gel formed as a function of the activator follow the following trend:

- $Na_2O{\cdot}2SiO_2$-activated M1 > Na_2SiO_3-activated M1 > NaOH-activated M1 > Na_2SO_4-activated M1 > Na_2CO_3-activated M1,

and for the amounts of strätlingite formed:

- $Na_2O{\cdot}2SiO_2$-activated M1 > Na_2SiO_3-activated M1 > Na_2SO_4-activated M1 > NaOH-activated M1 > Na_2CO_3-activated M1.

According to the quantities of C-(N-)A-S-H gel and strätlingite formed in NaOH and Na_2CO_3-activated M1, the extent of chloride binding is much lower for the latter and hence, the chloride ingress through Na_2CO_3-activated M1 should be faster. However, the lower surface concentration of chloride (due to the lower porosity in the binder – as seen in Figure 6-8A and Figure 6-8D) in Na_2CO_3-activated M1, the concentration of free chloride at any given point in space and time, defined on the basis of chloride per binder mass, is always lower than in NaOH-activated M1. As mentioned in Section 6.3.2.2, it must be noted that the chloride binding capacities for the cases of Na_2CO_3 and Na_2SO_4-activated M1 are underestimated, as chloride binding due to monocarboaluminate and monosulfoaluminate are not considered in this study.

In the case of slag M6 (Figure 6-11B), irrespective of the activator used except Na_2SO_4, very similar chloride ingress profiles are obtained. This is primarily due to the assumption made in Section 6.2.2 that irrespective of the activator, all activated M6 binders exhibit the same extent of chloride binding observed by Ke et al. [350] for Na_2SiO_3-activated M6. The assumption was made primarily due to lack of experimental chloride binding isotherms in the literature for various activators used to formulate AAS. Additionally, the amounts of reaction products, that were considered to contribute towards chloride binding in this study, formed for slag M6 activated using different activators were of similar quantities (Figure 6-7) leading to very similar chloride binding capacities for activated M6 slags. As seen in Table 6-5, the very minor differences in the chloride profiles arise only due to the total evaporable water content of the binders. The lower surface chloride concentration calculated for Na_2SO_4-activated M6 binders is the main reason why the observation of chloride ingress is much slower in these, when compared to M6 activated using other activators. As mentioned in Section 6.2.2, the chloride binding isotherms for Na_2CO_3-activated M6 obtained by Ke. et al. [350] showed a lower extent of binding when compared to their Na_2SiO_3-activated counterparts (but the chloride binding isotherm for Na_2CO_3-activated M6 from Ke. et al. [350] wasn't considered in this study), therefore in theory, the chloride ingress in Na_2CO_3-activated M6 should be much faster than those calculated in this study.

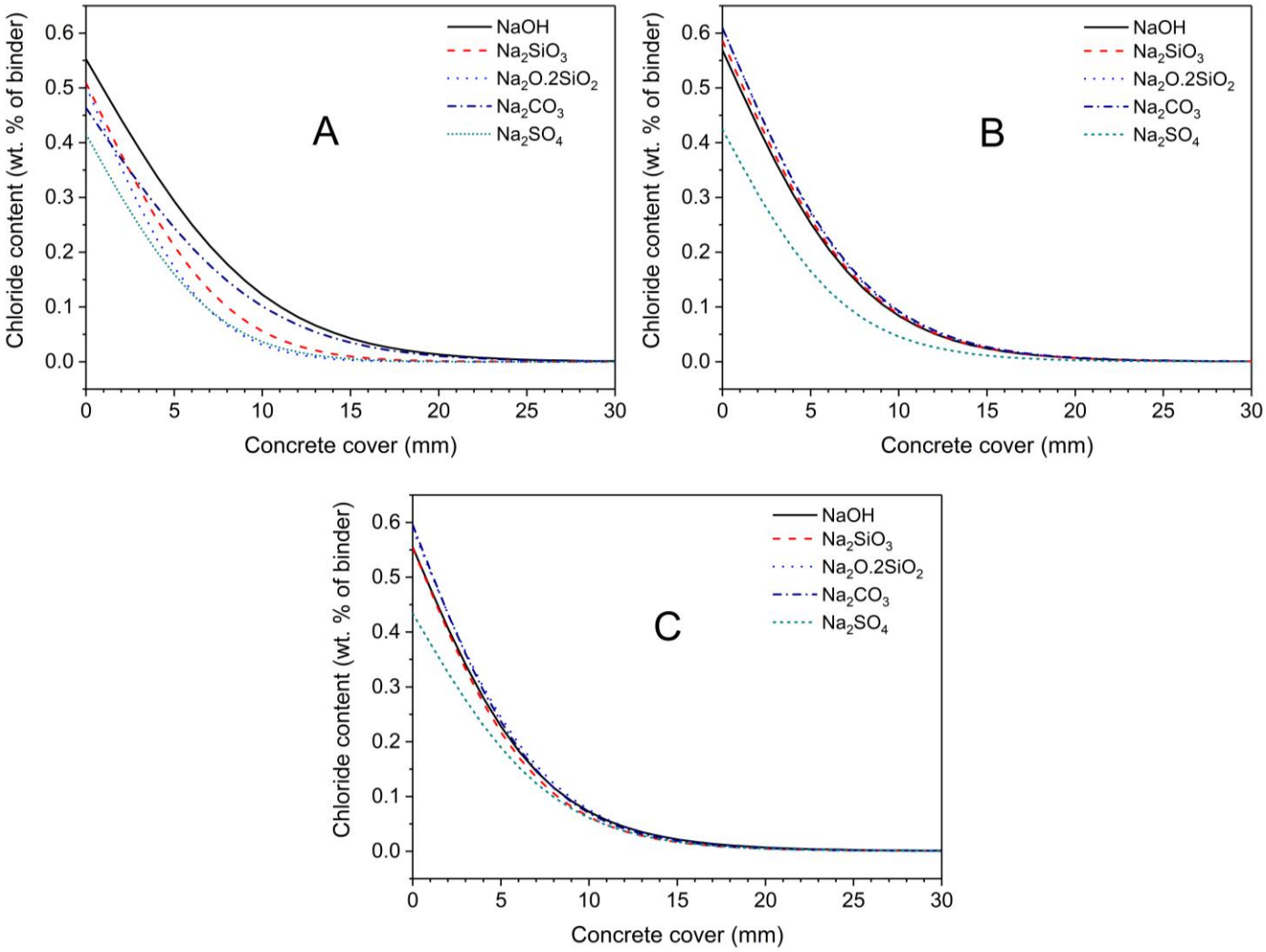

Figure 6-11: Influence of the activator (NaOH, Na_2SiO_3, $Na_2O{\cdot}2SiO_2$, Na_2CO_3 and Na_2SO_4) on the chloride ingress profiles calculated for activated (A) M1, (B) M6 and (C) M14 after 5 years of exposure. The x-axis in this figure has been reduced to 30 mm for a better indication of the differences in the chloride profiles for various activators. The exposure solution is assumed to be 0.6 mol/L (3.5 wt.%) NaCl solution.

The observations for M14 (Figure 6-11C) are fairly similar to those observed for slag M6 (Figure 6-11B), however, the extent of chloride binding primarily depends on the quantities of C-(N-)A-S-H gel and hydrotalcite like Mg-Al-OH-LDH phases formed for each of the activators. The amounts of C-(N-)A-S-H gel formed as a function of the activator follow the following trend:

- Na_2SiO_3-activated M14 > $Na_2O{\cdot}2SiO_2$-activated M14 > NaOH-activated M14 > Na_2CO_3-activated M14 > Na_2SO_4-activated M14,

and for the amounts of hydrotalcite like Mg-Al-OH-LDH phase formed:

- Na_2SiO_3-activated M14 > NaOH-activated M14 > Na_2CO_3-activated M14 > $Na_2O{\cdot}2SiO_2$-activated M14 > Na_2SO_4-activated M14.

When the free chloride concentration is intermediate, the chloride binding capacity of hydrotalcite like Mg-Al-OH-LDH phases is much higher compared to the C-(N-)A-S-H gel, and therefore, the chloride ingress into Na_2CO_3-activated M14 is slightly slower than its $Na_2O{\cdot}2SiO_2$-activated counterpart.

6.4 Conclusion

The slag chemistry and the type of activator have a significant influence on the chloride binding capacity of AAS concretes, and therefore impact the ingress of chloride in these materials. Additionally, the results shown in this Chapter successfully demonstrate the influence of various reaction products formed in AAS (based on slag and activator chemistry) on the chloride binding capacity. Figure 6-12 ranks the chloride ingress in various AAS as a function of slag chemistry for each activator. In the case of NaOH-and Na_2CO_3-activated slags, the rate of chloride ingress is correlated to the MgO content and the amounts of Mg-Al-OH LDH type phases formed. However, in the case of Na_2CO_3-activated slags, it must be noted that the influence of monocarbonate phases and the presence of minor quantities of CO_3^{2-} (aq.) species in the pore solution, have not been considered to contribute to chloride binding. In the case of Na_2SiO_3- and $Na_2O{\cdot}2SiO_2$-activated slags, M1 and M5 slags were found to have the slowest ingress of chloride due to the formation of strätlingite and their chloride binding capability. For slags M6-M14, the rate of chloride ingress is determined primarily by the amounts of Mg-Al-OH LDH phase formed. In $Na_2O{\cdot}2SiO_2$-activated M11, M13 and M14 the precipitation of Ca-heulandite and brucite influence the chloride binding capacity of the binder. In Na_2SO_4 activated slags, the chloride binding capacities of monosulfate and ettringite haven't been taken into account. The rate of chloride ingress in low MgO containing slags (M1 and M5) is primarily influenced by the precipitation of AFm, whereas in slags containing intermediate and high MgO (M6-M14), chloride ingress is dependent on the amounts of C-(N-)A-S-H gel and Mg-Al-OH LDH formed.

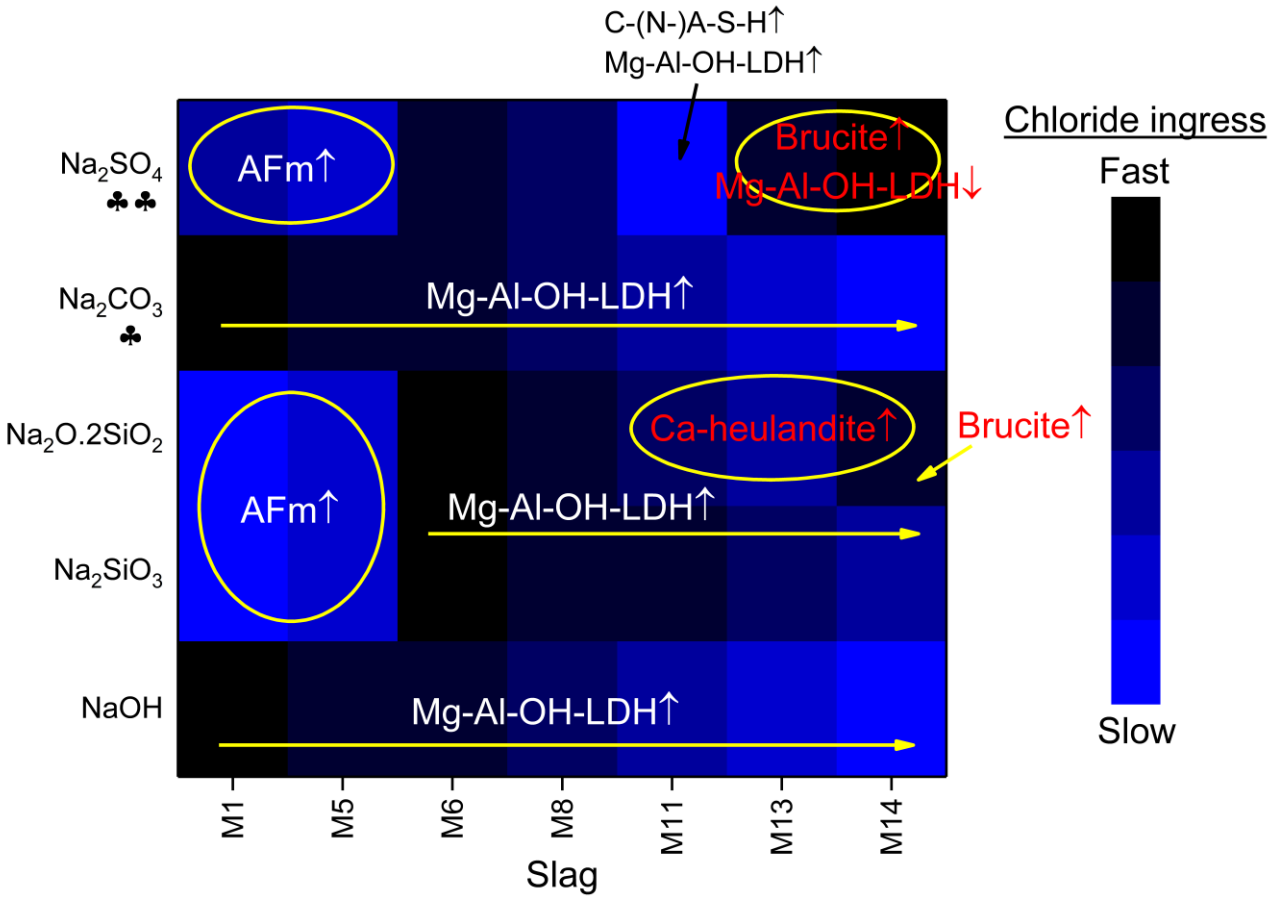

Figure 6-12: A schematic summarising the main parameters that influence chloride ingress in AAS concretes formulated using a wide range of GGBS and activators. ♣ It must be noted that in Na_2CO_3-activated GGBS, the influence of CO_3^{2-} ions in the pore solution and $C_4A\underline{c}H_{11}$ on chloride binding is not considered. ♣♣ In the case of Na_2SO_4-activated GGBS, chloride binding due to the presence of ettringite and $C_4A\underline{s}H_{12}$ have not been taken into account.

This study provides a modelling framework for potential use in estimating the time to chloride-induced depassivation in steel-reinforced concrete structures based on AAS. The model allows the user to input the composition of the slag and the activator of interest to estimate the chemistry of the concrete cover that can be used to estimate the total chloride binding capacity of the binder within the concrete, and thus predict the time required for chloride to diffuse to the steel-concrete interface (as shown in Figure 6-13). It must be noted that the applicability of this model currently only extends to saturated conditions and when the exposure solutions contains $[Cl^-] < 0.654$ M, and in its current state is conservative in nature as it does not take into account the influence of pore structure on chloride ingress, the time required for onset of corrosion and the propagation phase.

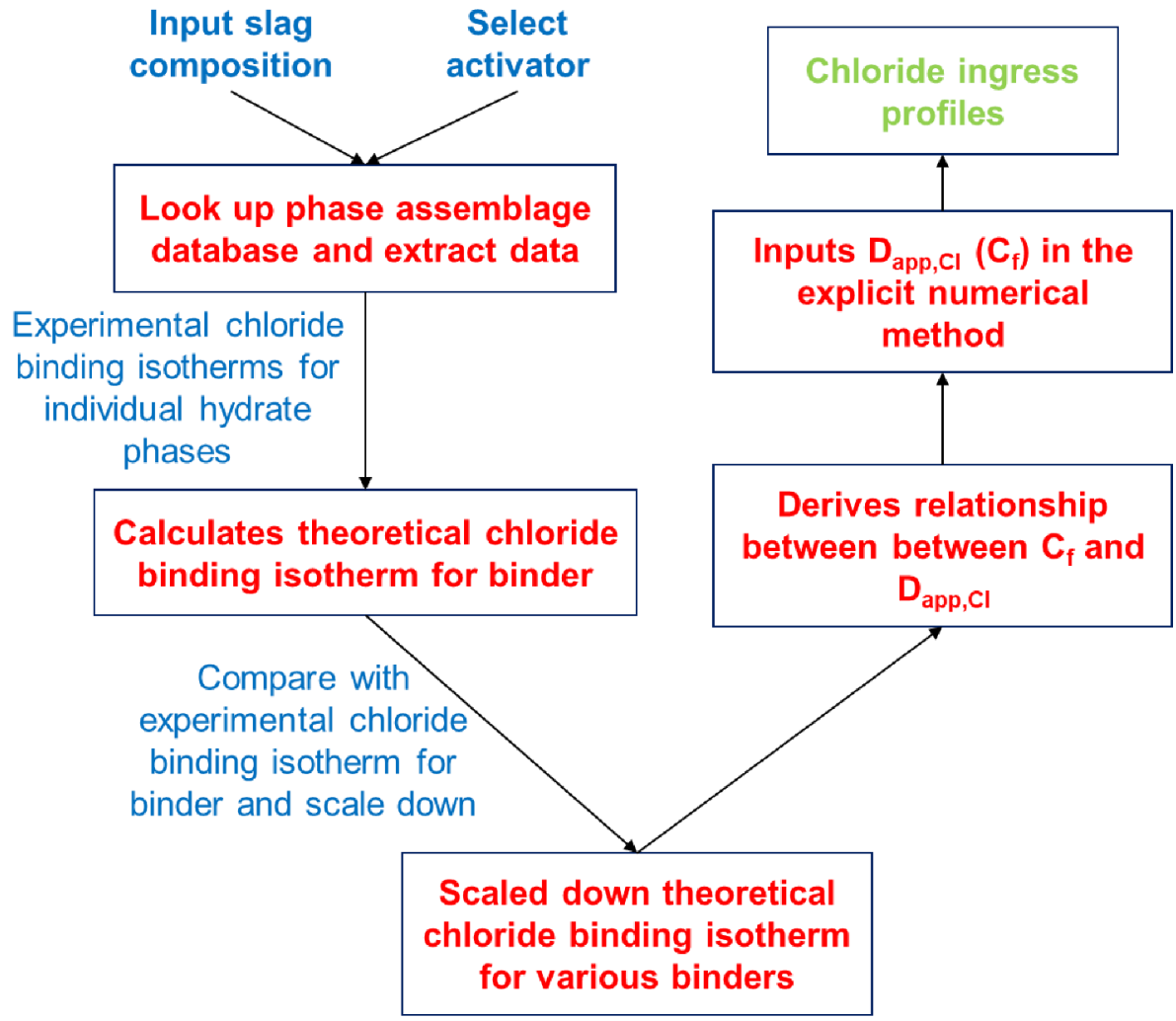

Figure 6-13: Schematic of the model developed in this study to calculate the ingress of chloride in steel-reinforced concrete structures based out of AAS. Additional information regarding chloride 'threshold' value need to be experimentally determined to estimate the service life steel-reinforced AAS concretes.

- The model presented here is a significant step forward in linking AAS chemistry and chloride binding to chloride transport, and thus in understanding the influence of material characteristics on the likely time to corrosion initiation. However, its extension is certainly possible, and several points have been identified where the existing body of data and literature require further development, to enable enrichment of the model and its use in the accurate prediction of service life for steel-reinforced structures based on AAS: The 'GEMS calculated database' created in this study only considered slags with

either 30 wt. % or 40 wt. % SiO_2, a constant SO_3 content of 2 wt. %, and fixed w/b ratios. However, a larger database for various SiO_2 and SO_3 contents and variable w/b ratio could be created to increase the accuracy in prediction of the chemistry of the binder. All parameters used in this study to quantify chloride binding and ingress relate to the solid and aqueous phase assemblages when the extent of slag reaction is 60 %. In theory, the extent of reaction could be extended from zero to 100 %.

- A major assumption made in this study was the scaling down of the theoretically calculated chloride binding isotherms to match the experimental binding isotherms for a particular AAS. The factor used for scaling down the theoretical chloride binding isotherms was extended to all slags and activators used. Most likely, this would be different for each of the slags, and therefore extensive experimental work needs to be carried out to draw empirical correlations between the activator used, the slag composition and the binding capacity of mortars/concretes based on AAS.

- The value of D_{Cl} in Eq. 6.7 was assumed to be the same for all AAS binders, and was based on the D_{nnsm} values observed experimentally [293,350]. However, in principle these values should vary for each of the slags considered in this study. Therefore, more experimental data are required to accurately separate the influence of chloride binding capacity and microstructure on the $D_{app,Cl}$ (Eq. 6.7).

- Chloride binding isotherms for synthetic phases such as monocarboaluminate, monosulfoaluminate, ettringite and Friedel's salt need to be experimentally determined in simulated pore solutions representative of AAS, to ensure that the contributions of all phases identified in AAS towards chloride binding are considered.

- Additionally, experimental chloride binding isotherms for various AAS need to be determined for free chloride concentrations much higher than 0.654 M, allowing an accurate description of chloride binding within these materials using the Freundlich adsorption isotherm. This would ensure the applicability of this model over a wider range of chloride concentrations in the exposure solution.

- In the case of Na_2CO_3-activated slags, the influence of carbonate ions in the pore solution on the binding capacity of individual hydrate phases needs to be systematically understood.

- The alkalinity in this study was assumed to be constant with respect to space and time, and therefore the influence of carbonation and leaching were not considered. Experimental data is required to empirically draw a relationship between the chloride binding capacity and a reduction in pH of the pore solution due to carbonation and leaching.

- To extend the modelling framework to actually predict the service-life of steel-reinforced AAS structures, the MATLAB script needs to take into account (currently not present) the concentration of chloride required for depassivation of the steel reinforcement or the chloride 'threshold' value. Chloride 'threshold' values for steel-reinforced AAS mortars/concretes have not been reported in the open literature and, therefore, it is imperative that research concerning the durability of steel-reinforced AAS in chloride environments be focussed on measuring the chloride 'threshold' value, to ensure an understanding of the long-term durability of these materials.

- Finally, the chloride ingress profiles obtained using this modelling framework need to be validated by comparing with field data or laboratory data.

Chapter 7: Conclusion and Future Work

This thesis presents a comprehensive understanding of the three less answered questions pertaining to long-term durability of alkali-activated materials (AAMs), as highlighted in Chapter 1:

- How does the chemistry of the AAMs influence the surface of the steel?
- What are the conditions required for the onset of chloride-induced steel corrosion in AAMs, once the chloride has passed through the cover concrete and begun to increase in concentration at the steel-concrete interface (SCI)?, and
- Can the service life of steel reinforced alkali-activated concretes be estimated using the answers to the first two objectives?

Steel embedded in binders based on low-Ca AAMs (alkali-activated fly ash or metakaolin) appears to follow similar passivation mechanisms to that observed in PC, due to the similar oxidising capabilities of the pore solutions in these cements. The passive film on the steel reinforcement in PC and in alkali-activated fly ash or metakaolin can be described as a complex assemblage of iron oxides, with the inner layer being a dense Fe(II, III) oxide, surrounded by an outer layer of a hydrated Fe(III) oxide. The mechanism of passivation in low-Ca AAMs can be given by the following reaction pathway:

$$Fe \rightarrow Fe(OH)_{ads} \rightarrow Fe(OH)^{+}_{ads} \rightarrow HFeO_2^{-} \rightarrow Fe(OH)_2 \rightarrow FeOOH \rightarrow \text{hydrated } FeOOH \text{ or } Fe_2O_3$$

Based on the electrochemical observation, the alkalinity of the pore solution in low-Ca AAMs was found to have a significant influence on the chloride 'threshold' value – very similar to observations in pore solutions of PC, but with observed initiation only at much higher $[Cl^-]/[OH^-]$ ratios in these highly alkaline simulated pore solutions. It is important to mention that unlike PC, alkali-activated binders in general do not form $Ca(OH)_2$ that can act as a pH buffer, and so any loss in alkalinity due to leaching or carbonation cannot be compensated by any of the reaction products formed in these binders. Therefore, the onset of pitting depends strongly on the ability to retain the alkalinity of the pore solution at the SCI (through curing to achieve a refined pore structure, and formulation to minimise porosity), as well as the local chloride concentration. It was determined in Chapter 4 that the onset of pitting in these highly alkaline

binders can be predicted by a relationship involving $[Cl^-]/[OH^-]^3$ rather than the simple ratio between chloride and hydroxide concentrations that is often used to define C_{crit}, where a value of $[Cl^-]/[OH^-]^3 < 1.25$ at the SCI would enable the steel reinforcement to be in the passive state while immersed in highly concentrated NaOH, while any value above 1.25 would indicate pitting (stable or metastable) of the steel. This functional form, with a third power relationship to hydroxide concentration, provides an improved descriptive power for solutions representative of the pore solution chemistry of low-calcium alkali-activated binders, and also confirms the passive film being composed of a hydrated FeOOH or Fe_2O_3 outer layer that plays an important part in the initiation of pitting corrosion. Once pitting has initiated and a local acidification has occurred, repassivation of the pit in the absence of $Ca(OH)_2$ would be solely reliant on the concentration of $[OH^-]$ around the pit. However, further research related to different passivation products needs to be done to confirm such a relationship for pit initiation, and particularly to understand its validity in actual concrete specimens, and also in pore solutions which are not as extremely alkaline as those studied here.

In alkali-activated fly ashes, Babaee and Castel [214] showed that the proportionality constant *B*, used in the modified Stern-Geary equation to calculate the corrosion rates, deviates significantly from those used in PC-based concretes. It was observed [214] that using conventional values [213] of *B*=52 (passive state) and *B*=26 (active state) for steel-reinforced alkali-activated fly ash concretes yields an overestimation of the corrosion current density in the passive state, but an underestimation in the active state. This was consistent with the calculation of i_{corr} values for steel immersed in simulated pore solutions of low-Ca AAMs (Chapter 4). Therefore, further attention must be paid to the validation of appropriate *B* values for these binders, to avoid discrepancies in predicting their service life. Similarly, analysing E_{corr} and i_{corr} values according to recommendations or classifications set for PC based concretes (ASTM C876-15 [181] and [183]) to characterise the passive or the active state would be misleading in the case of these low-Ca AAM binders, as the ionic strength, diffusivity and pore solution composition are very different from the conditions prevailing inside PC.

In the case of high-Ca AAMs such as alkali-activated slags, the chemistry of the steel surface is very different to that observed in low-Ca AAMs, primarily due to the presence of reduced sulfur species (HS^-) dissolved in the pore solution during the activation of slags. In the presence of HS^- in pore solutions of AAS, competitive adsorption between $[OH^-]$ and $[HS^-]$ results in the inhibition and retardation in the formation of a passive film composed of iron oxides, and

instead the steel surface is composed of a Fe-S complex. In these solutions, the mechanism of forming a surface film can be described as:

$$Fe + OH^- + HS^- \rightarrow Fe(OH)_{ads} + Fe(HS)_{ads} \rightarrow Fe(OH)^+_{ads} + Fe(HS)^+_{ads} \rightarrow Fe(OH)_2 + Fe(HS)_{2,ads} \rightarrow \text{hydrated FeOOH and Fe-S complex.}$$

Similar to the findings of Chapter 5, higher corrosion rates [116], higher i_{corr} and lower R_p values [115,284] have been reported for steel-reinforced AAS exposed to chloride solutions in comparison to those observed in PC. However, visual examination of the steel rebars in each of these studies found that the extent of corrosion for steel embedded in AAS was much lower than those in PC. For instance, no evidence of corrosion was observed by Criado et al. [284], which contrasts strongly with the electrochemical observations. The high i_{corr} and low R_p values are therefore likely to be related to the aqueous chemistry of the pore solution at the SCI, not necessarily the actual corrosion resistance of the steel. In particular, these values correspond mainly to the oxidation of the HS^- species in the pore solution (and not to the oxidation/reduction couple of Fe/Fe^{2+}), which takes place because of the potential imposed in the electrochemical test procedure used to determine these parameters.

This was confirmed by the anodic polarisation curves shown in Chapter 5 for steel immersed in alkaline sulfide solutions. As shown in Chapter 5, even though passivation of steel by an iron oxide film is not seen in AAS, the formation of a macro-cell or chloride-induced pitting is inhibited until the concentration of dissolved oxygen at the steel-concrete interface (SCI) is low. In the case of AAMs with a reducing environment such as AAS, the role of HS^- at the SCI is of significant importance. The high concentration of HS^- in the pore solution not only creates a highly reducing environment around the SCI and hinders the development of passive iron oxide film (and creates a different 'surface' film consisting of mackinawite), but also restricts the cathodic reduction of oxygen and the formation of a macro-cell. The high i_{corr} values generally observed for AAS are predominantly due to the loss of electrons from HS^- in the aqueous environment, and therefore, leading to misrepresentative conclusions on the corrosion resistance of the steel reinforcement if electrochemical test results are interpreted from the assumption that all redox processes taking place in the material involve the steel itself.

In the light of such major differences in the mechanisms of passivation and corrosion between various steel-reinforced AAMs and PC, analysis of electrochemical properties through classifications or standards recommended for PC would be misleading in the case of AAMs. Instead, the influence of the chemistry of various AAMs on the steel reinforcement and the SCI needs to be studied in greater detail, and a larger database of experimental results is required

to accurately characterise the electrochemical behaviour of the steel reinforcement in these binders. Given the various aqueous environments that can be encountered at the SCI of AAMs, and the strong influence of the presence or absence of reducing elements in the pore solution (depending on the nature of the precursor used for production of AAMs) on the mechanisms of passivation and the onset of pitting, AAMs need to be classified on the basis of internal redox conditions when considering durability in chloride-rich environments, as illustrated in Figure 7-1.

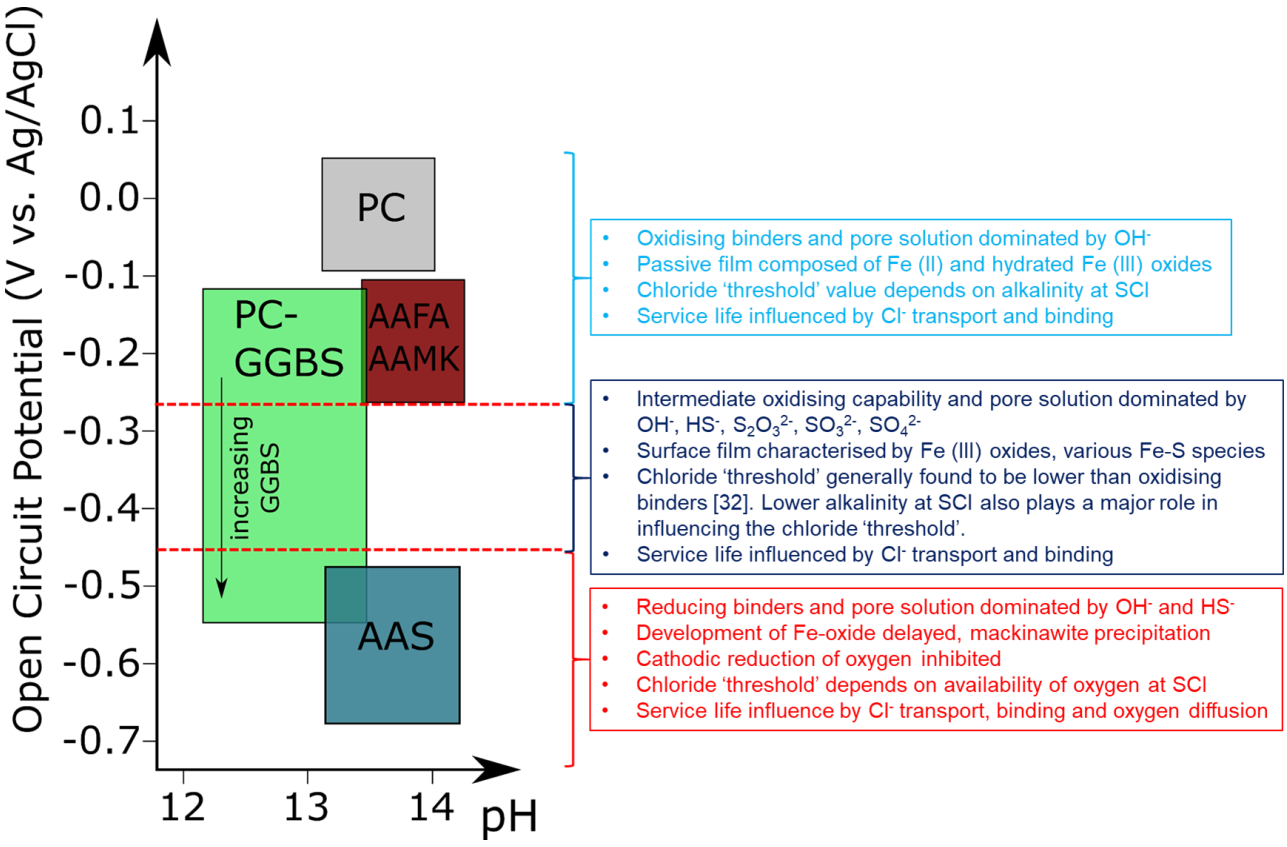

Figure 7-1: Overview of the proposed classification of cements, particularly of AAMs, based on internal redox conditions, and the parameters influencing the onset of steel pitting and the service-life of these binders. AAFA = alkali-activated fly ashes, AAMK = alkali-activated metakaolin.

Finally, a framework to estimate the ingress of chloride in steel-reinforced concrete structures based on AAS has been developed and implemented in MATLAB. The model allows the user to input the composition of the slag and the activator of interest to estimate the chemistry of

the concrete cover that can be used to estimate the total chloride binding capacity of the binder within the concrete, and thus model the concentration of chloride at the steel-concrete interface at any given time. The framework developed in this study presents a different approach and a significant advancement in the currently used models to predict the ingress of chloride in concretes. This framework negates the need to use a mathematically 'incorrect' solution to Fick's second law, with a varying diffusion coefficient (D_{app} (t)) and the empirically derived age exponent. However, it would be necessary to point out that the model in its current state is conservative in nature (and only applicable for submerged structures) and several areas requiring more attention have been identified to enable using the framework as a tool to estimate service life, as discussed in Chapter 6. Areas for further research can be broadly categorised as:

- GEMS database – A larger database of simulated solid and aqueous phase assemblages can be considered with varying SiO_2 and SO_3 contents, and w/b ratios; and the extent of slag reaction can be taken up to 100 %, although the rate of slag reaction is very slow above 60 %. Currently, the framework is restricted to high-Ca AAMs, as no quantitative chloride binding data exists for low-Ca AAMs.

- Chloride binding and diffusion – A broader set of experimental values for D_{Cl}, obtained using NT Build 492, and experimental chloride binding isotherms for various slags and activators needs to be stablished. Currently the model extrapolates from data obtained for Na_2SiO_3-activated M6 slag. The model also assumes only three reaction products (C-(N-)A-S-H gel, Mg-Al-OH LDH phase and strätlingite) to contribute towards chloride binding, however, in reality other reaction products formed in AAS may bind chlorides and therefore, the chloride binding capacity of each of the individual reaction products formed in AAS need to be assessed in simulated pore solutions of AAS. Additionally, the framework would benefit if the tortuosity of the of various AAMs could be identified.

- C_{crit} – Currently, there exists no data in the literature quantifying the concentration of chloride or C_{crit} that causes initiates corrosion in AAS. The C_{crit} is an important input parameter that would allow the framework to predict the onset of corrosion in steel-reinforced AAS concretes. It must be noted that this framework does not take into account the propagation period of steel corrosion in concrete structures.

- Experimental validation – The rate of chloride ingress in AAS concretes need to validated experimentally through field exposure.

As mentioned in Chapter 2, the durability of a steel-reinforced concrete structure can be divided into the initiation phase, the onset of corrosion, and the propagation phase. Based on the results presented in this thesis and various literature [264,355,356] concerning durability of AAMs, it would be reasonable to compare the initiation phase and the onset of corrosion in AAMs to that observed in PC-based binders. Based on the diffusion coefficient obtained by [264,355,356], the duration of the initiation phase (or time for chloride to move from the exterior to the SCI until depassivation of the steel reinforcement due to the presence of chlorides above a threshold concentration) in concretes made of various materials can be ranked as: High-Ca AAMs (alkali-activated slags) > PC-slag blends > PC > Low-Ca AAMs (alkali-activated fly ashes/metakaolin), indicating the rate of chloride ingress being slowest in alkali-activated slags and the fastest in alkali-activated fly ashes/metakaolin. However, the onset of corrosion or the C_{crit} for depassivation to start follows a different trend and depends on the exposure conditions. In submerged structures or saturated concretes, however, the C_{crit} as a function of the binder type can ranked as follows: High-Ca AAMs (alkali-activated slags) > Low-Ca AAMs (alkali-activated fly ashes/metakaolin) > PC > PC-slag blends. As shown in Chapter 5, the probability of corrosion or formation of a macrocell in high-Ca AAMs (AAS) would depend primarily on the availability of oxygen at the SCI, and therefore ranking the C_{crit} as a function of the binder type under partially saturated conditions would not be possible at this stage. Further research is required to understand passivation and chloride-induced corrosion in partially saturated high-Ca AAMs.

Chapter 8: Appendix

8.1 Supplementary information of Chapter 3

Figure 8-1 shows images of the reinforcement used in this study, the steel pellets (as mentioned in Chapter 3) used in electrochemical tests, and steel undergoing severe chloride-induced pitting corrosion when exposed to a solution containing 0.80 M NaOH and 2.40 M NaCl.

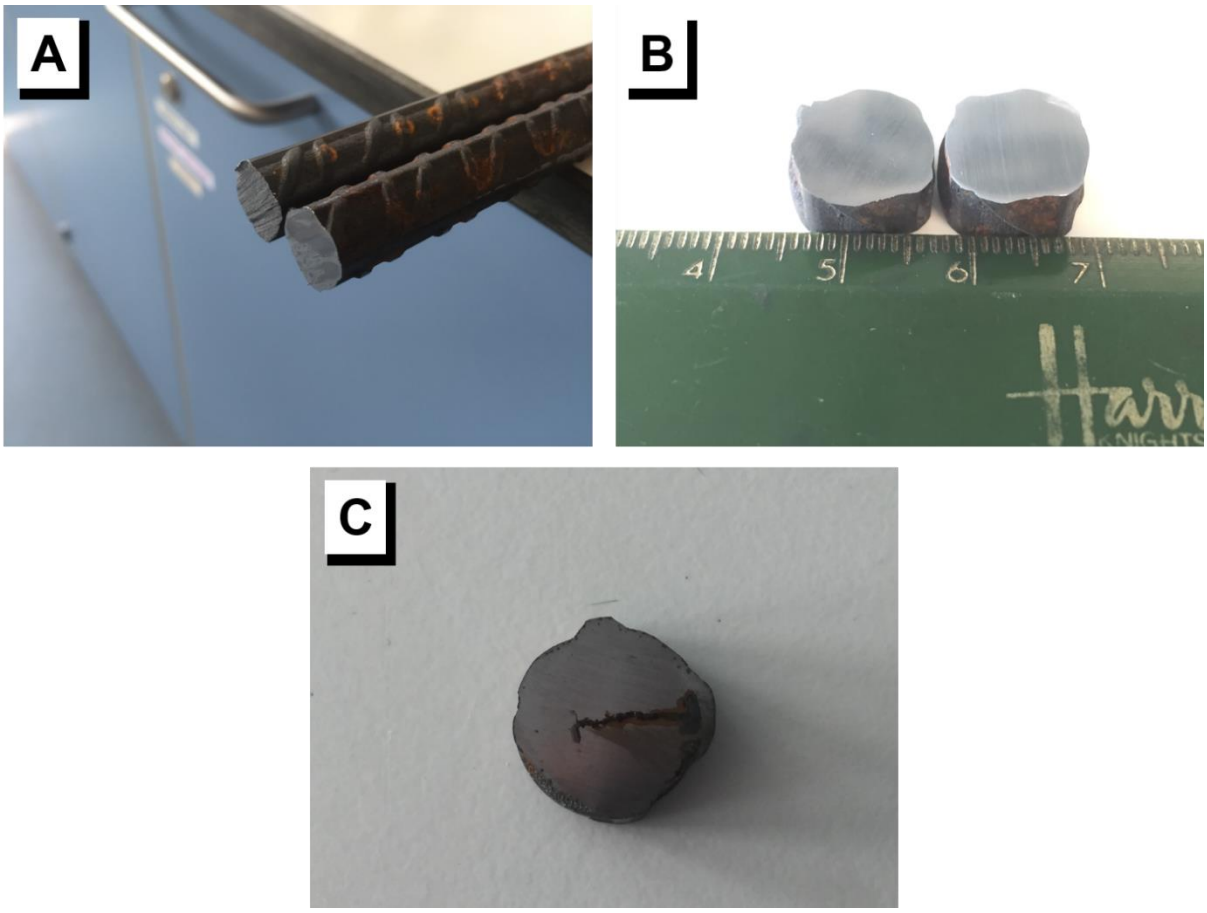

Figure 8-1: (A) Steel reinforcement bars used in this research, conforming to B500 grade (φ = 12 mm), (B) Small pellets obtained cut from mild steel rebars, thickness 5.5 - 6.5 mm, using an abrasive disc and the pellet surfaces were polished using SiC abrasive paper with 240 to 600 grit sizes and degreased using acetone, and (C) an image of chloride-induced pitting corrosion on the surface of steel pellets after exposure to a solution containing 0.80 M NaOH and 2.40 M NaCl

Figure 8-2 shows the Fe $2p_{3/2}$ and S $2p$ spectra obtained using XPS on steel specimens prior to exposure to an alkaline medium. The Fe $2p_{3/2}$ was analysed using the same parameters as mentioned in Chapter 5, Section 5.2.2.3. Several peaks were observed in the Fe $2p_{3/2}$ spectra confirming the presence of various Fe^{2+} and Fe^{3+} species on the surface of the steel reinforcement. Almost no sulfur was detected on the surface of the steel.

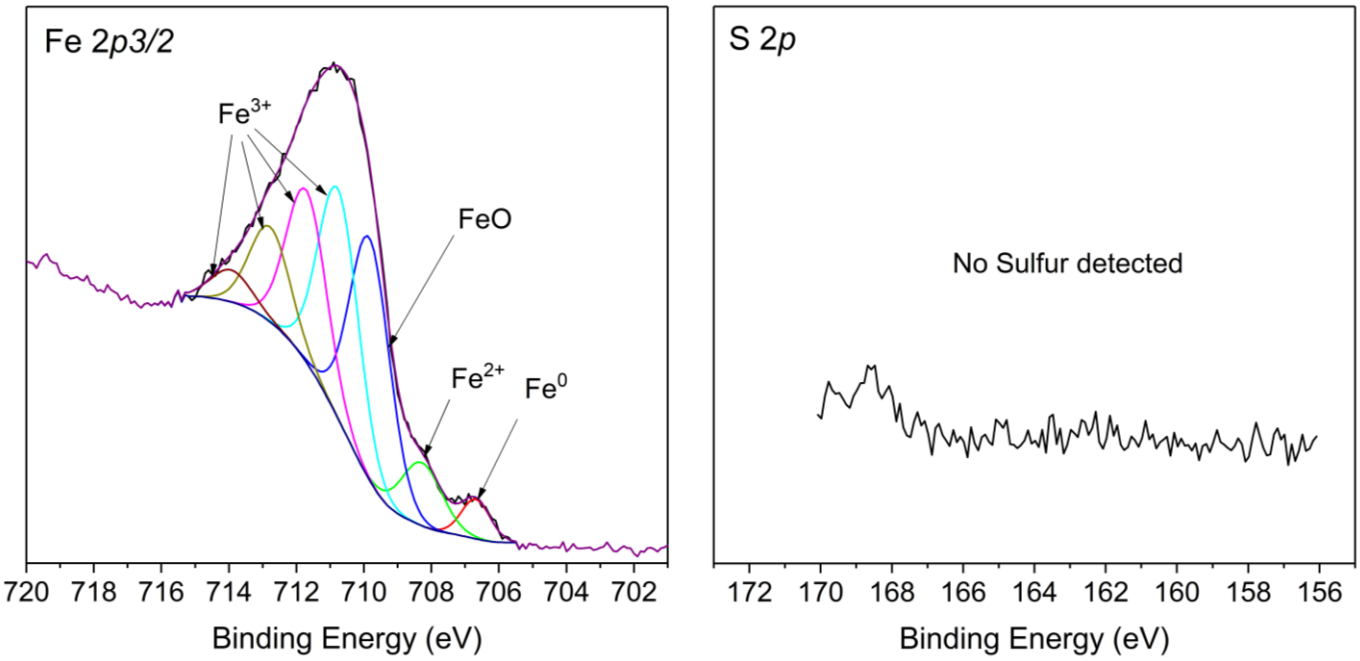

Figure 8-2: Fe $2p_{3/2}$ and S $2p$ spectra obtained using XPS on steel specimens prior to exposure to an alkaline medium.

8.2 Supplementary information of Chapter 4

Table 8-1 shows the pH of electrolytes recorded using a digital pH meter (Oakton Acorn Series). In alkaline chloride containing solutions, the pH of the bulk electrolytes measured before and after electrochemical tests showed negligible difference.

Table 8-1: pH of bulk electrolytes used in Chapter 4 recorded before and after conducting electrochemical tests. The values in parenthesis indicate the standard deviation.

	0.80 M NaOH		**1.12 M NaOH**		**1.36 M NaOH**	
$[Cl^-]$/ $[OH^-]$	**Before**	**After**	**Before**	**After**	**Before**	**After**
0.00	13.95 (0.05)	13.94 (0.02)	14.12 (0.10)	14.10 (0.07)	14.20 (0.07)	14.16 (0.01)
0.25	13.96 (0.02)	13.96 (0.03)	14.09 (0.05)	14.06 (0.09)	14.19 (0.10)	14.21 (0.11)
0.50	13.91 (0.02)	13.92 (0.06)	14.06 (0.12)	14.08 (0.02)	14.22 (0.11)	14.17 (0.10)
0.75	13.88 (0.04)	13.90 (0.01)	14.03 (0.00)	14.09 (0.10)	14.27 (0.13)	14.27 (0.07)
0.80	13.99 (0.03)	13.99 (0.02)	--	--	--	--
0.90	13.97 (0.02)	13.94 (0.07)	--	--	--	--
1.00	13.96 (0.03)	13.95 (0.01)	14.02 (0.00)	14.03 (0.01)	14.19 (0.15)	14.20 (0.13)
1.50	13.92 (0.01)	13.95 (0.04)	14.16 (0.03)	14.11 (0.07)	14.23 (0.00)	14.09 (0.06)
1.60	--	--	14.07 (0.06)	14.00 (0.03)	--	--
1.70	--	--	14.07 (0.09)	13.96 (0.01)	--	--
2.00	13.94 (0.06)	13.92 (0.00)	14.10 (0.05)	14.00 (0.02)	14.19 (0.07)	14.23 (0.15)
2.30	--	--	--	--	14.13 (0.11)	14.13 (0.07)
2.40	--	--	--	--	14.25 (0.09)	14.21 (0.03)
3.00	13.96 (0.10)	13.90 (0.05)	14.09 (0.06)	14.11 (0.07)	14.16 (0.02)	14.16 (0.00)

Figure 8-3 shows preliminary electrochemical results obtained for steel when exposed to solutions containing only 0.80 M OH^- (as used in this study) and solutions containing 0.80 M OH^-, 3 mM Al, 0.45 mM Ca and 0.9 mM Si. The electrochemical response (OCP and R_p) of steel in both the solutions clearly show that influence of Al, Si and Ca is negligible and the use of simple solutions containing OH^- to study mechanisms of steel passivation and chloride induced corrosion is justified.

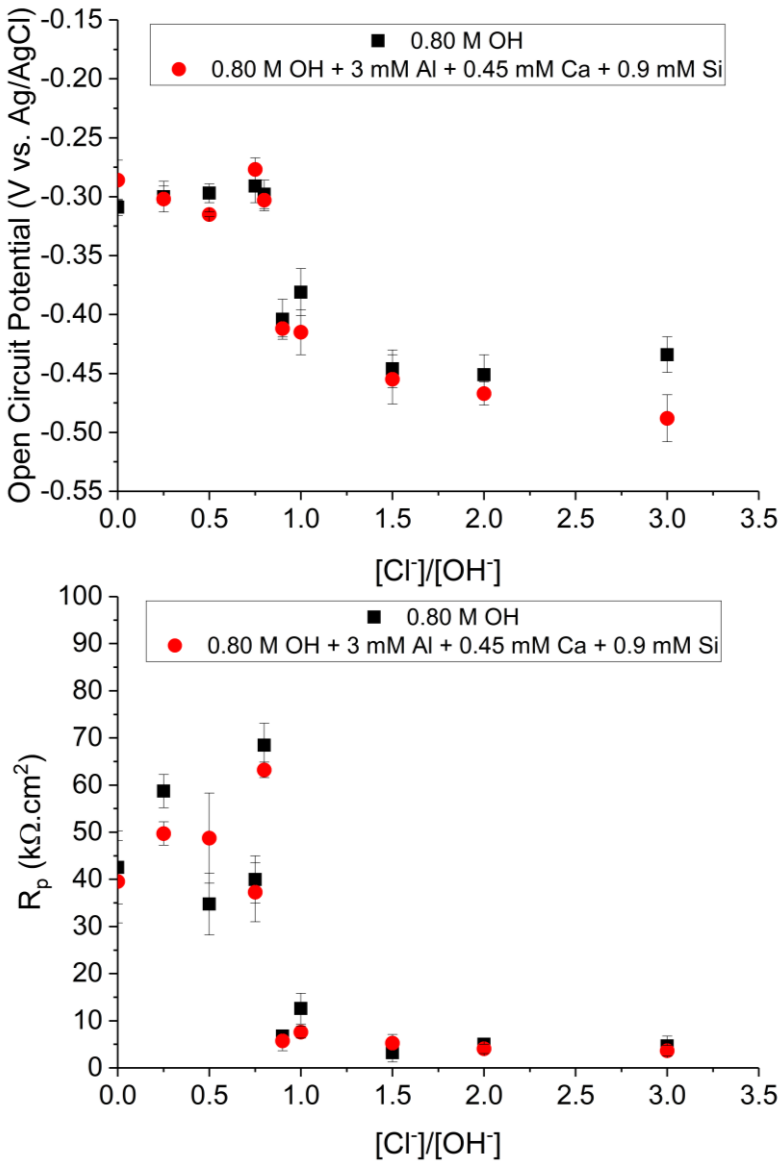

Figure 8-3: OCP and R_p obtained for steel when exposed to solutions containing only 0.80 M OH^- and to solutions containing 0.80 M OH^-, 3 mM Al, 0.45 mM Ca and 0.9 mM Si.

Figure 8-4 and Figure 8-5 show the cyclic voltammograms of steel immersed in simulated pore solution with NaOH concentrations of: (A) 0.80 M (B) 1.12 M and (C) 1.36 M, with sweep rates 5 mV/s and 10 mV/s, respectively.

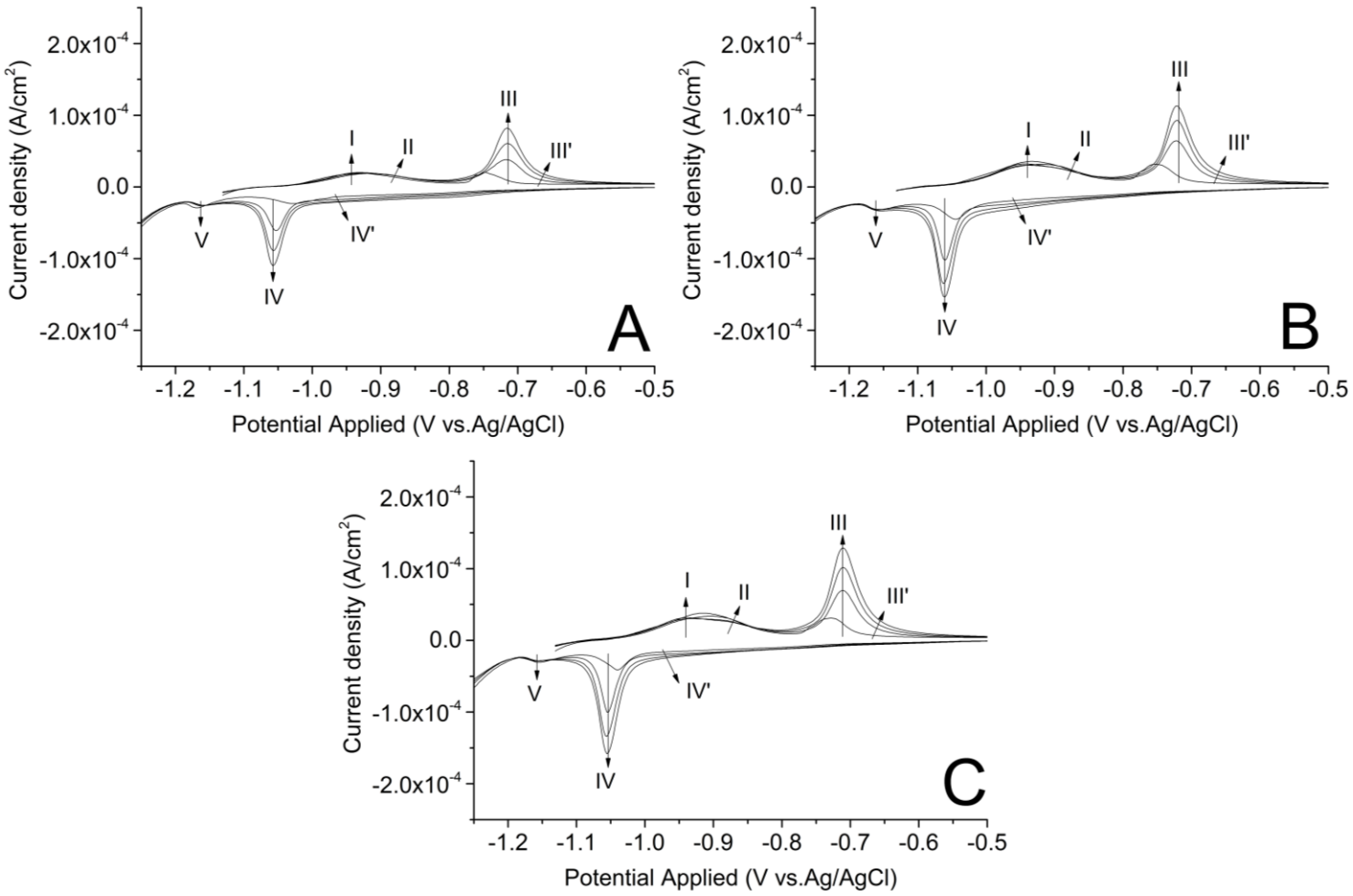

Figure 8-4: Cyclic voltammograms of steel immersed in simulated pore solution with NaOH concentrations of: (A) 0.80 M (B) 1.12 M and (C) 1.36 M. Data were collected at a sweep rate of 5 mV/s. Arrows indicate the current response from scan numbers 1 to 4. Data from -1.50 V to -1.13 V in the anodic sweeps are not presented to enable visibility of peak V.

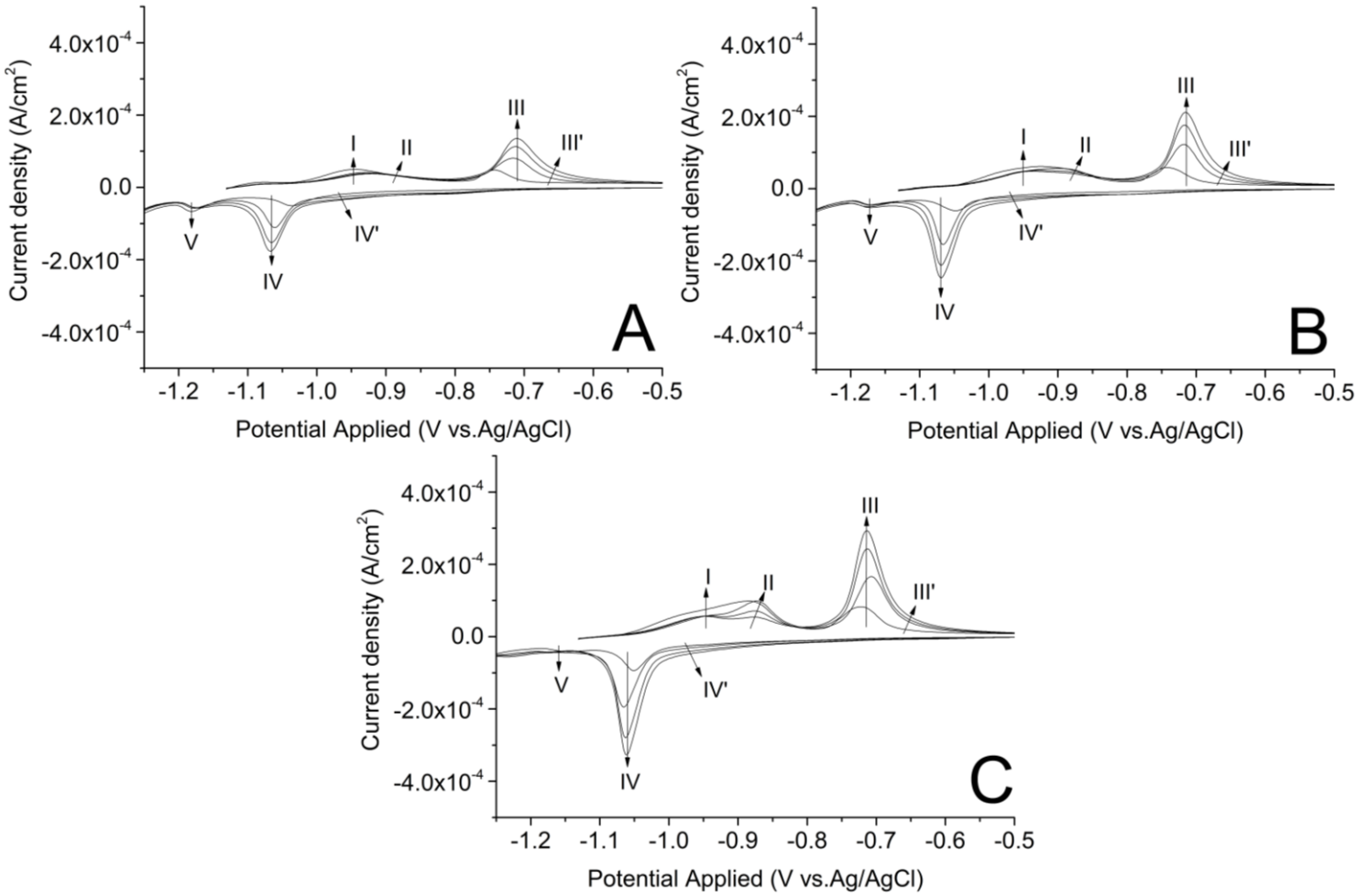

Figure 8-5: Cyclic voltammograms of steel immersed in simulated pore solution with NaOH concentrations of: (A) 0.80 M (B) 1.12 M and (C) 1.36 M. Data were collected at a sweep rate of 10 mV/s. Arrows indicate the current response from scan numbers 1 to 4. Data from -1.50 V to -1.13 V in the anodic sweeps are not presented to enable visibility of peak V.

8.3 Supplementary information of Chapter 5

Figure 8-6 shows the first 5 scans of cyclic voltammetry conducted on mild steel exposed to (A) 1.12 M OH^- + 0.01 M HS^-, and (B) 1.36 M OH^- + 0.45 M HS^-. On comparing with Figure 5-1B, the current density associated with anodic peaks I, II, III and III' were observed to increase with an increase in the [OH^-] in the electrolyte. The higher current densities (observed in Figure 8-6) associated with peak I are primarily due to increased competitive adsorption between [OH^-] and [HS^-] on the steel surface. As mentioned in Peaks II, III and III' are related to the formation of iron oxides and hydroxides, and the current densities at the peaks was observed to increase with an increase in the [OH^-] in the electrolyte (as shown in Figure 8-6A and B and Figure 5-1B). This is line with the conclusion of Chapter 4, where an increased alkalinity in the electrolyte leads to a higher degree of passivation on the steel surface.

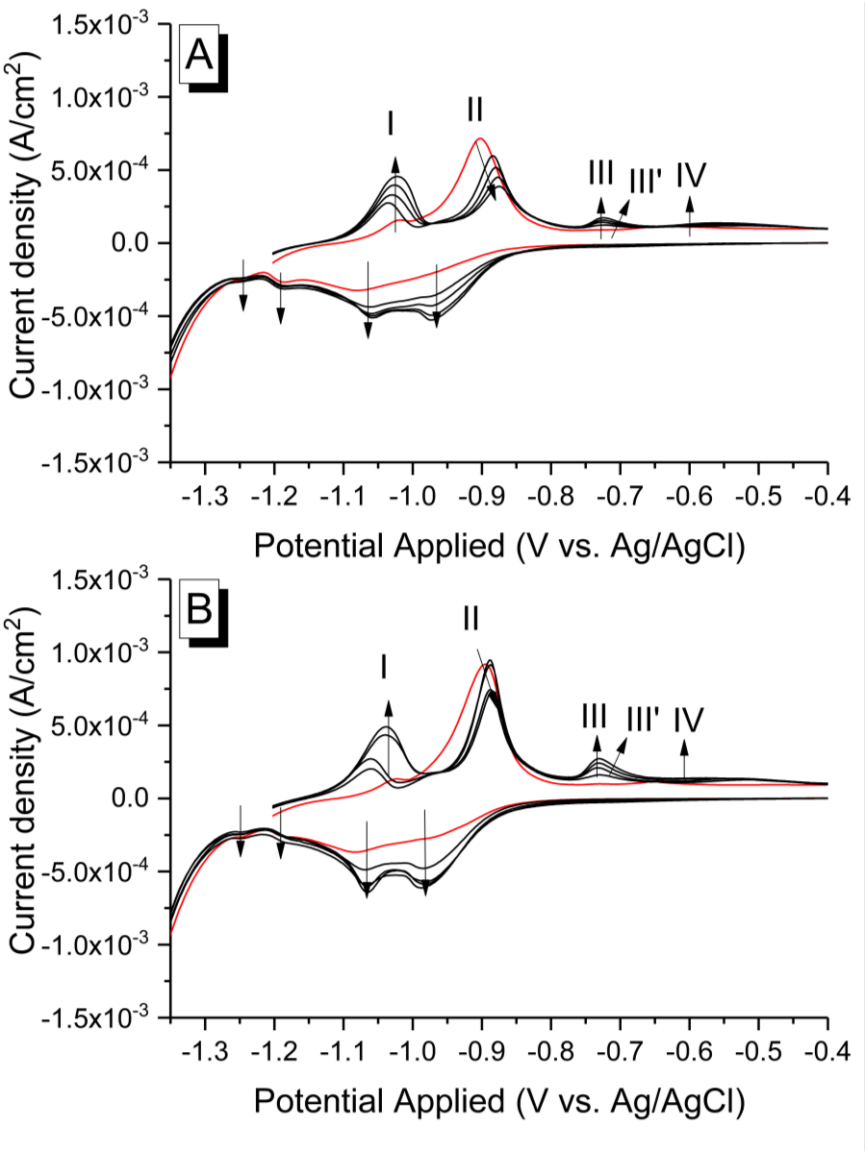

Figure 8-6: Cyclic voltammograms obtained for mild steel exposed to (A) 1.12 M OH^- + 0.01 M HS^-, and (B) 1.36 M OH^- + 0.45 M HS^-. Data were collected at a sweep rate of 2.5 mV/s. Arrows indicate the current response from scan numbers 1 to 5. Data from -1.50 V to -1.20 V in the anodic sweeps are not presented to enable visibility of all peaks. The red line indicates the first scan, and subsequent scans are represented by black lines.

Table 8-2 shows the evolution of pH of alkaline solutions (0.80 M OH^-) with varying concentrations of HS^- (0 M, 0.001 M, 0.01 M, 0.09 M, 0.45 M) over a period of 28 days. The pH values correspond to the solutions to which mild steel was exposed to prior to electrochemical tests.

Table 8-2: The evolution of pH of alkaline solutions (0.80 M OH^-) with varying concentrations of HS^- (0 M, 0.001 M, 0.01 M, 0.09 M, 0.45 M) over a period of 28 days. The pH values reported correspond to the solutions to which mild steel was exposed to prior to electrochemical tests. Values in parenthesis are the standard deviations.

Time (d)	**0.80 M OH^- + 0 M HS^-**	**0.80 M OH^- + 0.001 M HS^-**	**0.80 M OH^- + 0.01 M HS^-**	**0.80 M OH^- + 0.09 M HS^-**	**0.80 M OH^- + 0.45 M HS^-**
0	13.95 (0.02)	13.96 (0.00)	13.90 (0.03)	13.90 (0.06)	13.85 (0.01)
5	13.96 (0.03)	13.96 (0.04)	13.91 (0.01)	13.90 (0.00)	13.84 (0.03)
12	13.99 (0.06)	13.95 (0.03)	13.92 (0.02)	13.90 (0.03)	13.87 (0.01)
28	13.94 (0.05)	13.95 (0.07)	13.91 (0.00)	13.90 (0.02)	13.86 (0.02)

8.4 Supplementary information of Chapter 6

As mentioned in Chapter 6, the ‘Gems calculated database’ can be provided only as an electronic version, and therefore has been supplied in the electronic submission of the thesis.

Chapter 9: References

[1] K.L. Scrivener, V.M. John, E.M. Gartner, Eco-efficient cements: Potential, economically viable solutions for a low-CO_2, cement-based materials industry, United Nations Environment Program, 2017.

[2] P.C. Aïtcin, Cements of yesterday and today - concrete of tomorrow, Cem. Concr. Res. 30 (2000) 1349–1359.

[3] Cabinet Office HM Government, Government Construction Strategy, 2011.

[4] C.F. Choy, Revisiting the "Bon curve," Constr. Manag. Econ. 29 (2011) 695–712.

[5] S.T. Ng, R.Y.C. Fan, J.M.W. Wong, A.P.C. Chan, Y.H. Chiang, P.T.I. Lam, M. Kumaraswamy, Coping with structural change in construction: Experiences gained from advanced economies, Constr. Manag. Econ. 27 (2009) 165–180.

[6] The World Bank, Transformation through infrastructure: World Bank Group infrastructure strategy update FY 2012-2015, 2012.

[7] United Nations-Department of Economic and Social Affairs- Population Division (2017)., World Fertility Data 2017, (n.d.). http://www.un.org/en/development/desa/population/publications/dataset/fertility/wfd2017.shtml (accessed November 16, 2016).

[8] E.J. Moore, U . S . Geological Survey Professional Paper 1228-E Availability of Books and Maps of the U . S . Geological Survey, (1992).

[9] U.S. Geological Survey, Mineral commodity summaries: cement, (n.d.). https://minerals.usgs.gov/minerals/pubs/commodity/cement/index.html (accessed November 16, 2016).

[10] IEA/WBCSD, Cement Technology Roadmap 2009, OECD/IEA World Bus. Counc. Sustain. Dev. (2009) 36.

[11] A. Swenson, Building construction, Britanica Encycl. (2014).

[12] U.M. Angst, Challenges and opportunities in corrosion of steel in concrete, Mater. Struct. 51 (2018) 1–20.

[13] I. Galan, F.P. Glasser, Chloride in cement, Adv. Cem. Res. 27 (2015) 63–97.

[14] K. Tuutti, Corrosion of steel in concrete, Swedish Cement and Concrete Research Institute, Stockholm, 1982.

[15] De-icing – keeping our roads open, (n.d.). http://www.saltassociation.co.uk/de-icing-roads/ (accessed November 20, 2016).

[16] J.G.J. Olivier, G. Janssens-Maenhout, M. Muntean, J.A.H.W. Peters, Trends in Global CO_2 Emissions: 2016 Report, 2016.

[17] J. Lehne, F. Preston, Making concrete change, innovation in low-carbon cement and cncrete, Chatham House, London, 2018.

[18] R.J. Flatt, N. Roussel, C.R. Cheeseman, Concrete: An eco material that needs to be improved, J. Eur. Ceram. Soc. 32 (2012) 2787–2798.

[19] E.M. Gartner, D.E. Macphee, A physico-chemical basis for novel cementitious binders, Cem. Concr. Res. 41 (2011) 736–749.

[20] C. Shi, A. Fernández-Jiménez, A. Palomo, New cements for the 21st century: The pursuit of an alternative to Portland cement, Cem. Concr. Res. 41 (2011) 750–763.

[21] M.C.G. Juenger, F. Winnefeld, J.L. Provis, J.H. Ideker, Advances in alternative cementitious binders, Cem. Concr. Res. 41 (2011) 1232–1243.

[22] G. Habert, C. Billard, P. Rossi, C. Chen, N. Roussel, Cement production technology improvement compared to factor 4 objectives, Cem. Concr. Res. 40 (2010) 820–826.

[23] J.L. Provis, Geopolymers and other alkali activated materials: why, how, and what?, Mater. Struct. 47 (2014) 11–25.

[24] J.S.J. Van Deventer, J.L. Provis, P. Duxson, D.G. Brice, Chemical research and climate change as drivers in the commercial adoption of alkali activated materials, Waste and Biomass Valorization. 1 (2010) 145–155.

[25] J.L. Provis, J.S.J. Van Deventer, Alkali Activated Materials, Springer/RILEM, Dordrecht, 2014.

[26] J.S.J. Van Deventer, J.L. Provis, P. Duxson, Technical and commercial progress in the adoption of geopolymer cement, Miner. Eng. 29 (2012) 89–104.

[27] I. Ismail, S.A. Bernal, J.L. Provis, R. San Nicolas, S. Hamdan, J.S.J. van Deventer, Modification of phase evolution in alkali-activated blast furnace slag by the incorporation of fly ash, Cem. Concr. Compos. 45 (2014) 125–135.

[28] J.L. Provis, J.S.J. Van Deventer, Geopolymerisation kinetics. 2. Reaction kinetic modelling, Chem. Eng. Sci. 62 (2007) 2318–2329.

[29] B. Lothenbach, A. Gruskovnjak, Hydration of alkali-activated slag: thermodynamic modelling, Adv. Cem. Res. 19 (2007) 81–92.

[30] J.L. Provis, S.A. Bernal, Geopolymers and related alkali-activated materials, Annu. Rev. Mater. Res. 44 (2014) 299–327.

[31] J.L. Provis, G.C. Lukey, J.S.J. van Deventer, Do geopolymers actually contain nanocrystalline zeolites? A reexamination of existing results, Chem. Materails. 17 (2005) 3075–3085.

[32] B. Zhang, K.D. MacKenzie, I.M. Brown, Crystalline phase formation in metakaolinite geopolymers activated with NaOH and sodium silicate, J. Mater. Sci. 44 (2009) 4668–4676.

[33] J. Davidovits, Geopolymers, J. Therm. Anal. 37 (1991) 1633–1656.

[34] J.L. Bell, P. Sarin, J.L. Provis, R.P. Haggerty, P.E. Driemeyer, P.J. Chupas, J.S.J. van

Deventer, W.M. Kriven, Atomic structure of a cesium aluminosilicate geopolymer: A pair distribution function study, Chem. Mater. 20 (2008) 4768–4776.

[35] C.E. White, J.L. Provis, T. Proffen, J.S.J. Van Deventer, The effects of temperature on the local structure of metakaolin-based geopolymer binder: A neutron pair distribution function investigation, J. Am. Ceram. Soc. 93 (2010) 3486–3492.

[36] W. Loewenstein, The distribution of aluminum in the tetrahedra of silicates and aluminates., Am. Mineral. 39 (1954) 92–96.

[37] O. Bortnovsky, J. Dědeček, Z. Tvarůžková, Z. Sobalík, J. Šubrt, Metal ions as probes for characterization of geopolymer materials, J. Am. Ceram. Soc. 91 (2008) 3052–3057.

[38] R.J. Myers, S.A. Bernal, R. San Nicolas, J.L. Provis, Generalized structural description of calcium-sodium aluminosilicate hydrate gels: The cross-linked substituted tobermorite model, Langmuir. 29 (2013) 5294–5306.

[39] F. Puertas, M. Palacios, H. Manzano, J.S. Dolado, A. Rico, J. Rodríguez, A model for the CASH gel formed in alkali-activated slag cements, J. Eur. Ceram. Soc. 31 (2011) 2043–2056.

[40] A. Fernández Jiménez, F. Puertas, I. Sobrados, J. Sanz, Structure of calcium silicate hydrates formed in alkaline-activated slag: influence of the type of alkaline activator, J. Am. Ceram. Soc. 86 (2003) 1389–1394.

[41] I.G. Richardson, A.R. Brough, G.W. Groves, C.M. Dobson, The characterization of hardened alkali-activated blast-furnace slag pastes and the nature of the calcium silicate hydrate (C-S-H) phase, Cem. Concr. Res. 24 (1994) 813–829.

[42] E. Bernard, B. Lothenbach, C. Cau-Dit-Coumes, C. Chlique, A. Dauzères, I. Pochard, Magnesium and calcium silicate hydrates, Part I: Investigation of the possible magnesium incorporation in calcium silicate hydrate (C-S-H) and of the calcium in magnesium silicate hydrate (M-S-H), Appl. Geochemistry. 89 (2018) 229–242.

[43] S.-D. Wang, K.L. Scrivener, Hydration products of alkali activated slag cement, Cem. Concr. Res. 25 (1995) 561–571.

[44] S.A. Bernal, J.L. Provis, B. Walkley, R. San Nicolas, J.D. Gehman, D.G. Brice, A.R. Kilcullen, P. Duxson, J.S.J. Van Deventer, Gel nanostructure in alkali-activated binders based on slag and fly ash, and effects of accelerated carbonation, Cem. Concr. Res. 53 (2013) 127–144.

[45] T.C. Powers, T.L. Brownyard, Studies of the physical properties of hardened Portland cement paste, ACI J. Proc. 18 (1946).

[46] T.C. Powers, Structure and physical properties of hardened portland cement paste, J. Am. Ceram. Soc. 41 (1958) 1–6.

[47] T.C. Powers, L.E. Copeland, H.M. Mann, Capillary continuity or discontinuity in cement pastes, Portl. Cem. Assoc. (1959).

[48] R.S. Barneyback, S. Diamond, Expression and analysis of pore fluids from hardened cement pastes and mortars, Cem. Concr. Res. 11 (1981) 279–285.

[49] L. Bertolini, B. Elsener, P. Pedeferri, E. Redaelli, R.B. Polder, L. Bertolini, Corrosion of steel in concrete: prevention, diagnosis, repair, John Wiley & Sons, 2013.

[50] U. Angst, Chloride induced reinforcement corrosion in concrete - Concept of critical chloride content - methods and mechanisms, Thesis, Norwegian University of Science and Technology, 2011.

[51] T.C. Powers, Physical properties of cement paste, in: Proc. Chem. Cem., 1960: pp. 577–613.

[52] L. Bágel', V. Živica, Relationship between pore structure and permeability of hardened cement mortars: On the choice of effective pore structure parameter, Cem. Concr. Res. 27 (1997) 1225–1235.

[53] S. Lee, H.T. Jou, A. Van Riessen, W.D.A. Rickard, C.M. Chon, N.H. Kang, Three-dimensional quantification of pore structure in coal ash-based geopolymer using conventional electron tomography, Constr. Build. Mater. 52 (2014) 221–226.

[54] U.M. Angst, M.R. Geiker, A. Michel, C. Gehlen, H. Wong, O.B. Isgor, B. Elsener, C.M. Hansson, R. François, K. Hornbostel, R. Polder, M.C. Alonso, M. Sanchez, M.J. Correia, M. Criado, A. Sagüés, N. Buenfeld, The steel–concrete interface, Mater. Struct. 50 (2017) 143.

[55] C. Shi, P. V. Krivenko, D.M. Roy, Alkali-Activated Cements and Concretes, Taylor and Francis, Abingdon, 2006.

[56] C. Shi, Strength, pore structure and permeability of alkali-activated slag mortars, Cem. Concr. Res. 26 (1996) 1789–1799.

[57] C.E. White, D.P. Olds, M. Hartl, R.P. Hjelm, K. Page, Evolution of the pore structure during the early stages of the alkali-activation reaction: An in situ small-angle neutron scattering investigation, J. Appl. Crystallogr. 50 (2017) 61–75.

[58] Z. Zhang, H. Wang, Analysing the relation between pore structure and permeability of alkali-activated concrete binders, in: Handb. Alkali-Activated Cem. Mortars Concr., Woodhead Publishing Limited, 2015: pp. 235–264.

[59] V. Benavent, F. Frizon, A. Poulesquen, Effect of composition and aging on the porous structure of metakaolin-based geopolymers, J. Appl. Crystallogr. 49 (2016) 2116–2128.

[60] J. Melar, G. Renaudin, F. Leroux, A. Hardy-Dessources, J.M. Nedelec, C. Taviot-Gueho, E. Petit, P. Steins, A. Poulesquen, F. Frizon, The porous network and its interface inside geopolymers as a function of alkali cation and aging, J. Phys. Chem. C. 119 (2015) 17619–17632.

[61] C. Boher, I. Martin, S. Lorente, F. Frizon, Experimental investigation of gas diffusion through monomodal materials. Application to geopolymers and Vycor® glasses, Microporous Mesoporous Mater. 184 (2014) 28–36.

[62] A. Blyth, C.A. Eiben, G.W. Scherer, C.E. White, Impact of activator chemistry on permeability of alkali-activated slags, J. Am. Ceram. Soc. 100 (2017) 4848–4859.

[63] E. Kamseu, Z.N.M. Ngouloure, B.N. Ali, S. Zekeng, U.C. Melo, S. Rossignol, C. Leonelli, Cumulative pore volume, pore size distribution and phases percolation in

porous inorganic polymer composites: Relation microstructure and effective thermal conductivity, Energy Build. 88 (2015) 45–56.

[64] A. Keulen, Q.L. Yu, S. Zhang, S. Grünewald, Effect of admixture on the pore structure refinement and enhanced performance of alkali-activated fly ash-slag concrete, Constr. Build. Mater. 162 (2018) 27–36.

[65] C.F. Maitland, C.E. Buckley, B.H. Oconnor, P.D. Butler, R.D. Hart, Characterization of the pore structure of metakaolin-derived geopolymers by neutron scattering and electron microscopy, J. Appl. Crystallogr. 44 (2011) 697–707.

[66] C. Shi, R.L. Day, Alkali-slag cements for the immobilisation of radioactive wastes, in: T.M. GIlliam, C.C. WIles (Eds.), Stabilisation Solidif. Hazardous, Radioact. Mix. Wastes 3rd Vol. STP14111S, ASTM International, West Conshohocken, 1996: pp. 163–173.

[67] J.L. Provis, R.J. Myers, C.E. White, V. Rose, J.S.J. Van Deventer, X-ray microtomography shows pore structure and tortuosity in alkali-activated binders, Cem. Concr. Res. 42 (2012) 855–864.

[68] R. San Nicolas, J.L. Provis, The interfacial transition zone in alkali-activated slag mortars, Front. Mater. 2 (2015) 1–11.

[69] F.P. Glasser, J. Marchand, E. Samson, Durability of concrete - Degradation phenomena involving detrimental chemical reactions, Cem. Concr. Res. 38 (2008) 226–246.

[70] J.C. Maso, ed., Interfacial Transition Zone in Concrete, E & FN SPON, London, 1996.

[71] P. Halamickova, R.J. Detwiler, D.P. Bentz, E.J. Garboczi, Water permeability and chloride ion diffusion in portland cement mortars: Relationship to sand content and critical pore diameter, Cem. Concr. Res. 25 (1995) 790–802.

[72] A. Delagrave, J.. Bigas, J.P. Ollivier, J. Marchand, M. Pigeon, Influence of the interfacial zone on the chloride diffusivity of mortars, Adv. Cem. Based Mater. 5 (1997) 86–92.

[73] J. Zheng, H.S. Wong, N.R. Buenfeld, Assessing the influence of ITZ on the steady-state chloride diffusivity of concrete using a numerical model, Cem. Concr. Res. 39 (2009) 805–813.

[74] Y. Ma, J. Hu, G. Ye, The pore structure and permeability of alkali activated fly ash, Fuel. 104 (2013) 771–780.

[75] E. Samson, J. Marchand, J.J. Beaudoin, Modeling the influence of chemical reactions on the mechanisms of ionic transport in porous materials, Cem. Concr. Res. 30 (2000) 1895–1902.

[76] S. Song, H. Jennings, Pore solution chemistry of alkali-activated ground granulated blast-furnace slag, Cem. Concr. Res. 29 (1999) 159–170.

[77] F. Puertas, A. Fernández-Jiménez, M.. Blanco-Varela, Pore solution in alkali-activated slag cement pastes. Relation to the composition and structure of calcium silicate hydrate, Cem. Concr. Res. 34 (2004) 139–148.

[78] A. Gruskovnjak, B. Lothenbach, L. Holzer, R. Figi, F. Winnefeld, Hydration of alkali-activated slag: Comparison with ordinary Portland cement, Adv. Cem. Res. 18 (2006) 119–128.

[79] R.R. Lloyd, J.L. Provis, J.S.J. van Deventer, Pore solution composition and alkali diffusion in inorganic polymer cement, Cem. Concr. Res. 40 (2010) 1386–1392.

[80] R.J. Myers, S.A. Bernal, J.L. Provis, Phase diagrams for alkali-activated slag binders, Cem. Concr. Res. 95 (2017) 30–38.

[81] R.J. Myers, S.A. Bernal, J.L. Provis, A thermodynamic model for C-(N-)A-S-H gel: CNASH_ss. Derivation and validation, Cem. Concr. Res. 66 (2014) 27–47.

[82] M. Pourbaix, Atlas of Electrochemical Equilibria in Aqueous Solutions, 2nd ed., National Association of Corrosion Engineers, Houston, Texas, 1974.

[83] A.J. Bard, L.R. Faulkner, Electrochemical methods: fundamentals and applications, 2nd ed., Wiley, New York, 2001.

[84] M. Pourbaix, Thermodynamics and corrosion, Corros. Sci. 30 (1990) 963–988.

[85] M. Pourbaix, Lectures on Electrochemical Corrosion, Springer Science & Business Media, 1973.

[86] K. Kiani, H.M. Shodja, Prediction of the penetrated rust into the microcracks of concrete caused by reinforcement corrosion, Appl. Math. Model. 35 (2011) 2529–2543.

[87] C.H. Hamann, A. Hamnett, W. Vielstich, Electrochemistry, 2nd ed., Wiley-VCH, 2007.

[88] M. Pourbaix, Applications of electrochemistry in corrosion science and in practice, Corros. Sci. 14 (1974) 25–82.

[89] K.K. Sagoe-Crentsil, F.P. Glasser, Steel in concrete: Part II Electron microscopy analysis, Mag. Concr. Res. 41 (1989) 213–220.

[90] S. Haupt, H.H. Strehblow, Corrosion, layer formation, and oxide reduction of passive iron in alkaline solution: A combined electrochemical and surface analytical study, Langmuir. 3 (1987) 873–885.

[91] P. Ghods, O.B. Isgor, J.R. Brown, F. Bensebaa, D. Kingston, XPS depth profiling study on the passive oxide film of carbon steel in saturated calcium hydroxide solution and the effect of chloride on the film properties, Appl. Surf. Sci. 257 (2011) 4669–4677.

[92] L. Freire, X.R. Nóvoa, M.F. Montemor, M.J. Carmezim, Study of passive films formed on mild steel in alkaline media by the application of anodic potentials, Mater. Chem. Phys. 114 (2009) 962–972.

[93] S. Joiret, M. Keddam, X.R. Nóvoa, M.C. Pérez, C. Rangel, H. Takenouti, Use of EIS, ring-disk electrode, EQCM and raman spectroscopy to study the film of oxides formed on iron in 1 M NaOH, Cem. Concr. Compos. 24 (2002) 7–15.

[94] B.E. Deal, A.S. Grove, General relationship for the thermal oxidation of silicon, J. Appl. Phys. 36 (1965) 3770–3778.

[95] V.K. Gouda, Corrosion and corrosion inhibition of reinforcing steel: I.Iimmersed in

alkaline solutions, Br. Corros. J. 5 (1970) 198–203.

[96] V.K. Gouda, W.Y. Halaka, Corrosion and corrosion inhibition of reinforcing steel: II. Embedded in concrete, Br. Corros. J. 5 (1970) 204–208.

[97] H. Oranowska, Z. Szklarska-Smialowska, An electrochemical and ellipsometric investigation of surface films grown on iron in saturated calcium hydroxide solutions with or without chloride ions, Corros. Sci. 21 (1981) 735–747.

[98] A.H.-L. Goff, J. Flis, N. Boucherit, S. Joriet, J. Wilinski, Use of raman spectroscopy and rotating split ring disk electrode for identification of surface layers on iron in 1M NaOH, J. Electrochem. Soc. 137 (1990) 2684–2690.

[99] U. Angst, B. Elsener, C.K. Larsen, Ø. Vennesland, Critical chloride content in reinforced concrete - A review, Cem. Concr. Res. 39 (2009) 1122–1138.

[100] S. von Greve-Dierfeld, C. Gehlen, Performance based durability design, carbonation part 1-Benchmarking of European present design rules, Struct. Concr. 17 (2016) 309–328.

[101] L. Bertolini, B. Elsener, P. Pedeferri, E. Redaelli, R.B. Polder, Corrosion of steel in concrete: prevention, diagnosis, repair, John Wiley & Sons, 2013.

[102] M. Criado, The corrosion behaviour of reinforced steel embedded in alkali-activated mortar, in: Handb. Alkali-Activated Cem. Mortars Concr., Woodhead Publishing Limited, 2015: pp. 333–372.

[103] V.S. Ramachandran, Possible states of chloride in the hydration of tricalcium silicate in the presence of calcium chloride, Matériaux Constr. 4 (1971) 3–12.

[104] H.W. Song, C.H. Lee, K.Y. Ann, Factors influencing chloride transport in concrete structures exposed to marine environments, Cem. Concr. Compos. 30 (2008) 113–121.

[105] M. Castellote, C. Alonso, C. Andrade, G.A. Chadbourn, C.L. Page, Oxygen and chloride diffusion in cement pastes as a validation of chloride diffusion coefficients obtained by steady-state migration tests, Cem. Concr. Res. 31 (2001) 621–625.

[106] D. Roy, W. Jiang, M. Silsbee, Chloride diffusion in ordinary, blended, and alkali-activated cement pastes and its relation to other properties, Cem. Concr. Res. 30 (2000) 1879–1884.

[107] L. Tang, L.-O. Nilsson, P.A.M. Basheer, Resistance of Concrete to Chloride Ingress: Testing and Modeling, Taylor and Francis, U.K., 2011.

[108] fib Bulletin 34, Model Code for Service Life Design, 2006.

[109] E. Samson, J. Marchand, J.J. Beaudoin, Describing ion diffusion mechanisms in cement-based materials using the homogenization technique, Cem. Concr. Res. 29 (1999) 1341–1345.

[110] C. Andrade, J.M. Diez, C. Alonso, Mathematical modeling of a concrete surface `skin effect' on diffusion in chloride contaminated media, Adv. Cem. Based Mater. 6 (1997) 39–44.

[111] A. Boddy, R.. Hooton, K.. Gruber, Long-term testing of the chloride-penetration resistance of concrete containing high-reactivity metakaolin, Cem. Concr. Res. 31 (2001) 759–765.

[112] M.D.A. Thomas, P.B. Bamforth, Modelling chloride diffusion in concrete, Cem. Concr. Res. 29 (1999) 487–495.

[113] R. Talero, R. Mejía, C. Gutiérrez, S. Delvasto, Chloride diffusion measured by a modified permeability test in normal and blended cements, Adv. Cem. Res. 15 (2003) 113–118.

[114] I. Ismail, S.A. Bernal, J.L. Provis, R. San Nicolas, D.G. Brice, A.R. Kilcullen, S. Hamdan, J.S.J. Van Deventer, Influence of fly ash on the water and chloride permeability of alkali-activated slag mortars and concretes, Constr. Build. Mater. 48 (2013) 1187–1201.

[115] C. Tennakoon, A. Shayan, J.G. Sanjayan, A. Xu, Chloride ingress and steel corrosion in geopolymer concrete based on long term tests, Mater. Des. 116 (2017) 287–299.

[116] Q. Ma, S. V. Nanukuttan, P.A.M. Basheer, Y. Bai, C. Yang, Chloride transport and the resulting corrosion of steel bars in alkali activated slag concretes, Mater. Struct. 49 (2016) 3663–3677.

[117] L. Tang, J. Gulikers, On the mathematics of time-dependent apparent chloride diffusion coefficient in concrete, Cem. Concr. Res. 37 (2007) 589–595.

[118] S.-D. Wang, X.-C. Pu, K.L. Scrivener, P.L. Pratt, Alkali-activated slag cement and concrete: a review of properties and problems, Adv. Cem. Res. 7 (1995) 93–102.

[119] J.L. Provis, A. Palomo, C. Shi, Advances in understanding alkali-activated materials, Cem. Concr. Res. 78 (2015) 110–125.

[120] C. Arya, N.R. Buenfeld, J.B. Newman, Factors influencing chloride binding in concrete, Cem. Concr. Res. 20 (1990) 291–300.

[121] A. Fernández-Jiménez, R. Vallepu, T. Terai, A. Palomo, K. Ikeda, Synthesis and thermal behavior of different aluminosilicate gels, J. Non. Cryst. Solids. 352 (2006) 2061–2066.

[122] C. Labbez, A. Nonat, I. Pochard, B. Jönsson, Experimental and theoretical evidence of overcharging of calcium silicate hydrate, J. Colloid Interface Sci. 309 (2007) 303–307.

[123] O. Kayali, M.S. Ahmed, M.S.H. Khan, Friedel's salt and hydrotalcite – layered double hydroxides and the protection against chloride induced corrosion, Civ. Environ. Res. 5 (2013) 111–117.

[124] O. Kayali, M.S.H. Khan, M.S. Ahmed, The role of hydrotalcite in chloride binding and corrosion protection in concretes with ground granulated blast furnace slag, Cem. Concr. Compos. 34 (2012) 936–945.

[125] X. Ke, S.A. Bernal, J.L. Provis, Uptake of chloride and carbonate by Mg-Al and Ca-Al layered double hydroxides in simulated pore solutions of alkali-activated slag cement, Cem. Concr. Res. 100 (2017) 1–13.

[126] A. Pourbaix, Localized corrosion: behaviour and protection mechanisms, Corros. Chem.

Within Pits, Crevices Cracks, Natl. Phys. Lab. (1984) 1–15.

[127] R. P. Franlemthal, H. W. Pickering, On the mechanism of localized corrosion of iron and stainless steel, J. Electrochem. Soc. 119 (1972) 1304–1310.

[128] V. Jovancicevic, J.O. Bockris, J.L. Carbajal, P. Zelenay, T. Mizuno, Adsorption and absorption of chloride ions on passive iron systems, J. Electrochem. Soc. 133 (1986) 2219–2226.

[129] T.P. Hoar, W.R. Jacob, Breakdown of passivity of stainless steel by halide ions, Nature. 216 (1967) 1299–1301.

[130] T.P. Hoar, The production and breakdown of the passivity of metals, Corros. Sci. 7 (1967) 341–355.

[131] K. Osozawa, N. Okato, Passivity and its breakdown on iron and iron-base alloys, NACE, Houston, USA. (1976) 135.

[132] L.F. Lin, C.Y. Chao, D.D. MacDonald, A point defect model for anodic passive films II. Chemical breakdown and pit initiation, J. Electrochem. Soc. 128 (1981) 1194–1198.

[133] C.Y. Chao, L.F. Lin, D.D. MacDonald, A point defect model for anodic passive films I. Film growth kinetics, J. Electrochem. Soc. 128 (1981) 1187.

[134] C.L. Page, K.W.J. Treadaway, Aspects of the electrochemistry of steel in concrete, Nature. 297 (1982) 109–115.

[135] D.A. Hausmann, Steel corrosion in concrete: How does it occur?, J. Mater. Prot. (1967) 19–23.

[136] L. Li, A. a. Sagues, Chloride corrosion threshold of reinforcing steel in alkaline solutions - Open circuit immersion tests, Corrosion. 57 (2001) 19–28.

[137] K.S. Rajagopalan, K. Venu, K. Balakrishnan, Anodic polarization studies in neutral and alkaline solutions containing corrosion inhibitors: 1. NaOH-NaCl systems, J. Electrochem. Soc. 109 (1962) 81–87.

[138] S. Diamond, Chloride concentrations in concrete pore solutions resulting from calcium and sodium chloride admixtures, Cem. Concr. Aggregates. 8 (1986) 97–102.

[139] S. Goñi, C. Andrade, Synthetic concrete pore solution chemistry and rebar corrosion rate in the presence of chlorides, Cem. Concr. Res. 20 (1990) 525–539.

[140] W. Breit, Critical chloride content-Investigations of steel in alkaline chloride solutions, Mater. Corros. Und Korrosion. 49 (1998) 539–550.

[141] M. Moreno, W. Morris, M.G. Alvarez, G.S. Duffó, Corrosion of reinforcing steel in simulated concrete pore solutions, Corros. Sci. 46 (2004) 2681–2699.

[142] G.K. Glass, N.R. Buenfeld, The presentation of the chloride threshold level for corrosion of steel in concrete, Corros. Sci. 39 (1997) 1001–1013.

[143] G.K. Glass, B. Reddy, N.R. Buenfeld, The participation of bound chloride in passive film breakdown on steel in concrete, Corros. Sci. 42 (2000) 2013–2021.

[144] C. M. Hansson, B. Sørensen, The Threshold value of chloride concentration for the corrosion of reinforcement in concrete, in: N.S. Berke, V. Chaker, D. Whiting (Eds.), Corros. Rates Steel Concr., ASTM STP 1, American Society for Testing and Materials, Philadelphia, 1990: pp. 3–16.

[145] P. Schiessl, M. Raupach, Influence of concrete composition and microclimate on the critical chloride content in concrete, in: Corros. Reinf. Concr., Elsevier Science Publishers, The Belfry Hotel, Wishaw, Warwickshire, UK, n.d.: pp. 49–58.

[146] C.L. Page, P. Lambert, P.R.W. Vassie, Investigations of reinforcement corrosion. 1. The pore electrolyte phase in chloride-contaminated concrete, Mater. Struct. 24 (1991) 243–252.

[147] P. Lambert, C.L. Page, P.R.W. Vassie, Investigations of reinforcement corrosion. 2. Electrochemical monitoring of steel in chloride-contaminated concrete, Mater. Struct. 24 (1991) 351–358.

[148] K. Pettersson, Corrosion threshold value and corrosion rate in reinforced concrete, 1992.

[149] P. Schiessl, W. Breit, Local repair measures at concrete structures damaged by reinforcement corrosion - aspects of durability, in: C.L. Page (Ed.), 4th Int. Symp. Corros. Reinf. Concr. Constr., Royal Society of Chemistry, Cambridge UK, 1996: pp. 525–534.

[150] W. Breit, Kritischer korrosionsauslösender Chloridgehalt – Untersuchungen an Mörtelelektroden in chloridhaltigen alkalischen Lösungen, Mater. Corros. 54 (2003) 430–439.

[151] L. Zimmermann, Korrosionsinitiierender Chloridgehalt von Stahl in Beton, ETH Zurich, 2000.

[152] C. Alonso, M. Castellote, C. Andrade, Chloride threshold dependence of pitting potential of reinforcements, Electrochim. Acta. 47 (2002) 3469–3481.

[153] M. Castellote, C. Andrade, C. Alonso, Accelerated simultaneous determination of the chloride depassivation threshold and of the non-stationary diffusion coefficient values, Corros. Sci. 44 (2002) 2409–2424.

[154] D. Trejo, R.G. Pillai, Accelerated Chloride Threshold Testing: Part I-ASTM A 615 and A 706 Reinforcement, ACI Mater. J. 100 (2003) 519–527.

[155] W. Morris, A. Vico, M. Vázquez, Chloride induced corrosion of reinforcing steel evaluated by concrete resistivity measurements, Electrochim. Acta. 49 (2004) 4447–4453.

[156] W. Morris, A. Vico, M. Vazquez, S.R. de Sanchez, Corrosion of reinforcing steel evaluated by means of concrete resistivity measurements, Corros. Sci. 44 (2002) 81–99.

[157] P. V. Nygaard, M.R. Geiker, A method for measuring the chloride threshold level required to initiate reinforcement corrosion in concrete, Mater. Struct. 38 (2005) 489–494.

[158] D. Trejo, P.J. Monteiro, Corrosion performance of conventional (ASTM A615) and low-alloy (ASTM A706) reinforcing bars embedded in concrete and exposed to chloride

environments, Cem. Concr. Res. 35 (2005) 562–571.

[159] T.U. Mohammad, H. Hamada, Corrosion of Steel Bars in Concrete with Various Steel Surface Conditions, Mater. J. 103 (2006) 233–242.

[160] E. Zitrou, J. Nikolaou, P.E. Tsakiridis, G.D. Papadimitriou, Atmospheric corrosion of steel reinforcing bars produced by various manufacturing processes, Constr. Build. Mater. 21 (2007) 1161–1169.

[161] U.M. Angst, B. Elsener, Forecasting chloride-induced reinforcement corrosion - effect of realistic reinforcement steel surface conditions, in: 4th Int. Conf. Concr. Repair, Rehabil. Retrofit. (ICCRRR), Leipzig, Ger., 2015.

[162] P. Ghods, O.B. Isgor, G.A. McRae, J. Li, G.P. Gu, Microscopic investigation of mill scale and its proposed effect on the variability of chloride-induced depassivation of carbon steel rebar, Corros. Sci. 53 (2011) 946–954.

[163] K. Karadakis, V.J. Azad, P. Ghods, O.B. Isgor, Numerical investigation of the role of mill scale crevices on the corrosion initiation of carbon steel reinforcement in concrete, J. Electrochem. Soc. 163 (2016) C306–C315.

[164] L.T. Mammoliti, L.C. Brown, C.M. Hansson, B.B. Hope, The influence of surface finish of reinforcing steel and pH of the test solution on the chloride threshold concentration for corrosion initiation in synthetic pore solutions, Cem. Concr. Res. 26 (1996) 545–550.

[165] P. Ghods, O.B. Isgor, G. McRae, T. Miller, The effect of concrete pore solution composition on the quality of passive oxide films on black steel reinforcement, Cem. Concr. Compos. 31 (2009) 2–11.

[166] P.J.M. Monteiro, O.E. Gjorv, P.K. Mehta, Microstructure of the steel-cement interface in the presence of chlorides, Cem. Concr. Res. 15 (1985) 781–784.

[167] R. Zhang, A. Castel, R. François, Influence of steel-concrete interface defects owing to the top-bar effect on the chloride- induced corrosion of reinforcement, Mag. Concr. Res. 63 (2011) 773–781.

[168] S.A. Bernal, The resistance of alkali-activated cement-based binders to carbonation, in: Handb. Alkali-Activated Cem. Mortars Concr., Woodhead Publishing Limited, 2015: pp. 319–332.

[169] A. Morandeau, M. Thiéry, P. Dangla, Investigation of the carbonation mechanism of CH and C-S-H in terms of kinetics, microstructure changes and moisture properties, Cem. Concr. Res. 56 (2014) 153–170.

[170] A. Morandeau, M. Thiéry, P. Dangla, Impact of accelerated carbonation on OPC cement paste blended with fly ash, Cem. Concr. Res. 67 (2015) 226–236.

[171] K. Adamczyk, M. Prémont-Schwarz, D. Pines, E. Pins, E.T.J. Nibbering, Real-time observation of carbonic acid formation in aqueous solutions, Science (80-.). 326 (2009) 1690–1694.

[172] L. Black, C. Breen, J. Yarwood, K. Garbev, P. Stemmermann, B. Gasharova, Structural features of C-S-H(I) and its carbonation in air-A Raman spectroscopic study. Part II:

Carbonated phases, J. Am. Ceram. Soc. 90 (2007) 908–917.

[173] D.I. Rodway, G.W. Groves, I.G. Richardson, The carbonation of hardened cement pastes, Adv. Cem. Res. 3 (1990) 117–125.

[174] D.J. Anstice, C.L. Page, M.M. Page, The pore solution phase of carbonated cement pastes, Cem. Concr. Res. 35 (2005) 377–383.

[175] S.A. Bernal, J.L. Provis, D.G. Brice, A. Kilcullen, P. Duxson, J.S.J. van Deventer, Accelerated carbonation testing of alkali-activated binders significantly underestimates service life: The role of pore solution chemistry, Cem. Concr. Res. 42 (2012) 1317–1326.

[176] R. Pouhet, M. Cyr, Carbonation in the pore solution of metakaolin-based geopolymer, Cem. Concr. Res. 88 (2016) 227–235.

[177] M. Palacios, F. Puertas, Effect of Carbonation on Alkali-Activated Slag Paste, J. Am. Ceram. Soc. 89 (2006) 3211–3221.

[178] S.A. Bernal, R. San Nicolas, R.J. Myers, R. Mejía De Gutiérrez, F. Puertas, J.S.J. Van Deventer, J.L. Provis, MgO content of slag controls phase evolution and structural changes induced by accelerated carbonation in alkali-activated binders, Cem. Concr. Res. 57 (2014) 33–43.

[179] S.A. Bernal, R.M. de Gutierrez, J.L. Provis, V. Rose, Effect of silicate modulus and metakaolin incorporation on the carbonation of alkali silicate-activated slags, Cem. Concr. Res. 40 (2010) 898–907.

[180] M. Criado, A. Palomo, A. Fernández-Jiménez, Alkali activation of fly ashes. Part 1: Effect of curing conditions on the carbonation of the reaction products, Fuel. 84 (2005) 2048–2054.

[181] ASTM C876-15, Standard test method for corrosion potentials of uncoated reinforcing steel in concrete, ASTM International, 2015.

[182] C. Andrade, C. Alonso, Corrosion rate monitoring in the laboratory and on-site, Constr. Build. Mater. 10 (1996) 315–328.

[183] C. Andrade, M.C. Alonso, J.A. González, An initial effort to use the corrosion rate measurements for estimating rebar durability, in: N. Berke, V. Chaker, D. Whiting (Eds.), Corros. Rates Steel Concr., STP25013S ed., ASTM International, West Conshohocken, PA, 1990: pp. 29–37.

[184] P. Ghods, O.B. Isgor, G.A. McRae, G.P. Gu, Electrochemical investigation of chloride-induced depassivation of black steel rebar under simulated service conditions, Corros. Sci. 52 (2010) 1649–1659.

[185] M. Stern, A.L. Geary, Electrochemical Polarization, J. Electrochem. Soc. 104 (1957) 559.

[186] C. Wagner, W. Traud, Über die deutung von korro- sionsvorgängen durch Überlagerung von elektrochemischen teilvorgängen und Über die potentialbildung an mischelektroden (german version), Zeitschrift Für Elektrochemie Und Angew. Phys. Chemie. 44 (1938) 391–402.

[187] U. Angst, M. Büchler, On the applicability of the Stern-Geary relationship to determine instantaneous corrosion rates in macro-cell corrosion, Mater. Corros. 66 (2015) 1017–1028.

[188] RILEM TC 154-EMC, Recommendations of RILEM TC 154-EMC: "Electrochemical Techniques for Measuring Metallic Corrosion" Test methods for on-site corrosion rate measurement of steel reinforcement in concrete by means of the polarization resistance method, Mater. Struct. 37 (2004) 623–643.

[189] ASTM G3-14, Standard practice for conventions applicable to electrochemical measurements in corrosion testing, 2014.

[190] B.-Y. Chang, S.-M. Park, Electrochemical impedance spectroscopy, Annu. Rev. Anal. Chem. 3 (2010) 207–229.

[191] A. Carnot, I. Frateur, S. Zanna, B. Tribollet, I. Dubois-Brugger, P. Marcus, Corrosion mechanisms of steel concrete moulds in contact with a demoulding agent studied by EIS and XPS, Corros. Sci. 45 (2003) 2513–2524.

[192] C.Q. Ye, R.G. Hu, S.G. Dong, X.J. Zhang, R.Q. Hou, R.G. Du, C.J. Lin, J.S. Pan, EIS analysis on chloride-induced corrosion behavior of reinforcement steel in simulated carbonated concrete pore solutions, J. Electroanal. Chem. 688 (2013) 275–281.

[193] M. Sánchez, J. Gregori, C. Alonso, J.J. García-Jareño, H. Takenouti, F. Vicente, Electrochemical impedance spectroscopy for studying passive layers on steel rebars immersed in alkaline solutions simulating concrete pores, Electrochim. Acta. 52 (2007) 7634–7641.

[194] E. Volpi, A. Olietti, M. Stefanoni, S.P. Trasatti, Electrochemical characterization of mild steel in alkaline solutions simulating concrete environment, J. Electroanal. Chem. 736 (2015) 38–46.

[195] C. Andrade, M. Keddam, X.R. Nóvoa, M.C. Pérez, C.M. Rangel, H. Takenouti, Electrochemical behaviour of steel rebars in concrete: Influence of environmental factors and cement chemistry, Electrochim. Acta. 46 (2001) 3905–3912.

[196] D.A. Harrington, P. Van Den Driessche, Mechanism and equivalent circuits in electrochemical impedance spectroscopy, Electrochim. Acta. 56 (2011) 8005–8013.

[197] M. Cabeza, P. Merino, A. Miranda, X.R. Nóvoa, I. Sanchez, Impedance spectroscopy study of hardened Portland cement paste, Cem. Concr. Res. 32 (2002) 881–891.

[198] S.W. Tang, Z.J. Li, E. Chen, H.Y. Shao, Impedance measurement to characterize the pore structure in Portland cement paste, Constr. Build. Mater. 51 (2014) 106–112.

[199] G.A. Mabbott, An introduction to cyclic voltammetry, J. Chem. Educ. 60 (1983) 697–702.

[200] D.D. Macdonald, B. Roberts, The cyclic voltammetry of carbon steel in concentrated sodium hydroxide solution, Electrochim. Acta. 23 (1978) 781–786.

[201] ISO/DIS 6935-2, Steel for the reinforcement of concrete - Part 2: Ribbed bars, International Organization for Standardization, 2015.

[202] A. Vollpracht, B. Lothenbach, R. Snellings, J. Haufe, The pore solution of blended cements: a review, Mater. Struct. 49 (2016) 3341–3367.

[203] D.J. Graham, B. Jaselskis, C.E. Moore, Development of the glass electrode and the pH response, J. Chem. Educ. 90 (2013) 345–351.

[204] RILEM TC 154-EMC, Recommendations of RILEM TC 154-EMC: 'Electrochemical Techniques for Measuring Metallic Corrosion'- Half-cell potential measurements-Potential mapping on reinforced concrete structures, Mater. Struct. 36 (2003) 461–471.

[205] R.G. Kelly, J.R. Scully, D.W. Shoesmith, R.G. Buchheit, Electrochemical Techniques in Corrosion Science and Engineering, Marcel Dekker, Inc., New York, 2003.

[206] M. Sánchez-Moreno, H. Takenouti, J.J. García-Jareño, F. Vicente, C. Alonso, A theoretical approach of impedance spectroscopy during the passivation of steel in alkaline media, Electrochim. Acta. 54 (2009) 7222–7226.

[207] M. Sánchez, J. Gregori, M.C. Alonso, J.J. García-Jareño, F. Vicente, Anodic growth of passive layers on steel rebars in an alkaline medium simulating the concrete pores, Electrochim. Acta. 52 (2006) 47–53.

[208] O. Poupard, A. Ait-Mokhtar, P. Dumargue, Corrosion by chlorides in reinforced concrete: Determination of chloride concentration threshold by impedance spectroscopy, Cem. Concr. Res. 34 (2004) 991–1000.

[209] B.J. Christensen, T. Coverdale, R.A. Olson, S.J. Ford, E.J. Garboczi, H.M. Jennings, T.O. Mason, Impedance spectroscopy of hydrating cement-based materials: Measurement, interpretation, and application, J. Am. Ceram. Soc. 77 (1994) 2789–2804.

[210] W.J. McCarter, R. Brousseau, The A.C. response of hardened cement paste, Cem. Concr. Res. 20 (1990) 891–900.

[211] S. Guangling, Equivalent circuit model for AC electrochemical impedance spectroscopy of concrete, Cem. Concr. Res. 30 (2000) 1723–1730.

[212] B. Elsener, H. Böhni, Corrosion of steel in mortar studied by impedance measurements, Mater. Sci. Forum. 8 (1986) 363–372.

[213] C. Andrade, J.A. González, Quantitative measurements of corrosion rate of reinforcing steels embedded in concrete using polarization resistance measurements, Mater. Corros. 29 (1978) 515–519.

[214] M. Babaee, A. Castel, Chloride-induced corrosion of reinforcement in low-calcium fly ash-based geopolymer concrete, Cem. Concr. Res. 88 (2016) 96–107.

[215] D.A. Kulik, M. Kersten, Aqueous solubility diagrams for cementitious waste stabilization systems. 4. A carbonation model for Zn-doped calcium silicate hydrate by Gibbs energy minimization, J. Am. Ceram. Soc. 84 (2001) 3017–3026.

[216] D.A. Kulik, T. Wagner, S. V. Dmytrieva, G. Kosakowski, F.F. Hingerl, K. V. Chudnenko, U.R. Berner, GEM-Selektor geochemical modeling package: Revised algorithm and GEMS3K numerical kernel for coupled simulation codes, Comput. Geosci. 17 (2013) 1–24.

[217] B. Lothenbach, F. Winnefeld, Thermodynamic modelling of the hydration of Portland cement, Cem. Concr. Res. 36 (2006) 209–226.

[218] T. Matschei, B. Lothenbach, F.P. Glasser, Thermodynamic properties of Portland cement hydrates in the system CaO-Al_2O_3-SiO_2-$CaSO_4$-$CaCO_3$-H_2O, Cem. Concr. Res. 37 (2007) 1379–1410.

[219] R.J. Myers, Thermodynamic modelling of CaO-Al_2O_3-SiO_2-H_2O based cements, Thesis, The Univerity of Sheffield, 2015.

[220] R.J. Myers, B. Lothenbach, S.A. Bernal, J.L. Provis, Thermodynamic modelling of alkali-activated slag cements, Appl. Geochemistry. 61 (2015) 233–247.

[221] J. Crank, The Mathematics of Diffusion, 2nd ed., Oxford University Press, 1975.

[222] G.D. Smith, Numerical Solution of Partial Differential Equations, 3rd ed., Oxford University Press, 1965.

[223] L. Li, A.A. Sagues, Chloride corrosion threshold of reinforcing steel in alkaline solutions - open-circuit immersion tests, Corrosion. 57 (2001) 19–28.

[224] H.E.H. Bird, B.R. Pearson, P.A. Brook, The breakdown of passive films on iron, Corros. Sci. 28 (1988) 81–86.

[225] O.A. Kayyali, M.N. Haque, The Cl-/OH- ratio in chloride -contaminated concrete - A most important criterion, Mag. Concr. Res. 47 (1995) 235–242.

[226] U.M. Angst, B. Elsener, C.K. Larsen, Ø. Vennesland, Chloride induced reinforcement corrosion: Electrochemical monitoring of initiation stage and chloride threshold values, Corros. Sci. 53 (2011) 1451–1464.

[227] G.K. Glass, N.R. Buenfeld, The inhibitive effects of electrochemical treatment applied to steel in concrete, 2000.

[228] J.A. González, E. Otero, S. Feliu, W. López, Initial steps of corrosion in the steel/Ca(OH)2 + Cl- system: the role of heterogeneities on the steel surface and oxygen supply, Cem. Concr. Res. 23 (1993) 33–40.

[229] P. Duxson, G.C. Lukey, F. Separovic, J.S.J. Van Deventer, Effect of alkali cations on aluminum incorporation in geopolymeric gels, Ind. Eng. Chem. Res. 44 (2005) 832–839.

[230] J.M. Miranda, A. Fernández-Jiménez, J.A. González, A. Palomo, Corrosion resistance in activated fly ash mortars, Cem. Concr. Res. 35 (2005) 1210–1217.

[231] D.M. Bastidas, A. Fernández-Jiménez, A. Palomo, J.A. González, A study on the passive state stability of steel embedded in activated fly ash mortars, Corros. Sci. 50 (2008) 1058–1065.

[232] M. Criado, D.M. Bastidas, S. Fajardo, A. Fernández-Jiménez, J.M. Bastidas, Corrosion behaviour of a new low-nickel stainless steel embedded in activated fly ash mortars, Cem. Concr. Compos. 33 (2011) 644–652.

[233] C. Monticelli, M.E. Natali, A. Balbo, C. Chiavari, F. Zanotto, S. Manzi, M.C. Bignozzi,

Corrosion behavior of steel in alkali-activated fly ash mortars in the light of their microstructural, mechanical and chemical characterization, Cem. Concr. Res. 80 (2016) 60–68.

[234] B. Kabanov, R. Burstein, A. Frumkin, Kinetics of electrode processes on the iron electrode, Discuss. Faraday Soc. 1 (1947) 259–269.

[235] M. Jayalakshmi, V.S. Muralidharan, Passivation and hydrogen evolution studies on iron in alkali solutions, Corros. Rev. 12 (1994) 305–320.

[236] R.S. Schrebler Guzman, J.R. Vilche, A.J. Arvia, The voltammetric detection of intermediate electrochemical processes related to iron in alkaline aqueous solutions, J. Appl. Electrochem. 11 (1981) 551–561.

[237] R.S. Schrebler Guzman, J.R. Vilche, A.J. Arvia, The potentiodynamic behaviour of iron in alkaline solutions, Electrochim. Acta. 24 (1979) 395–403.

[238] D.M. Drazic, C.S. Hao, Anodic Processes on an Iron Electrode in Neutral Electrolytes, Doc. Chem. Yugosl. 47 (1982) 649–659.

[239] J.O. Bockris, S.U.M. Khan, Surface electrochemistry: a molecular level approach, Springer Science & Business Media, 2013.

[240] H. Neugebauer, G. Nauer, N. Brinda-konopik, G. Gidaly, The in situ determination of oxidation products on iron electrodes in alkaline electrolytes using multiple internal reflection fourier transform infrared spectroscopy, J. Electroanal. Chem. 122 (1981) 381–385.

[241] L.D. Burke, M.E.G. Lyons, The formation and stability of hydrous oxide films on iron under potential cycling conditions in aqueous solution at high pH, J. Electroanal. Chem. 198 (1986) 347–368.

[242] W. Tschinkel, H. Neugebauer, A. Neckel, In situ FTIR spectroscopy of iron electrodes in alkaline solutions II. External reflection absorption spectroscopy, J. Electrochem. Soc. 137 (1990) 1475.

[243] D.D. Macdonald, D. Owen, The electrochemistry of iron in 1M lithium hydroxide solution at 22° and 200°C, J. Electrochem. Soc. 120 (1973) 317–324.

[244] J.R. MacDonald, Impedence Spectroscopy-Emphasizing Solid Materials and Systems, Wiley-Interscience, John Wiley and Sons, 1987.

[245] G.T. Burstein, P.C. Pistorius, S.P. Mattin, The nucleation and growth of corrosion pits on stainless-steel, Corros. Sci. 35 (1993) 57–62.

[246] N.J.J. Laycock, R.C.C. Newman, Localised dissolution kinetics, salt films and pitting potentials, Corros. Sci. 39 (1997) 1771–1790.

[247] U. Angst, B. Elsener, C.K. Larsen, Ø. Vennesland, Chloride induced reinforcement corrosion: Rate limiting step of early pitting corrosion, Electrochim. Acta. 56 (2011) 5877–5889.

[248] U. Angst, A. Rønnquist, B. Elsener, C.K. Larsen, Ø. Vennesland, Probabilistic considerations on the effect of specimen size on the critical chloride content in

reinforced concrete, Corros. Sci. 53 (2011) 177–187.

[249] S.M. Abd El Haleem, S. Abd El Wanees, E.E. Abd El Aal, A. Diab, Environmental factors affecting the corrosion behavior of reinforcing steel. IV. Variation in the pitting corrosion current in relation to the concentration of the aggressive and the inhibitive anions, Corros. Sci. 52 (2010) 1675–1683.

[250] F. Zhang, J. Pan, C. Lin, Localized corrosion behaviour of reinforcement steel in simulated concrete pore solution, Corros. Sci. 51 (2009) 2130–2138.

[251] A. Poursaee, C.M. Hansson, Reinforcing steel passivation in mortar and pore solution, Cem. Concr. Res. 37 (2007) 1127–1133.

[252] J. Williamson, O.B. Isgor, The effect of simulated concrete pore solution composition and chlorides on the electronic properties of passive films on carbon steel rebar, Corros. Sci. 106 (2016) 82–95.

[253] F. Winnefeld, M. Ben Haha, G. Le Saoût, M. Costoya, S.C. Ko, B. Lothenbach, Influence of slag composition on the hydration of alkali-activated slags, J. Sustain. Cem. Mater. 4 (2014) 85–100.

[254] D.E. Macphee, H.T. Cao, Theoretical description of impact of blast-furnace slag (BFS) on steel passivation in concrete, Mag. Concr. Res. 45 (1993) 63–69.

[255] A. Scott, M.G. Alexander, Effect of supplementary cementitious materials (binder type) on the pore solution chemistry and the corrosion of steel in alkaline environments, Cem. Concr. Res. 89 (2016) 45–55.

[256] F.P. Glasser, K. Luke, M.J. Angus, Modification of cement pore fluid compositions by pozzolanic additives, Cem. Concr. Res. 18 (1988) 165–178.

[257] W.J. Lorenz, K.E. Heusler, Anodic dissolution of iron group metals, in: F. Mansfeld (Ed.), Corros. Mech., Marcell-Dekker, New York, 1987: pp. 1–84.

[258] M.J. Angus, F.P. Glasser, The chemical environment in cement matrices, in: MRS Proc., Cambridge University Press, 1985: pp. 547–556.

[259] N.R. Jarrah, O.S.B. Al-Amoudi, M. Maslehuddin, O.A. Ashiru, A.I. Al-Mana, Electrochemical behavior of steel in plain and blended cement concretes in sulphate and/or chloride environments, Constr. Build. Mater. 9 (1995) 97–103.

[260] P. Schiessl, W. Breit, Investigation on the threshold value of the critical chloride content, in: V.M. Malhotra (Ed.), Fourth CANMET/ACI Conf. Durab. Concr. Spec. Publ. 170, Sydney, Australia, 1997.

[261] V.K. Gouda, M.A. Shater, R.S. Mikhail, Hardened portland blast-furnace slag cement pastes II. The corrosion behavior of steel reinforcement, Cem. Concr. Res. 5 (1975) 1–13.

[262] B.H. Oh, S.Y. Jang, Y.S. Shin, Experimental investigation of the threshold chloride concentration for corrosion initiation in reinforced concrete structures, Mag. Concr. Res. 55 (2003) 117–124.

[263] H.T. Cao, D. Baweja, H. Roper, Corrosion characteristics of steel in solutions derived

from cements and blended cements, Cem. Concr. Res. 20 (1990) 325–334.

[264] M. Babaee, A. Castel, Chloride diffusivity, chloride threshold, and corrosion initiation in reinforced alkali-activated mortars: Role of calcium, alkali, and silicate content, Cem. Concr. Res. 111 (2018) 56–71.

[265] M. Holloway, J.M. Sykes, Studies of the corrosion of mild steel in alkali-activated slag cement mortars with sodium chloride admixtures by a galvanostatic pulse method, Corros. Sci. 47 (2005) 3097–3110.

[266] H.W. Nesbitt, I.J. Muir, X-ray photoelectron spectroscopic study of a pristine pyrite surface reacted with water vapour and air, Geochim. Cosmochim. Acta. 58 (1994) 4667–4679.

[267] A. Matamoros-Veloza, O. Cespedes, B.R.G. Johnson, T.M. Stawski, U. Terranova, N.H. de Leeuw, L.G. Benning, A highly reactive precursor in the iron sulfide system, Nat. Commun. 9 (2018).

[268] D.W. Shoesmith, P. Taylor, M.G. Bailey, B. Ikeda, Electrochemical behaviour of iron in alkaline sulphide solutions, Electrochim. Acta. 23 (1978) 903–916.

[269] J. Vera, S. Kapusta, N. Hackerman, Localized corrosion of iron in alkaline sulfide solutions, J. Electrochem. Soc. 133 (1986) 461–467.

[270] C. Chanson, P. Blanchard, A. Wattiaux, J.-C. Grenier, A ring-disk study of electrochemical behavior of iron in strong alkaline medium: influence of additive sulfide ions, J. Electrochem. Soc. 136 (1989) 3690–3695.

[271] R.C. Salvarezza, H.A. Videla, A.J. Arvia, The electrodissolution and passivation of mild steel in alkaline sulphide solutions, Corros. Sci. 22 (1982) 815–829.

[272] Y. Liu, H. Liu, X. Guo, N. Hu, Influence of ionic strength on electrochemical responses of myoglobin loaded in polysaccharide layer-by-layer assembly films, Electroanalysis. 22 (2010) 2261–2268.

[273] D. Tromans, Anodic Polarization Behavior of Mild Steel in Hot Alkaline Sulfide Solutions, J. Electrochem. Soc. 127 (1980) 1253–1253.

[274] H. Von Kaesche, Elektrochemische untersuchungen über die korrosion des eisens in sulfidhaltigen lösungen (in German), Mater. Corros. Und Korrosion. 21 (1970) 185–195.

[275] D.W. Shoesmith, M.G. Bailey, B. Ikeda, Electrochemical formation of mackinawite in alkaline sulphide solutions, Electrochim. Acta. 23 (1978) 1329–1339.

[276] K.Y. Chen, J.C. Morris, Kinetics of oxidation of aqueous sulfide by O_2, Environ. Sci. Technol. 6 (1972) 529–537.

[277] J.B. Lefers, W.T. Koetsier, W.P.M. Van Swaaij, The oxidation of sulphide in aqueous solutions, Chem. Eng. J. 15 (1978) 111–120.

[278] M.P.J. Brennan, The anodic evolution of sulphur from sodium polysulphide melts-I. Voltammetric measurements on planar carbon electrodes, Electrochim. Acta. 22 (1977) 279–283.

[279] N. Ramasubramanian, Anodic behavior of platinum electrodes in sulfide solutions and the formation of platinum sulfide, J. Electroanal. Chem. 64 (1975) 21–37.

[280] M. Avrahami, R.. Golding, The oxidation of the sulfide ion at very low concentrations in aqueous solutions, J. Chem. Soc. A Inorganic, Phys. Theor. (1968) 647–651.

[281] A.J. Calandra, N.R. de Tacconi, R. Pereiro, A.J. Arvia, Potentiodynamic current/potential relations for film formation under OHMIC resistance control, Electrochim. Acta. 19 (1974) 901–905.

[282] V. Garcia, R. François, M. Carcasses, P. Gegout, Potential measurement to determine the chloride threshold concentration that initiates corrosion of reinforcing steel bar in slag concretes, Mater. Struct. 47 (2013) 1483–1499.

[283] M. Criado, J.L. Provis, Alkali activated slag mortars provide high resistance to chloride-induced corrosion of steel, Front. Mater. 5 (2018) 34.

[284] M. Criado, S. Mundra, S.A. Bernal, J.L. Provis, A study on the passive state stability of steel embedded in alkali activated slag mortars, in: 14th Int. Conf. Durab. Build. Mater. Components (XIV DBMC)., Ghent, Belgium, 2017.

[285] C.F. Jones, S. LeCount, R.S.C. Smart, T.J. White, Compositional and structural alteration of pyrrhotite surfaces in solution: XPS and XRD studies, Appl. Surf. Sci. 55 (1992) 65–85.

[286] R.B. Herbert Jr, A.R. Pratt, D.W. Blowes, S.G. Benner, Surface oxidation of iron monosulphide: an X-ray photoelectron spectroscopic study, in: Goldschmidt Conf. Mineral. Mag., Toulouse, France, 1998: p. 1998.

[287] A.N. Buckley, R. Woods, X-ray photoelectron spectroscopy of oxidised pyrrhotite surfaces, Appl. Surf. Sci. 20 (1985) 472–480.

[288] A.L. Neal, S. Techkarnjanaruk, A. Dohnalkova, D. Mccready, B.M. Peyton, G.G. Geesey, Iron sulfides and sulfur species produced at hematite surfaces in the presence of sulfate-reducing bacteria, Geochim. Cosmochim. Acta. 65 (2001) 223–235.

[289] M. Criado, S.A. Bernal, P. Garcia-Triñanes, J.L. Provis, Influence of slag composition on the stability of steel in alkali-activated cementitious materials, J. Mater. Sci. 53 (2018) 5016–5035.

[290] H.A. Videla, L.K. Herrera, Understanding microbial inhibition of corrosion. A comprehensive overview, Int. Biodeterior. Biodegrad. 63 (2009) 896–900.

[291] R. Zuo, Biofilms: Strategies for metal corrosion inhibition employing microorganisms, Appl. Microbiol. Biotechnol. 76 (2007) 1245–1253.

[292] A. Pedersen, M. Hermansson, Inhibition of metal corrosion by bacteria, J. Bioadhesion Biofilm Res. 3 (1991) 1–11.

[293] X. Ke, Improved durability and sustainability of alkali-activated slag cements - Thesis, The University of Sheffield, 2017.

[294] S.A. Bernal, V. Rose, J.L. Provis, The fate of iron in blast furnace slag particles during alkali-activation, Mater. Chem. Phys. 146 (2014) 1–5.

[295] X. Ke, S.A. Bernal, J.L. Provis, Controlling the reaction kinetics of sodium carbonate-activated slag cements using calcined layered double hydroxides, Cem. Concr. Res. 81 (2016) 24–37.

[296] M. Ben Haha, G. Le Saoût, F. Winnefeld, B. Lothenbach, Influence of activator type on hydration kinetics, hydrate assemblage and microstructural development of alkali activated blast-furnace slags, Cem. Concr. Res. 41 (2011) 301–310.

[297] T. Wagner, D.A. Kulik, F.F. Hingerl, S. V Dmytrieva, GEM-Selektor geochemical modeling package: TSolMod library and data interface for multicomponent phase models, Can. Mineral. 50 (2012) 1173–1195.

[298] CEMDATA14, (2017). https://www.empa.ch/web/s308/cemdata (accessed November 23, 2017).

[299] H.C. Helgeson, D.H. Kirkham, G.C. Flowers, Theoretical prediction of the thermodynamic behavior of aqueous electrolytes by high pressures and temperatures. IV, Calculation of activity coefficients, osmotic coefficients, and apparent molal & standard relative partial molal properties to 600°C & 5kB, Am. J. Sci. 281 (1981) 1249–1516.

[300] B. Lothenbach, L. Pelletier-Chaignat, F. Winnefeld, Stability in the system CaO-Al_2O_3-H_2O, Cem. Concr. Res. 42 (2012) 1621–1634.

[301] R.A. Robie, B.S. Hemingway, Thermodynamic properties of minerals and related substances at 298.15 K and 1 bar (10^5 pascals) pressure and at higher temperatures, Washington D.C., 1995.

[302] H.C. Helgeson, J.M. Delany, H.W. Nesbitt, Summary and critique of the thermodynamic properties of rock-forming minerals, Am. J. Sci. (1978) 1–229.

[303] B. Lothenbach, T. Matschei, G. Möschner, F.P. Glasser, Thermodynamic modelling of the effect of temperature on the hydration and porosity of Portland cement, Cem. Concr. Res. 38 (2008) 1–18.

[304] W. Hummel, U. Berner, E. Curti, F.J. Pearson, T. Thoenen, Nagra/PSI Chemical Thermodynamic Data Base 01/01, Parkland, Florida, 2002.

[305] T. Thoenen, W. Hummel, U. Berner, E. Curti, The PSI/Nagra Chemical Thermodynamic Database 12/07, Villigen PSI, Switzerland, 2014.

[306] R.K. Allada, A. Navrotsky, J. Boerio-Goates, Thermochemistry of hydrotalcite-like phases in the MgO-Al_2O_3-CO_2-H_2O system: A determination of enthalpy, entropy, and free energy, Am. Mineral. 90 (2005) 329–335.

[307] I.G. Richardson, Clarification of possible ordered distributions of trivalent cations in layered double hydroxides and an explanation for the observed variation in the lower solid-solution limit, Acta Crystallogr. B. 69 (2013) 629–633.

[308] G.K. Johnson, H.E. Flotow, P.A.G. O'Hare, W.S. Wise, Thermodynamic studies of zeolites: natrolite, mesolite and scolecite., Am. Mineral. 68 (1983) 1134–1145.

[309] I. Kiseleva, A. Navrotsky, I. Belitsky, B. Fursenko, Thermochemical study of calcium zeolites—heulandite and stilbite, Am. Mineral. 86 (2001) 448–455.

[310] D.A. Kulik, Improving the structural consistency of C-S-H solid solution thermodynamic models, Cem. Concr. Res. 41 (2011) 477–495.

[311] E.L. Shock, D.C. Sassani, M. Willis, D.A. Sverjensky, Inorganic species in geologic fluids: Correlations among standard molal thermodynamic properties of aqueous ions and hydroxide complexes, Geochim. Cosmochim. Acta. 61 (1997) 907–950.

[312] D.A. Sverjensky, E.L. Shock, H.C. Helgeson, Prediction of the thermodynamic properties of aqueous metal complexes to 1000°C and 5 kb, Geochim. Cosmochim. Acta. 61 (1997) 1359–1412.

[313] E.L. Shock, H.C. Helgeson, D.A. Sverjensky, Calculation of the thermodynamic and transport properties of aqueous species at high pressures and temperatures: Standard partial molal properties of inorganic neutral species, Geochim. Cosmochim. Acta. 53 (1989) 2157–2183.

[314] E.L. Shock, H.C. Helgeson, Calculation of the thermodynamic and transport properties of aqueous species at high pressures and temperatures: Standard partial molal properties of organic species, Geochim. Cosmochim. Acta. 54 (1990) 915–945.

[315] J.W. Johnson, E.H. Oelkers, H.C. Helgeson, SUPCRT92: A software package for calculating the standard molal thermodynamic properties of minerals, gases, aqueous species, and reactions from 1 to 5000 bar and 0 to 1000°C, 1992.

[316] D.D. Wagman, W.H. Evans, V.B. Parker, R.H. Schumm, I. Halow, The NBS tables of chemical thermodynamic properties. Selected values for inorganic and C_1 and C_2 organic substances in SI units, National Standard Reference Data System, New York, 1982.

[317] B. Martin-Pérez, H. Zibara, R.D. Hooton, M.D.A. Thomas, A study of the effect of chloride binding on service life predictions, Cem. Concr. Res. 30 (2000) 1215–1223.

[318] G. Sergi, S.W. Yu, C.L. Page, Diffusion of chloride and hydroxyl ions in cementitious materials exposed to a saline environment, Mag. Concr. Res. 44 (1992) 63–69.

[319] L. Tang, L.O. Nilsson, Chloride binding capacity and binding isotherms of OPC pastes and mortars, Cem. Concr. Res. 23 (1993) 247–253.

[320] H. Zibara, Binding of external chloride by cement pastes - Thesis, University of Torronto, Canada, 2001.

[321] NT Build 492, Concrete, mortar and cement-based repair materials: Chloride migration coefficient from non-steady-state migration experiments, Nordtest Methods, 1999.

[322] L. Tang, Chloride trasnport in concrete - Measurement and Prediction -Thesis, Chalmers University of Technology, 1996.

[323] European Union - Brite EuRam III, DuraCrete - General guidelines for durability design and redesign. Probabilistic performance based durability design of concrete structures, 2000.

[324] International Federation of Structural Concrete (fib), fib Model Code for Service Life Design, 2006.

[325] P. Spiesz, M.M. Ballari, H.J.H. Brouwers, RCM: A new model accounting for the non-linear chloride binding isotherm and the non-equilibrium conditions between the free- and bound-chloride concentrations, Constr. Build. Mater. 27 (2012) 293–304.

[326] Q. Yuan, Fundamental studies on test methodes for the transport of chloride ions in cementitious materials - Thesis, University of Gent, 2009.

[327] Y. Elakneswaran, T. Nawa, K. Kurumisawa, Electrokinetic potential of hydrated cement in relation to adsorption of chlorides, Cem. Concr. Res. 39 (2009) 340–344.

[328] H. Hirao, K. Yamada, H. Takahashi, H. Zibara, Chloride binding of cement estimated by binding isotherms of hydrates, J. Adv. Concr. Technol. 3 (2005) 77–84.

[329] BS 8500-1:2015+A1:2016, Concrete - Complementary British Standard to BS EN 206. Method of specifying and guidance for the specifier, BSI. (2015).

[330] M. Ben Haha, B. Lothenbach, G. Le Saoût, F. Winnefeld, Influence of slag chemistry on the hydration of alkali-activated blast-furnace slag - Part II: Effect of Al_2O_3, Cem. Concr. Res. 42 (2012) 74–83.

[331] G. Le Saoût, M. Ben Haha, F. Winnefeld, B. Lothenbach, Hydration degree of alkali-activated slags: A ^{29}Si NMR study, J. Am. Ceram. Soc. 94 (2011) 4541–4547.

[332] M. Ben Haha, B. Lothenbach, G. Le Saoût, F. Winnefeld, Influence of slag chemistry on the hydration of alkali-activated blast-furnace slag - Part I: Effect of MgO, Cem. Concr. Res. 41 (2011) 955–963.

[333] I.G. Richardson, G.W. Groves, Microstructure and microanalysis of hardened cement pastes involving ground granulated blast-furnace slag, J. Mater. Sci. 27 (1992) 6204–6212.

[334] F. Bonk, J. Schneider, M.A. Cincotto, H. Panepucci, Characterization by multinuclear high-resolution NMR of hydration products in activated blast-furnace slag pastes, J. Am. Ceram. Soc. 86 (2003) 1712–1719.

[335] M.U. Okoronkwo, F.P. Glasser, Stability of strätlingite in the CASH system, Mater. Struct. 49 (2016) 4305–4318.

[336] R.J. Myers, S.A. Bernal, J.D. Gehman, J.S.J. Van Deventer, J.L. Provis, The role of Al in cross-linking of alkali-activated slag cements, J. Am. Ceram. Soc. 98 (2015) 996–1004.

[337] A. Dauzeres, G. Achiedo, D. Nied, E. Bernard, S. Alahrache, B. Lothenbach, Magnesium perturbation in low-pH concretes placed in clayey environment - Solid characterizations and modeling, Cem. Concr. Res. 79 (2016) 137–150.

[338] D. Nied, K. Enemark-Rasmussen, E. L'Hopital, J. Skibsted, B. Lothenbach, Properties of magnesium silicate hydrates (M-S-H), Cem. Concr. Res. 79 (2016) 323–332.

[339] S.A. Bernal, J.L. Provis, R.J. Myers, R. San Nicolas, J.S.J. Van Deventer, Role of carbonates in the chemical evolution of sodium carbonate-activated slag binders, Mater. Struct. 48 (2014) 517–529.

[340] A.R. Sakulich, S. Miller, M.W. Barsoum, Chemical and microstructural characterization

of 20-month-old alkali-activated slag cements, J. Am. Ceram. Soc. 93 (2010) 1741–1748.

[341] X. Hua, J.L. Provis, J.S.J. Van Deventer, P. V. Krivenko, Characterization of aged slag concretes, ACI Mater. J. 105 (2008) 131–139.

[342] A.M. Rashad, Y. Bai, P.A.M. Basheer, N.B. Milestone, N.C. Collier, Hydration and properties of sodium sulfate activated slag, Cem. Concr. Compos. 37 (2013) 20–29.

[343] N. Mobasher, S.A. Bernal, J.L. Provis, Structural evolution of an alkali sulfate activated slag cement, J. Nucl. Mater. 468 (2016) 97–104.

[344] N. Mobasher, S.A. Bernal, O.H. Hussain, D.C. Apperley, H. Kinoshita, J.L. Provis, Characterisation of $Ba(OH)_2$-Na_2SO_4-blast furnace slag cement-like composites for the immobilisation of sulfate bearing nuclear wastes, Cem. Concr. Res. 66 (2014) 64–74.

[345] S.A. Bernal, Advances in near-neutral salts activation of blast furnace slags, RILEM Tech. Lett. 1 (2016) 39–44.

[346] G.K. Glass, N.R. Buenfeld, The influence of chloride binding on the chloride induced corrosion risk in reinforced concrete, Corros. Sci. 42 (2000) 329–344.

[347] K.Y. Foo, B.H. Hameed, Insights into the modeling of adsorption isotherm systems, Chem. Eng. J. 156 (2010) 2–10.

[348] F. Haghseresht, G.Q. Lu, Adsorption characteristics of phenolic compounds onto coal-reject-derived adsorbents, Energy Fuels. 12 (1998) 1100–1107.

[349] M.V.A. Florea, H.J.H. Brouwers, Chloride binding related to hydration products Part I : Ordinary Portland Cement, Cem. Concr. Res. 42 (2012) 282–290.

[350] X. Ke, S.A. Bernal, O.H. Hussein, J.L. Provis, Chloride binding and mobility in sodium carbonate-activated slag pastes and mortars, Mater. Struct. 50 (2017) 1–13.

[351] A. Mesbah, J.P. Rapin, M. Franąois, C. Cau-Dit-Coumes, F. Frizon, F. Leroux, G. Renaudin, Crystal structures and phase transition of cementitious Bi-anionic AFm-(Cl^-, CO_3^{2-}) compounds, J. Am. Ceram. Soc. 94 (2011) 261–268.

[352] A. Mesbah, C. Cau-Dit-Coumes, F. Frizon, F. Leroux, J. Ravaux, G. Renaudin, A new investigation of the Cl^--CO_3^{2-} substitution in AFm phases, J. Am. Ceram. Soc. 94 (2011) 1901–1910.

[353] L. Châtelet, J.Y. Bottero, J. Yvon, A. Bouchelaghem, Competition between monovalent and divalent anions for calcined and uncalcined hydrotalcite: anion exchange and adsorption sites, Colloids Surfaces A Physicochem. Eng. Asp. 111 (1996) 167–175.

[354] U.A. Birnin-Yuari, F.P. Glasser, Friedel's salt, $Ca_2Al(OH)_6(Cl,OH).2H_2O$: Its solid solutions and their role in chloride binding, Cem. Concr. Res. 28 (1998) 1713–1723.

[355] A. Noushini, A. Castel, Performance-based criteria to assess the suitability of geopolymer concrete in marine environments using modified ASTM C1202 and ASTM C1556 methods, Mater. Struct. 51 (2018) 1–16.

[356] P. Hlaváček, S. Reinemann, G.J.G. Gluth, M. Rünger, G. Ebell, J. Mietz, H.-C. Kühne,

Durability-related properties of geopolymer mortars, in: 6th Int. Conf. Non-Traditional Cem. Concr., Brno, Czech Republic, 2017.

Outputs from this thesis

Published articles in peer-reviewed journals

1. Shishir Mundra, Maria Criado, Susan A. Bernal, John L. Provis. 'Chloride-induced corrosion of steel rebars in simulated pore solutions of alkali-activated concretes.' Cement and Concrete Research, 100 (2017), 385-397.
2. Shishir Mundra, Susan A. Bernal, Maria Criado, Petr Hlaváček, Gino Ebell, Steffi Reinemann, Gregor J. G. Gluth, John L. Provis. 'Steel corrosion in reinforced alkali-activated materials.' RILEM Technical Letters, 2 (2017), 33-39. *(Invited Publication)*

Publications under preparation

1. Shishir Mundra, John L. Provis. 'Influence of sulfide on the passivation and chloride-induced corrosion of steel in highly alkaline solutions.'
2. Shishir Mundra, Dale P. Prentice, Susan A. Bernal, John L. Provis. 'A service-life framework for alkali-activated slags in the presence of chlorides.'

Conference publications

1. Heeren N., Mundra S., Myers R.J. 'Monte Carlo approach to integrated chemical, physical, and life cycle impact assessments of cement related materials.', 15th International Congress on the Chemistry of Cement, ICCC2019. Prague, Czech Republic, September 16-20, 2019.
2. Mundra S., Prentice D.P, Ke X., Bernal S.A., Provis J.L. 'Modelling the service life of alkali-activated concretes', in 15th International Congress on the Chemistry of Cement, ICCC2019. Prague, Czech Republic, September 16-20, 2019.
3. J.L. Provis, S.A. Bernal, Z. Tan, M. Criado, S. Mundra, X. Ke. 'Designing durable and sustainable alkali-activated cements and concretes, from the fresh to the hardened state.' Conference in Honour of Karen Scrivener's 60th birthday. Lausanne, Switzerland, 2018.
4. Criado M., Mundra S., Bernal S.A., Provis J.L. 'Influence of sulfide on the onset of chloride-induced corrosion of steel reinforcement in alkali-activated slags', in 6th

International Conference on Durability of Concrete Structures (ICDCS2018). Leeds, United Kingdom, July 18-20, 2018.

5. Bernal S.A., Ke X., Criado M., Mundra S., Provis J.L. 'Factors controlling carbonation resistance of alkali-activated materials', in 10th ACI/RILEM International Conference in Cementitious Materials and Alternative Binders for Sustainable Concrete. Montreal, Canada, October 2-4, 2017.
6. Mundra S., Bernal S.A., Provis J.L. 'Chloride induced corrosion of steel in alkali-activated cements: A review', in 71st RILEM Annual Week, and International Conference in Advances in Construction Materials and Systems. Chennai, India, September 3-8, 2017
7. Criado M., Mundra S., Bernal S.A., Provis J.L. 'A study on the passive state stability of steel embedded in alkali activated slag mortars', in XIV DBMC - 14th International Conference on Durability of Building Materials and Components. Ghent, Belgium, May 29-31, 2017.
8. Mundra S., Bernal S.A., Provis J.L. 'Corrosion initiation of steel reinforcement in simulated alkali-activated slag pore solution', in 1st International Conference of Construction Materials for Sustainable Future, CoMS2017. Zadar, Croatia, April 19-21, 2017.
9. Mundra S., Criado M., Bernal S.A., Provis J.L. 'Breakdown of the passivity of steel in simulated alkali-activated concrete pore solutions', in 36th Cement and Concrete Science Conference, Cardiff, Wales, September 5 - 6 2016.

Other presentations at conferences of TC meetings:

1. Mundra S., Provis J.L. 'Steel corrosion in alkali-activated slags' 3rd meeting EFC-WP 11 Task Group: Steel Corrosion in Alkali-Activated Concrete, Sheffield, United Kingdom, June 21st, 2018.
2. Mundra S., Bernal S.A., Provis J.L. 'Corrosion of the steel reinforcement in alkali-activated cements', talk presented in the 1st meeting EFC-WP 11 Task Group: Steel Corrosion in Alkali-Activated Concrete, Berlin, Germany, March 28-29, 2017.
3. Criado M., Mundra S., Bernal S.A., Provis J.L. 'Corrosion behaviour of alkali-activated slag mortars under exposure to different environments', talk presented in the 1st meeting EFC-WP 11 Task Group: Steel Corrosion in Alkali-Activated Concrete, Berlin, Germany, March 28-29, 2017.

4. Mundra S., ‘Eco-efficient cements: Less CO2, less energy but still more durable?’, IOM3 Young Persons’ Lecture Competition, Sheffield UK, March 9, 2017.
5. Mundra S., Criado M., Bernal S.A., Provis J.L. ‘Effect of pH on the passivity of steel in simulated alkali-activated concrete pore solutions’, talk presented in Advances in Linking Science to Engineering, EUROCORR 2016. Montpellier, France, September 11- 15, 2016.

Posters

1. Criado M., Mundra S., Liang D., Bernal S.A., Provis J.L., ‘Effect of sulfides in the passive layer of steel reinforcement in alkali-activated slags’, in International Conference on Alkali Activated Materials and Geopolymers: Versatile Materials Offering High Performance and Low Emissions. Tomar, Portugal, May 28 - June 1, 2018.
2. Mundra S., Bernal S.A., Provis J.L., ‘Durability of steel reinforced alkali-activated concretes in the presence of chloride’, The Future of Cement, UNESCO Paris, France, June 6 - 8, 2017.